

Molecular absorption in the cores of AGN:  
On the unified model

Dissertation  
zur  
Erlangung des Doktorgrades (Dr. rer. nat.)  
der  
Mathematisch-Naturwissenschaftliche Fakultät  
der  
Rheinischen Friedrich-Wilhelms-Universität Bonn

vorgelegt von  
Caterina Maria Violetta Impellizzeri  
aus  
Palermo (Italien)

Bonn, 2008

Angefertigt mit Genehmigung der Mathematisch-Naturwissenschaftlichen Fakultät der Rheinischen Friedrich-Wilhelms-Universität Bonn

Referent: Prof. Dr. U. Klein  
Koreferent: Priv.-Doz. Dr. W. K. Huchtmeier

Tage der Promotion: 05.09.2008

Diese Dissertation ist auf dem Hochschulschriftenserver der ULB Bonn  
[http://hss.ulb.uni-bonn.de/diss\\_online](http://hss.ulb.uni-bonn.de/diss_online) elektronisch publiziert.

Erscheinungsjahr: 2008

*A mamma e papà*



# Preface

One of the fundamental concepts in the unified scheme of AGN is that both Seyfert 1 and Seyfert 2 galaxies harbour supermassive black holes that act as nuclear engines, but in Seyfert 2 galaxies the nucleus is blocked from direct view by an optically and geometrically thick molecular torus. However, whilst the unified scheme has proven very successful, little is known about the physical properties of the torus itself. Searches for absorption lines of common molecules like CO and OH have mostly yielded non-detections. Before concluding that tori are not molecular, radiative excitation effects, which suppress the opacity in the lowest transitions due to the proximity to the high brightness temperature radio radiation from the nucleus causing excitation into higher states, must be investigated.

To explore these effects, we conducted a survey searching for excited OH from a sample of 31 Seyfert 2 galaxies. Here, I present the results of Effelsberg observations at 6.0 GHz yielding five new detections, and at 4.7 GHz yielding no detections. I also present spectral-line VLBI observations carried out at 13.4 GHz, which detected excited OH towards the cores of Cygnus A and NGC 1052. These observations confirm the presence of a molecular torus in these sources. A subsample of the 31 Seyfert 2 galaxies was further searched for methanol at 6.7 GHz, yielding the first ever extragalactic detection of methanol towards NGC 3079. It is, however, unclear if the methanol is associated with the active nucleus or the starburst around the source or possibly connected to the superbubble in this source. A blue-shifted feature in the spectrum also indicates that methanol is present in the large-scale molecular outflows.

Finally, I present the exciting new discovery of a water maser at redshift 2.64, which is the most distant source where water has ever been found. Luminous extragalactic water masers are associated with the nuclear activity of their host galaxies. The maser emission originates from within a few parsecs of the central engine, being associated nuclear accretion disks or through interactions between the jet emerging from the nucleus and ambient molecular clouds, or nuclear outflows. The transition observed requires gas temperatures in excess of 300 K and particle densities  $n(\text{H}_2) \geq 10^7 \text{ cm}^{-3}$ . It is the first time that such a dense interstellar gas component has been observed in the early Universe. This discovery has been possible only due to the magnification provided by a foreground galaxy; it acts as a cosmic telescope reducing the integration time required for a detection by a factor of  $\sim 1000$ .



# Contents

<b>Preface</b>	<b>i</b>
<b>1 Introduction</b>	<b>1</b>
1.1 Active Galactic Nuclei and the Unified Scheme . . . . .	1
1.1.1 The “flavours” of AGN . . . . .	2
1.1.2 The unification of AGN . . . . .	4
1.1.3 Orientation effects and the radio-quiet unification . . . . .	6
1.2 The molecular torus . . . . .	9
1.2.1 HI absorption . . . . .	10
1.2.2 Maser emission and the circumnuclear tori . . . . .	11
1.3 OH surveys and the scope of this thesis . . . . .	13
1.3.1 OH surveys . . . . .	14
1.3.2 Radiative Excitation . . . . .	15
1.3.3 A new search strategy . . . . .	17
<b>2 A survey for excited OH</b>	<b>21</b>
2.1 The sample . . . . .	21
2.2 Effelsberg observations . . . . .	24
2.2.1 Sensitivity considerations . . . . .	26
2.2.2 Data reduction . . . . .	28
2.3 Results . . . . .	29
2.3.1 Notes on individual sources . . . . .	30
2.4 Discussion . . . . .	49
2.4.1 Detections vs nondetections . . . . .	50
2.4.2 OH excitation temperatures . . . . .	51
2.4.3 Excitation of OH . . . . .	54
2.5 Conclusions . . . . .	54
<b>3 Observations of Cygnus A and NGC 1052</b>	<b>57</b>
3.1 Introduction . . . . .	57
3.2 VLBA Observations . . . . .	59
3.3 Data Calibration . . . . .	60
3.4 Results . . . . .	63
3.4.1 Cygnus A . . . . .	63
3.4.2 NGC 1052 . . . . .	66
3.5 Conclusions . . . . .	69

<b>4</b>	<b>A survey for extragalactic methanol</b>	<b>71</b>
4.1	Introduction . . . . .	71
4.2	Enhanced absorption in the 6.7 GHz methanol line . . . . .	72
4.3	The sample . . . . .	73
4.4	Observations and data reduction . . . . .	74
4.5	Results and individual sources: The detections . . . . .	75
4.5.1	NGC 3079 . . . . .	76
4.5.2	Mrk 3 . . . . .	85
4.5.3	Mrk 348 . . . . .	88
4.5.4	NGC 6240 . . . . .	90
4.6	Results and individual sources: The non-detections . . . . .	93
4.6.1	Cygnus A (3C 405) . . . . .	93
4.6.2	Mrk 231 . . . . .	94
4.6.3	NGC 1052 . . . . .	95
4.6.4	NGC 2110 . . . . .	95
4.6.5	NGC 4261 (3C 270) . . . . .	96
4.6.6	NGC 5135 . . . . .	97
4.7	Conclusions . . . . .	98
<b>5</b>	<b>Water in the early Universe</b>	<b>101</b>
5.1	Introduction . . . . .	101
5.2	MG J0414+0534 . . . . .	103
5.3	Single dish 100 m Effelsberg radio telescope observation . . . . .	104
5.3.1	Observations . . . . .	104
5.3.2	Data reduction . . . . .	107
5.3.3	Results . . . . .	107
5.4	The Expanded Very Large Array . . . . .	108
5.4.1	Observations . . . . .	108
5.4.2	EVLA Data Reduction . . . . .	111
5.4.3	Results . . . . .	114
5.5	Results from combined datasets . . . . .	114
5.6	Discussion . . . . .	116
5.6.1	The highest redshift water maser . . . . .	116
5.6.2	An extremely luminous water maser . . . . .	116
5.6.3	Where does the maser originate? . . . . .	119
5.7	Conclusions . . . . .	120
<b>6</b>	<b>Summary and Outlook</b>	<b>121</b>
6.1	A search for radiatively excited OH . . . . .	121
6.1.1	Effelsberg observations . . . . .	122
6.1.2	VLBA observations . . . . .	122
6.1.3	Future Work . . . . .	123
6.2	A survey for extragalactic methanol . . . . .	124
6.2.1	Future Work . . . . .	124
6.3	The detection of water vapour in the early Universe . . . . .	125
6.3.1	Future work . . . . .	125

*CONTENTS*

v

<b>A 6016 MHz satellite lines</b>	<b>127</b>
<b>B 6049 MHz satellite lines</b>	<b>131</b>
<b>C 4765 MHz satellite lines</b>	<b>135</b>
<b>D 4660 MHz satellite lines</b>	<b>139</b>
<b>Bibliography</b>	<b>143</b>
<b>Danksagung</b>	<b>160</b>



# List of Figures

1.1	Emission lines characteristic of various AGN types . . . . .	3
1.2	Active galactic nucleus in the unified scheme . . . . .	7
1.3	Picture of the tracers of an AGN . . . . .	11
1.4	Water masers in NGC 4258 . . . . .	12
1.5	Distribution of column densities, $N_{\text{H}}$ , for type 1 to type 2 AGN . . . . .	14
1.6	Lower hyperfine states of the OH rotational ladder . . . . .	18
2.1	The Effelsberg telescope in autumn . . . . .	25
2.2	Spectra of sources from Effelsberg survey at 6 GHz . . . . .	31
2.2	continued. . . . .	32
2.2	continued. . . . .	33
2.2	continued. . . . .	34
2.3	Collection of HST and MERLIN images of NGC 3079 . . . . .	34
2.4	Effelsberg spectrum and continuum map of Mrk 231 . . . . .	38
2.5	Effelsberg spectrum and continuum map of Mrk 273 . . . . .	40
2.6	The OH absorption spectra of NGC 5793 and NGC3079 at 1.67 GHz and 6 GHz . . . . .	52
3.1	$\text{CO}^+$ spectrum of Cygnus A . . . . .	58
3.2	VLBA $uv$ -coverage of Cygnus A . . . . .	61
3.3	A data cube . . . . .	61
3.4	VLBA calibration steps . . . . .	64
3.5	VLBA image of Cygnus A at 1.4 GHz . . . . .	65
3.6	VLBA image of NGC 1052 at 13.4 GHz . . . . .	66
3.7	The 22 GHz continuum image of NGC 1052 . . . . .	67
3.8	Absorption profiles of NGC 1052 . . . . .	68
4.1	Brightness distribution of the 6.7 GHz transition . . . . .	74
4.2	Cygnus A: Baseline ripples at 6.7 GHz . . . . .	76
4.3	Effelsberg methanol survey resulting spectra . . . . .	77
4.4	The 6.7 GHz methanol absorption profile toward NGC 3079 . . . . .	80
4.5	VLBI images of NGC 3079 at 1.67 GHz, 2.3 GHz, 5 GHz and 15.4 GHz . . . . .	81
4.6	6.7 GHz Effelsberg spectra of Mrk 3 . . . . .	86
4.7	6.7 GHz Effelsberg spectrum of Mrk 3 over all epochs . . . . .	86
4.8	6.7 GHz Effelsberg spectra of Mrk 348 . . . . .	89
4.9	A collection of optical, X-ray and infra-red images showing the double nuclei in NGC 6240 . . . . .	90

4.10	MERLIN 5 GHz continuum map of NGC 6240 . . . . .	91
4.11	NGC 6240: Effelsberg spectrum at 6.7 GHz . . . . .	92
4.12	Doubled-peaked Effelsberg pointing of NGC 4261 . . . . .	96
5.1	Spectral signature from a jet and disk maser . . . . .	102
5.2	Redshift distribution of known H <sub>2</sub> O masers . . . . .	103
5.3	HST and MERLIN imaging of MG J0414+0534 . . . . .	104
5.4	VLBI imaging of MG J0414+0534 . . . . .	105
5.5	CO emission from MG J0414+0534 . . . . .	106
5.6	H I absorption from MG J0414+0534 . . . . .	106
5.7	Effelsberg spectra of MG J0414+0534 . . . . .	109
5.8	Baseline calibration of MG J0414+0534 using 3C 161 . . . . .	110
5.9	The planned band availability of EVLA . . . . .	110
5.10	The 6.1 GHz EVLA radio images of MG J0414+0534 . . . . .	115
5.11	The 6.1 GHz radio spectra of MG J0414+0534 taken with Effelsberg and the EVLA . . . . .	117

# Chapter 1

## Introduction

Active galactic nuclei (AGN) are the spectacular manifestation of accretion onto super-massive black holes (SMBH). The active nucleus, with a size comparable to the solar system, is embedded in an otherwise typical galaxy, emitting an enormous concentration of luminosity which ranges between  $10^5 L_\odot$  to  $10^{13} L_\odot$  (e.g. Tacconi et al. 2002), and in the most luminous cases contributes more to the total luminosity than the entire stellar component of its host galaxy ( $10^{11} L_\odot$ ). The emission covers the whole electromagnetic spectrum, from radio emission to  $\gamma$  rays. AGN are the most luminous nontransient objects ever discovered and are accordingly the most intriguing. How is such an energy output produced? Years of research have proven they play a fundamental role in the overall dynamics of their host galaxy and in the formation of cosmological structures.

In this work, a sample of AGN was selected and studied in detail with the goal of understanding the properties of the material surrounding the active nucleus. The large amounts of gas and dust, which will eventually feed the SMBH, are entrained in large molecular clouds - forming the so-called **torus** around the AGN. Determining whether such torus is present and indeed molecular is the subject of much ongoing research. The aim of this thesis was to find evidence for a molecular torus at the centre of AGN. The main observational tools for this work were molecular absorption spectroscopy at cm-wavelength using single-dish observations with the 100 m telescope in Effelsberg and higher-resolution interferometric observations to resolve the innermost regions of a few selected candidates.

In this Chapter, an introduction to AGN is presented, providing the motivation for this particular study. An emphasis will be given to the role of the torus and its predicted properties.

### 1.1 Active Galactic Nuclei and the Unified Scheme

In 1908, an unusual object was discovered by Edward A. Fath, which, in addition to the normal continuum emission and to absorption lines commonly seen in other nebulae also showed strong emission lines (Fath 1908). The galaxy was NGC 1068, and the emission lines were the fingerprints of its yet unknown active nucleus. Following this initial discovery, more such galaxies were found to produce emission lines. In 1943, Carl K. Seyfert published his fundamental paper on emission line galaxies (Seyfert 1943), in which he described the main features of the emission lines of six sources. Seyfert was the first to recognise that these galaxies formed a new class of object. He also noted that the emission

lines originated from a point-like nucleus at the centre of the galaxies which contributed a sometimes sizeable (6 % to 48 %) fraction of the total light in those systems. From the large width of the emission lines, he could further derive a high velocity dispersion in the emitting medium. These types of objects are now known as Seyfert galaxies. But it was not until the discovery of quasars and their subsequent identification as being the centres of distant galaxies that AGN became a prime field of astrophysical research. In 1963, Maarten Schmidt studying the emission lines in the spectrum of the radio star 3C 273 deduced that the redshift of the object was 0.16 and therefore cosmological, implying a gigantic intrinsic luminosity. This new class of object was named quasi-stellar radio sources (quasars), and owed their stellar (point-like) appearance simply due to the host galaxy being too faint to be detected. Apart from quasars and Seyfert galaxies, there are other classes of AGN now known, such as radio galaxies and blazars. Figure 1.1 shows an example of the different emission line characteristics in the optical spectra for various types of AGN.

### 1.1.1 The “flavours” of AGN

The subclasses, or flavours, of AGN are classified according to their observational properties. These can be mainly grouped into radio quiet and radio loud AGN. Also, properties like polarization, and whether or not emission lines are present can also vary. A few different types of AGN are presented in the following, sorted according to decreasing luminosity.

**Quasars** (QSOs) are the most luminous subclass of AGN and the most energetic sources in the Universe. A small fraction (5 % to 10 %) are the strong radio sources which originally defined the quasar class. The nuclear emission dominates the host galaxy light. The host galaxies of quasars can be spirals, irregulars or ellipticals. There is a correlation between the quasar’s luminosity and the mass of its host galaxy, so that the most luminous quasars inhabit the most massive galaxies (ellipticals). Their number density peaks at  $z \sim 2.5$  (Richards et al. 2006; Hopkins et al. 2007), roughly coinciding with the peak in star formation (Hopkins & Beacom 2006). Their spectra are similar to the Seyfert 2 galaxies (see below), showing only broad lines (width  $\geq 1000 \text{ km s}^{-1}$ ). They are further divided into radio-loud and radio-quiet. Radio-loud quasars behave like radio-quiet quasars with the addition of emission from a jet and tend to have an elliptical host galaxy.

**BL Lacs** are named after the prototype BL Lacertae which was thought to be a variable star in the Lacerta constellation. They are very bright radio objects and show continuum emission from the AGN over the whole electro-magnetic spectrum, however they lack strong emission or absorption lines in their spectra. A related class of objects are the Optically Violently Variables (OVVs), showing very large variations on short time-scales. Collectively, BL Lacs, OVVs and QSOs are called **blazars**, the name deriving from a combination of BL Lac and Quasar. BL Lacs are essentially strong, have flat radio spectra and are strongly variable both in brightness and polarization.

**Radio Galaxies** are typically associated with giant elliptical galaxies. The radio emission is not confined to the nucleus alone but also appears in extended jets which originate in the nucleus. The jets, mostly symmetric, consist of a collimated outflow

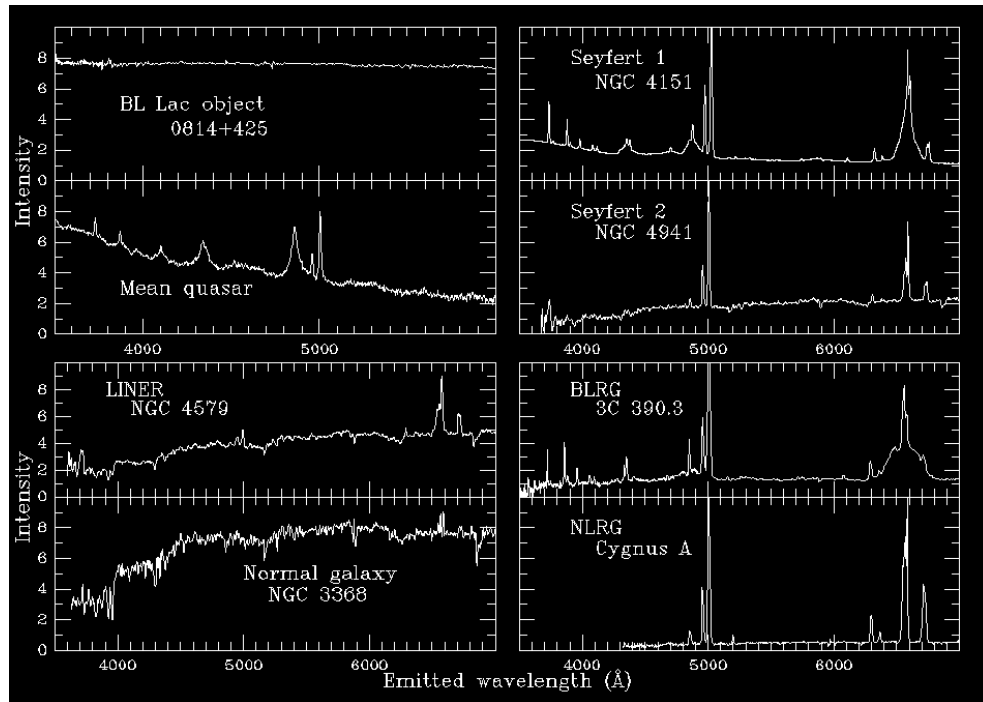


Figure 1.1: Different types of AGN can be distinguished based on their spectroscopic characteristics. The plot shows a compilation of emission line spectra as an example of various types of AGN. Seyfert galaxies are less luminous local counterparts of quasars. The emission lines from Seyfert and radio galaxies have similar widths; Seyfert 2 galaxies show narrower linewidths whereas those of Seyfert 1 galaxies are much broader. The spectra of quasars are similar to those of Seyfert 1 nuclei, with very broad lines believed to originate in a region closer to the central black hole. Thus, the broad line components are in the spectra of Seyfert 1 and broad line radio galaxies (BLRGs) and quasars. They are missing in the spectra of Seyfert 2 and narrow line radio galaxies (NLRGs). The spectra of BL Lacertae objects are virtually featureless, and their redshifts cannot be determined unless the surrounding galaxy is detected. LINERs (low-ionization nuclear emission-line Regions) show low activity levels, are a low-luminosity end of the processes seen in most AGN. The spectrum of a non-active galaxy, NGC 3368, is also shown for comparison. The data for individual spectra are taken from the following sources: 0814+425 & 3C 390.3 by Lawrence et al. (1996), mean quasar by Francis et al. (1991), NGC 4579 & NGC 4941 by Keel (1983), NGC 3368 by Kennicutt (1992), Cygnus A by Owen et al. (1990), NGC 4151 by Osterbrock et al. (1990) and Thompson (1995). The spectrum compilation is by C. W. Keel (<http://www.astr.ua.edu/keel/agn/spectra.html>).

of relativistic particles spiralling in a magnetic field. These emit synchrotron radiation and are observed at radio and sometimes optical frequencies. The jets can reach out to several 100 kpc or even Mpc from the active nucleus. Hotspots and large radio lobes are observed when the jets impact the intergalactic medium. Radio galaxies are classified following Fanaroff & Riley (1974). Fanaroff-Riley type 1 (FR I) galaxies are lower luminosity radio sources, which are brightest at the centre and whose radio spectra are steepest at the radio lobes. An example of a FR I galaxy is M87. Fanaroff-Riley type 2 (FR II) galaxies are more luminous in the radio regime. They have edge-brightened radio lobes (called hot spots) and have the steepest radio spectra in the inner regions. A prominent FR II galaxy is Cygnus A (which forms part of the sample studied in this thesis, see Chapter 3). Similarly to Seyfert galaxies, they are divided into broad-line (BLRG; FR I) and narrow-line radio galaxies (NLRG; FR II).

**Seyfert Galaxies** are gas and dust-rich spiral galaxies with a bright nucleus. About 3% to 5% of all galaxies belong to this class (Maiolino & Rieke 1995; Maia et al. 2003). Seyfert galaxies are generally weak radio sources and rarely show clearly defined, linear radio jets. They are divided into two subclasses, according to their line emission:

- Seyfert 1 (Sy 1) galaxies have two sets of emission lines in their spectra; narrow lines originating in the narrow line regions (NLR), with velocities of several hundreds of  $\text{km s}^{-1}$  and broad lines originating in the broad line region (BLR) with widths up to  $10^4 \text{ km s}^{-1}$ . An example is NGC 4151 (see Chapter 2).
- Seyfert 2 (Sy 2) galaxies show only narrow-line emission. A prominent example is NGC 1068 (see Chapter 2). They are thought to be intrinsically the same as type 1 galaxies, but with our view of the broad line region being obscured by a torus. There are about three times more Seyfert 2 than Seyfert 1 galaxies. They are now also given a fractional classification depending on the relative strengths of the narrow and broad components (e.g. type 1.5 or type 1.9).

**LINERs** (low-ionization nuclear emission-line regions) are galaxies that show only weak nuclear emission lines, and no other signatures of AGN emission. They constitute the lowest-luminosity class of radio-quiet AGN.

A popular quest over the last decade has been to find some order on this zoo of subclasses, in the search for an underlying physics common to all sources.

### 1.1.2 The unification of AGN

Unified schemes of AGN try to unite two or more classes of objects, by suggesting that they are really a single type of physical object observed under different conditions. The one property that all the AGN types have in common is a very large amount of energy that is released in a very small volume. The bolometric energy of a bright quasar corresponds to  $\sim 10^{41} \text{ W}$  ( $10^{14} L_{\odot}$ ). The lifetime of such an active phase is estimated to be roughly  $10^7$  years from the size of the radio lobes<sup>1</sup>. Therefore, the total energy output is of the

---

<sup>1</sup>The lifetime estimates also comes from the mass build-up in the central black hole. If, for example, radiating  $10^{41} \text{ W}$  and the radiative efficiency is 10%, then the build-up of a  $10^9 M_{\odot}$  central mass will take place in  $10^8$  years.

order of  $10^{56}$  J. From the variability of its flux density on scales of hours, the emitting region size is estimated to be of the order of a few light hours to light days, or 10 AU. It becomes clear that nuclear fusion cannot be the source of energy in those sources since, having an efficiency factor for conversion of matter into energy of  $\epsilon \sim 0.8\%$ , the mass required to power the luminosity would far exceed that seen in the central system.

Accretion onto a supermassive black hole was proposed in different models to explain the enormous energy output (Salpeter 1964; Zeldovich 1964). However, the idea became popular only when the collapsed bodies proposed by Lynden-Bell (1969) became detectable through their effect on the mass-to-light ratio. Further support came from the discovery of variable X-ray sources which were likely to contain accreting black holes of stellar masses (e.g. see Webster & Murdin, 1972; Tananbaum et al. 1972; Thorne & Price 1975). The accretion luminosity is given by

$$L_{\text{acc}} = \epsilon \dot{M} c^2 \quad (1.1)$$

where  $\epsilon$  is the radiative efficiency,  $\dot{M}$  is the accretion rate and  $c$  is the speed of light.

The current picture of AGN requires a fraction of the gravitational energy that is created by contraction or collapse to be radiated. The radiative efficiency,  $\epsilon$ , for accretion of matter onto a black hole ranges from 6% for a non-rotating black hole to 42% for a rapidly rotating black hole (Krolik 1999). The masses of the black holes located at the centre of galaxies range from  $10^6 M_{\odot}$  to  $10^{10} M_{\odot}$  (e.g. Shankar et al. 2004) which built up by the accumulated accretion over a Hubble time. These are referred to as supermassive black holes (SMBHs).

As gas falls onto a black hole, an accretion disk is formed from the cold material close to the central black hole, with high accretion rates corresponding to high luminosities (Fabian & Rees 1995). The accretion rates depend further on the mass of the black hole and on the amount of fuel available. The Eddington luminosity,  $L_E$ , gives an upper limit for the luminosity from accretion, assuming spherical symmetry (Eddington 1925). The Eddington luminosity is the luminosity that is reached when the radiation pressure balances the gravitational pull of the black hole

$$L_{\text{acc}} \leq L_E = 3.3 \times 10^{11} L_{\odot} \frac{M_{\text{BH}}}{10^7 M_{\odot}} \quad (1.2)$$

where  $M_{\text{BH}}$  is the mass of the black hole. When the luminosities and accretion rates are higher than the Eddington limit, super-Eddington accretion can occur for a short period. The fuelling further depends on the large-scale structure of its host galaxy. Dissipative processes in the accretion disk transport matter inwards and angular momentum outwards. It is still, however, not clear how the momentum transfer occurs. The accretion disk heats up, and its spectrum peaks in the optical-ultraviolet waveband (the blue bump). The fuelling mechanism is not fully understood, however, merger events and instabilities in the galaxies such as spirals and bars are thought to trigger the inflow of matter to the nucleus (Combes 2001). A corona of hot material forms above the accretion disk and can inverse-Compton scatter photons up to X-ray energies. The radiation from the accretion disk excites cold atomic material close to the black hole and this radiates via emission lines. A large fraction of AGN output is obscured by interstellar gas and dust close to the accretion disk. This may be re-radiated most likely in the infrared.

Another characteristic of AGN are the powerful jets, which take place in the form of synchrotron radiation, line-radiation and inverse-Compton radiation. They radiate in all wavebands from radio to the gamma-rays via the synchrotron and inverse-Compton processes. Jets are made of highly relativistic plasma streams extending in opposite directions, perpendicular to the accretion disk. Highly collimated and fast outflows that emerge from close to the disk are seen in some cases. The direction of the jet ejection must be determined either by the angular momentum axis of the disk or the spin axis of the black hole. The jet production mechanism and indeed the jet composition on very small scales are not known at present, though magnetic fields are likely to play an important role in the launching of the jets (e.g. Meier 2002).

The common source of energy in all AGN suggests a similar process occurring in all active galaxies. It is thus expected that a few free parameters can explain the observational differences between them. These parameters are the orientation, the luminosity of the accretion disk and the presence of radio jets. This is the main idea behind the *unified schemes* of AGN. The currently favoured unified scheme is orientation based, proposing to explain that apparent differences between different types of objects arise simply because of their different orientations to the observer. Orientation effects are thought to be responsible for the Seyfert 1 and the Seyfert 2 dichotomy. For an overview, see Antonucci (1993; for both radio-loud and radio-quiet AGN unification) and Urry & Padovani (1995; for a radio-loud unification only).

### 1.1.3 Orientation effects and the radio-quiet unification

In the unified scheme of AGN a single physical model is used to reproduce radio-quiet type 1 AGN (with broad lines) and type 2 AGN (without broad lines). The physics of radio-loud and radio-quiet AGN is somewhat different, as the formation of jets from accretion disks, which will power the radio lobes in radio-loud AGN, is still poorly understood. It is still not known why some AGN have powerful jets, while others only have weak ones or in some cases none at all. However, some aspects of the diverse appearance of AGN, specifically in the radio-quiet regime, can be attributed to orientation effects.

The unification of radio-quiet AGN consists mainly of four classes of objects: Sy 1 and Sy 2 galaxies at low luminosities and their high-luminosity counterparts, type 1 and type 2 QSOs. The basic idea of orientation-dependent obscuration models is that the two types of object are the same if observed along the same line of sight. The standard picture is of an axi-symmetric absorber containing molecular gas and large amounts of dust surrounding the accretion disk.

The geometry of this absorber is thought to be either that of a torus or of a warped disk (see Fig. 1.2, for the torus picture). Tori can exist where energetic processes can provide vertical support, e.g., as in heating or magnetic turbulence at sub-parsec radii. Where infalling material can cool, it forms a thin accretion disk (Shakura & Sunyaev 1973), which may be warped by radiative, magnetic, gravitational, and relativistic effects (Pringle, 1996; Neufeld & Maloney 1995).

For systems at high inclination from the absorber (for an inclination  $i = 90^\circ$  the objects are face-on, or fully inclined), we can see the inner region towards the nucleus, and these objects are classified as Seyfert 1 nuclei. From the free line of sight towards the high velocity gas close to the nucleus, both the narrow line and the broad line region

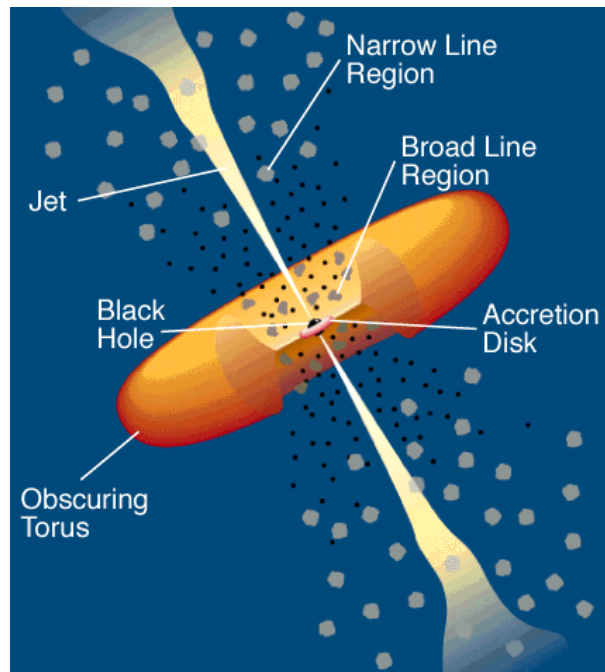


*Figure 1.2:* A schematic picture of an active nucleus in the unified scheme. A luminous accretion disk surrounds the black hole. Near the core, high velocity clouds ionized by the radiation from the accretion disk orbit above the disk emitting broad emission lines. A geometrically and optically thick torus (or warped disk) consisting of molecular clouds obscures the broad line region though the torus. Narrow lines are produced in low velocity clouds farther out from the central source. Radio jets are ejected at relativistic speeds spreading over large scales. The figure, not to scale, has been reproduced from Urry & Padovani (1995).

can be seen<sup>2</sup>. For an object viewed edge-on (for an inclination  $i = 0^\circ$ ), the view towards the centre is obscured by the dusty torus, and these are classified as Seyfert 2 nuclei. Therefore, in this case we see only the low-density, low-velocity gas at a greater distance from the heating source; the narrow line region. From the observed ratio of Seyfert 1 to Seyfert 2 galaxies, which is 1:3 (Maiolino & Rieke 1995; Maia et al. 2003), and assuming a random orientation of sources in the sky, one can estimate the opening angle of the obscuring torus to be  $\sim 70^\circ$ .

Strong support for this picture came from the first observation of broad emission lines in the polarized light towards the Seyfert 2 galaxy NGC 1068 (Antonucci & Miller 1985). The polarized spectrum in this case showed broad lines and a strong continuum, typical of type 1 AGN, with the polarization position angle being perpendicular to the radio jet. The broad component observed in polarized light is believed to come from the broad-line region that is scattered by a hot, gaseous halo above (or below) the plane of the torus, allowing us to view it indirectly. Subsequently, many more type 2 AGN were shown to exhibit a type-1 spectrum in polarized light (e.g. by Tran et al. 1992; Lumsden et al. 2004; Zakamska et al. 2005). These hidden polarized broad lines (HPBL) seem to be present in at least 30% of all Seyfert 2 galaxies (Tran 2001). Another argument for the axi-symmetry of the absorber is given by observations of ionisation cones. These have sharply defined conical or biconical shapes and are well aligned with the radio jet axis (e.g. Pogge 1989; Evans et al. 1991; Storchi-Bergmann et al. 1992).

The building blocks of AGN can be summarized as follows:

1. **the nucleus** which is point-like and variable. The nucleus emits continuum radiation, which extends over a large energy range, and is significantly polarized. At the centre, there is a **supermassive black hole** with a mass of  $10^6 M_\odot$  to  $10^{10} M_\odot$  and a size of  $R_s \ll 10^{-3}$  pc. A relatively small ( $\leq 1$  pc), hot ( $10^4$  K to  $10^6$  K) **accretion disk** is the source of the optical and ultra-violet continuum radiation.
2. Strong narrow and broad emission lines (**NLR**: 10 pc to 100 pc and **BLR**: 0.01 pc to 0.1 pc). Ionized gas clouds orbit around the black hole, emitting allowed, broad emission lines. The broad-line region is compact and close to the nucleus, displaying higher velocities. The narrow-line region is more distant from the nucleus and consists of lower density gas orbiting slowly.
3. **The dusty molecular torus** is a dense ring of molecular gas and dust with a size thought to be  $\sim 1$  pc to 10 pc. It is opaque to optical radiation from the central region and may supply the observed infrared luminosity of the nucleus. The inner border of the torus is set by the dust sublimation temperature ( $T_{\text{sub}} = 1500$  K).
4. **Jets** are linear and symmetric, and can extend up to  $10^6$  pc from the nucleus, i.e. well beyond the stellar component of the galaxy. A continuous energy supply from

---

<sup>2</sup>The broad emission lines exhibit strong Doppler broadening with velocities from  $500 \text{ km s}^{-1}$  to  $4000 \text{ km s}^{-1}$  and are believed to originate near the accretion disk surrounding the black hole. Each part of the accretion disk has a different velocity relative to our line of sight, and the faster the gas is rotating around the black hole, the broader the line will be. Similarly, an illuminated disk wind also has a position-dependent velocity. The narrow lines are believed to originate from the outer part of the AGN where velocities are lower. This is confirmed by the fact that the narrow lines do not vary detectably, which implies that the emitting region is large, contrary to the broad lines which can vary on relatively short time-scales.

the nucleus is necessary for emission at these distances.

Despite the great success of the unification scenario, AGN can have different individual appearances. This is not surprising since an AGN will be strongly affected by its interaction with the environment. Also, in some cases, the type of activity is not easily determined (for example starburst or AGN). Ultra-luminous infrared galaxies (ULIRGs), for example, are very dusty objects, which always contain a strong starburst contribution (Sanders & Mirabel 1996), in addition, in some cases, to an embedded AGN. One famous example is the double-nucleus of NGC 6240 (see Chapter 2 and Chapter 4).

One of the questions in AGN research is: what is the geometry of the obscuring material? While most theoretical work is done on models for tori, some groups favour the idea of a geometrically thin but warped disk (e.g. Phinney 1989). The study of the structure, kinematics, and excitation of the material in the cores of these objects is the only way to directly study massive compact objects, which are not otherwise directly visible and which influence evolution of the central engines and their environments. These studies can be achieved through observations at radio wavelengths of emission and absorption by the neutral atomic, ionized, and molecular components of the torus. The role of gas and dust in AGN is an important one because it feeds the central engines and because it affects the degree of shielding of the strong continuum from various viewing angles. Also, the accreting gas emits intense radiation from the radio to X-ray bands, which further affects the structure and energetics of the parent galaxies.

## 1.2 The molecular torus

An obscuring torus is the key ingredient of the AGN unification scenario. The composition and size of the torus are still, however, poorly known. The dusty molecular torus surrounding the central engine is thought to consist of molecular gas as well as hot ( $T \sim 100$  K to 1500 K) dust. The torus is heated by the nuclear radiation in the optical and ultraviolet, and re-radiated mainly in the IR. In the widespread picture of Urry & Padovani (1995) (shown in Figure 1.2), the torus is depicted as a large toroidal object, yet the origin of the cloud vertical motion which is able to sustain a steady state has been difficult to explain.

Arguments for clumpiness have been given by Krolik & Begelman (1988), from the dynamics of the torus. In order to dynamically support the geometric thickness, random velocities  $\leq 100 \text{ km s}^{-1}$  are needed. Were these velocities thermal, the resulting temperature ( $10^6$  K) would be too high to allow for the existence of dust and molecules. In sufficiently cold gas, however, these velocities would be highly supersonic. Dissipation of such motion can be avoided only if the collision rate between streams of different velocities is small, which can be achieved if the cool gas is organized in clouds. In this scenario, the clouds inner side see the unobscured continuum and are heated by photo-ionization to temperatures  $\sim 10^4$  K. Deeper inside the clouds, the gas is shielded from the nuclear continuum and remains cooler. Hard X-ray photons penetrate the farthest into the clouds, keeping the clouds' mass in a state of high ionization and temperature ( $T \sim 10^3$  K), but it is not enough to dissociate the majority of the molecules (Krolik & Lepp 1989).

Later, an alternative scenario was suggested to explain the thickness of the torus by radiation pressure in a uniform medium (Pier & Krolik 1992). Such pressure could be provided either by the radiation from the accretion disk, or by a large number of luminous

stars combined with supernovae. The first possibility has been recently further investigated by Krolik (2007), who found a solution for a radiatively supported torus. Since, however, inwardly directed IR radiation is not considered in his model, its applicability is not evident. Another possibility, which requires a very recent episode of intensive star formation which, in turn, requires fragmentation of the molecular gas was suggested by Schartmann et al. (2005). Therefore, even if the torus was supported by radiation pressure from stars and supernovae, one would expect the medium to be clumpy. However, for the modelling of a smooth torus, the authors had to use a supernova rate that significantly exceeds the observed value.

Inconsistencies also exist in the expected size of such a torus. While the inner radius,  $R_{\text{in}} \sim 1$  pc, of the torus is set by the temperature at which dust particles sublimate (Barvainis 1987; Krolik & Begelman 1988), the existence of a sharp outer radius is much less obvious. Pier & Krolik (1992) performed the first detailed calculations of dust radiative transfer for a toroidal geometry. They concluded that the torus has an outer radius,  $R_{\text{out}}$ , of 5 pc to 10 pc. Later, it was estimated that the torus size might be much larger and more diffuse with  $R_{\text{out}} \sim 30$  pc to 100 pc (Pier & Krolik 1993). Extending the smooth density calculations and from the comparison with observed IR emission in the wavelength range ( $\sim 10 \mu\text{m}$  to  $25 \mu\text{m}$ ), Granato & Danese (1994) found that the torus must have an outer radius as large as  $R_{\text{out}} \leq 300$  pc to 1000 pc. However, high resolution IR observations of NGC 1068 showed the emission region to be  $R \sim 1$  pc (Weigelt et al. 2004). VLTI interferometric observations of the same source showed that the  $10 \mu\text{m}$  flux comes from a central, hot ( $T > 100$  K) region of 1 pc and a cooler ( $T \sim 320$  K) surrounding region within 2 pc to 3 pc of the nucleus (Jaffe et al. 2004). It should be pointed out, that the IR observations only determine the size of the emission regions and that the torus might in fact be much larger.

The size and composition of the tori remain unclear, however studies of the molecular absorption and emission can give further clues. For example, observations of CO carried out on NGC 1068 by Schinnerer et al. (2000) traced rotating molecular clouds with an outer radius of 13 pc from the nucleus. Also, observations of NGC 3227 by Davies et al. (2006) showed an ordered velocity field of molecular hydrogen out to radii of 10 pc to 20 pc. Finally, it should be pointed out that the constant radial density profile deduced from the torus models is the consequence of the large amounts of cool dust needed to produce the observed IR fluxes. In a clumpy medium, there is no direct correspondence between the distance and the temperature. The temperature of an optically thick cloud is higher on the side illuminated by the AGN than on the dark side (Nenkova et al. 2002), so even at the compact dimensions, AGN can contain cool dust (Elitzur 2006).

### 1.2.1 H I absorption

The existence of circumnuclear gas in AGN is greatly supported by H I absorption measurements of type 2 radio sources, whose jet axes lie close to the plane of the sky. Evidence of a circumnuclear torus of atomic gas has been seen in Cygnus A (Conway 1999), NGC 4151 (Mundell et al. 1995) and TXS 1946+708 (Peck et al. 1999). In Cygnus A, H I absorption measurements detected a torus-like structure with a radius of 50 pc. In NGC 4151, H I absorption measurements indicate a torus size of 70 pc in radius and 50 pc in height. In the compact symmetric object (CSO) TXS 1946+708, H I absorption consists of a very broad line and a lower velocity narrow line which are visible toward the entire 100 pc of

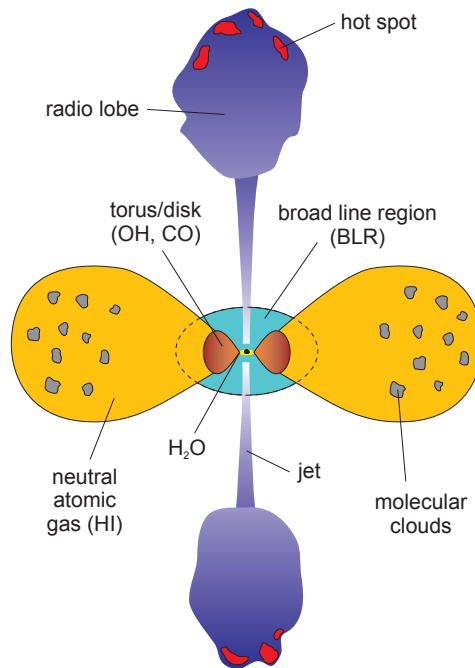


*Figure 1.3:* Schematic representation of the cross section of the inner kilo-parsec structure of an active galaxy. The different structures are labelled by their tracers and displayed in schematic sizes. The accretion disk is at parsec and sub-parsec scale, the molecular disk or torus can extend up to a few hundred parsecs. The neutral atomic gas and the molecular clouds extend further out to a region up to kilo-parsecs. The jets can extend up to several megaparsecs. The picture is not to scale.

the continuum source (Peck et al. 1999). The broad line has low optical depth and peaks in column density near the core of the source. These examples are consistent with a thick torus scenario in which gas closer to the central engine has a higher temperature, so that a longer pathlength through the torus would not necessarily result in a higher optical depth. The high velocity dispersion toward the core of TXS 1946+708 is indicative of fast moving circumnuclear gas, perhaps in a rotating toroidal structure.

Also, from the spectral index distribution, evidence for free-free absorption gives a further indication for obscuration along the line of sight toward the core. Free-free absorption is caused by an ionized region around the central engine, as well as an accretion disk or torus. In TXS 1946+708 the scale height is estimated to be  $\leq 10$  pc at the inner radius and at least 80 pc at the outer radius, and contains mainly atomic gas (Peck & Taylor 2001). Also, the presence of a thin disk has been determined from HI observations in NGC 4261 (van Langevelde et al. 2000; this source is part of the sample studied in this thesis). VLBI observations of this source indicate that the HI absorption is confined to a disk of 1.3 pc thickness seen in projection against the counter-jet.

However, the study of the HI associated with tori is generally possible only for a limited number of cases where a compact jet is present and the background radio source is strong.

### 1.2.2 Maser emission and the circumnuclear tori

The existence of HI absorption towards the cores of AGN provides the selection criterion for picking prime candidates in which to search for molecular absorption (of abundant

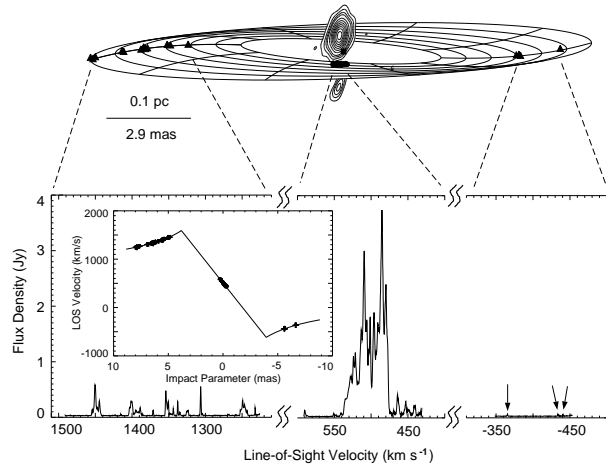


*Figure 1.4:* Water masers in NGC 4258. In the top panel the distribution of the water masers is shown. Also shown is the continuum image of the central jet and a warped disk model. In the bottom panel the spectrum of the masers is shown. The maser velocities are shown as a function of offset from the central source. The line indicates a Keplerian rotation curve model. The figure is reproduced from Herrnstein et al. (1999).

species like CO and OH), maser emission and ionized gas. For example, in NGC 1068 OH absorption, H<sub>2</sub>O maser emission, HI absorption, and a compact source of free-free emission are all present (Gallimore et al. 1996). Figure 1.3 shows a schematic representation of the inner region of an AGN and the location of some tracers relative to the core. Water maser studies have further proven to be a great tool to understand the properties of the inner regions of AGN and have presented strong evidence for the existence of a warped disk. In fact, in NGC 1068, the example given above, and in NGC 4258 (see Fig. 1.4), the maser emission indicates that the molecular disk might be more warped (Greenhill & Gwinn 1997; Herrnstein et al. 1999).

These masers are thought to arise in a disk-shape plane, where orientation with respect to the line of sight, velocity shear, and background amplification determine which favoured maser gain paths are found within the disks. Maser amplification is made possible by the large-scale orderly dynamics of accretion disks. The pumping mechanism is thought to be supplied by the heating of disk gas via irradiation by a central X-ray source (Neufeld & Maloney 1995). The phenomenon is closely associated with Seyfert 2 galaxies and LINERS (Braatz et al. 1996), though there are a few examples in narrow-line Seyfert-1 systems (Hagiwara et al. 2003), and transition objects between Seyfert 1 and 2 classes (e.g. Braatz et al. 1996), and FR II radio galaxies (Tarchi et al. 2003).

A more specific introduction to the properties of water masers in AGN is given in Chapter 5. However, I would like to point out that the study of water masers in AGN research has returned detailed results of the physical properties on very small scales. The best cases so far studied are NGC 4258 (Humphreys et al. 2005; Herrnstein et al. 1999 and Moran et al. 1999), NGC 1068 (Greenhill & Gwinn 1997), and the Circinus galaxy (Greenhill et al. 2003). In NGC 4258, studies of the maser spots were used to determine the size and shape of the warped molecular disk (Herrnstein et al. 1999; see Figure 1.4). In this source, the circumnuclear disk is found to extend from 0.13 pc to 0.25 pc from the central engine. Also, maps of the maser emission in NGC 3079 (Trotter et al. 1998;

the source is also studied in this thesis, see Chapter 2 and Chapter 4), have also shown suggestive evidence of a circumnuclear disk.

### 1.3 OH surveys and the scope of this thesis

In the unified schemes, the obscuring material is generally assumed to be an approximately parsec-scale torus of molecular gas but may also have a significant atomic component (e.g. Krolik & Begelman 1986; Krolik & Begelman 1988). The broad line region and a non-thermal continuum source are situated inside the torus, whereas the narrow line region is outside. That opaque tori can block the BLR from direct view has been demonstrated by spectropolarimetry, where the polarized flux spectra show broad permitted lines from the BLR in spectra which are normally characterized by forbidden narrow lines only, i.e. light from a hidden BLR nevertheless reaches the observer by scattering off an electron mirror located above the torus and is polarized in the scattering process (Antonucci & Miller 1985). X-ray studies confirm this picture, with column densities derived for type 1 and type 2 Seyferts revealing absorbing columns that are much larger towards the centre of type 2 AGN, consistent with the torus model (Risaliti et al. 1999). X-ray spectra reveal absorbing columns towards the centre of type 2 AGN of up to  $10^{24} \text{ cm}^{-2}$ , whereas in type 1 objects, column densities are  $\sim 10^{22} \text{ cm}^{-2}$  (see Fig. 1.5; Salvati et al. 2000).

The high column densities required for effective obscuration offer us the prospect of finding tori by looking for molecular absorption lines at centimetre wavelengths against a strong nuclear radio synchrotron core. However, despite many efforts to detect the expected molecular absorption or emission in a number of surveys, only in very few cases could molecular absorption be confirmed. The small molecular masses combined with the low beam filling factor of nuclear tori means that observations of thermal emission lines from distant sources will be beyond the capacity of present centimetre- and millimetre-wave telescopes.

In nearby AGN there is some evidence for the presence of molecular gas that may be associated with dusty tori, for example Planesas et al. (1991) found a circumnuclear CO ring with a radius of 130 pc in NGC 1068, a prototypical Seyfert 2 galaxy, and in NGC 4945, Bergman et al. (1992) inferred a thick torus consisting of a large number of small but dense molecular clouds from single-dish CO observations. Yet, although there is indirect evidence for the existence of such a torus, little information exists on its physical state.

The study of neutral gas in radio sources allows one to investigate and confirm this prediction central to unified schemes, that an obscuring torus surrounds the central engine of the AGN. One would like to study the structure and extent of the obscuring material, however studying those AGN whose radio axes are close to the plane of the sky is challenging at optical and infrared wavelengths because of high obscuration and due to a superposition of structures along the line of sight. In the radio, there are three methods by which it is possible to detect circumnuclear structures; molecular gas seen either masing or in absorption, atomic gas seen in absorption, and ionized gas revealed through free-free absorption. The study of molecular absorption against a strong continuum source has a great advantage over emission-line studies since it is much easier to detect and it is not distance limited, i.e. absorption can be observed at any distance as long as the background source has a reasonably strong continuum flux density at the line frequency. Indeed, absorption

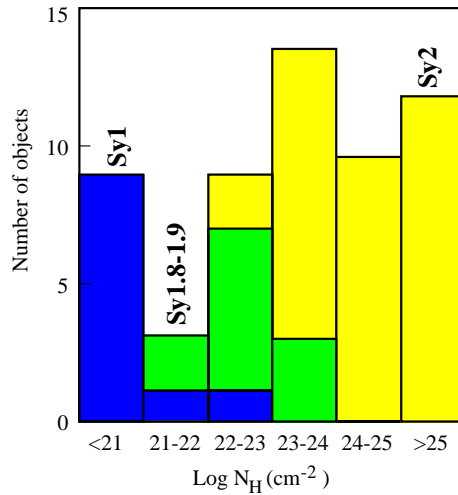


Figure 1.5: The distribution of column densities,  $N_{\text{H}}$  for type 1 to type 2 AGN selected in [O III]  $\lambda 5007$  line flux, which is assumed to trace the intrinsic AGN flux density (Salvati & Maiolino 2000). From this plot, a good correspondence is seen between optical classification and X-ray absorption: type 1 Seyferts tend to have little or no absorption, type 2 Seyferts tend to be heavily absorbed ( $N_{\text{H}} > 10^{23} \text{ cm}^{-2}$ ), and intermediate type 1.8 to 1.9 Seyferts are absorbed by intermediate column densities  $\sim 10^{22} \text{ cm}^{-2}$  to  $10^{23} \text{ cm}^{-2}$ .

has been seen at a redshift of 0.89 towards the lensing galaxy in PKS 1830-211 (Chengalur et al. 1999). The high sensitivity of molecular absorption line observations means that molecular species much rarer than CO can be observed. For instance  $\text{HCO}^+$ , HCN, HNC, CS and CN absorption has been observed, but with survey detection rates of only a few percent. However, the picture remains incomplete because the studies have been limited by the sensitivity, spectral resolution, instantaneous bandwidth, and bandpass stability of present and past instruments so that an overall picture is still not clear.

### 1.3.1 OH surveys

Observations of water vapour and hydroxyl (OH) megamaser emission, which are millions of times more luminous than their Galactic counterparts (Baan 1985) have provided unique information about distinct regions within galactic nuclei. Water-vapour masers can map out the central few parsecs of an active nucleus, tracing the rotation of nuclear accretion disks and the state of material surrounding the radio jets (Maloney 2002). The theoretically-inferred geometry and small thickness of these disks cannot account for the frequently observed spatial obscuration (Herrnstein et al. 1998).

Extragalactic OH, either in absorption or as maser emission, has been shown to display the characteristics of the circumnuclear environment of active galaxies, tracing the low density component of the molecular environment in the inner kiloparsec of the nuclear region of such galaxies. The structures traced by the OH are spread across tens to hundreds of parsecs, as seen, e.g., from observations of OH megamasers in III Zw 35 and IRAS 17208-0014 by Diamond et al. (1999), from the symmetric pc-scale OH megamasers seen in Arp 220 by Lonsdale et al. (1998) and from EVN and MERLIN observations of III Zw 35 by Pihlstrom et al. (2001). In some cases there is evidence for a nuclear disk or torus (e.g. Klöckner & Baan 2002). The tight correlation with the FIR emission (Baan 1989)

indicates a strong association with the dusty obscuring material along the line of sight towards the nucleus.

Despite many efforts to directly detect the expected molecular absorption or emission in a number of surveys, only in very few cases could molecular absorption be confirmed. A systematic search for tori, looking for line absorption, has been carried out by Drinkwater et al. (1997). They looked for CO, HCN, HCO<sup>+</sup> and CS against the strong radio synchrotron cores of 13 radio galaxies and red quasars. No absorption was detected in any of the sources, despite having a good sensitivity, they were able to detect an equivalent hydrogen column density,  $N_{\text{H}}$ , down to  $10^{20} \text{ cm}^{-2}$ . OH absorption is the second most common molecular absorption line seen in galaxies after CO, and should be present with reasonable abundance. Moreover, in contrast to water masers, OH masers are found in the central few hundred parsecs and should therefore be better tracer for the extended molecular torus. Single-dish OH surveys at 18 cm wavelength of several hundred galaxies by Schmelz et al. (1986), Garwood et al. (1987), Norris et al. (1989), Baan et al. (1992), Staveley-Smith et al. (1992), Darling & Giovanelli (2002), and Gupta et al. (2006) revealed OH absorption towards two Seyferts only and maser emission in five. Baan et al. (1992) reported one detection out of 25 galaxies. This low detection rate suggests that the tori may be atomic or ionized, perhaps by X-rays from the AGN. In 1994, two groups (Bravainis & Antonucci 1994, and Conway & Blanco 1995) searched for and failed to detect CO  $J=0-1$  absorption from the obscuring torus in the nearby, powerful galaxy Cygnus A. The non-detection of CO was very surprising as, in an obscuring torus, the carbon monoxide molecule should be present with a substantial abundance. The lack of absorption in these surveys seems to be in contradiction with the unified schemes. There are a few possible causes for the absence of detectable molecular absorption: (1) the molecular abundances are low due to harsh conditions, as mentioned above, (2) the gas temperature and hence state of excitation due to collisional excitation are high enough that the lowest transitions probe an undetectably small fraction of the molecules and (3) the non-thermal continuum radiation of the central source enforces a high excitation temperature, much higher than the kinetic temperature, that suppresses the opacity in the lowest transitions (Maloney, Begelman & Rees 1994).

So, do the tori really exist? And if so, in molecular form as predicted? Or are they atomic or ionized perhaps by X-rays from the AGN? Before concluding that tori are not molecular, the last of these points, the radiative coupling to the non-thermal continuum, deserves further attention and influences the selection of the most favourable transitions to observe.

### 1.3.2 Radiative Excitation

Prompted by the surprising CO non-detection in Cygnus A, Maloney, Begelman & Rees (1994) introduced the possibility of radiative excitation effects to explain the lack of absorption. Assuming that the ionization parameter within the torus is low enough for the gas to be molecular and if the torus is sufficiently compact, the CO molecule can radiatively couple to the bright radio continuum source increasing the rotation temperature and lowering the fractional population of the low  $J$ -levels, increasing the excitation temperature of the lower rotational levels, and thus suppressing the absorption optical depths in the lower transitions. Then, a large mass of CO could exist in the torus but produce no significant absorption at the observed frequencies.

The OH molecule forms efficiently at the elevated temperature of X-ray heated or

shocked gas by the high temperature reaction of O with H<sub>2</sub>. However, OH suffers similar excitation effects that may make its detection also difficult towards the cores of AGN with strong radio continuum emission. Radiative excitation effects have been predicted for the OH molecule in the <sup>2</sup>Π<sub>3/2</sub> J=3/2 ground state by Black (1998), which could explain the widespread lack of 18 cm OH absorption. The rate of absorption,  $\rho$  in s<sup>-1</sup>, in any atomic or molecular transition can be written

$$\rho = \frac{g_u A_{ul} / g_l}{e^{(-h\nu/kT_{\text{rad}})}} \quad (1.3)$$

where  $A_{ul}$  is the probability of spontaneous transitions between the upper state  $u$  and the lower state  $l$  in s<sup>-1</sup>, and  $g_u$  and  $g_l$  are the statistical weights of the upper and lower states,  $h$  is Planck's constant,  $k$  is Boltzmann's constant, and  $\nu$  is the frequency of the transition. The relative populations of any pair of states can be written in terms of excitation temperature,  $T_{\text{ex}}$ , as the ratio of number densities in the upper and lower level

$$\frac{n_u}{n_l} = \frac{g_u}{g_l} e^{(-h\nu_{ul}/kT_{\text{ex}})} \quad (1.4)$$

where  $h\nu_{ul} = E_u - E_l$  is the energy difference between two states. In the high-density limit, the rates of collisional transitions dominates over radiative transitions and the excitation temperature will approach the kinetic temperature,  $T_{\text{ex}} \sim T_{\text{kin}}$ . In the low-density limit, radiative processes will dominate and the excitation temperature will approach the radiation temperature  $T_{\text{ex}} \sim T_{\text{rad}}$ . In the Galactic interstellar medium, the low-density limit often leaves the distribution of low-energy levels locked to the temperature of the cosmic background radiation,  $T_{\text{ex}} = T_{\text{cmb}}$  ( $T_{\text{cmb}}=2.7$  K at  $z=0$ ). However, in the vicinity of AGN, molecules can be exposed to intense non-thermal radiation with a range of  $T_{\text{rad}}(\nu)$ , and their excitation will be a complex response to the different temperatures that characterize the rotational, vibrational and electronic transition states.

The detectability of a molecular transition can be given in terms of its line optical depth, which is a direct measure of the strength of absorption. The optical depth of a spectral line formed in a slab of gas of column density  $N_l$  is given by

$$\tau = 3.738 \times 10^{-7} \text{m}^3 \text{s}^{-3} \frac{A_{ul}}{\nu^3} \frac{N_l}{\Delta V} \frac{g_u}{g_l} (1 - e^{(-h\nu/kT_{\text{ex}})}) \quad (1.5)$$

where  $N_l$  is the lower state column density in cm<sup>-2</sup>,  $\Delta V$  is the full width at half-maximum of the Gaussian line shape in km s<sup>-1</sup> and  $\nu$  is the line frequency in Hz. So the fractional abundance in the lower state,  $N_l$ , is a declining function of  $T_{\text{ex}}$  for low lying states and high values of  $T_{\text{ex}}$ .

Maloney et al. (1994) pointed out that the effect of radiative coupling to a non-thermal radio source is to maintain a high excitation temperature in the lowest rotational levels so that their populations account for a very small fraction of the molecules. Calculations done for radiative coupling of OH at 18 cm by Black (1998), have shown that for a source like Cygnus A, even at a distance  $R$  of 100 pc from the central continuum source,  $T_{\text{rad}} > 5 \times 10^6$  K. At  $R = 10$  pc, the pumping rate in the 18 cm transition,  $\rho \approx 1 \text{ s}^{-1}$ , is five times greater than the strongest pure rotational transition of the ground state at 119  $\mu\text{m}$ . Collisional processes are very slow at densities below 10<sup>10</sup> cm<sup>-3</sup>, so that the 18 cm absorption line will be suppressed. The  $\Lambda$ -doubling transitions of OH at 5 cm, however, couple to the microwave part of the spectrum at the same rate as these levels are pumped in the

Molecule	$N/\Delta V$ ( $\text{cm}^{-2} (\text{km s}^{-1})^{-1}$ )	$\nu$ (GHz)	$\tau_{10}$	$\tau_{300}$
OH	$10^{15}$	1.67	$-7.7 \times 10^{-4}$	3.0
		6.03	$8.1 \times 10^{-4}$	0.3
		13.4	$1.9 \times 10^{-3}$	$9.6 \times 10^{-4}$
		7.79	$6.8 \times 10^{-4}$	$-4.5 \times 10^{-4}$

*Table 1.1:* Non-LTE excitation calculation for the OH molecule showing molecular line optical depths near an AGN (Black 1998) for a column density total width ratio,  $N/\Delta V$ , of OH. The columns  $\tau_{10}$  and  $\tau_{300}$  correspond to expected optical depths at 10 pc and at 300 pc from a strong nuclear radio continuum source like in Cygnus A. The opacities are given for four transitions, whose frequencies are given the column  $\nu$ .

far-infrared (at  $\mu\text{m}$  wavelength), so that the excitation temperatures of these states might be significantly lower than  $T_{\text{rad}}$ , hence the 5 cm transition is more likely to be observed in a molecular torus close to the central nucleus. Table 1.1 shows some of the results for limited non-LTE calculations carried out by Black (1998) for the OH molecule.

In these calculations, the radiative transfer has been treated with mean escape probabilities, such that the line optical depth depends on the ratio of column density to line width,  $N/\Delta V$ . The values given in the table correspond to the molecules being exposed to the continuum spectrum at  $R = 10$  pc from Cygnus A and for comparison at  $R = 300$  pc. The kinetic temperature,  $T_{\text{kin}}$ , is 500 K and the number density,  $n$ , of neutral collision partners (H or  $\text{H}_2$ ) is  $10^5 \text{ cm}^{-3}$ . These results show that excitation at  $R = 10$  pc is dominated by the continuum source and is not sensitive to density and temperature. The low-density limit of excitation prevails at densities that would be considered quite high in Galactic molecular clouds.

### 1.3.3 A new search strategy

Thus, the opacity in the 1.67 GHz transitions of OH located 10 pc from the AGN will be suppressed by a factor of  $10^3$  due to the proximity of the bright nuclear radio continuum source. In contrast, the opacity of the 6 GHz transitions will be suppressed by a factor of  $10^2$ , and the opacity of the 13.4 GHz transition will increase slightly by a factor of two. Therefore, radiative excitation effects depend strongly on the transition one chooses to observe, and on how close the gas is located to the bright radio nucleus. If the molecular gas is concentrated in a 1 pc to 10 pc scale torus, then radiative excitation effects should be strong at 1.67 GHz in Cygnus A and the gas would then be best found by looking at higher-order transitions. If the molecular gas in Cygnus A is extended over 300 pc, rather than being concentrated in the central 10 pc, then radiative excitation effects should become minimal and the existing lack of molecular absorption line detections at 1.67 GHz would imply a lack of molecular gas. In both cases, upper limits to both the 1.67 GHz and 13.4 GHz absorption line strengths would place stringent limits on the molecular content on both large and small scales.

So according to these models, searches for the 6 GHz transition of OH, where the effects are reduced due to higher excitation and statistical weights, are likely to be more profitable than at 1.67 GHz. This line has so far not been subject of a (published) systematic

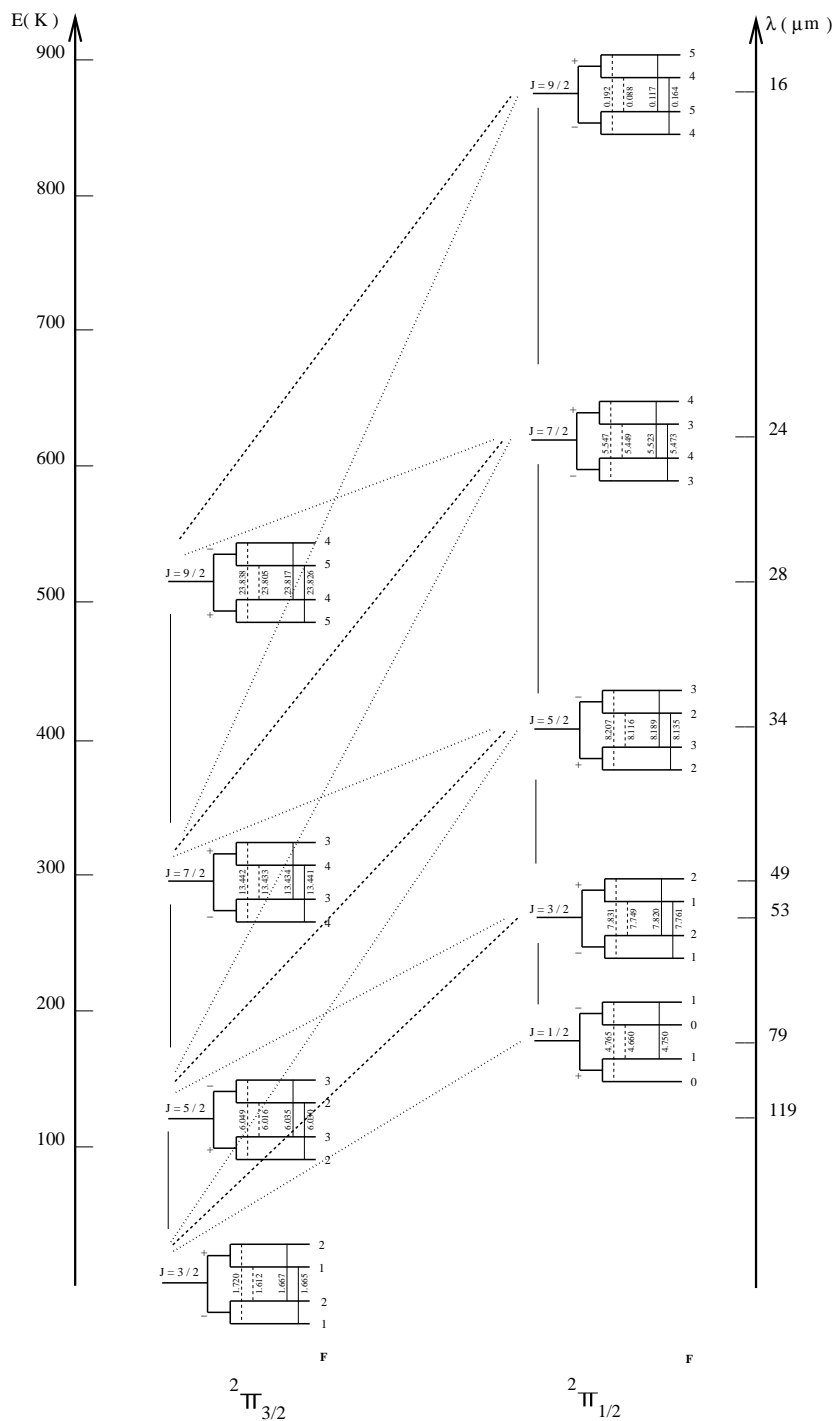


Figure 1.6: Rotational energy diagram showing the electronic ground state ( ${}^2\Pi$ ) with the OH the lower hyperfine levels of the OH rotational ladder. The  ${}^2\Pi_{3/2}$  and  ${}^2\Pi_{1/2}$  rotational ladders are produced by the spin-orbit interaction.  $J$  is the rotational angular momentum due to the rotation of the molecule. The  $\Lambda$ -doubling splitting of each rotational level causes a splitting of the  $J$  states, in which the higher energy levels have an electron distribution along the axis of the molecular rotation, whereas the lower energy levels have a distribution on the plane rotation. The quantum number  $F$  indicates a hyperfine splitting due to the spin flip of the the H atom. Solid lines indicate the main-line transitions of the hyperfine levels ( $\Delta F=0$ ) and the dashed lines indicate the satellite transitions. The solid, dashed, and dotted lines indicate the dipole transition rules ( $\Delta J = -1, 0, +1$ ) connecting the rotational levels of the ground state. (Illustration courtesy of H.-R. Klöckner 2004)

investigation<sup>3</sup>.

In this work, we changed the search strategy for detecting OH by looking for higher excited states at 4.7 GHz, 6 GHz, and 13.4 GHz (see Fig. 1.6). A sample of Seyfert 2 galaxies was selected, mainly for the presence of polarized broad line emission, high soft X-ray absorption indicating a large foreground gas column, and 6 cm flux density  $>50$  mJy. In Chapter 2, I describe the single-dish observations at 4.7 GHz and 6 GHz of this sample. Observations at 6 GHz yielded a detection rate of 19 %, whereas no detections were made at 4.7 GHz.

In Chapter 3, interferometric observation searching for OH at 13.4 GHz in Cygnus A and NGC 1052 are described. These two sources are a subset of the sample described in Chapter 2. The observations yielded a firm detection of OH at 13.4 GHz in NGC 1052 towards the centre of this source and a tentative detection in Cygnus A.

In Chapter 4, I describe observations of a sub-sample of the sample sources described in Chapter 2, which were searched for methanol emission or absorption. The first detection of extragalactic methanol was made here in absorption towards the source NGC 3079. Two further tentative detections were made in Mrk 3 in emission and in Mrk 348 in absorption.

Finally, in Chapter 5, both single-dish and interferometric observation of a water maser towards the high-redshift, gravitationally lensed quasar MG 0414+0534 are presented. The water maser was discovered with Effelsberg and later confirmed with the EVLA. At a redshift of 2.64, this is the most distant water maser ever discovered.

---

<sup>3</sup>Though an unpublished VLA observation of 8 compact steep spectrum sources yielded no detections (Pihlström, private communication).



## Chapter 2

# A survey for excited OH

AGN unification schemes have been successful in explaining the spectroscopic differences between Seyfert 1 and Seyfert 2 galaxies as a result of different orientations of the observer's line of sight to the central obscuring disk or torus. Central to the unification hypothesis is a compact system of gas existing in small dense clouds which should mostly be molecular if the pressure is sufficiently high. Although molecular rings with diameters of a few hundred parsecs are common in the centres of galaxies, the expected small-scale tori ( $< 10$  pc) have been difficult to detect and a large number of molecular spectroscopic surveys at cm-wavelength have yielded non-detection. In this chapter, I present a search conducted towards a sample of Seyfert 2 galaxies with the aim of detecting the molecular species that so often eluded previous surveys. This survey, carried out with the Effelsberg 100 m telescope, made use of a new search strategy, namely looking for excited OH and selecting a sample with known large X-ray absorption and type 2 spectra. In Section 2.1, the sample of selected sources is introduced. In Section 2.2, I describe the Effelsberg observations and finally, in Sections 2.3 and 2.3.1, the results and a discussion are presented.

### 2.1 The sample

Searches for extragalactic OH have been done based on samples selected for their far-infrared flux (FIR) density and yielded a detection rate of a few percent. So far only about one hundred galaxies in total are known to exhibit this tracer and make the search for extragalactic OH and the study of its general characteristics a main goal of current research. OH absorption is the most common molecular absorption line seen in galaxies after CO; it is present with reasonable abundance and produces reasonable line optical depths. However, the FIR selection includes mostly galaxies without AGN and so is not suitable for the present work.

The sample selection for this survey was designed to find AGN with optimum conditions for absorption, by searching the literature for Seyfert 2 galaxies with evidence for an obscuring torus or high column densities and a strong nuclear radio continuum.

The main selection criteria were the presence of polarized broad line emission, which indicates an obscured broad line region (e.g. Tran et al. 2001), high soft X-ray absorption indicating a large foreground gas column, and a 6 cm flux density  $> 50$  mJy to provide the continuum emission against which the absorption could be seen.

I began the sample selection with the AGN samples of Risaliti et al. (1999), Maiolino

et al. (1998), Pappa et al. (2001), Gu et al. (2001), and Comastri (2004), for which X-ray spectra were measured yielding X-ray absorbing column estimates, and selected those 260 galaxies that have Seyfert 2 classification and a high column density ( $N_{\text{H}} > 10^{23} \text{ cm}^{-2}$ ).

X-ray band absorbing column estimates are made in the 1 keV to 10 keV energy range in which the interaction between X-rays and matter is dominated by photoelectric absorption by metals. At higher energies Compton scattering dominates. Foreground absorption is recognized by a characteristic turnover in the soft end of the spectrum. Primary X-rays are able to penetrate gas with a column density of less than  $\sim 1.5 \times 10^{24} \text{ cm}^{-2}$  termed as a Compton thin source. For column densities greater than a few  $10^{24} \text{ cm}^{-2}$ , soft X-rays are completely absorbed and only X-rays in the 10 keV to 100 keV range pass through the torus. Such a source is termed Compton thick.

X-ray emission from Compton-thick Seyfert 2 galaxies can still be detected in the 1 keV to 10 keV band covered by present X-ray satellites by means of the reflection from the visible inner surface of the torus (termed the cold reflected component) or via scattering by the material responsible for producing the broad lines observed in polarized light near the nucleus (termed the warm scattered component). In these cases, the photoelectric cutoff in the observed spectrum does not provide information on the real column density absorbing the primary X-ray source, and so the galaxy may be erroneously classified as a low-absorption object and until recently only a few such sources were recognized (Matt 1997). The expected observable features in X-rays are: a 2 keV to 10 keV continuum flatter than the canonical slope observed in Seyfert 1 galaxies, a Fe K $\alpha$  feature around 6.4 keV with large strong equivalent width (EW) of  $\geq 1 \text{ keV}$ , and a reflection ‘‘hump’’ at energies  $> 10 \text{ keV}$  (e.g. Ghisellini et al. 1994).

Of these 260 sources, the 26 sources with a continuum flux density above 50 mJy at 5 GHz were selected for observing since a strong background continuum radiation source is needed for a high sensitivity detection of the absorption line. The sample was extended by including candidates with classic indications for a torus, like the existence of hidden polarized broad lines (HPBL; Tran et al. 2001) or detection of other molecular absorption lines (Hydra A, Cygnus A, NGC 1052, NGC 2639, NGC 4261, NGC 5793, Mrk 1073 and IRAS F01475-0740) and which satisfy the requirement of a high core continuum flux density over 50 mJy. A luminous infrared source was also included, where OH has previously been detected in absorption at 1.67 GHz (IRAS 05414+5840), bringing the sample to 30. The final sample is summarized in Table 2.1.

Of the 30 Seyfert 2 galaxies originally selected (Table 2.1), three sources (NGC 1365, NGC 1808, and NGC 7130) could not be observed due to their low declinations, making their scheduling difficult. Very strong sources like Hydra A ( $S_{5 \text{ GHz}} \sim 14 \text{ Jy}$ ; Griffith et al. 1994) and Cygnus A ( $S_{5 \text{ GHz}} \sim 213 \text{ Jy}$ ; Becker et al. 1991) and to a lesser extent also NGC 1052, NGC 1275, and NGC 1068 also did not deliver good spectra due to the prominent ripples in the baseline, despite applying the  $\lambda/8$  technique during the observations (see Section 2.2 for details). A few more sources, which were not in the original sample, were thus selected with the same criteria, but relaxing the minimum required continuum flux density of 50 mJy. These were NGC 1667, NGC 2273, NGC 3982, NGC 4258, NGC 5005, NGC 5194, and NGC 6251. These sources are not listed in the original sample given in Table 2.1.

Source	RA (J2000)	Dec (J2000)	z	S <sub>6cm</sub> mJy	N <sub>H</sub> X-ray 10 <sup>21</sup> cm <sup>-2</sup>	OH detection 1.67 GHz	H I detection	comment	Ref
Hydra A	09 18 05.67	-12 05 44.0	0.055	154	60	-	abs		21, 26
Cygnus A	19 59 28.36	40 44 01.9	0.056	1400 <sup>a</sup>	170	abs	abs	CO not observed	23, 24, 27
NGC 1052	02 41 04.80	-08 15 20.8	0.005	1500 <sup>b</sup>	>10 <sup>b</sup>	abs	abs	CO, H <sub>2</sub> O	1, 18, 25
NGC 1068	02 42 40.71	-00 00 47.8	0.004	1090	>10 <sup>d</sup>	em	abs	H <sub>2</sub> , H <sub>2</sub> O, HBLR	1, 9, 10, 12, 13, 18, 19, 25
NGC 1167	03 01 42.37	35 12 20.7	0.002	243	<2000	-	abs		2, 11
NGC 1275	03 19 48.16	41 30 42.1	0.017	16623 <sup>c</sup>	14.9	-	abs		10, 25
NGC 1365	03 33 36.37	-36 08 25.4	0.006	191	200	-	abs		1, 10, 25
NGC 1808	05 07 42.34	-37 30 47.0	0.003	207 <sup>d</sup>	32	abs	abs		3, 10, 25
NGC 2110	05 52 11.38	-07 27 22.4	0.007	175	28.9	no	-	HPBL, H <sub>2</sub>	1, 9, 10, 12, 19
NGC 2639	08 43 38.08	50 12 20.0	0.040	54.5	-	no	-	H <sub>2</sub> O	4, 18
NGC 2992	09 45 42.05	-14 19 35.0	0.008	77	6.9	-	-	H <sub>2</sub>	1, 9, 10, 11
NGC 3079	10 01 57.80	55 40 47.1	0.004	145	16	abs, em	abs	H <sub>2</sub> O	5, 10, 11, 13, 16, 17, 18, 20
NGC 4151	12 10 32.58	39 24 20.6	0.003	125	2.26	-	abs		1, 25
NGC 4261	12 19 23.22	12 39 43.5	0.007	80 <sup>d</sup>	-	-	abs		22, 25
NGC 4388	12 25 46.75	05 49 30.8	0.008	76	420	no	-	HBLR, H <sub>2</sub>	1, 10, 9, 12, 19
NGC 5135	13 25 44.06	-29 50 01.2	0.014	598	> 1000	-	-		4, 10, 12
NGC 5506	14 13 14.87	-03 12 27.0	0.006	160	27	abs	abs	HBLR, H <sub>2</sub> O	1, 10, 12, 17, 19
NGC 5793	14 59 24.76	-16 41 36.1	0.011	96	-	abs	abs	H <sub>2</sub> O	6, 17, 18, 25
NGC 6240	16 52 58.89	02 24 03.4	0.024	131	2200	abs	abs	H <sub>2</sub>	7, 3, 17, 18, 25
NGC 7130	21 48 19.50	-34 57 05.0	0.016	62	> 1000	-	-	H <sub>2</sub> O	8, 12, 16, 17, 18
NGC 7674	23 27 56.72	08 46 44.5	0.029	66.5	> 1000	no	abs	HBLR	8, 13, 19
Mrk 3	06 15 36.36	71 02 15.1	0.013	361	1100	-	-	no H <sub>2</sub> , HPBL	1, 9, 12, 13, 19
Mrk 231	12 56 14.20	56 52 25.0	0.042	419	2000	em	abs		16, 20, 28, 29, 30, 31
Mrk 273	13 44 42.10	55 53 13.0	0.038	103	400	em	abs		20, 28, 31, 32, 33
Mrk 348	00 48 47.14	31 57 25.1	0.015	254	125	no	-	HBLR, H <sub>2</sub> , H <sub>2</sub> O	9, 12, 18, 19
Mrk 463E	13 56 02.87	18 22 19.5	0.050	100	160	-	-	HBLR, H <sub>2</sub>	1, 9, 12, 19
Mrk 1210	08 04 05.86	05 06 49.8	0.013	45	1000	-	-	HBLR, H <sub>2</sub>	9, 12, 19
Mrk 1073	03 15 01.42	42 02 09.4	0.023	44	-	-	-	H <sub>2</sub>	9, 10
IRAS F01475-0740	01 50 02.70	-07 25 48.5	0.017	127	-	-	-	HBLR	19
IRAS 05414+5840	05 45 47.77	58 42 03.0	0.015	55	-	abs	-	-	20

Table 2.1: The AGN sample for the Effelsberg survey for excited OH absorption. (1) Ulvestad & Wilson 1984; (2) Giovannini et al. 2001; (3) Condon et al. 1996; (4) Ulvestad & Wilson 1989; (5) Edelson et al. 1987; (6) Hagiwara et al. 2000; (7) Colbert et al. 1994; (8) Rush et al. 1996; (9) Veilleux et al. 1997; (10) Risaliti et al. 1999; (11) Pappa et al. 2001; (12) Gu et al. 2001; (13) Comastri 2004; (14) Rodriguez-Ardila et al. 2004; (15) Schmelz et al. 1986; (16) Baan et al. 1985; (17) Baan et al. 1989; (18) <http://www.astron.nl/hagiwara/research/h2omaserlist.htm>; (19) Tran et al. 2001; (20) Klöckner PhD thesis 2004; (21) Taylor et al. 1996; (22) van Langevelde et al. 2000; (23) Drinkwater et al. 1996; (24) Conway & Blanco 1995; (25) [http://www.atnf.csiro.au/people/bkoribal/hi\\_absorption.html](http://www.atnf.csiro.au/people/bkoribal/hi_absorption.html); (26) Rinn et al. 2005; (27) Evans et al. 2006; (28) Gregory & Condon 1991; (29) Braito et al. 2004; (30) Dickey 1982; (31) Carilli et al. 1998; (32) Xia et al. 200; (33) Baan et al. 1982. (a) U. Bach, priv. comm.; (b) M. Kadler, priv. comm.; (c) A. Kraus, priv. comm.; (d) 6 cm flux density derived from 20 cm value assuming  $\alpha = -0.7$ .

## 2.2 Effelsberg observations

Observations with the Effelsberg 100 m telescope were performed over the time range from August 2004 to March 2007. Spectral line observations were performed of the  ${}^2\Pi_{3/2}J = 5/2$  transitions of OH at 6035 MHz, 6030 MHz, 6049 MHz and 6016 MHz for 30 Seyfert 2 galaxies. Of the 31 sources that were overall observed at 6 GHz (Table 2.3), 20 sources were selected also for observations of the  ${}^2\Pi_{1/2}J = 1/2$  transitions at 4765 MHz, 4750 MHz, and 4660 MHz in July 2005 with the Effelsberg telescope (Table 2.4). One concern before starting the survey was that the increased line opacity of the higher transitions could be partially offset by the reduced core flux density with increasing frequency, since most of the sources have steep continuum spectra. However, one could not tell a priori which one of the two effects would be “faster”.

Both the 6 GHz and the 4.7 GHz receivers have dual circular polarizations which were mixed against a local oscillator down to an intermediate frequency and bandpass filtered to 500 MHz bandwidth for transmission on two coaxial IF cables to the 1024 channel autocorrelation spectrometer (AK90). The autocorrelator, located in the central building, provides 8 spectra simultaneously, each with 40 MHz bandwidth and 512 channels to observe 4 transitions in two polarizations. In the spectrometer, each IF input was split four ways and fed into four independent IF-processing sections including frequency synthesizers and mixers for down-conversion and a set of video filters, before sampling and autocorrelation.

The 40 MHz sampled video bands were correlated with 512 channels leading to a spectral resolution of about 78 kHz per channel ( $4 \text{ km s}^{-1}$  per channel) with a total span of  $2000 \text{ km s}^{-1}$  which is broad compared to the typical line widths for OH at 6 GHz of  $170 \text{ km s}^{-1}$  to  $420 \text{ km s}^{-1}$  (Schmelz et al. 1986).

The four 6 GHz transitions all lie within 33 MHz of each other so they all lay within the 40 MHz bandwidth. I centred two pairs of IFs at the main line 6035 MHz on both polarizations with a factor two redundancy, and the other two pairs on both polarizations at the lower and higher frequency satellite lines, at 6016 MHz and 6049 MHz. Similarly, for the 4.7 GHz transitions, two pairs of IFs were centred on the main line at 4750 MHz, and the other two pairs of IFs were centred on the satellite lines at 4765 MHz and 4660 MHz.

The receivers were tuned to the redshifted frequencies of the transitions:  $\nu = \nu_0/(1+z)$ , where  $\nu_0$  is the rest frequency of a transition, with Doppler corrections for earth rotation and earth orbital motion around the sun were applied by the Effelsberg online system.

The observations were made in position-switching mode, in which pairs of on-source and off-source scans separated by  $600''$  on the sky and covering identical azimuth and elevation tracks were differenced to subtract sky emission, which is common in both scans. Each scan was integrated for 170 seconds.

A problem in spectral line observations is due to baseline ripples. Sources stronger than 1000 mJy (or in some cases even a few hundreds of millijansky) tend to produce complex baselines due to frequency-dependent gain across the bandpass. These ripples are mainly caused by standing waves between the feed and the dish, excited by the received noise from external sources like the sun, the ground, and the observed sources partially reflecting from around the feed. The characteristic frequency scale is related to the focal length and the wavelength being observed. Where standing waves are present for the 30 m subreflector-dish spacing in Effelsberg and at 5 cm wavelength they appear with a period of 5 MHz. To reduce these baseline fluctuations, the focal point in the prime focus cabin



*Figure 2.1:* The 100 m Effelsberg telescope in autumn (courtesy of N. Tacke).

of Effelsberg was shifted between subscans by a length corresponding to an eighth of the observing wavelength ( $\lambda/8$ ) to invert the phase of the standing wave, in our case this shift corresponded to 6.2 mm. At the end of each scan, the subscans were added together, so reducing the effects of standing waves.

Each source was observed with  $\sim 4$  hours integration (total time, half of which was on-source) as a compromise between achieving a reasonable sensitivity and observing a sizable sample in reasonable time. Four hours gave a  $5\sigma$  sensitivity of 6 mJy with channels  $4 \text{ km s}^{-1}$  wide. When necessary, Hanning smoothing was applied (see next Section for details).

### 2.2.1 Sensitivity considerations

The rms sensitivity in kelvin,  $\Delta T$ , of an observation is given by

$$\Delta T = \frac{1}{\eta_{\text{corr}}} \frac{T_{\text{sys}}}{\sqrt{2\Delta\nu \Delta t}} \quad (2.1)$$

where  $T_{\text{sys}}^1$  is the system temperature (in kelvin),  $\Delta\nu$  is the channel width (in Hz) and  $\Delta t$  is the integration time of the observations (in seconds). The factor two is for two polarizations and  $\eta_{\text{corr}}$  represents the correlator efficiency. Note that these radiometric temperature fluctuations can be reduced by increasing the bandwidth and using longer integration times.

To relate these fluctuations to a source strength uncertainty, we need to express the  $T_{\text{sys}}$  in terms of a system equivalent flux density (SEFD) in units of jansky ( $1 \text{ Jy} = 10^{-26} \text{ W m}^{-2} \text{ Hz}^{-1}$ ). The SEFD is the strength that a source would have to be to deliver at the antenna terminals an amount of power equal to that arising from a resistor with a physical temperature equal to  $T_{\text{sys}}$ . To calculate the power arising from the system noise with temperature  $T_{\text{sys}}$ , we use the expression for Johnson noise from a resistor:

$$P = \kappa_B T_{\text{sys}} \Delta\nu \quad (2.2)$$

where  $P$  is the power in watts delivered by a resistor at a temperature  $T_{\text{sys}}$ ,  $\kappa_B = 1.380 \times 10^{-23} \text{ J K}^{-1}$  is the Boltzmann constant and  $\Delta\nu$  is the observing bandwidth in Hz.  $T_{\text{sys}}$  includes contributions from the receiver noise, feed loss, spillover, atmospheric emission, Galactic background and cosmic background.

The power at the antenna terminals from the source,  $P_a$ , can be directly related to the source flux density,  $S$ , in  $\text{W m}^{-2} \text{ Hz}^{-1}$ , the area of the antenna,  $A$ , in  $\text{m}^2$ , the aperture efficiency,  $\eta_{\text{aperture}}$ , and the bandwidth by the expression:

---

<sup>1</sup>The system temperature is comprised of a few terms: receiver noise, sky emission, ground emission, atmospheric emission, which depends on the elevation.

$$T_{\text{sys}} = T_{\text{receiver}} + T_{\text{sky}} + T_{\text{ground}} + T_A.$$

The contributions of these terms range from several tens of kelvin to a few kelvin. The atmospheric emission,  $T_A$ , depends on the column density of atmospheric constituents and elevation of the antenna as  $1/\sin(\text{el})$  and on the water vapour content, which affects observations at higher frequencies. The atmospheric emission is:

$$T_A \sim T_{\text{atm}} \cdot (1 - e^{-\tau/\sin(\text{el})})$$

where  $T_{\text{atm}}$  is a weighted average of the physical temperature of the atmosphere over altitude and  $\tau$  is the zenith atmospheric opacity.

$$P_a = \frac{1}{2} \eta_{\text{aperture}} A S \Delta\nu. \quad (2.3)$$

The factor of 1/2 in the equation accounts for the fact that a single channel is able to receive only half of the total radiation from an unpolarized source and the aperture efficiency is the product of several efficiencies describing the loss of power due to, e.g. surface inaccuracies, aperture blockage and tapering of the aperture illumination.

Equating Eq. 2.3, the power (in watts) at the antenna terminals due to a source of flux density  $S$  and Eq. 2.2, the noise power from a resistor, yields the temperature of a resistor that delivers the same power as comes from the antenna terminals due to the source

$$\frac{1}{2} \eta_{\text{aperture}} A S = \kappa_B T_{\text{sys}}. \quad (2.4)$$

Making  $S$  the subject and recalling that this gives the SEFD, i.e. the strength of a source whose power at the antenna terminals equals that due to the system noise yields

$$\text{SEFD} = \frac{2\kappa_B T_{\text{sys}}}{\eta_{\text{aperture}} A}. \quad (2.5)$$

From this and Eq. 2.1,

$$\Delta S = \frac{2\kappa_B \Delta T}{\eta_{\text{aperture}} A} = \frac{1}{\eta_{\text{corr}}} \frac{\text{SEFD}}{\sqrt{2\Delta\nu\Delta t}}. \quad (2.6)$$

The SEFD is an important measure of the system performance since it takes into account the efficiency, the antenna collecting area and the system noise. Moreover it can be measured easily by determining the fractional increase in power obtained when going on and off a source of known flux density, whereas measurements of system temperature and gain are uncertain since they depend on the difficult system calibration against hot and cold loads.

At Effelsberg, the zenith  $T_{\text{sys}}$  of the 6 GHz receiver is 30 K, the antenna efficiency is 51 % and hence the SEFD is 22 Jy. To compare this value with the SEFDs of other single dish antennas, see Table 2.2.

For the typical Effelsberg observation time of 4 h<sup>2</sup>, a bandwidth,  $\Delta\nu$ , of 78 kHz (equal to a velocity resolution of 4 km s<sup>-1</sup> at 6 GHz) and SEFD of 22 Jy,  $\Delta S = 0.93$  mJy. This setup results in a 3 $\sigma$  noise of 2.8 mJy assuming the line width is the same as the channel width.

If the line is resolved by the spectral channels, the rms per channel can be decreased by applying Hanning smoothing after observing, during the data reduction. Hanning smoothing takes three adjacent channels and averages them with weights  $\frac{1}{4}, \frac{1}{2}, \frac{1}{4}$  to smooth the spectrum. Taking every even channel,  $i$ , of the original dataset and creating a new channel,  $i' = i/2$ , such that  $i' = (0.5 \times i) + (0.25 \times (i - 1)) + (0.25 \times (i + 1))$  increases the signal-to-noise ratio of the spectrum. It comes at the cost of doubling the instrumental line width; the effective resolution will be  $2\delta\nu$  (where  $\delta\nu$  is the channel spacing). After such a smoothing, one retains only the alternate channels. This smoothing reduces the first spectral sidelobe from 22 % to 2.7 %.

---

<sup>2</sup>with half the time spent on source, half off source, and then differencing the two spectra to produce a sky-subtracted spectrum with  $\sqrt{2}$  higher noise than that in the individual spectra.

Antenna Location	Diameter (m)	SEFD at 5 GHz (Jy)	SEFD at 6 GHz Jy
Jodrell Bank, UK	76 m	35 (Lovell)	910 (Mark II; 25 × 38 m)
Cambridge, UK	32 m	136	900
Westerbork, NL	14 × 25 m	60	1600 (1 × 25 m)
Effelsberg, D	100 m	20	22
Medicina, I	32 m	170	840
Noto, I	32 m	260	1100
Onsala, S	85 m	600	1500
Torun, PL	32 m	220	400
Arecibo, USA	305 m	5	5
VLA, USA	1 × 25 m	319	280
Saint Croix, VLBA, USA	25 m	255	–
Fort Davies, VLBA, USA	25 m	308	–

Table 2.2: Antenna and receiver performance of the VLBI antennas at 5 GHz and 6 GHz; measured SEFD values as at June 2008 from the EVN status report at [www.evlbi.org/user\\_guide/EVNstatus.txt](http://www.evlbi.org/user_guide/EVNstatus.txt) and [www.vla.nrao.edu/astro/guides/vlas/current](http://www.vla.nrao.edu/astro/guides/vlas/current).

### 2.2.2 Data reduction

During each observing session, several primary calibrators (strong, non-variable sources) of known flux density were observed, in particular the calibrators 3C 286, 3C 295 and 3C 48 were observed either at the beginning or at the end of the observations. The conversion from the observed value in counts (correlator units) to Jy was carried out by observing an appropriate calibrator of known flux density and deriving a calibration factor (in Jy/counts) to apply to the target source counts. This value was typically  $\sim 2.8$  Jy/counts for observations at 6 GHz and  $\sim 4$  Jy/counts at 4.7 GHz. The data were then multiplied by this value. The antenna properties such as gain changes with time or elevation effects, and weather are normally corrected in the calibration procedure. However, these become critical at higher frequencies, i.e.  $\nu \geq 10$  GHz, where atmospheric absorption and atmospheric effects should be considered. Measurements of a known OH absorber, typically W3(OH), were performed at the beginning of all observations to ensure that the whole system from receiver to autocorrelator was working.

The data consisted of individual 3 min spectra on and off source and  $\lambda/8$  defocusing with total integration times of 4 hours. Repeated runs of observations were in some cases necessary to complete the sample of sources at different elevations and in some cases due to bad weather conditions or technical problems. After observing, careful inspection of each individual scan was carried out for all sources, bad scans were removed and bad channels were flagged. After averaging all on-source scans and off-source scans and differencing the averages to subtract the sky emission, a low-order polynomial (second or third order) was fitted and removed from the baseline to remove the source continuum and residual calibration errors and the rms noise level was derived. Table 2.3 shows a summary of all sources observed at 6 GHz, and Table 2.4 shows a summary for all sources observed at 4.7 GHz.

Source Name	Date	integration time (min)	$S_6$ GHz (mJy)	$T_{\text{sys}}$ K	rms <sup>1</sup> (mJy)	rms <sup>2</sup> (mJy)	rms <sup>3</sup> (mJy)	Notes
NGC 1052	21 Aug 2004	202	1220 ± 180	25	2.9	2.6	2.0	ripples
NGC 1068	21 Aug 2004	101	1439 ± 210	25	2.3	2.4	2.6	ripples
NGC 1167	22 Aug 2004	154	635 ± 95	23	2.1	1.7	2.0	
NGC 1275	21 Aug 2004	54	1606 ± 240	39	30.0	21	21	ripples
NGC 1667	12 Nov 2004	102	-	20	2.5	2.7	3.2	
NGC 2110	8 Nov 2004, 8 Feb 2005	297	131 ± 19	19	1.0	1.8	1.9	
NGC 2273	5 Dec 2004	100	20±2	17	1.8	3.2	1.2	
NGC 2639	23 Aug 2004, 11 Nov 2004	254	93 ± 14	23	1.1	1.0	1.2	
NGC 2992	21 Aug 2004	185	77 ± 11	27	2.5	2.8	2.7	
NGC 3079	22 Aug 2004	65	283 ± 42	22	2.3	3.8	2.9	ABS
NGC 3982	13 Nov 2004	102	-	16	1.8	1.9	4.8	
NGC 4151	21 Aug 2004, 28 Nov 2004	376	155 ± 23	18	0.9	1.1	1.2	
NGC 4258	6 Dec 2004	152	68 ± 10	17	1.2	1.8	1.3	
NGC 4261	7 Nov 2004	134	1320 ± 200	23	2.7	2.5	3.3	ABS
NGC 4388	22 Aug 2004	205	62 ± 9	21	1.5	1.3	1.3	
NGC 5005	28 Nov 2004	57	42 ± 6	22	2.1	3.1	2.2	
NGC 5135	6 Dec 2004, 9 Feb 2005	140	76 ± 11	29	2.5	3.9	2.5	
NGC 5194	12 Nov 2004, 6 Dec 2004	240	71 ± 10	16	0.9	1.5	1.0	
NGC 5506	22 Aug 2004	230	157 ± 23	24	1.5	1.5	1.5	
NGC 5793	21 Aug 2004	167	263 ± 38	26	1.9	1.3	0.8	ABS
NGC 6240	18 Aug 2004	102	122 ± 18	24	1.9	1.8	2.0	
NGC 6251	28 Nov 2004	32	680 ± 102	17	2.1	3.5	3.4	
NGC 7674	22 Aug 2004	205	75 ± 11	22	1.3	1.1	1.0	
Mrk 3	21 Aug 2004, 9 Feb 2005	274	243 ± 36	21	1.1	1.3	1.1	
Mrk 231	16 Mar 2007	113	190 ± 28	15	1.5	-	-	ABS
Mrk 273	16 Mar 2007	83	30 ± 4	14	1.5	-	-	ABS
Mrk 348	23 Aug 2004, 12 Nov 2004	564	616 ± 92	22	0.7	1.5	1.3	
Mrk 1210	13 Nov 2004, 9 Feb 2005	345	57 ± 8	22	0.9	1.1	0.9	
Mrk 1073	22 Aug 2004	358	26 ± 3	21	1.0	0.9	1.0	
IRAS F01475-0740	23 Aug 2004, 28 Nov 2004	254	92 ± 15	23	1.1	1.8	2.0	
IRAS 05414+5840	19 Aug 2004	135	62 ± 9	23	1.4	1.4	1.6	

Table 2.3: Observing parameters of the 6 GHz OH observations with Effelsberg of a subset of 31 sources from Table 2.2. The channel width was  $3.8 \text{ km s}^{-1}$  for all observations, except for Mrk 231 and Mrk 273 for which it was  $4.8 \text{ km s}^{-1}$ .

The rms noise levels in the spectra are given for spectra centred on: <sup>1</sup> 6035 MHz, <sup>2</sup> 6016 MHz, and <sup>3</sup> 6049 MHz.

Notes column: 'ABS' means OH absorption was detected, and 'ripples' means a large standing ripple was seen in the spectral baseline which raised the rms.

Source Name	Date	int. time (min)	$S_{4.7}$ GHz (mJy)	$T_{\text{sys}}$ K	rms <sup>1</sup> (mJy)	rms <sup>2</sup> (mJy)	rms <sup>3</sup> (mJy)
NGC 1052	10 Jul 2005	680	730 ± 95	25	2.1	4.5	4.0
NGC 1167	9 Jul 2005	147	718 ± 107	19	3.6	5.0	4.2
NGC 2110	9 Jul 2005	141	266 ± 40	23	5.4	4.5	5.0
NGC 2639	9 Jul 2005	146	178 ± 26	19	5.6	4.3	4.9
NGC 2992	17 Jul 2005	144	145 ± 22	22	4.0	4.3	4.8
NGC 3079	13 Jan 2005, 10 Jul 2005	153	364 ± 54	20	4.8	5.2	3.7
NGC 4151	9 Jul 2005	150	130 ± 20	19	3.3	3.3	3.8
NGC 4261	13 Jan 2005, 1 Jul 2005	300	1820 ± 270	38	3.5	8.4	8.6
NGC 4388	17 Jul 2005	146	218 ± 33	19	3.3	3.5	4.4
NGC 5135	19 Jul 2005	140	115 ± 17	28	4.7	6.8	6.8
NGC 5506	9 Jul 2005	244	201 ± 30	20	2.5	2.9	3.2
NGC 5793	17 Jul 2005	146	328 ± 49	24	3.0	3.7	4.4
NGC 6240	1 Jul 2005	227	217 ± 32	25	2.9	9.3	4.8
NGC 7674	1 Jul 2005	148	202 ± 30	20	4.1	4.9	4.9
Mrk 3	8 Jul 2005	244	425 ± 63	36	3.7	6.2	4.5
Mrk 348	1 Jul 2005	84	243 ± 36	23	2.2	2.3	2.4
Mrk 463E	1 Jul 2005	159	143 ± 21	36	1.8	6.6	1.9
Mrk 1210	17 Jul 2005	145	75 ± 11	38	6.8	9.8	9.8
Mrk 1073	9 Jul 2005	150	-	40	7.2	7.5	6.8
IRAS 05414+5840	8 Jul 2005	144	90 ± 13	68	10.0	11.7	12.2

Table 2.4: Observing parameters of the 4.7 GHz OH observations with Effelsberg of a subset of 20 sources from Table 2.2. The channel width was  $1.2 \text{ km s}^{-1}$  for all observations, except for Mrk 348 and Mrk 463E for which it was  $4.9 \text{ km s}^{-1}$  and for NGC 4261 for which it was  $0.6 \text{ km s}^{-1}$ .

The rms noise levels are given for spectra centred on: <sup>1</sup>4750 MHz, <sup>2</sup>4660 MHz, and <sup>3</sup>4765 MHz.

## 2.3 Results

The results of the 6 GHz observations are summarized in Table 2.3 and the spectra are shown in Fig. 2.2. Of the 31 sources observed at 6 GHz, absorption was detected towards five (NGC 3079, NGC 4261, NGC 5793, Mrk 231, and Mrk 273) with both wide absorption components and narrow troughs at the systemic velocities of the two lines at 6035 MHz

and 6030 MHz. No absorption was seen in the satellite lines at 6049 MHz and 6016 MHz for any of those sources (the spectra are shown in Appendix A & B). For those sources with a high flux density (NGC 1275, NGC 1068, and NGC 1052), the strong ripples obscured whether any absorption or emission components were present, despite these being excellent candidates. For the remaining 23 sources, no spectral line feature was seen in any of the 6 GHz transitions.

Of the 20 sources observed at 4.7 GHz, none showed detections, either in emission or in absorption. The parameters of these observations shown in Table 2.4. The spectra of the sources are shown in the Appendix C & D. All velocities in this thesis are given in the local standard of rest (LSR) reference frame following the optical definition ( $V = (\Delta\lambda/\lambda_0)c$ ), unless otherwise stated.

### 2.3.1 Notes on individual sources

In this section, I give background information on each source and describe the results of the Effelsberg OH observations.

#### Sources with detections

*NGC 3079* is a nearby, edge-on spiral galaxy with a Seyfert 2 nucleus (Ford et al. 1986; Ho et al. 1997). *NGC 3079* is host to the most powerful windblown superbubble known (Filippenko & Sargent 1992; Veilleux et al. 1994), which appears to originate within the nucleus due to a combination of stellar winds and supernova explosions in a site of massive star formation (see Figure 2.5; left panel). Infrared and radio measurements suggest an AGN coexists with the nuclear starburst (Lawrence et al. 1985; Irwin & Seaquist 1988; Haschick et al. 1990; Irwin & Sofue 1992; Baan & Irwin 1995). At the base of the superbubble, a dense molecular kpc-scale disk traced by CO (Koda et al. 2002), HCN, and HCO<sup>+</sup> emission (Nguyen et al. 1992) has been observed. The molecular disk is aligned with the much larger galaxy disk and these rotate in the same direction. Evidence for the existence of an active nucleus comes from X-ray observations such as a continuum excess in the 20 keV to 100 keV band and a 6.4 keV Fe K $\alpha$  line (Iyomoto et al. 2001; Cecil et al. 2002). Also, a large X-ray absorbing column density of  $\sim 10^{25}$  cm<sup>-2</sup> (Iyomoto et al. 2001) towards the nucleus was derived from both soft and hard X-ray data. Radio continuum observations revealed a linear structure consisting of double radio lobes extending 1.5 kpc on either side of the major axis of the galaxy and a complex nuclear structure on parsec scales consistent with a jet (Irwin & Seaquist 1988). Due to the complexity of the radio continuum structure, it is not clear where the true nucleus is located. However, broad (200 km s<sup>-1</sup> to 400 km s<sup>-1</sup>) and deep ( $\tau \sim 0.5$ ) HI absorption and weaker but equally broad and deep OH absorption are found towards those compact radio sources in the nucleus. Based on VLA observations, Baan & Irwin (1995) concluded that the two components of HI and OH absorptions are associated with an obscuring torus in the nuclear region. MERLIN observations resolved the rotation of the HI absorption (Pedlar et al. 1996; Figure 2.3, right panel) to be in the same sense as the rotational traced by HI emission and CO(1-0) emission on galactic scales (Irwin & Seaquist 1991; Irwin & Sofue 1992). However, the three HI absorption components viewed against the double-peaked radio source appear to be counter-rotating relative to the rotation in the outer galaxy (Sawada-Satoh et al. 2000). The galaxy harbours one of the most luminous water masers known

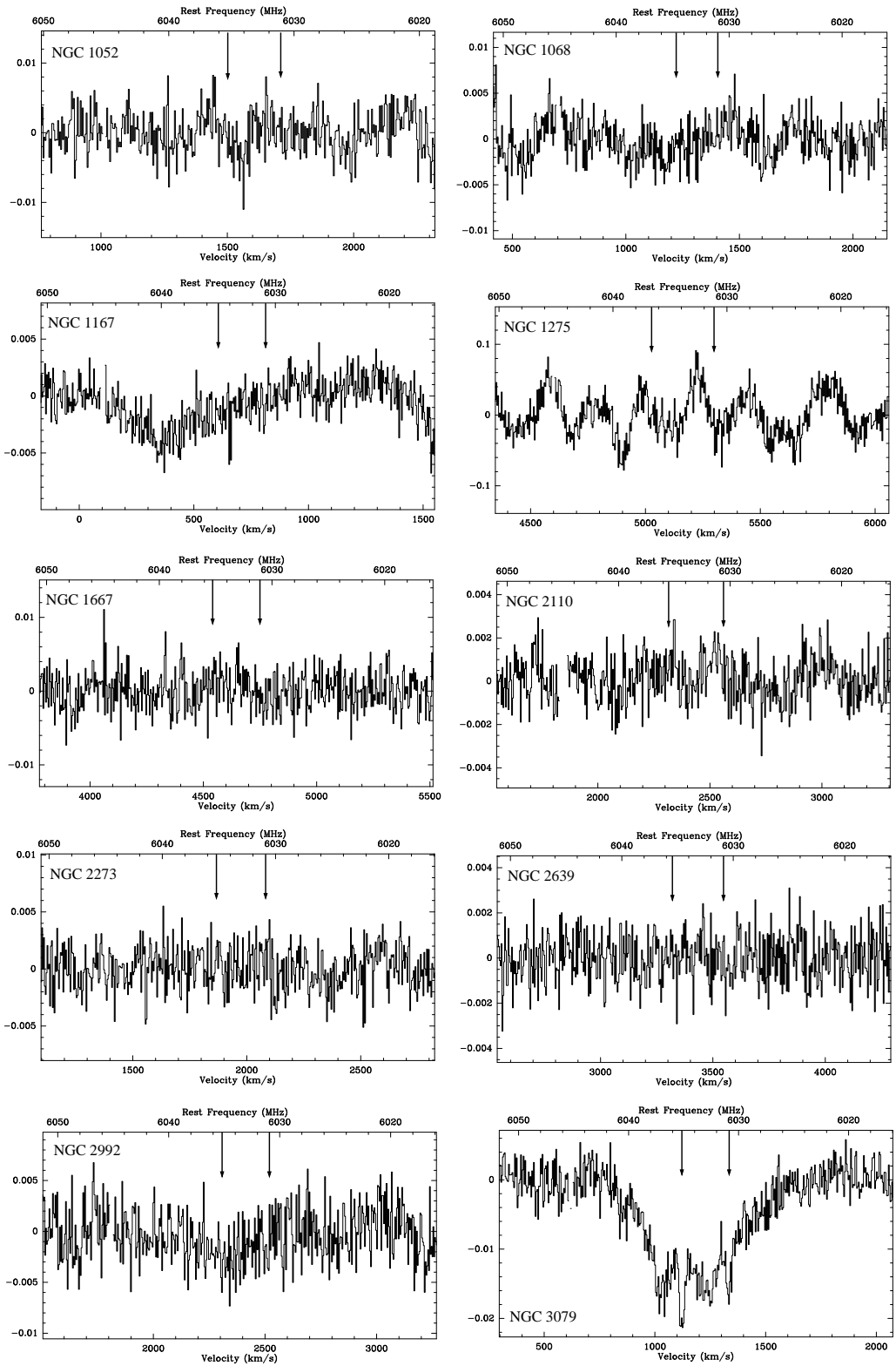


Figure 2.2: Spectra of the sources observed in the main transition of excited OH at 6035 MHz and 6030 MHz with Effelsberg. The line rest frequencies are marked by the arrows at the top of each plot. The velocity axis is the LSR optical definition for the transition at 6035 MHz. The vertical axis is in mJy. The channel widths and rms are given in Table 2.3.

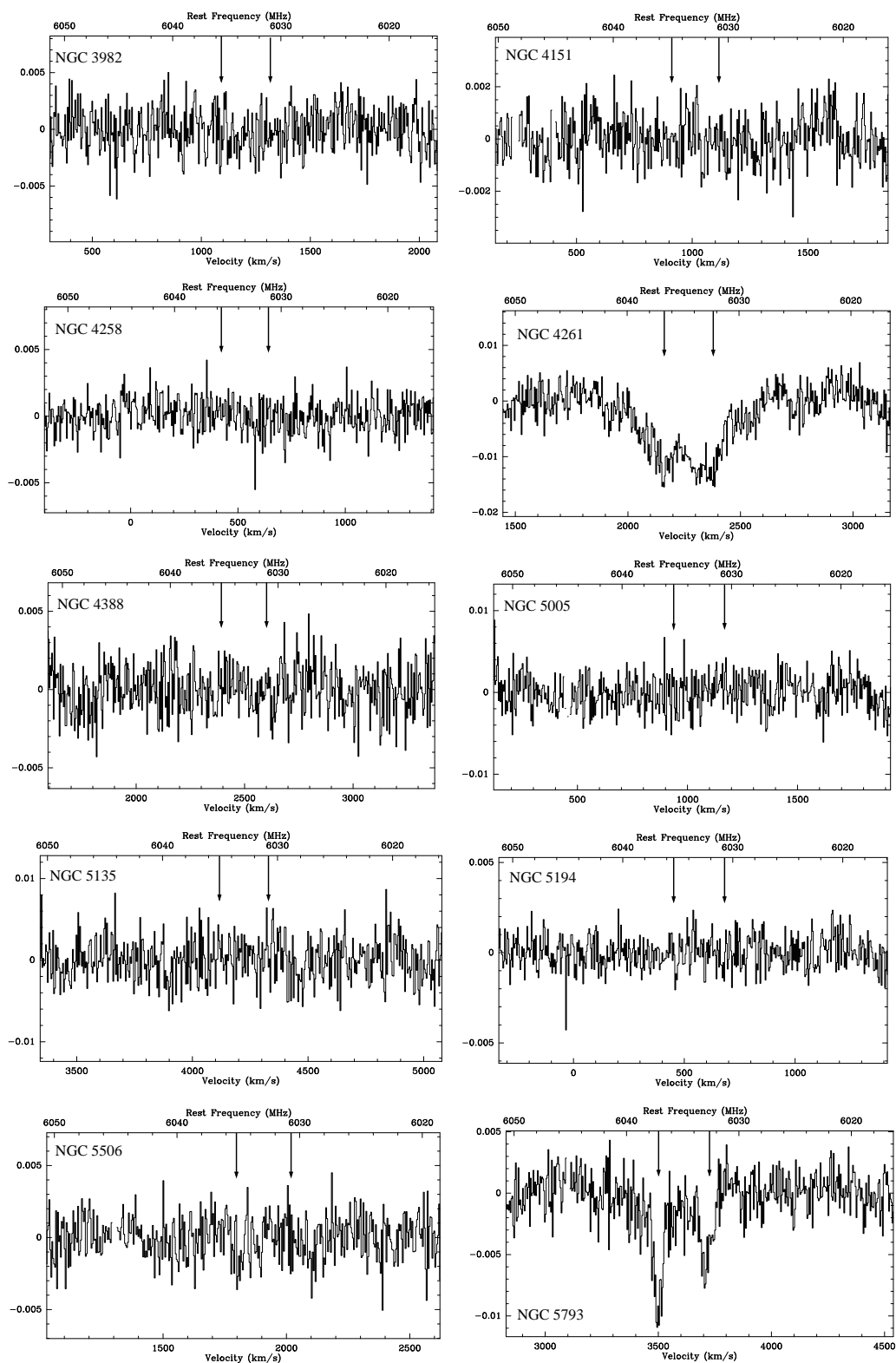


Figure 2.2: continued.

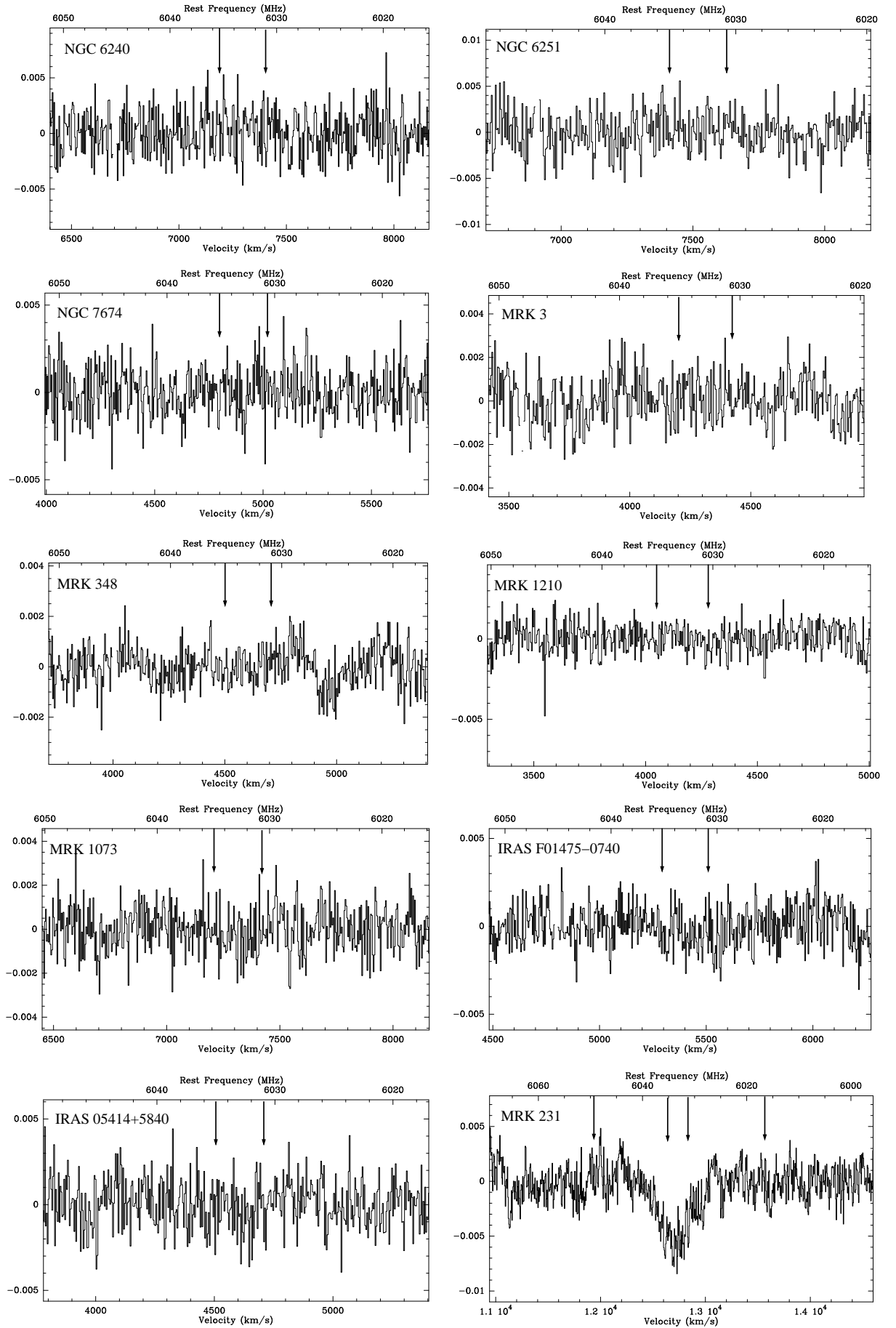


Figure 2.2: continued.

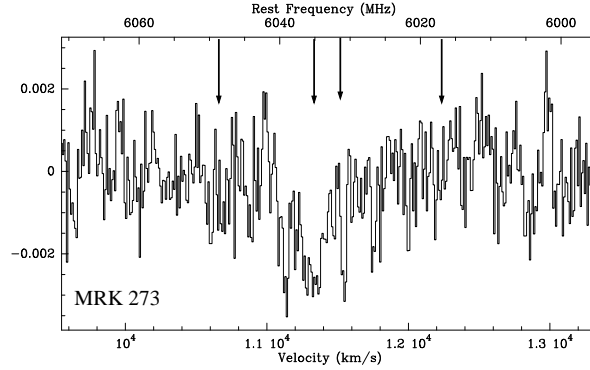


Figure 2.2: continued.

(Henkel et al. 1984; Haschick & Baan 1985), such maser emission is generally associated with AGN activity (Braatz et al. 1997) and their dynamics can be used to locate the centre of mass of the nucleus. No hidden polarized broad lines have been observed in this source (Tran 2001).

NGC 3079 was observed at 6 GHz with Effelsberg in August 2004. The source was observed for a total of 65 minutes, however a broad absorption component was already visible after just a few minutes integration time. The resulting rms noise in the spectrum, after a second-order polynomial was fitted and subtracted from the spectrum, was 2.3 mJy (channel width  $3.8 \text{ km s}^{-1}$ ). The final spectrum is shown in Figure 2.2. The line parameters from Gaussian fits are given in Table 2.5.

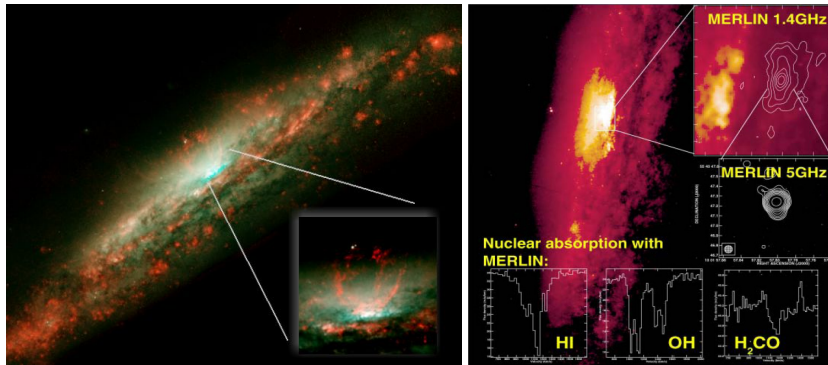


Figure 2.3: *Left:* composite images showing the red superbubble of hot gas originating from the core of NGC 3079, which can be seen as gaseous filaments that tower above the galaxy's disk. The bubble is probably produced by star formation and AGN activity (Cecil et al. 2001). *Right:* high resolution MERLIN radio continuum images of the core of NGC 3079 and MERLIN spectra showing molecular gas absorption of OH, HI and H<sub>2</sub>CO superimposed on an HST optical image (Strong et al. 2004, ASP conf, 320, 109; Pedlar et al. 1996).

Transition (MHz)	$V_{\text{abs}}^{(1)}$ ( $\text{km s}^{-1}$ )	$\Delta V_{1/2}^{(2)}$ ( $\text{km s}^{-1}$ )	Line peak (mJy)	$\int S dv$ (mJy $\text{km s}^{-1}$ )	$\tau(\text{OH})^{(3)}$	$N_{6\text{ GHz}}$ ( $\text{cm}^{-2}$ )	$N_{\text{OH}}$ ( $\text{cm}^{-2}$ )
<b>NGC 3079</b>							
6030	$974 \pm 6$	$421.8 \pm 10.2$	$-15.6 \pm 2.3$	$6069 \pm 135$	$0.055 \pm 0.008$	$1.2 \times 10^{17}$	$1.5 \times 10^{18}$
6035	$1021 \pm 4$	$59.4 \pm 11.5$	$-6.2 \pm 0.9$	$341 \pm 67$	$0.022 \pm 0.003$		
<b>NGC 4261</b>							
6030	$2125 \pm 11$	$214.6 \pm 27.8$	$-12.7 \pm 1.9$	$3492 \pm 371$	$0.009 \pm 0.001$	$1.6 \times 10^{16}$	$2.2 \times 10^{17}$
6035	$2136 \pm 10$	$172.1 \pm 19.6$	$-9.3 \pm 1.4$	$1478 \pm 323$	$0.007 \pm 0.001$		
<b>NGC 5793</b>							
6030	$3494 \pm 3$	$59.2 \pm 8.7$	$-5.9 \pm 0.8$	$364 \pm 43$	$0.022 \pm 0.003$	$1.9 \times 10^{16}$	$1.7 \times 10^{17}$
6035	$3499 \pm 2$	$52.5 \pm 6.3$	$-9.5 \pm 1.2$	$529 \pm 45$	$0.036 \pm 0.004$		
<b>Mrk 231</b>							
6030	$12534 \pm 8$	$319.1 \pm 18.3$	$-5.7 \pm 0.7$	$1950 \pm 101$	$0.030 \pm 0.004$	$4.6 \times 10^{16}$	$6.3 \times 10^{17}$
6035	-	-	-	-	-	-	-
<b>Mrk 273</b>							
6030	$11344 \pm 4$	$30.3 \pm 7.9$	$-3.5 \pm 0.5$	$113 \pm 37$	$0.117 \pm 0.017$	$1.7 \times 10^{17}$	$2.3 \times 10^{18}$
6035	$11420 \pm 20$	$341.6 \pm 52.0$	$-3.1 \pm 0.4$	$1124 \pm 129$	$0.103 \pm 0.015$		

Column densities calculated with  $T_{\text{ex}} = 53\text{ K}$  for all transitions. For NGC 5793  $T_{\text{ex}}$  is 67 K.

1) Local standard of rest (LSR) velocities following the optical definition.

2) Full width to half power (FWHP) linewidth.

3) The peak optical depths are based on the observed total 6 GHz continuum flux density and a unity source covering factor. The errors include uncertainties in line and continuum flux densities and are  $1\sigma$ .

Table 2.5: 6 GHz Effelsberg observations: line parameters obtained from Gaussian fits.

The absorption line width is  $800 \text{ km s}^{-1}$ , with two deeper components corresponding to the two transitions (6030 MHz and 6035 MHz) at the systemic velocity ( $V_{\text{LSR}} = 1116 \text{ km s}^{-1}$ , Hagiwara et al. 2004) with fitted peak flux densities of the two transitions of  $-6.2 \text{ mJy}$  and  $-15.6 \text{ mJy}$ , respectively. The continuum flux density of the source at 6.0 GHz was measured to be  $(283 \pm 42) \text{ mJy}$ , yielding line opacities of 0.02 and 0.05 (assuming a covering factor of unity). Two further, slightly broader lines corresponding to the two transitions were also observed blue-shifted relative to the systemic velocity by  $\sim 100 \text{ km s}^{-1}$ , indicating the presence of some outflowing gas. Alternatively, these two troughs, symmetric around the 6035 MHz line, might suggest the presence of gas rotating around a central source. The 6 GHz absorption is likely to come from the central region, where the torus is expected to be since the lines are broad, the 1.6 GHz absorption in this source has been found to come from the nuclear region, and the VLBI jets against which the absorption is likely to extend to 1.5 pc from the central engine. No absorption was observed in the 4.7 GHz transition.

*NGC 4261* is a nearby elliptical galaxy with a large near edge-on nuclear disk of gas and dust, seen with the HST. The disk is offset with respect to the nucleus by  $(4 \pm 2) \text{ pc}$ , probably as a consequence of a past merging event where the equilibrium position has not yet been reached (Ferrarese et al. 1996). It is classified as a FR-I radio galaxy with a pair of highly symmetric kpc-scale jets. A disk radius 0.2 pc has been derived from free-free absorption within the disk (Jones et al. 2001), with an inferred column density of  $0.6 \times 10^{22} \text{ cm}^{-2}$ . This column density is a bit less than what was measured with XMM-Newton ( $N_{\text{H}} = 4 \times 10^{22} \text{ cm}^{-2}$ ; Sambruna et al. 2003). VLBI observations revealed neutral hydrogen absorption towards the counter-jet at a projected distance of  $\sim 2.5 \text{ pc}$  from the core with a column density of  $N_{\text{HI}} = 2.5 \times 10^{21} \text{ cm}^{-2}$  (van Langevelde et al. 2000). Consistent with the torus unified models, CO(2-1) absorption has also been detected in this source (Jaffe & McNamara 1994).

*NGC 4261* was observed with Effelsberg at 6 GHz in November 2004 for 134 minutes. The measured continuum flux density at 6.0 GHz was  $(1320 \pm 200) \text{ mJy}$ , which was strong enough to create considerable ripples across the band. A third-order polynomial was subtracted from the spectrum after calibration, with a resulting rms of 2.7 mJy (channel width  $3.8 \text{ km s}^{-1}$ ). The resulting spectrum is seen in Figure 2.2. A clear, broad absorption feature is seen in this source. Deep absorption is seen corresponding to the two transitions at 6035 MHz and 6030 MHz with a fitted peak flux density of  $-9.3 \text{ mJy}$  and  $-12.7 \text{ mJy}$ , respectively. The fitted parameters are given in Table 2.6.

*NGC 5793* is an edge-on spiral galaxy with a Seyfert 2 nucleus. HI (Jerkins 1983) and OH absorption at 1.67 GHz (Whiteoak & Gardner 1987) have been observed against a compact radio source (Gardner et al. 1992), indicating large amounts of absorbing material in front of the active nucleus. Higher resolution VLBI observations could resolve OH absorption towards the central (weak) continuum source (Hagiwara et al. 2000). The direction of the OH velocity field is opposite to the sense of rotation of the outer galactic disk traced by CO(1-0), implying the existence of an independent kinematical system in the central few parsec region of the galaxy. Water maser emission has also been observed towards the nucleus of *NGC 5793* (Hagiwara et al. 1997), as part of a maser disk.

*NGC 5793* was observed with Effelsberg at 6 GHz in August 2004 for 167 minutes. After calibration, a second-order polynomial was fitted to the baseline and subtracted,

yielding an rms noise of 1.9 mJy (channel width  $3.8 \text{ km s}^{-1}$ ). A clear absorption feature can be seen, shown in Figure 2.2. The absorption spectrum in NGC 5793 shows a very broad line width, which ranges up to  $1000 \text{ km s}^{-1}$ . Two narrow troughs are seen corresponding to the two transitions (6030 MHz and 6035 MHz) at the systemic velocity and with corresponding peak line opacities of  $\sim 0.04$  and  $0.03$  (assuming a source covering factor of unity). For comparison, the optical depth in the OH line at 1667 MHz, derived with the VLA in A-configuration was 0.065 (Gardner & Whiteoak 1986) and those derived from VLBA observations (Hagiwara et al. 2000) at 1665 MHz and 1667 MHz were 0.086 and 0.085, respectively. While these values are consistent with each other, they are slightly higher than those derived with Effelsberg. Indeed, Hagiwara et al. (2000) find from VLBA observations that the foreground absorbing gas is spatially confined. Since the Effelsberg beam includes more diffuse emission that was not absorbed in the 1.67 GHz OH line, it is likely that the covering factor in the 6 GHz OH line is  $\ll 1$ . Also, the velocity width of the absorption line in the 1667 MHz transition observed with the VLBA was  $28.4 \text{ km s}^{-1}$ , which is narrower by 30% than that observed with the VLA of  $39.4 \text{ km s}^{-1}$ . The velocity width of the 6 GHz observations are  $\sim 55 \text{ km s}^{-1}$ , even broader than those observed with the VLA. It is thus likely that a part of the absorption is more extended than that seen with the VLBA or VLA. The fitted line parameters are given in Table 2.5.

*Mrk 231* is one of the most luminous infrared galaxies known, with  $L_{\text{FIR}} = 10^{12.04} L_{\odot}$ . Its nuclear optical spectrum is classified as Seyfert 1, from optical spectroscopic observations of broad lines (Boksenberg et al. 1977). In the radio, it shows a jet extending from sub-pc scales to hundreds of parsecs (Ulvestad et al. 1999). The large IR luminosity has been attributed partly to starburst activity (Downes & Solomon 1998) and partly to the AGN (Soifer et al. 2000), however the AGN dominates the radio continuum emission on scales  $< 100 \text{ pc}$  from the centre (Lonsdale et al. 2003). Previous X-ray measurements have yielded different values for the X-ray absorbing column density, which are very model dependent. However, recently Braito et al. (2004), analyzed XMM-Newton and BeppoSax data, concluding that the AGN is highly absorbed, with a corresponding column density,  $N_{\text{H}}$ , of  $\sim 2 \times 10^{24} \text{ cm}^{-2}$ . *Mrk 231* contains a strong OH megamaser in the transitions at 1667 MHz, 1665 MHz, 1720 MHz and 1612 MHz (Baan 1985; Baan et al. 1992). The maser emission extends over  $(760 \pm 100) \text{ km s}^{-1}$  (Staveland-Smith et al. 1987). OH megamaser activity seen with WSRT and imaged using MERLIN and the EVN revealed the characteristics of a rotating, dusty molecular torus located between 30 pc and 100 pc from the central engine (Klößner et al. 2003). The integrated line emission seen by EVN and MERLIN at 1.67 GHz accounts for only half of the emission observed by WSRT, indicating an extended distribution of OH. Water maser emission has been searched for, but not found (Braatz et al. 1996).

*Mrk 231* was observed with Effelsberg in March 2007 for 113 minutes using the FFTS digital spectrometer, which delivered a broad-band spectrum ranging over  $3000 \text{ km s}^{-1}$  and contained all four transitions in one spectrum. A second-order polynomial was fitted and removed from the baseline after calibration, resulting in an rms of 1.5 mJy (channel width  $4.8 \text{ km s}^{-1}$ ).

A broad absorption component was observed in both the 6030 MHz and 6035 MHz transitions which overlapped to produce a single wide absorption profile of  $\sim 900 \text{ km s}^{-1}$ . In addition, a narrow absorption component was observed in both transitions with widths of  $90 \text{ km s}^{-1}$  centred on the systemic velocity. No detections were made of the satellite

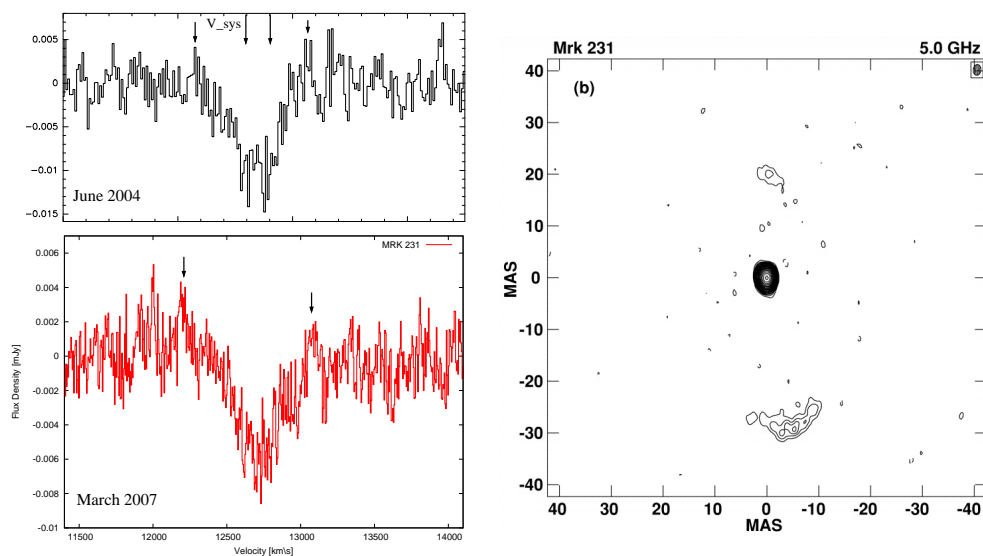


*Figure 2.4: Left:* 6 GHz Effelsberg spectra of Mrk 231. The top panel shows the smoothed spectrum ( $\Delta V = 15.5 \text{ km s}^{-1}$ ) taken in June 2004 (C. Henkel, priv. comm.). Two clear absorption lines are seen corresponding to the two transitions (6035 MHz and 6030 MHz), which overlap to produce a broad absorption profile extending over  $\sim 900 \text{ km s}^{-1}$ . The long arrows mark the systemic velocity of the two transitions on the velocity scale of the 6035 MHz transition. The bottom left panel shows the spectrum obtained in March 2007 at a higher resolution ( $\Delta V = 4.8 \text{ km s}^{-1}$ ). The spectra are very similar, with a broad overall absorption profile and possible weaker emission components at the sides of the broad absorption profile (marked by the short arrows). **Right:** VLBA image of Mrk 231 by Ulvestad et al. 1999 at 5.0 GHz; peak intensity  $140.0 \text{ mJy beam}^{-1}$ ; lowest positive contour  $250 \mu\text{Jy beam}^{-1}$ . Restoring beam is  $2.08 \text{ mas} \times 1.47 \text{ mas}$  in P.A.  $-5^\circ$ .

lines (6016 MHz and 6049 MHz). The final spectrum is shown in Figure 2.4 along with a previous, un-published, observation made in June 2004 (C. Henkel, priv.comm.). The two spectra show a very similar profile. The spectrum from Henkel has been smoothed to  $\sim 15.5 \text{ km s}^{-1}$  and has a higher signal-to-noise, thus the narrow absorption lines at the systemic velocity in both transitions are better visible. At the edges of the absorption profile, two possible weak emission components can be seen, in both spectra.

The absorption is stronger in the June 2004 observations, showing a depth of 11.5 mJy corresponding to an optical depth of 0.06 for a source covering factor of unity, compared to the absorption depth in March 2007 of 5.7 mJy, corresponding to an optical depth of 0.03. The same continuum flux density of 190 mJy was used to estimate the optical depths at both epochs. The fitted parameters of the absorption profile from the March 2007 observation are given in Table 2.5. The change in absorption depth could be due to variability in the source flux density or intrinsic changes in the OH absorbing column. Since, however, the 6 GHz lines require higher excitation than the 1.67 GHz lines, it is likely that absorption arises in regions that lie closer to the nucleus. The masing components at 1.67 GHz are located at a distance between 30 pc and 100 pc from the central engine (Klöckner et al. 2003).

The existence of OH absorption and maser emission in Mrk 231 is puzzling, as unified schemes predict no molecular gas on lines of sight towards the nucleus of a Seyfert 1. It may still be reconciled with the unified model if the torus is viewed face-on and absorption is seen against the lobes of the nuclear continuum source seen in Fig. 2.4 (right panel) rather than against the core. Evidence supporting this scenario is that the integrated line emission measured at high resolution by EVN and MERLIN at 1.67 GHz accounts for only half of that observed at lower resolution by WSRT, indicating that the OH absorber is extended. This scenario has already been invoked by Carilli et al. (1998), who found HI absorption towards the lobes and none towards the core. They proposed that the lobes form where the jet impacts the inner surface of an HI shell or disk. If the 6 GHz OH absorption is seen towards the compact core, it would be in contradiction with unified schemes or might require a new model for the orientation of this system with respect to the observer.

*Mrk 273* is an IR luminous ( $\sim 10^{12} L_{\odot}$ ) Seyfert 2 with a heavily obscured core as indicated by X-ray absorption ( $N_{\text{H}} = 10^{23} \text{ cm}^{-2}$ ). It is a merging galaxy showing a disturbed morphology on the kpc scale. The nuclear region as seen in the radio is extremely complex, probably due to the merging process (Carilli & Taylor 2000). Three extended radio components (Yates et al. 2000) are detected within 1 arcsecond in the nucleus. OH line emission at 1.67 GHz shows the morphology and line-of-sight velocities that are indicative of an edge-on torus with Keplerian rotation (Klöckner et al. 2004). The emission observed with the EVN accounts for 12% of the total OH emission. The source displays a number of distinct structural components in the 0.25 square arcsec central region (see Fig. 2.5, right panel).

Mrk 273 was observed at 6 GHz with Effelsberg in March 2007 for 83 minutes using the FFTS, which spanned over  $3000 \text{ km s}^{-1}$  and thus included the satellite lines. A second-order polynomial was fitted and subtracted from the baseline, reaching an rms noise of 1.5 mJy (channel width  $9.7 \text{ km s}^{-1}$ ). A broad absorption component was centred on the systemic velocity of the galaxy and is shown in Figure 2.5 (bottom left). In addition, a narrow absorption component was seen in both transitions blue-shifted by  $100 \text{ km s}^{-1}$  with

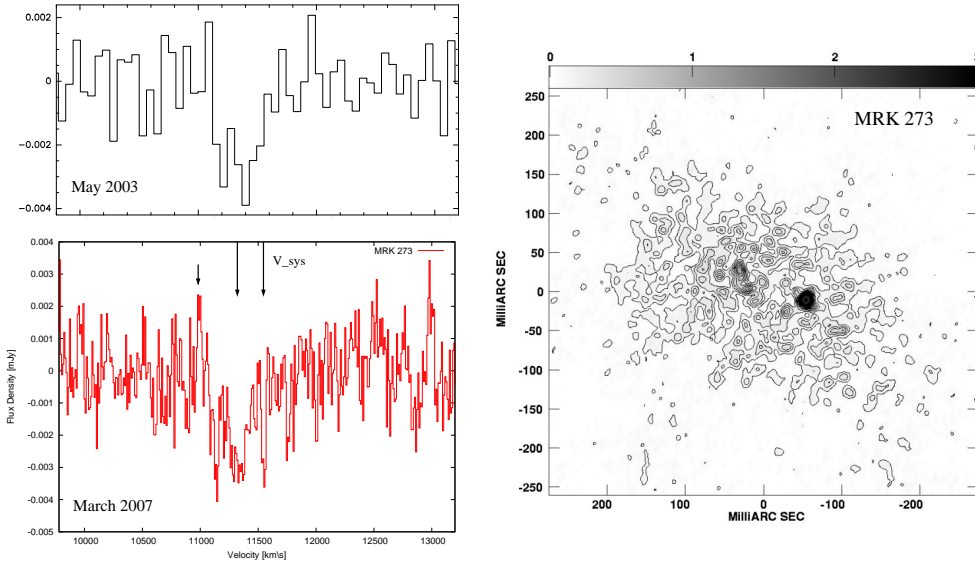


*Figure 2.5: Left:* 6 GHz Effelsberg spectra of Mrk 273. The top panel shows the smoothed spectrum ( $\Delta v = 62 \text{ km s}^{-1}$ ) taken in May 2003 (C. Henkel). The bottom panel shows the spectrum obtained in March 2007 at the resolution of  $\sim \Delta v = 10 \text{ km s}^{-1}$ . The two OH transitions are visible in absorption. The arrows in the bottom panel mark the systemic velocity of the two transitions on the velocity scale of the 6035 MHz transition. *Right:* VLBA image of Mrk 273 at 1.4 GHz and 10 mas resolution from Carilli & Taylor (2000). The source is resolved, consisting of diffuse emission punctuated by a number of compact sources. The contours are linear with an increment of  $0.1 \text{ mJy beam}^{-1}$ . The peak surface brightness is  $3.05 \text{ mJy beam}^{-1}$ .

respect to the systemic velocity and with widths of  $30 \text{ km s}^{-1}$  in the 6030 MHz transition and  $340 \text{ km s}^{-1}$  in the 6035 MHz transition. The difference between these line widths is unusual, and the very narrow linewidth of the 6030 MHz transition could be caused by an overlapping of emission and absorption components within the velocity range. Indeed, the March 2007 spectrum shows a  $3\sigma$  peak (arrowed), which may be blue-shifted maser emission in one of the 6 GHz transitions. The satellite lines (6049 MHz and 6016 MHz) were not detected. In Figure 2.5, the top left panel shows a previous un-published 6.0 GHz observation made in May 2003 (C. Henkel, priv. comm), smoothed to  $62 \text{ km s}^{-1}$  per channel. The line parameters of the March 2007 observation are given in Table 2.5. The two spectra agree well. A slight asymmetry can be seen at both epochs, with a broad redshifted wing extending to high velocity, which can be due to infalling material. This picture is consistent with the fact that ultra luminous infrared galaxies, such as Mrk 273, show large quantities of gas and dust being channelled in the inner regions. The maximum OH absorption depth at 6 GHz is  $4 \text{ mJy}$  in both epochs, corresponding to an optical depth of  $0.017$  for a source covering factor of unity and a continuum flux of  $(30 \pm 4) \text{ mJy}$ . When the 6 GHz transitions have been seen in emission, they have been associated with shocked regions resulting from interactions between supernova remnants and molecular clouds. In particular, the 6049 MHz and 4765 MHz masers become more significant at increased OH column densities (Pavlakis & Kylafis 2000; Wardle 2007; Pihlström et al. 2008). Whether these emission components are associated with dense gas around the AGN or with star-forming sites cannot be distinguished with the current data. Nevertheless, since the 6 GHz lines require higher excitation than the 1.67 GHz lines, they are likely to arise from regions

that lie closer to the nucleus.

VLBA observations of Mrk 273 by Carilli & Taylor (2000) show a northern and a southern nucleus separated by  $\sim 400$  mas. It is the northern component toward which the 1.67 GHz emission is seen (with a notable southern extension of  $\sim 80$  mas) and therefore it is likely to be the component against which the 6 GHz absorption arises. The image of the northern component is reproduced in Figure 2.5 and shows two features,  $\sim 100$  mas apart in the E-W direction and surrounding diffuse emission.

### Sources with no detections

*NGC 1052* is a nearby Seyfert 2, with strong evidence for the existence of a torus coming from radio observations. The source has a parsec-scale “twin-jet” structure with a highly inverted spectrum of the western jet base explained as pronounced free-free absorption. A more detailed introduction to the source is presented in Chapter 3.

NGC 1052 is a strong, variable source in the radio regime. The flux density of the source at 6 GHz was measured with Effelsberg to be  $(1220 \pm 180)$  mJy. No spectral line features were seen in the spectrum down to an rms noise of 2.9 mJy (channel width  $3.8 \text{ km s}^{-1}$ ). However, the continuum flux density of this source was strong enough to produce severe baseline ripples. For this reason, interferometric observations (shown in Chapter 3) were carried out to search for even higher OH transitions at 13.4 GHz.

*NGC 1068* is one of the best studied Seyfert 2 sources in the frame of the unified scheme. One of the reasons is its proximity which allows high resolution observations of the core to be carried out. X-ray observations of the central region have suggested large obscuration (Iwasawa et al. 1997; Matt et al. 1997). Also, OH and H<sub>2</sub>O maser emission was resolved towards the nucleus (Claussen & Lo 1986; Gallimore et al. 1996) who found the H<sub>2</sub>O masers to be located  $\sim 50$  mas (5 pc) from the position of the central engine. Gallimore et al. (1996) find an inner radius of the maser disk of 1.3 pc, and an outer radius of  $\sim 2.5$  pc. Also, the HI absorption profile is consistent with the Keplerian model for the H<sub>2</sub>O maser disk kinematics, and the velocity range of the OH masers, so that it is likely that the OH masers and HI absorption also originate in the obscuring material surrounding the central engine.

However, the most striking piece of direct evidence for the presence of a torus comes from the mid-infrared observations ( $8 \mu\text{m}$  and  $13 \mu\text{m}$ ) of NGC 1068 carried out with MIDI (Mid-Infrared Interferometer) of the large interferometer VLTI (Very Large Telescope Interferometer) in Chile, with an angular resolution of about 10 mas to 20 mas (Jaffe et al. 2004). The authors could detect and resolve the emission of the torus in this source, and could model it with two components; a hot and compact component of  $\sim 1$  pc (12 mas) with a temperature higher than 800 K, and a more extended component of  $\sim 3.4$  pc (50 mas) with a temperature of about 320 K. Previous adaptive optics observations had led to a maximum size of 120 mas for this structure. The observations by MIDI showed that the nature of the object was in excellent agreement with current unification scenario.

All this makes NGC 1068 *the* candidate for torus studies. NGC 1068 was observed with Effelsberg at 6 GHz in August 2004 for  $\sim 1.5$  h. The flux density of the source was measured to be  $(1439 \pm 210)$  mJy, which produced standing wave ripples across the spectrum that were strong enough to limit the sensitivity to any spectral line absorption (see Fig. 2.2). It is therefore critical that radio studies of this very special source should be

carried out at high resolution to resolve out the extended high-flux-density emission.

*NGC 1167* is a Seyfert 2 with an X-ray absorbing column of  $N_{\text{H}} = 1.14 \times 10^{21} \text{ cm}^{-2}$ . From the analysis of its X-ray spectrum, *NGC 1167* is a candidate Compton thick Seyfert 2 galaxy (Pappa et al. 2001). This galaxy contains a substantial amount of HI (Noordermeer et al. 2005), and the gas is distributed over a very large area.

The source was observed with Effelsberg in August 2004 for 154 minutes, reaching an rms noise level of  $\sim 2 \text{ mJy}$  (with a channel width of  $3.8 \text{ km s}^{-1}$ ). After calibration, a second-order polynomial was fitted and subtracted from the spectrum. The resulting spectrum in Figure 2.2 shows a broad absorption-like feature at a velocity of  $(409 \pm 12) \text{ km s}^{-1}$ , which is  $192 \text{ km s}^{-1}$  from the systemic velocity. The width of this feature is  $\sim 461 \text{ km s}^{-1}$  (with a fitted peak of  $-4.3 \text{ mJy}$ ). It is likely, though, that this feature, being isolated and offset from systemic, is caused by a residual baseline ripple. The continuum flux density measured with Effelsberg was  $(635 \pm 95) \text{ mJy}$ .

*NGC 1275 (3C 84, Perseus A)*, a Seyfert 2 galaxy, is the dominant galaxy located at the centre of the Perseus Cluster and resembles a normal elliptical galaxy on low-resolution plates (Hubble & Humason 1931). Humason (1932) and Seyfert (1943) discovered strong emission lines in the galaxy. The source consists of two merging galaxies, and as early as in 1955, Baade found two distinct emission-line systems; the central cD galaxy in the Perseus Cluster, and the so-called ‘‘high velocity system’’ (HVS) which is moving at  $3000 \text{ km s}^{-1}$  towards the dominant system. The HVS is probably a galaxy falling into the Perseus cluster. Van Gorkom & Ekers (1983) find an upper limit of  $2.5 \times 10^9 M_{\odot}$  on the HI mass of the galaxy and it has been suggested that the low mass could be evidence of ram pressure stripping or a past interaction with another galaxy (Conselice et al. 2001). A column density map of the HVS taken from a deep 200 ks Chandra observation showed an average column density,  $N_{\text{H}}$ , of  $10^{21} \text{ cm}^{-2}$  (Gillmon et al. 2004). Also, Risaliti et al. (1999) estimated absorbing HI columns derived from X-ray observations to be  $1.49 \times 10^{22} \text{ cm}^{-2}$ . However, these values are likely to be lower limits, as the source has shown characteristics of a Compton-thick source (Matt et al. 1997). CO observations of the central regions have detected giant molecular clouds (Inoue et al. 1996), revealing the majority of the gas to be in a ring structure of radius  $\approx 4 \text{ arcsec}$ . The ring has a westerly extension up to  $30 \text{ arcsec}$  from the nucleus, and nearly 80% of the total CO is on the western side. Deep interferometric observations of the nucleus show no CO absorption from very cold gas (Braine et al. 1995). A VLA search for OH absorption at 1665 MHz and 1667 MHz against the nucleus of *NGC 1275* showed no absorption in the low-velocity system within velocities of up to  $2200 \text{ km s}^{-1}$  (O’Dea & Baum 1987).

*NGC 1275* was observed with Effelsberg at 6 GHz in August 2004 for 54 minutes. The rms reached was  $\sim 30 \text{ mJy}$  (with a channel width of  $3.8 \text{ km s}^{-1}$ ), which was high due to the large standing-wave ripple created by the strong continuum emission (see Fig. 2.4). No spectral features could be discerned, though with poor sensitivity due to the baseline ripples. The continuum strength was measured to be  $(1606 \pm 240) \text{ mJy}$ .

*NGC 1667* has a Seyfert 2 nucleus, surrounded by extended HI regions, the ionization of which is only weakly influenced by the central engine. Radovich & Rafanelli (1996) find evidence for intense star formation activity in the inner 10 kpc of this source. The source was selected for its X-ray properties. It was not detected by GINGA and presented a very

low flux in an ASCA observation (Turner et al. 1997; Pappa et al. 2001). A similarly low emission was found in an XMM-Newton observation (Bianchi et al. 2005). A new model favoured a pure reflection component and soft excess, which, together with a relatively low X-ray flux and the large ratio between the [O III] and the FIR fluxes, suggests that the source is Compton-thick.

NGC 1667 was observed at 6 GHz in August 2004 for 102 minutes. A second-order polynomial was fitted and subtracted from the spectrum, with a resulting rms noise of  $\sim 2.7$  mJy (channel width  $3.8 \text{ km s}^{-1}$ ). No OH absorption or emission was observed in this source. The continuum flux density of the source at 6.0 GHz was very low and was not detected in the pointing scans, and so it was estimated to be below a few millijansky.

*NGC 2110* is an early-type Seyfert 2 galaxy whose AGN activity was discovered through its X-ray emission (Bradt et al. 1978). Narrow-band images show high-excitation gas extending up to 10 arcsec from the nucleus (Wilson et al. 1985; Mulchaey et al. 1994), in a similar direction to a jet-like radio source (Ulvestad & Wilson 1983). Hidden polarized broad lines were detected towards the nucleus of this source (Gu et al. 2001). The hard X-ray emission of NGC 2110 (Malaguti et al. 1999) is highly absorbed and indicates an obscured Seyfert 1 nucleus. Storch-Bergmann et al. (1999) found extended  $\text{H}_2$  emission, which is probably excited by the central X-rays source. An X-ray absorbing column density of  $N_{\text{H}} = 2.89 \times 10^{24} \text{ cm}^{-2}$  has been derived (Risaliti et al. 1999). OH at 1.67 GHz was searched for and not found by Baan et al. (1992), with a  $3\sigma$  upper limit of 10 mJy corresponding to an optical depth of  $< 0.13$ .

The source was observed with Effelsberg in August 2004 and February 2005 for a total of 297 minutes. After flux-density calibration, a second-order polynomial was fitted and subtracted from the baseline, reaching an rms of  $\sim 1$  mJy (channel width  $3.8 \text{ km s}^{-1}$ ). No detection of OH emission or absorption was made in this source, down to a  $3\sigma$  level of 3 mJy assuming a line width equal to the channel width (i.e.  $\tau < 0.02$ ). The continuum flux density at 6.0 GHz was measured to be  $(131 \pm 19)$  mJy.

*NGC 2273* is a Seyfert 2 galaxy with significant nuclear star formation activity (Mulchaey et al. 1996), and a nuclear ring of dust (Yankulova 1999). HI observations have indicated that the galaxy is not very gas rich for a barred spiral galaxy with such a wide variety of nuclear activity (van Driel & Buta 1991). This picture was supported by CO spectra (Young & Devereux 1991) showing narrow linewidths and suggesting that most of the molecular gas must be contained in the central few arcseconds of the nucleus. The main selection criterion was the large absorbing column,  $N_{\text{H}}$ , on the light of sight of  $> 10^{25} \text{ cm}^{-2}$  measured by Maiolino et al. (1998) using BeppoSAX data, which were best fitted by a Compton-thick reflection-dominated model.

NGC 2273 was observed with Effelsberg at 6 GHz in December 2004 for 100 minutes. A first-order polynomial was fitted and subtracted from the spectrum after flux-density calibration, yielding an rms noise of  $\sim 1.8$  mJy (channel width  $3.8 \text{ km s}^{-1}$ ). No detection of OH emission or absorption was made in this source. The continuum flux density of the source at 6.0 GHz was  $(20 \pm 2)$  mJy.

*NGC 2639* is generally considered to be a LINER (e.g. Ho, Filippenko, & Sargent 1993), though is sometimes described as a Seyfert (e.g. Keel 1984). Water megamaser emission was detected towards the nuclear region (Braatz et al. 1994) showing evidence for an

accretion disk (Wilson et al. 1995) with bright, narrow ( $4.4 \text{ km s}^{-1}$ ) lines and a broad ( $50 \text{ km s}^{-1}$ ) feature extending blueward. Also, strong CO(1-0) emission was observed and mapped towards the centre (Raluy et al. 1998).

NGC 2639 was observed with Effelsberg at 6 GHz in August 2004 for 254 minutes. A first-order polynomial was fitted and subtracted from the final spectrum, yielding an rms of 1.0 mJy (channel width  $3.8 \text{ km s}^{-1}$ ). No detection of OH was made towards this source. The continuum flux density was measured at 6.0 GHz to be  $(93 \pm 14) \text{ mJy}$ .

NGC 2992 is a gas-rich (Sanders & Mirabel 1985) galaxy classified as having a Seyfert 1.9 active nucleus. It is interacting with NGC 2993, which is connected to the southern part of NGC 2992 by a tidal tail. NGC 2992 is one of the brightest AGN in the X-ray sky (Ward et al. 1978; Griffiths et al. 1979; Maccararo et al. 1982). The X-ray spectral properties are described as having a significant absorbing column of  $N_{\text{H}} \sim 5 \times 10^{21} \text{ cm}^{-2}$  (Turner & Pounds 1989) or  $10^{22} \text{ cm}^{-2}$  (Gilli et al. 2000), and a prominent Fe K $\alpha$  fluorescence emission line (Weaver et al. 1996). Also, a delayed response of the reflection component to the variation in the nuclear X-ray source strength was detected by Weaver et al. (1996), who derived a distance of  $\sim 3.2 \text{ pc}$  between the primary X-ray source and the reflecting material, which they inferred to be dense, neutral gas in the central region but outside the accretion disk, with column densities of  $N_{\text{H}} \sim (10^{23} \text{ to } 10^{25}) \text{ cm}^{-2}$ .

The source was observed with Effelsberg at 6 GHz in August 2004 for 185 minutes. After calibration, a second-order polynomial was fitted and subtracted from the baseline, reaching an rms of 2.5 mJy (channel width  $3.8 \text{ km s}^{-1}$ ). The final spectrum is shown in Figure 2.2. Despite a slight depression in the spectrum due to a residual baseline ripple, no spectral features were seen at the expected velocity of the OH line. The measured flux density at 6.0 GHz was  $(77 \pm 11) \text{ mJy}$ .

NGC 3982 has been identified as a Seyfert 2 galaxy. The source appears unobscured based on optical and UV HST data and does not show broad lines in either direct or polarized light. The apparent lack of obscuration made this source a good candidate for a Seyfert 2 that might genuinely lack a BLR. X-rays are presumed to originate close to the central engine and therefore may see absorbing material that exists on very small scales. Hard X-rays have high enough energy that they are expected to penetrate such absorbing material and soft X-rays should show absorption. However, NGC 3982 proved to be a faint hard X-ray source with most of the emission in the soft X-ray band. An X-ray absorbing column density of  $N_{\text{H}} \sim 2.3 \times 10^{21} \text{ cm}^{-1}$  was derived from the soft X-rays (Ghosh et al. 2007). Those authors suggest that the faintness of the hard X-ray band emission might indicate Compton-thick absorption on the line of sight to the nucleus and that the soft X-rays originate in the NLR. Thus, this object probably has a large X-ray absorbing column towards the nucleus, despite the moderate absorption seen in soft X-rays, and despite the original expectation of being a “true” Seyfert 2 with low obscuration and no BLR. It is therefore a candidate to look for molecular absorption.

NGC 3982 was observed at 6 GHz in November 2004 for 102 minutes. A first-order polynomial was fitted to the calibrated spectrum and subtracted, reaching an rms noise of 1.8 mJy (channel width  $3.8 \text{ km s}^{-1}$ ). No detection of OH in emission or absorption was made towards the source. The continuum flux density measured at 6.0 GHz was too low to be detected in the cross scans.

*NGC 4151* was one of the twelve emission-line sources to be classified in the original Seyfert catalogue in the 1940s (Seyfert 1943). It shows both broad and narrow components in the Balmer emission line spectrum, leading to a classification as a type 1.5 Seyfert galaxy (Osterbrock & Koski 1976). However, due to the variability of the optical broad emission, the source is sometimes classified as a Seyfert 2 (e.g. Sergeev, Pronik & Sergeeva 2001). NGC 4151 contains an elongated radio continuum structure and significant amounts of HI in its two optically faint spiral arms, a weak bar, and nuclear region (e.g. Mundell et al. 1995; for a review see Urlich et al. 2000). Both a compact hard X-ray source and extended soft X-ray emission have been detected at or near the nucleus (Elvis et al. 1983; Weaver et al. 1994; Yang et al. 2001). Near-infrared variability (Minezaki et al. 2004) and interferometric imaging (Swain et al. 2003) indicate the presence of a dust torus with an inner radius of 0.05 pc, possibly with a geometrically thin accretion disk at a smaller radius. Deep Chandra observations towards the unresolved nuclear source have revealed a heavily absorbed nucleus with an X-ray absorbing column density of  $N_{\text{H}} = 3 \times 10^{23} \text{ cm}^{-2}$ . The X-ray derived column density is roughly two orders of magnitude larger than that found for a typical Seyfert 1, thus resembling column densities typical of Seyfert 2s (Turner et al. 1997). Also, it is interesting that the source hosts water masers in its nucleus (Braatz et al. 2004), though it is not strictly classified as a type 2 Seyfert.

NGC 4151 was observed with Effelsberg in August 2004 and in November 2004 for a total of 376 minutes. A second-order polynomial was fitted and subtracted from the baseline after calibration, reaching an rms noise of 0.9 mJy (channel width  $3.8 \text{ km s}^{-1}$ ). The final spectrum is shown in Figure 2.2. No OH absorption or emission was detected. The measured continuum flux density at 6.0 GHz was  $(155 \pm 23) \text{ mJy}$ .

*NGC 4258* is a low luminosity Seyfert 2 galaxy, with a nearly edge-on nuclear disk, where direct evidence for a link between the supermassive black hole and the nuclear activity could be established. Wilkes et al. (1995) discovered that the emission lines and continuum are polarized, with the angle of polarization nearly parallel to the disk plane. This coincident orientation was interpreted as evidence that the polarization is due to scattering by electrons or dust grains in clouds located above the plane of an optically thick torus. The nucleus exhibits hard X-ray emission (Makishima et al. 1994), broad H $\alpha$  emission (Filippenko & Sargent 1985), and radio jets which extend on subparsec scales (Herrnstein et al. 1997). The discovery of a rotating molecular disk emitting H $_2$ O maser lines has provided a unique way to trace the nuclear rotation curve in the inner parsec. Miyoshi et al. (1995) have shown that the disk rotation is Keplerian and implies a central mass of  $3.6 \times 10^7 M_{\odot}$  within a radius of 0.13 pc (for a distance of 6.4 Mpc).

NGC 4258 was observed with Effelsberg in December 2004 for 152 minutes. A first-order polynomial was fitted and subtracted from the baseline after calibration. The final spectrum has an rms noise of 1.2 mJy (channel width  $3.8 \text{ km}^{-1}$ ). No OH detection was made towards the source. The continuum flux density at 6.0 GHz was measured to be  $(68 \pm 10) \text{ mJy}$ .

*NGC 4388* is a Seyfert 2 galaxy, showing hidden polarized broad lines (Moran et al. 2001; Tran 2001). The source has been detected in X-rays for over 20 years showing a column density of  $(2 \text{ to } 5) \times 10^{23} \text{ cm}^{-2}$  (see Elvis et al. 2004, and references therein). Risaliti et al. (2002) found that a few X-ray-absorbed AGN showed  $N_{\text{H}}$  variability by a factor of 2 to 3 on the shortest accessible time-scale of months, which is rather fast if it is to be attributed

to Keplerian motion of absorbing clouds at parsec radii. Kartje et al. (1999) suggested an alternative location of the torus in the cool outer parts of an accretion disk wind which would explain much faster  $N_{\text{H}}$  variability, down to a time-scale of days. X-ray observation of NGC 4388 by Elvis et al. (2004) found the source in an unusually low X-ray absorption state, with  $N_{\text{H}} = 3 \times 10^{22} \text{ cm}^{-2}$ , a factor of 10 lower than normal. Four hours later, the column density was another factor of ten lower,  $2 \times 10^{21} \text{ cm}^{-2}$ , putting the absorber at a few hundred Schwarzschild radii, similar to the broad emission line region or smaller. This small scale for the X-ray absorber seems to be in contradiction with the parsec scale of the obscuring torus paradigm. A search for OH at 1.67 GHz, yielded no detection of OH (Schmelz et al. 1986).

NGC 4388 was observed with Effelsberg at 6 GHz in August 2004 for 205 minutes. A second-order polynomial was fitted to the baseline after calibration, reaching an rms noise of 1.5 mJy (channel width  $3.8 \text{ km s}^{-1}$ ). No OH absorption or emission was seen in this source. Following the arguments of Elvis et al. (2004), the non-detection of OH absorption at both 1.67 GHz and 6 GHz could be due to the absorbing material being confined to much smaller regions and hence hot and dissociated. Thus, it may be that there is no pc-scale molecular torus in the source. The measured flux density at 6.0 GHz was  $(62 \pm 9) \text{ mJy}$ .

*NGC 5005* is a Seyfert 2 galaxy, selected for its high X-ray absorbing column density. Risaliti et al. (1999) infer a lower limit on the X-ray absorbing column of  $10^{24} \text{ cm}^{-2}$  from the absence of a reflected component in the X-ray spectrum, which maybe due to the reflecting torus being almost perfectly edge-on.

This source was observed with Effelsberg at 6 GHz in November 2004 for 57 minutes. A second-order polynomial was subtracted from the calibrated spectrum, yielding an rms noise of 2.1 mJy (channel width  $3.8 \text{ km s}^{-1}$ ). No detection of OH was made towards this source. The measured continuum flux density was  $(42 \pm 6) \text{ mJy}$ .

*NGC 5135* belongs to a group of seven galaxies (Kollatschny & Fricke 1989). The nucleus shows high-excitation lines with line ratios typical of a Seyfert 2 nucleus (Phillips et al. 1983). The spectrum, though, shows mixed Seyfert and starburst characteristics (Kinney et al. 1993). A very large absorbing column,  $N_{\text{H}} > 10^{24} \text{ cm}^{-2}$ , has been derived from X-ray observations (Risaliti et al. 1999). However, no hidden polarized broad lines have been observed (Moran et al. 2001). Water maser emission has also been searched for and not found (Braatz et al. 2004).

NGC 5135 was observed with Effelsberg in December 2004 and February 2005 for a total of 140 minutes. After the flux-density calibration, a second-order polynomial was fitted and subtracted from the baseline reaching an rms noise of 2.5 mJy (channel width  $3.8 \text{ km s}^{-1}$ ). No detection of OH absorption or emission was made in this source. The measured continuum flux density at 6.0 GHz was  $(76 \pm 11) \text{ mJy}$ .

*NGC 5194* (M 51, whirlpool galaxy) is a classical example of an interacting galaxy pair. The primary galaxy (NGC 5194) shows a significant disruption in the shape of one of its spiral arms, caused by the gravitational attraction from its companion NGC 5195. The interaction caused intense star formation in the centre and along the spiral arms of NGC 5194. X-ray observations towards its Seyfert 2 nucleus have revealed a large quantity of absorbing column gas with a density of  $N_{\text{H}} = 7.5 \times 10^{23} \text{ cm}^{-2}$  (Bassani et al. 1999).

NGC 5194 was observed with Effelsberg in November 2004 and in December 2004, for a total of 240 minutes. A first-order polynomial was fitted to the calibrated spectrum, yielding an rms noise of 0.9 mJy (channel width  $3.8 \text{ km s}^{-1}$ ). OH was not detected in this source. The 6.0 GHz measured flux density was  $(71 \pm 10) \text{ mJy}$ .

*NGC 5506* has a Seyfert nucleus whose classification as a type 1 or type 2 has been debated. The presence of broad optical lines has been reported e.g. by Blanco et al. (1990). Veilleux et al. (1997) found that the narrow emission line profiles become broader at longer wavelengths due to decreasing obscuration of the inner parts of the narrow line region (Goodrich et al. 1994). The source is luminous in the X-ray with absorbing columns of  $N_{\text{H}} = 3.4 \times 10^{22} \text{ cm}^{-2}$  (Bassani et al. 1999), which is intermediate between values typical of Seyfert 1s and Seyfert 2s. Moreover, nuclear water masers, normally associated with type 2 AGN, have been detected in this source (Braatz et al. 1994). Hidden polarized broad lines have also been observed (Tran 2001; Gu et al. 2001).

NGC 5506 was observed with Effelsberg in August 2004, for 230 minutes. A second-order polynomial was fitted and subtracted from the baseline after calibration, resulting in an rms noise of 1.5 mJy (channel width  $3.8 \text{ km s}^{-1}$ ). No features were seen in the spectrum. The spectrum is shown in Figure 2.4. The measured continuum flux density at 6.0 GHz was  $(157 \pm 23) \text{ mJy}$ .

*NGC 6240*, dubbed the “binary AGN” (Komossa et al. 2003), consists of a pair of merging galaxies, with two nuclei (Fried & Schulz 1983). Due to the merging process, NGC 6240 produces a large far-infrared luminosity (Sanders et al. 2003). The FIR luminosity is powered by extremely intense star formation activity and partly by an embedded AGN. Beswick et al. (2001) found that the radio continuum emission from the galaxy is mostly dominated by a starburst component, with only a small portion arising from a low luminosity AGN. However, the inverted spectrum at low frequency confirms the AGN nature at each of the nuclei (Gallimore & Beswick 2004). Tacconi et al. (1999) found a significant peak of CO molecular gas between the double radio nuclei. Hagiwara et al. (2002) reported the detection of a water maser in the galaxy. Also, HI and OH absorption at 1.67 GHz has been detected towards the core (Baan et al. 2007). The hard X-ray component is compatible with a highly absorbed AGN with an absorbing column density of  $\sim 2 \times 10^{24} \text{ cm}^{-2}$  (Vignati et al. 1999). Iwasawa & Comastri (1998) reported the detection of a Fe K $\alpha$  emission line.

Due to its molecular richness and its high X-ray absorption column density, NGC 6240 was a very good candidate for further searches of OH absorption at 6 GHz. The source was observed with Effelsberg at 6 GHz in August 2004 for 102 minutes. After flux-density calibration, a second-order polynomial was fitted to the baseline and subtracted, giving an rms noise of 1.9 mJy (channel width  $3.8 \text{ km s}^{-1}$ ). The final spectrum is shown in Figure 2.2. Surprisingly, no detection of OH emission or absorption was made in this source. The continuum flux density at 6.0 GHz was measured to be  $(122 \pm 18) \text{ mJy}$ .

*NGC 6251* is a giant radio galaxy known for its spectacular radio jet, aligned from pc to Mpc scales (e.g. Jones et al. 1986). The source has a Fanaroff-Riley I morphology, a Seyfert 2 nucleus (Werner et al. 2000), and almost edge-on dust lanes (Nieto et al. 1983). The nucleus is likely to contain a supermassive black hole with a mass of  $(4 \text{ to } 8) \times 10^8 M_{\odot}$  (Ferrarese & Ford 1999), as suggested by the presence of nuclear gas and a dust disk on

scales of a few hundreds parsecs. From BeppoSAX and ASCA measurements an X-ray absorption column density,  $N_{\text{H}}$ , of  $1.06 \times 10^{21} \text{ cm}^{-2}$  has been estimated (Guainazzi et al. 2003).

NGC 6251 was observed with Effelsberg at 6 GHz in November 2004 for 32 minutes. A third-order polynomial was removed from the baseline, resulting in an rms noise of 2.1 mJy per channel (channel width  $3.8 \text{ km s}^{-1}$ ). No detection of OH was made in this source. The measured flux density at 6.0 GHz was  $(680 \pm 102) \text{ mJy}$ .

*NGC 7674* is a spiral galaxy with a Seyfert 2 nucleus with asymmetrical arms and a tidal connection to a nearby compact elliptical galaxy. Hidden broad polarized lines were detected in this source (Miller & Goodrich 1990; Tran 2001). Arecibo observations have shown two clearly separated HI absorption features that are blueshifted with respect to a wider emission line (Mirabel 1982). However, neutral hydrogen interferometric observations with MERLIN revealed a single absorption feature against the central component (Beswick et al. 2002). From X-ray observations, the source appears completely hidden at all energies, implying a column density  $> 10^{25} \text{ cm}^{-2}$  (Malaguti et al. 1998). Searches for water maser emission at 22.2 GHz and OH absorption at 1.67 GHz have been unsuccessful (Braatz et al. 2004; Schmelz et al. 1986).

NGC 7674 was observed with Effelsberg at 6 GHz in August 2004 for 75 minutes. A second-order polynomial was fitted and removed from the baseline after calibration, giving an rms noise of 1.3 mJy (channel width  $3.8 \text{ km s}^{-1}$ ). No detection of OH at 6 GHz was made in this source. The measured flux density was  $(75 \pm 11) \text{ mJy}$ .

*Mrk 3* is a Seyfert 2 galaxy with evidence for a hidden Seyfert 1 nucleus from broad polarized emission lines (Schmidt & Miller 1985; Miller & Goodrich 1990; Tran 1995). BeppoSax X-ray spectra of Mrk 3 have shown that Mrk 3 is a Compton-thick galaxy, with  $N_{\text{H}} \sim 1.1 \times 10^{24} \text{ cm}^{-2}$ .

Mrk 3 was observed with Effelsberg at 6 GHz in August 2004 and February 2005 for a total of 274 minutes. A third-order polynomial was fitted and removed from the baseline after calibration, resulting in a noise rms of 1.1 mJy (channel width  $3.8 \text{ km s}^{-1}$ ). The final spectrum is shown in Figure 2.2. No detection of absorption or emission was made towards this source. The measured continuum flux density at 6.0 GHz was  $(243 \pm 36) \text{ mJy}$ .

*Mrk 348* is a Seyfert 2 galaxy with broad H $\alpha$  emission lines in polarized light indicating the presence of an obscured Seyfert 1 nucleus (Miller & Goodrich 1990). This is also supported by GINGA X-ray observations revealing a hard X-ray spectrum photoelectrically absorbed by a column density,  $N_{\text{H}}$ , of  $\sim 10^{23} \text{ cm}^{-2}$  (Warwick et al. 1989). It shows indications from a large HI halo for interactions with a companion, NGC 266 (Heckman et al. 1982), and from ground-based observations that show evidence for a dust lane crossing the nucleus and for an ionization cone (Simpson et al. 1996). A broad, variable jet water maser has been observed in this source (Peck et al. 2003). A search for OH at 1.67 GHz carried out by Schmelz et al. (1986) placed an upper limit on the OH absorption of 9 mJy ( $\tau < 0.22$ ).

Mrk 348 was observed with Effelsberg in August 2004 and November 2004 for 564 minutes. A third-order polynomial was fitted and subtracted from the baseline, yielding an rms of 0.7 mJy (channel width  $3.8 \text{ km s}^{-1}$ ). The final spectrum is shown in Figure 2.2. No detection of either absorption or emission was made towards the source. The flux density

at 6 GHz was measured to be  $(616 \pm 92)$  mJy.

*Mrk 1210* is a Seyfert 2 galaxy, where broad  $H\alpha$  and  $H\beta$  lines have been detected in polarized light (Tran et al. 1992; Tran 1995). The column density derived from X-ray observations is  $1.0 \times 10^{24} \text{ cm}^{-2}$  (Gu et al. 2001). However, by comparing XMM Newton observations with ASCA, six years apart, a dramatic change from a Compton-thick to a Compton-thin state has been observed in this source (Guainazzi et al. 2002). Water maser emission has been detected (Braatz et al. 1994).

Mrk 1210 was observed with Effelsberg at 6 GHz in November 2004 and February 2005 for 345 minutes. A first-order polynomial was fitted and subtracted from the baseline, yielding an rms noise of 0.9 mJy (channel width  $3.8 \text{ km s}^{-1}$ ). No detection of absorption or emission was made. The measured flux density at 6.0 GHz was  $(57 \pm 8)$  mJy.

*Mrk 1073* is a Seyfert 2 galaxy chosen for having a high X-ray absorbing column density of  $\sim 1.7 \times 10^{24} \text{ cm}^{-2}$  (Levenson 2001). Water maser emission has been searched for and not found (Braatz et al. 2004).

The source was observed with Effelsberg at 6 GHz in August 2004 for 358 minutes. A second-order polynomial was fitted to the spectrum and subtracted, yielding an rms noise of 1.0 mJy (channel width  $3.8 \text{ km s}^{-1}$ ). No detection of absorption or emission was made. The continuum flux density at 6.0 GHz was measured to be  $(26 \pm 3)$  mJy.

*IRAS F01475-0740* is a Seyfert 2 galaxy with polarized broad lines of  $H\alpha$  (Tran 2001). The column density derived from X-ray observations has been measured to be  $N_{\text{H}} > 1.0 \times 10^{25} \text{ cm}^{-2}$  (Risaliti et al. 1999).

IRAS F01475-0740 was observed with Effelsberg at 6 GHz in August 2004 and November 2004 for a total of 254 minutes. A second-order polynomial was fitted to the calibrated spectrum and subtracted, yielding an rms noise of 1.1 mJy (channel width  $3.8 \text{ km s}^{-1}$ ). No detection of absorption or emission was made in this source. The continuum flux density at 6.0 GHz was measured to be  $(92 \pm 15)$  mJy.

*IRAS 05414+5840* is an ultra-luminous infrared galaxy with a Seyfert 2 nucleus. The source has shown OH emission at 1.67 GHz, but a later observation revealed instead OH absorption (Klöckner 2004, PhD thesis).

IRAS 05414+5840 was observed with Effelsberg at 6 GHz in August 2004 for 135 minutes. A second-order polynomial was fitted to the calibrated spectrum and subtracted, yielding an rms noise of 1.4 mJy (channel width  $3.8 \text{ km s}^{-1}$ ). No detection of absorption or emission was made in this source. The measured flux density at 6 GHz was  $(62 \pm 9)$  mJy.

## 2.4 Discussion

Of the 31 sources observed with Effelsberg at 6 GHz, rotationally excited hydroxyl absorption was observed towards five sources (NGC 3079, NGC 4261, NGC 5793, Mrk 231, and Mrk 273) resulting overall in a detection rate of 19%, which is higher than the detection rates achieved in any previous OH survey carried out at 1.67 GHz (e.g. Schmelz et al. 1986: nine detections in 240 galaxies; Norris et al. 1989: one detection in 32 galaxies; Staveley-Smith et al. 1992: two detections in 122 galaxies; Baan et al. 1992: 11 detec-

tions in 321 galaxies; Darling & Giovanelli 2002: 52 detections in 311 galaxies; Gupta et al. 2006: no detections in 9 galaxies). Three of the selected sources were too strong for single-dish observations (NGC 1052, NGC 1068, and NGC 1275), resulting in strong ripples across the band. Of the 20 sources observed with Effelsberg at 4.7 GHz, excited OH was detected in none.

Previous selection criteria were based on radio sources having observed or suspected neutral-hydrogen absorption (see Schmelz et al. 1988 and references therein). Later, a strong influence of  $L_{\text{FIR}}$  (at  $60 \mu\text{m}$ ) and the FIR colours on the OH megamaser (OHM) fraction in ultra-luminous infrared galaxies (ULIRG, where  $L_{\text{FIR}}/L_{\odot} > 10^{12}$ ) was established (Baan 1991; Staveley-Smith et al. 1992, Baan et al. 1992), providing new selection criteria and subsequent higher detection rates (52 in 311, or 17%; Darling & Giovanelli 2002). However, a significant relationship between the OHM action and their host galaxy properties has been difficult to establish.

The detection of OHM emission is dependent on having a significant column density of OH and an intense far-infrared field to pump the OH masers. The flux density, and thus detectability, of the emission depends on the distance of the galaxy. Searches for OH absorption, on the other hand, depend on the absorption optical depth which is independent of the galaxy's distance and on the strength of the background continuum, and strong continuum sources are present in many AGN even at large distances. Thus, if significant OH columns are present, these should be easily detected in absorption. However, whilst our detection rate was higher than the detection rates in any previous survey, absorption systems remain rare (81% of the galaxies in my sample did not show OH absorption or emission).

### 2.4.1 Detections vs nondetections

The galaxies in the sample presented here ranged over different properties and morphologies. Moreover, no considerations were made on the IR properties of the parent galaxy, since the aim was to find OH in absorption against the radio nucleus. All sources, however, were selected for having indications of obscuration towards the core (hidden polarized broad lines, Compton thick sources, other known molecules). This selection proved efficient in the number of detections, however, given the high X-ray absorbing columns in our systems, the non-detections still need to be explained. Since the nature of the absorbing material is unknown, one possibility is that it may be non-molecular in most galaxies.

The results show a distinct bimodal distribution of detections. In those sources where OH was found, the absorption profile was visible after a very short integration time. The best candidates were those Compton-thick sources with a high continuum flux density and with HPBL, like Mrk 348 and Mrk 3. These sources had yielded non detections of OH at 1.67 GHz, and thus were suitable to test excitation effects. Some of those best candidates (for example Mrk 348 and Mrk 1073) yielded non detections in excited OH in the Effelsberg observations, and so the integration times were extended to reduce the noise in the spectrum to possibly detect fainter features. However this approach did not yield any further detections. It seemed that OH is either present and obvious or there is none at all to very sensitive limits.

Since the sample here is not large enough or complete for statistical analysis, some qualitative conclusions will be drawn from the results obtained here. The sample selection criteria, though overall successful, did not guarantee detections. The HPBL systems and

the presence of water masers, usually associated with the accretion disks and the inflow of gas toward the nucleus, i.e. in spirals where the process is triggered by bars, did not correlate with the OH absorbing sources. Of the OH detections, H<sub>2</sub>O emission is known only towards NGC 3079. Moreover, although all the sources where OH was detected have a high X-ray-derived column density, other sources with even higher column densities, the Compton-thick sources, did not show either absorption or emission. The high column density inferred in those sources may therefore be in a region more compact and close to the core where molecules would be dissociated. Although it is not clear where the X-ray absorption takes place, from the variability of the X-ray absorbing columns (e.g. NGC 4388, see page 45) Elvis et al. (2004) argued that the absorber was located  $\sim 100$  Schwarzschild radii from the central engine, far too close to the X-ray source for material to remain molecular, which requires the torus to be parsec-scale. In the case of smaller-scale absorbing tori, OH molecules would be destroyed in the harsher environments. Risaliti et al. (1999) however found from the large fraction of Compton-thick objects that most of the obscuring gas is located within a radius of a few tens of parsec from the nucleus, and in these cases could remain molecular.

Finally, all of the five detections observed here show a strong starburst component, indications for an interaction with another galaxy (although they are not ULIRGs like the OH megamaser galaxies) and a large quantity of previously detected molecules (CO, H I, HCN). Four of them were also detected in OH at 1.67 GHz, two in absorption (NGC 3079 and NGC 5793) and two in emission (Mrk 231 and Mrk 273), one was not observed at 1.67 GHz (NGC 4261). Mrk 231 and Mrk 273, which showed emission at 1.67 GHz, also showed tentative emission at 6 GHz. Note also that in the eight systems where a detection of OH was made at 1.67 GHz (see Table 2.2) not all were detected in the 6 GHz higher excitation level (NGC 5135, NGC 5506, IRAS 05414+5840). Also, those sources that show no OH absorption at 1.67 GHz (NGC 2110, NGC 2639, NGC 4388, NGC 7674, Mrk 348) were also not detected at 6 GHz, ruling out, for those sources, radiative excitation effects as the cause for the previous non-detections. The non-detection of NGC 6240 is even more puzzling, since it has properties like those of the systems that displayed detections, namely a merging galaxy with a large quantity of CO, H<sub>2</sub>O masers, and OH absorption at 1.67 GHz,

#### 2.4.2 OH excitation temperatures

For those sources that have been detected at 1.67 GHz and 6 GHz in OH absorption, an estimate of the excitation temperature of the rotational transitions between the  $^2\Pi_{3/2}J = 3/2$  ground states and the  $^2\Pi_{3/2}J = 5/2$  excited state can be made. For this, it must be assumed that the absorption, at 1.67 GHz and 6 GHz, originates from the same volume of gas, i.e. that the absorption lines arise in front of the same continuum source. This assumption seems plausible in the case of NGC 3079 due to the striking similarity of the profiles at 1.67 GHz and at 6 GHz although multifrequency VLBI by Middelberg et al. (2007) shows a 17 mas shift between the 1.6 GHz and the 5 GHz nuclear continuum components. At 1.67 GHz (Haschick & Baan 1985) find broad nuclear absorption with two distinct velocity components (see Figure 2.6, bottom left). The two absorption troughs at  $1013 \text{ km s}^{-1}$  and  $1114 \text{ km s}^{-1}$  with a separation of  $100 \text{ km s}^{-1}$ , correspond to the separation found between the two absorption troughs in both the 6035 MHz and 6030 MHz main lines. Baan & Irwin (1995) argued that a foreground expanding shell driven by the nuclear

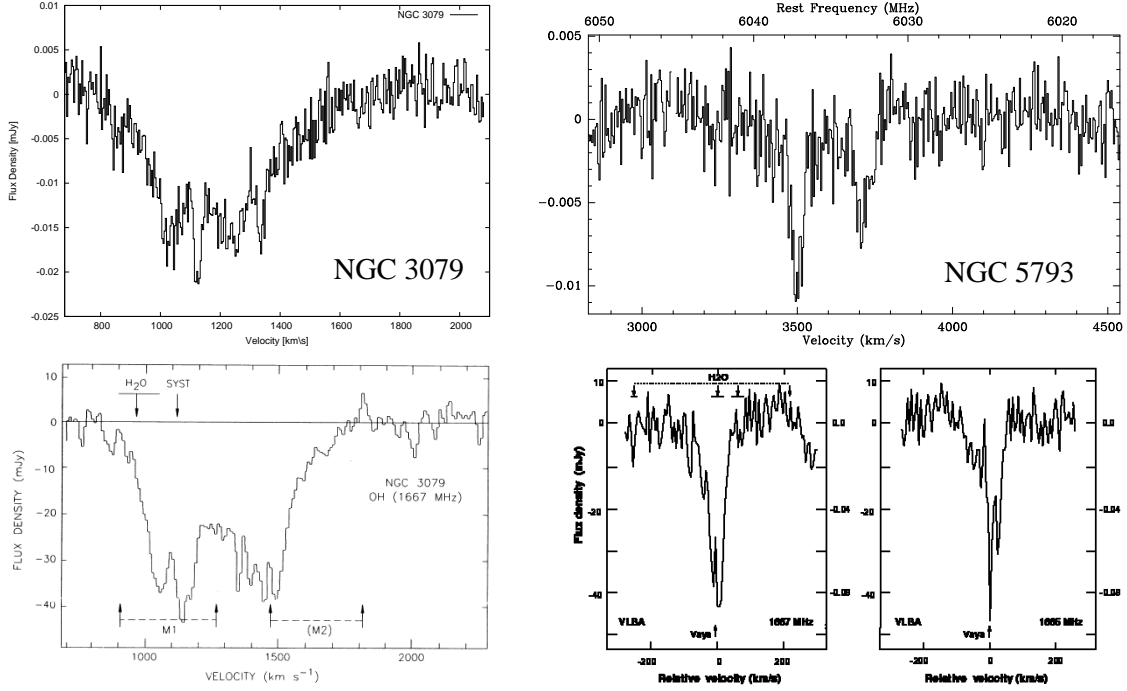


Figure 2.6: The OH absorption spectra NGC 3079 (left) and NGC 5793 (right). *Top Left*: the 6035 MHz and 6035 MHz absorption spectrum of NGC 3079 taken with Effelsberg. *Bottom left*: the 1667 MHz absorption spectrum taken with the NRAO 300-foot telescope (Haschick & Baan 1985), where the systemic velocity and the components of the H<sub>2</sub>O megamasers are also indicated. Note that the velocity range of the two spectra are not perfectly aligned. *Top Right*: the 6035 MHz and 6030 MHz absorption spectrum of NGC 5793 taken with Effelsberg. The two absorption troughs are the two transitions. *Bottom right*: the 1667 MHz (left) and 1665 MHz (right) spectra taken with VLBI (Hagiwara et al. 2000). The relative LSR velocities are referred to the rest frequency of each OH transition and the velocity ranges of the H<sub>2</sub>O maser emission are indicated in the 1667 MHz frame by downward-pointing arrows and thick lines.

superbubble could explain the blue-shifted OH component, and that the systemic OH absorption component is associated with the radio-double nucleus and thus with a parsec-scale torus.

Also, in NGC 5793 similar velocity profiles are seen in the 1.67 MHz and 6 GHz lines of OH (Figure 2.6, right). Spectral line VLBI by Hagiwara et al. (2000) finds one narrow velocity component in each of the lines at the rest frequencies of 1667 MHz and 1665 MHz with velocities of  $28 \text{ km s}^{-1}$  and  $18 \text{ km s}^{-1}$  with respect to systemic, respectively. Similarly, I found one narrow absorption component in each of the lines, at 6030 MHz and 6035 MHz trough with velocities of  $59 \text{ km s}^{-1}$  and  $52 \text{ km s}^{-1}$  with respect to the systemic velocity. The velocity difference indicates that some of the absorbing gas is extended and was not seen in the VLBI observations or that the spatial distribution of 1.67 GHz and 6 GHz absorption is different. In fact, VLA observations of the 1667 MHz line towards NGC 5793 (Gardner & Whiteoak 1986) reveal a velocity width of  $40 \text{ km s}^{-1}$ .

To derive the excitation temperature requires that the absorption line strength be expressed as an optical depth. The line optical depths are derived from

$$\tau = -\ln(1 + T_L/T_c) \quad (2.7)$$

assuming a covering factor of unity for the Effelsberg observations. These values represent lower limits on  $\tau$  since, for  $T_c$ , I used the integrated continuum emission within the Effelsberg beam, whereas the absorption most likely occurs in front of only a small fraction of that emission. For the 6035 MHz line, the line optical depth,  $\tau_{6035}$ , was 0.0216 for NGC 3079, and 0.0224 for NGC 5793. For the 1667 MHz line, the optical depths were  $\tau_{1667} = 0.5$  for NGC 3079 from the VLA observation of Baan & Irwin (1995) assuming a continuum flux density of 84 mJy towards the core, and  $\tau_{1667} = 0.06$  for NGC 5793 from the VLA observations of Gardner & Whiteoak (1986).

The total population of the  $^2\Pi_{3/2}J = 3/2$  ground state is

$$N_{1667} = 2.4 \times 10^{14} \text{ cm}^{-2} \text{ K}^{-1} \text{ km s}^{-1} T_{\text{ex}} \Delta v_{1/2} \tau_{1667} \quad (2.8)$$

The total population of the  $^2\Pi_{3/2}J = 5/2$  state is,

$$N_{6035} = 1.7 \times 10^{14} \text{ cm}^{-2} \text{ K}^{-1} \text{ km s}^{-1} T_{\text{ex}} \Delta v_{1/2} \tau_{6035} \quad (2.9)$$

Assuming that the excitation temperature is equal in both states, one can derive the excitation temperature defined for a population of particles from the Boltzmann relation

$$\frac{N_{6035}}{N_{1667}} = \frac{g_{6035}}{g_{1667}} \exp(\Delta E/kT_{\text{ex}}) \quad (2.10)$$

where  $g_{6035}$  and  $g_{1667}$  are the statistical weights of the two levels, and  $N_{6035}$  and  $N_{1667}$  are the number of particles in each of the two states. The rotational temperature,  $T_{\text{rot}}$ , representing the population ratio of the two  $J$  energy states is given by

$$T_{\text{rot}} \approx 120 \text{ K} / \ln[2.2(\tau_{1667}/\tau_{6035})(T_{1667}/T_{6035})] \quad (2.11)$$

where  $T_{1667}$  and  $T_{6035}$  are the excitation temperatures of the two transitions, which are assumed to be similar, and 120 K is the energy difference,  $\Delta E$ , between the energy levels. We then find for  $T_{\text{ex}} = T_{\text{rot}}$ ,  $T_{\text{ex}} = 30$  K for NGC 3079 and 67 K for NGC 5793. These values are probably lower limits, since the optical depths used for the 1667 MHz transition were observed at higher resolution than the Effelsberg observations, and give a more accurate estimate of the true optical depths, whereas the values from the Effelsberg data are strictly lower limits. Comparing these values to the values found in the literature for other galaxies, Henkel et al. (1987) found for the IR-luminous galaxy IC 4553, comparing the 1.67 GHz and the 4.7 GHz lines, a rotational temperature,  $T_{\text{rot}}$ , of 74 K. A similar analysis of the same source between the 1.67 GHz and the 6 GHz lines, Henkel et al. (1986a) found a value for the rotational temperature of 44 K.

A better estimate of the 6 GHz line opacity in NGC 3079 can be derived if we can estimate the region over which the line absorption takes place and use existing high resolution continuum images to measure the background continuum source strength over that same region. At 1.67 GHz the compact OH absorbing gas was found to extend no more than the beam size of 45 mas, or  $\sim 4$  pc, and was interpreted primarily to be a part of the circumnuclear gas traced by the CO(1-0) emission (Baan & Irwin 1995). I assume that the 6 GHz OH absorption arises within the same central 4 pc diameter region. The continuum emission in this central region was measured using VLBI by Middelberg et al. (2007) in September 2002. At 5 GHz, Middelberg found three components, A, B, and E, all within 2.4 pc of each other, with a combined continuum emission of 53 mJy. Using 53 mJy as the

strength of the background emission, I find an optical depth,  $\tau_{6035}$ , of 0.117, which yields a new rotational temperature of 53 K for the OH absorbing gas in NGC 3079. This is compatible with the results from a single blackbody fit to the FIR flux densities at  $12\ \mu\text{m}$  to  $100\ \mu\text{m}$  integrated over the whole area of NGC 3079, yielding a temperature of 43 K (Hagiwara et al. 2004). The maximum extent of this large-scale FIR source (e.g. torus) was about 130 pc.

A final word of caution is that the excitation temperature is the temperature of a system defined by the ratio of level populations and this value has no real physical meaning except when in local thermodynamical equilibrium (LTE). For a system of inverted levels for example, maser emission, the excitation temperature can even be negative. For the calculations above, I have assumed LTE conditions. These are not necessarily justified when the gas density is so low that the level populations are typically not in thermal equilibrium. For example, under LTE conditions we expect an intensity ratio for the 6 GHz transitions (S(6016):S(6030):S(6035):S(6049)) of 1:14:20:1. For NGC 3079 this ratio is  $< 1:15:6:< 1$  and for NGC 5793 the ratio is  $< 1:9:6:< 1$ , suggesting departure from LTE conditions.

### 2.4.3 Excitation of OH

The results presented in this chapter show absorption in the 6035 MHz and 6030 MHz transitions in 19% (5 out of 29) of the sources observed, and no evidence for absorption in the 4750 MHz transition or in the satellite lines at 6016 MHz or 6049 MHz in any of the sources observed. This is surprising since the 4750 MHz transition has been seen previously, predominantly in absorption, in a number of infrared-luminous OH megamaser galaxies (Henkel et al. 1987a).

The purely radiative excitation processes involve both far-infrared and non-thermal radio emission, contributing to the complex OH spectra seen in emission and in absorption in some galaxies (Henkel et al. 1986a). The high luminosities in the nuclei of galaxies excite the OH gas with a consequent population increase in the higher energy states and hence detectable transitions between the levels, like those at 6 GHz observed here. It is possible that the infrared and non-thermal luminosity in the galaxies of the sample observed here is not high enough to sustain an adequate excitation of the 4.7 GHz state.

## 2.5 Conclusions

Rotationally-excited, broad OH lines were detected in absorption towards five of the 29 sources observed with the 100 m telescope at Effelsberg, yielding a detection rate of 19%. Previous studies targeted mainly red quasars, where an infrared excess is indicative of large columns of dust on the line of sight and creates the conditions for OH maser emission. However, the detection rates in those targeted surveys have been typically a few percent.

I have investigated here whether radiative excitation conditions, suppressing the line opacity in the lower transitions and increasing the level population of the higher  $J$  rotational states, could explain the previous numerous non detections in the ground-state OH transition. The source selection in this study was based for the first time on X-ray column densities. The results obtained here confirm through the 6 GHz detections that some of the objects are subject to radiative excitation. However, the detections in this survey do not support the hypothesis of radiative excitation models alone to explain the previous

lack of molecular detections, since almost all the sources that have been detected at 6 GHz have also been detected at 1.67 GHz either in absorption or emission. The only possible exception is NGC 4261, where OH has not been searched for at 1.67 GHz. Moreover, all of the sources with known non-detections at 1.67 GHz also yielded non-detections at 6 GHz (except for Cygnus A, see Chapter 3). Also, the search for 4.7 GHz absorption turned up only non-detections, showing that the excitation in the OH clouds by the non-thermal radiation is not large enough to populate the higher 4.7 GHz energy levels.

The observed line widths ranged from a few  $100 \text{ km s}^{-1}$  to  $2000 \text{ km s}^{-1}$ , with narrow absorption features at the systemic line frequency. The broad component suggests that the gas in all sources is close to the central region, either rotating around the central engine, or infalling or outflowing. For NGC 3079, the OH absorbing gas is most likely in the central 2.4 pc region, based upon the distance between continuum components A and E, which probably provide the continuum background for absorption. The OH column densities obtained for the  ${}^2\Pi_{3/2}J = 5/2$  excited state range from  $\sim 10^{17} \text{ cm}^{-2}$  to  $\sim 10^{18} \text{ cm}^{-2}$ . Two of the sources observed in absorption (Mrk 231 and Mrk 273) also show indications for OH maser emission at 6 GHz in their spectra.

A further interesting result of this survey is that the absorption optical depth at 6 GHz shows no trend with the absorbing column densities inferred from X-ray observations. Given the high X-ray absorbing columns in these systems, the non-detections still need to be explained. Since the nature of the X-ray and optically absorbing material is unknown, one possibility is that it may be non-molecular in most galaxies. Notably, Mrk 3, one of the best candidates, did not show absorption despite having an X-ray column  $> 10^{24} \text{ cm}^{-2}$  and a continuum flux density of 360 mJy at 5 GHz. The overall picture that emerged from this work was of a bimodal distribution of molecular abundances, where some sources seem to be devoid of OH, whereas those detected at 6 GHz show a large variety of molecular species. I have found that, in the five systems with detections, the lines were strong and were visible after short integration times, whereas in the non-detections no lines were visible even after longer integration times. This bimodal distribution of absorption could be explained by invoking the presence of compact clouds that cross the line of sight in a few sources, producing absorption. The covering factor of such clouds, from the detection rate, is  $\sim 20\%$ .



## Chapter 3

# Interferometric observations Cygnus A and NGC 1052

As the nearest ( $z = 0.0565$ ) powerful FR II radio galaxy, Cygnus A has been the subject of a number of studies aimed at testing the predictions of the unified scheme of AGN (Antonucci 1993). However, despite expectations, the absorption of abundant molecules like CO, OH and H<sub>2</sub>CO in their ground-state transition has not been detected in the putative torus of Cygnus A. Unless the torus is highly ionized or atomic, Maloney et al. (1994) discussed the possibility that radiative excitation effects may be suppressing the absorption optical depths in the lower transitions. Such models suggest that searches for higher excitation transitions might be more profitable (Black 1998; see Chapter 2, Section 2.2). Thus, a single-dish multi-line survey was carried out for a sample of 31 objects searching for higher excitation OH absorption (see Chapter 2). Unfortunately, a detection experiment could not be carried out for Cygnus A as its bright radio lobes required unachievably high spectral dynamic range from a single dish and its redshift shifted the line out of the receiver band at Effelsberg. NGC 1052 was another prime candidate to search for excited OH, as there is observational evidence for obscuration towards the core. However this source was also too strong for single-dish observations. Interferometric observations can resolve out most of the continuum emission and provide better spectral dynamic range on the nuclear emission. In this Chapter, I describe VLBA observations of Cygnus A and NGC 1052 at 13.4 GHz. This experiment was the first attempt to detect excited OH at this frequency in any source.

### 3.1 Introduction

Several lines of evidence suggest that Cygnus A harbours an active nucleus, hidden from direct view in the visible spectrum and in soft X-rays by a dusty obscuring torus (e.g., Ward et al. 1991; Antonucci, Hurt, & Kinney 1994). Furthermore, X-ray spectroscopy with the GINGA satellite (Ueno et al. 1994) has confirmed the presence of a highly absorbed hard X-ray source with an equivalent foreground absorbing column density of  $N_{\text{H}} = 3.75 \times 10^{23} \text{ cm}^{-2}$ , consistent with the notion of a buried nucleus in Cygnus A. The molecular component of Cygnus A has been detected through infra-red emission lines of H<sub>2</sub> (Wars et al. 1991; Thornton et al. 1999).

In 1994, Barvainis & Antonucci searched for and failed to detect CO ( $J=1-0$ ) absorp-

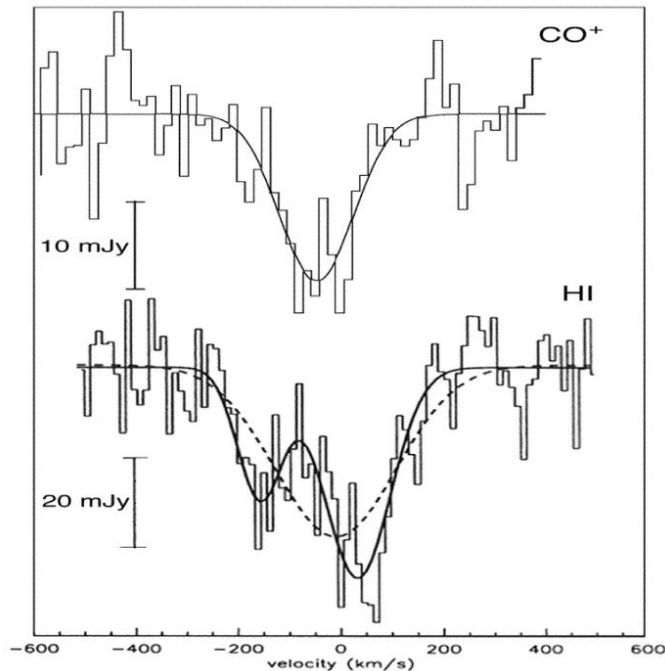


Figure 3.1: Absorption spectra of  $\text{CO}^+$  (Fuente et al. 2000) and  $\text{HI}$  (Conway & Blanco 1995) towards Cygnus A.

tion from the obscuring torus of Cygnus A. This lack of absorption presents a challenge to the torus model for Cygnus A. Barvainis & Antonucci suggested possible solutions. First, it may be that there is no such torus. Second, the sizes of the molecular clouds in the torus may be smaller than the size of the background continuum source. Alternatively, Maloney et al. (1994) discussed the possibility that the radio continuum emission from the nucleus radiatively excites the  $\text{CO}$ , increasing the excitation temperature and suppressing the absorption optical depths in the lower transitions. Interestingly, Fuente et al. (2000) detected  $\text{CO}^+$  absorption at 118 GHz towards the nucleus of Cygnus A, in agreement with  $\text{CO}$  excitation due to radiative coupling of millimeter-wave continuum source (see Fig. 3.1).

In the search for absorption towards Cygnus A,  $\text{HI}$  21 cm absorption has been detected at the systemic velocity by Conway & Blanco (1995). The absorption line seen towards the nucleus is broad ( $270 \text{ km s}^{-1}$ ). However, in the same experiment neither 1.67 GHz  $\text{OH}$  nor 6 cm  $\text{H}_2\text{CO}$  absorption were detected, with a sensitive upper limit of 1% on the optical depth, challenging the torus model for Cygnus A. Given the abundance of  $\text{OH}$  predicted in some molecular torus models (e.g. Krolik & Lepp 1989), the non-detection of  $\text{OH}$  absorption is hard to explain unless this too is radiatively excited. Radiative excitation effects have been predicted by Black (1995; see Chapter 2, Section 2.2) for the 1.67 GHz  $\text{OH}$  transitions, and if such an effect is dominant, the 4.7 GHz, 6 GHz and 13.4 GHz transitions might be more profitable targets than the 1.67 GHz line, and constituted the motivation for the VLBA observations presented here. At 13.4 GHz, Cygnus A is lobe-dominated, having 200 Jy total flux density. High-resolution interferometry can, however, resolve out the extended emission, leaving correlated flux only from the nucleus, where the absorption

is expected, which contains less than 1% of the total luminosity and so relaxes the spectral dynamic range by a factor of 100 over single-dish observations.

NGC 1052 is a LINER galaxy with 1 Jy to 2 Jy in a central radio source, with only  $\sim 15\%$  of the flux density in extended emission when observed with the VLA. Broad H $\alpha$  emission lines have been observed in polarized light (Barth et al. 1999) indicating the presence of the obscuring region invoked by unification models (Antonucci et al. 1993). NGC 1052 is a LINER prototype, with nuclear jets that are visible at radio, optical and X-ray frequencies (Kadler et al. 2004). The soft X-ray spectrum shows strong absorption, indicating a substantial, and possibly inhomogeneous column depth of ionized gas towards the active nucleus (Guainazzi & Antonelli 1999; Guainazzi et al. 2000; Weaver et al. 1999; Kadler et al. 2002). Using the Chandra X-ray Observatory, an H I equivalent absorbing column density of  $N_{\text{HI}} = 10^{22} \text{ cm}^{-2}$  to  $10^{24} \text{ cm}^{-2}$  was found. Multi-frequency radio observations between 2.3 GHz and 43.2 GHz show that the jets are oriented near to the plane of the sky. Free-free absorption was found in the inner few parsecs around the nucleus (Kameno et al. 2001; Vermeulen et al. 2003), apparently due to a geometrically-thick, patchy structure oriented roughly orthogonal to the jets. Since the western jet is covered more deeply and extensively, it is thought to be receding. Opacities have been measured implying a dense ( $n_e = 10^5 \text{ cm}^{-3}$ ) plasma associated with the central 0.5 pc (Guainazzi et al. 2000). H I absorption was first reported by Shostak et al. (1983) and van Gorkom et al. (2003). Later, spectral line VLBI observations by Vermeulen et al. (2003) could locate a clumpy H I structure in front of both the approaching and the receding jet (Vermeulen et al. 2001). The atomic gas shows various absorption components which are broad, shallow and asymmetric around the systemic velocity and are seen at relatively low velocity ( $-35 \text{ km s}^{-1}$  to  $8.5 \text{ km s}^{-1}$  with respect to systemic), probably associated with the AGN environment, or distributed on galactic scales. Several narrower velocity components located between  $25 \text{ km s}^{-1}$  and  $95 \text{ km s}^{-1}$  with respect to the systemic velocity are detected along the inner 2 pc of the approaching jet and several high-velocity H I components at  $125 \text{ km s}^{-1}$  to  $200 \text{ km s}^{-1}$  with respect to the systemic velocity, were also found. The derived column density is of the order of  $10^{20} \text{ cm}^{-2}$  to  $10^{21} \text{ cm}^{-2}$ , in agreement with the X-ray observations. OH absorption at 1.67 GHz was found at velocities ranging from  $-35 \text{ km s}^{-1}$  to  $200 \text{ km s}^{-1}$  with respect to systemic by Omar et al. (2002) with the VLA. A higher signal-to-noise spectrum with WSRT was shown by Vermeulen et al. (2003) showing 0.4% peak opacity, or 5 mJy. The OH profiles are similar to H I, suggesting co-location of the atomic and molecular gas. Global VLBI follow-up observations of the 1.67 GHz absorption have been made and the data reduction is in progress (Vermeulen, priv. comm.). H<sub>2</sub>O maser emission has been detected at around  $130 \text{ km s}^{-1}$  with respect to the systemic velocity (Braatz et al. 1994) and imaged with the VLBA (Claussen et al. 1998).

All this indicates that Cygnus A and NGC 1052 might both harbour molecular tori. The VLBA experiment presented here is the first attempt to detect excited OH in these sources.

## 3.2 VLBA Observations

VLBA observations of Cygnus A and NGC 1052 with the aim of looking for the highly excited states  ${}^2\Pi_{\frac{3}{2}}$ ,  $J = \frac{7}{2}$  of OH (290 K above the ground-level) at 13441 MHz ( $F = 4 - 4$ )

and 13435 MHz ( $F = 3 - 3$ ) were carried out in December 2005. Cygnus A was observed on December 10, 2005 for a total of 8 h (including the calibrators) and NGC 1052 was observed on December 6 and 8, 2005 for 7 h each day (including observations of the calibrators). The sampled  $uv$ -coverage of the Cygnus A observations is shown Figure 3.2. Cygnus A, having a higher continuum flux density, needed to be observed for less time than NGC 1052. The rms noise in an image from an interferometer with  $N$  antennas and single polarization is given by

$$\Delta S_{\text{rms}} = \frac{SEFD}{\sqrt{N(N - N)}} \text{ mJy beam}^{-1} \quad (3.1)$$

where the SEFD (in milli-jansky) was discussed in Chapter 2 (Section 2.5.1). The sensitivity required to detect a line optical depth of 0.5% at  $5\sigma$ , corresponded to an rms noise in the spectrum of  $0.5 \text{ mJy beam}^{-1}$  for both sources. Observations were carried out with four IFs to observe two polarizations with 16 MHz bandwidth, corresponding to  $357 \text{ km s}^{-1}$ , per IF. The IFs were centred at the source frame rest frequencies of 13.434 GHz and 13.441 GHz, providing 19 MHz total span and 13 MHz of overlap. The expected line frequency was redshifted to 12.716 GHz for Cygnus A and to 13.361 GHz for NGC 1052. With 256 channels per IF, a spectral line velocity resolution of  $1.4 \text{ km s}^{-1}$  per channel was obtained. After offline Hanning smoothing this expected to give a velocity resolution of  $3 \text{ km s}^{-1} \text{ channel}^{-1}$ , which was comfortably less than the expected line width if it is as broad as the  $113 \text{ km s}^{-1}$  of the  $\text{CO}^+$  line seen by Fuente et al. (2000). The total velocity span was  $700 \text{ km s}^{-1}$  when two IFs were placed adjacent to each other to form a single spectrum, which allowed one third of the channels to measure the line-free continuum level. Two bandpass calibrators were observed in cycles of 13 minutes for Cygnus A (2005+403 and 2013+370) and two were observed in cycles of 22 minutes for NGC 1052 (0423-01 and 3C 84).

### 3.3 Data Calibration

Spectral line data calibration and imaging produces a cube giving the sky at different frequencies for different positions or, alternatively, information on the sky brightness distribution at different frequencies. The cube consists of a three dimensional matrix  $\mathbf{I} = (I_{ijk})$  with intensities  $I_{ijk}$  corresponding to the sky brightness distribution  $I(x, y, \nu)$  at position  $(x, y)$  and frequency  $\nu$ . Thus, one produces a series of two-dimensional images of the sky, in two spatial coordinates, at each of the different frequencies (see Figure 3.3).

The data calibration was carried out in AIPS following the calibration steps given below:

- read in the data
- apply a prior amplitude calibration
- check the data quality and edit (flag)
- initial phase calibration (fringe)
- bandpass calibration

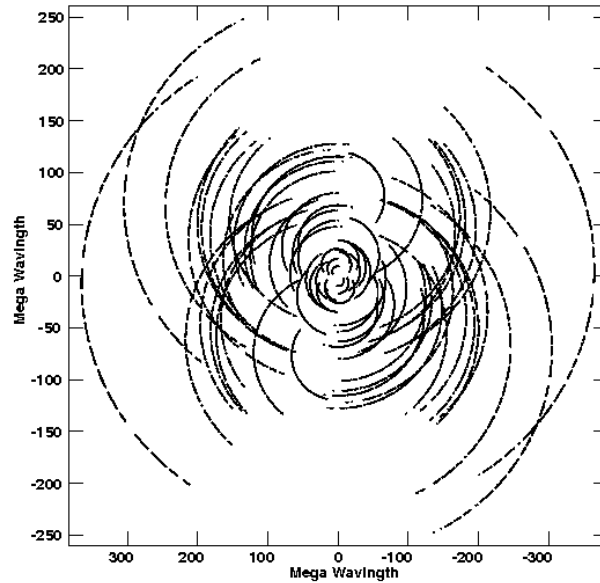


Figure 3.2: The response of an interferometer is the Fourier transform of the sky brightness distribution. Each baseline samples a discrete point in the Fourier plane. In order to recover the full sky brightness distribution would require a complete coverage of the Fourier plane. In practice this is not possible, even though aperture synthesis (i.e. tracking the source using the natural rotation of the Earth) can improve the sampling of the Fourier  $uv$ -plane. The effect of an incomplete sampling causes sidelobes in the image plane (the recovered sky-brightness distribution after doing the inverse Fourier transform). These sidelobes, which will degrade the quality of the image, are removed from the image using CLEAN (Hogbom 1983), which will also replace the dirty beam with the restoring beam (deconvolution). The plot shows the  $uv$ -coverage during the VLBA observations of Cygnus A. The gaps between tracks show the distance between the individual antennas which causes discrete sampling in the Fourier plane. The gaps in each track show the observing cycle, where observations of the Cygnus A were interspaced with observations of primary and secondary calibrators.

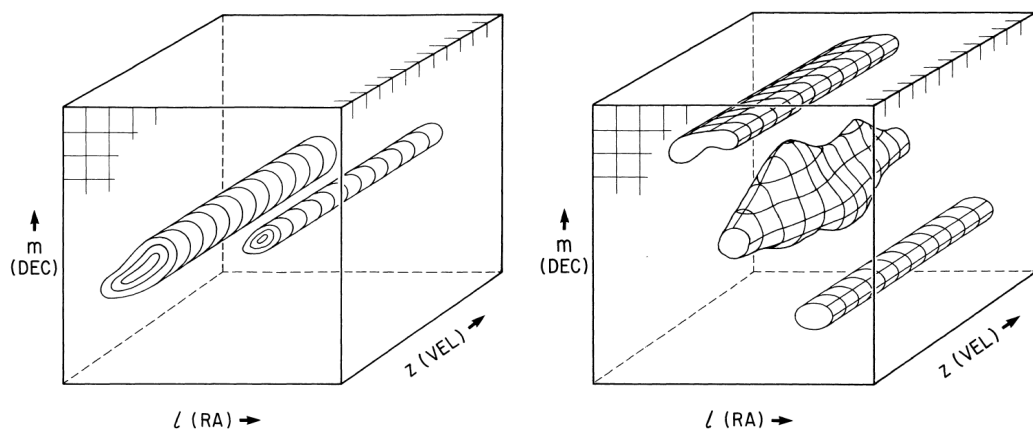


Figure 3.3: Plot showing a data cube containing continuum emission (on the left) and with line emission (on the right). The axes show the dimensions of the cube (RA, Dec, Velocity or Frequency) (P. Roelfsema 1989, Synthesis Imaging in Radio astronomy, ASPCS, Volume 6, p. 329, 330).

- make a continuum image (using the central 75% of the spectral channels)
- determine antenna gain solutions (self calibration)
- copy gain solutions from continuum to spectral line data
- split program source, applying calibration
- continuum subtraction
- make a spectral line data cube (no cleaning since spectral line is weak and continuum has been subtracted)

Generally, the calibration is standard concerning amplitude and phase calibration, and a few extra steps are required for spectral line data. A critical step in the spectral line calibration is the calibration of the complex antenna-based bandpass function. One great advantage of interferometric spectral lines studies, compared with single-dish observations, is that the standing wave modulation (i.e. ripples, see Chapter 2, Section 2.5.2) does not affect the quality of the spectra, since most of the received noise is not correlated between the elements. However, the bandpasses are not perfectly flat due to the atmosphere (small effect), front-end filters and amplifiers, IF transmission system from the antenna to the correlator (causing delay errors, i.e. a phase slopes with frequency), back-end filters, the correlator generating frequency variations, and also standing waves. These effects are however different for all antennas and usually are not time dependent. Also, the so-called Gibbs ringing can be a problem near a sharp edge in the frequency spectrum, introduced by the finite time sampling. The ringing occurs around sharp changes in the frequency spectrum because the temporal cross-correlation measurements are truncated. If the filter which sets the bandwidth has a sharp upper and lower frequency edges, they will show ringing due to the truncation of the lag spectrum. This problem was minimized by observing with a large number of channels to reduce the effects of ringing and by smoothing the data in frequency.

One can divide the calibration into two steps, measurement of the average response on relatively short time-scales and measurements of the spectral variation on long time-scales. Splitting the time and frequency dependence of the gain, we can write,

$$g_{ij}(\nu, t) = G_{ij}(t)B_{ij}(\nu, t) \quad (3.2)$$

where  $g_{ij}(\nu, t)$  is the total gain on baseline  $i - j$ ,  $G_{ij}(t)$  is the time-variable continuum gain, and  $B_{ij}(\nu, t)$  is the frequency-dependent part of the gain. Assuming that the frequency dependence is mild enough that the signal does not decorrelate when averaging across the band, one can average the raw data in frequency to gain sensitivity when measuring time variability. In this way, the overall gain and bandpass can be solved independently.

The bandpass is calibrated by interspersing observations of a calibrator of known spectral shape between those of the target source, with long enough integration times to reach a high signal-to-noise ratio (which should be comparable to that on the target source). The long integration on the calibrator is required because noise in the calibrator bandpass spectrum will introduce systematic noise in the map channels. In this process, one should be careful in choosing flat spectrum sources, i.e. sources with a constant flux

density across the band. The source structure is then removed by dividing visibilities at each frequency by those of the continuum (created using the central 75 % of the spectral line channels), the complex gains  $G_{ij}(t)$  are determined, leaving a spectrum  $B_{ij}$  on each baseline which depends only on the bandpass. The baseline based gains and bandpass shapes are decomposed into antenna-based gains and bandpass shapes, which are stored in calibration tables for later application to the data. The results of a few calibration steps on the Cygnus A spectrum are illustrated in Figure 3.4 for one baseline (Fort Davis-Los Alamos).

The data calibration then followed standard procedures for phase and amplitude self-calibration. Since NGC 1052 and Cygnus A were strong enough, self-calibration could be applied iteratively, using a continuum dataset created by averaging all the spectral channels together (using 75 % of the band, to avoid residual edge band effects). The solutions obtained during self-calibration and bandpass calibration were finally applied to the line data and a data cube could finally be created. The Fourier transforms of the  $uv$  data in each spectral channel into the image domain to create the data cube was performed in AIPS using the task IMAGR.

Continuum subtraction is another critical step in the calibration of spectral line data. The reason to subtract the continuum from the spectrum is mainly that it makes it easier to detect weak spectral features and to compare the emission in different channels by filtering out the emission common to all channels. Also, continuum subtraction minimizes (or avoids) the need to deconvolve the line signal, since the continuum emission has already been removed from every channel. This is particularly useful since deconvolution is a non-linear process and may introduce noise to the spectra. There are two main methods of doing continuum subtraction: subtract the continuum in the  $uv$  domain or to subtract the continuum in the image domain. For doing this, one must know (or guess) which channels are line free and use the maximum number of line-free channels. The selection of channels can therefore be an iterative process. For the data presented here, I tested both methods, in the  $uv$ -domain (UVLSF in AIPS), and in the image domain (IMLIN in AIPS), where a first-order polynomial was fitted to the selected channels in every visibility spectrum for every baseline in the  $uv$  domain at every pixel in the image cube, and the fitted line was then subtracted from all channels, thus removing the continuum from every channel. Subtraction in the image domain gave better results.

The line data were not deconvolved, since the continuum had been subtracted which removed strong continuum signal and its sidelobes.

Finally, I would like to point out that thorough data editing (flagging) is critical during the calibration of spectral line data, since various channels at different antennas are often corrupted by radio frequency interference (RFI). During data editing one of the ten observing antennas was completely flagged (Brewster) due to interference at the site.

## 3.4 Results

### 3.4.1 Cygnus A

The 13.4 GHz continuum image of Cygnus A (Fig. 3.5) shows an extended radio source, extending east–west up to 4 pc from the core, with a peak flux density of  $453 \text{ mJy beam}^{-1}$ . The noise in the map is  $5 \text{ mJy beam}^{-1}$ . Fig.3.5 shows the spectra for different positions over the source. Absorption by the rotationally excited OH transition at a rest frequency

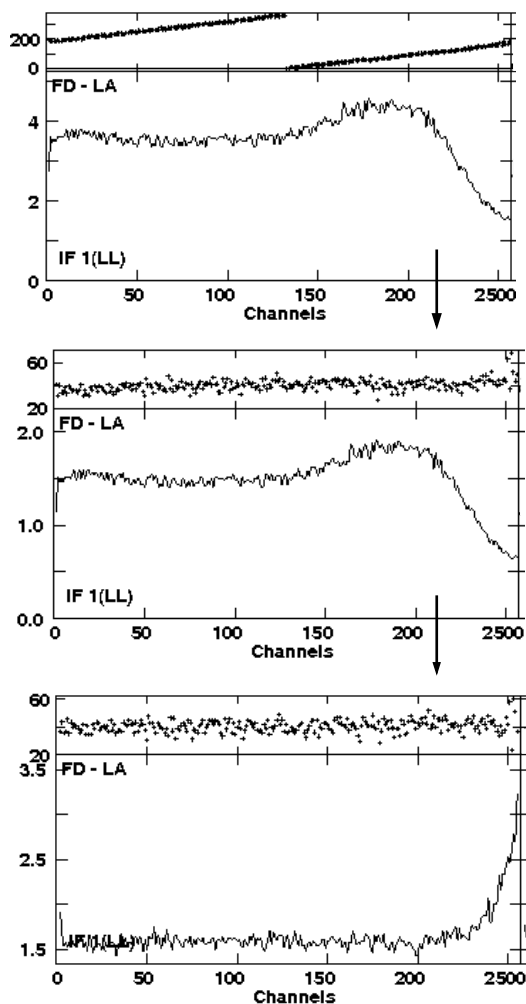


*Figure 3.4:* Some of the calibration steps carried out during the VLBA spectral line data reduction. The plots refer to a 30 minute scan of Cygnus A on the baseline between Fort Davies and Los Alamos. In the top panel, the raw spectrum is shown, the residual phase errors (generally dominated by the atmosphere, top panels) have not been calibrated and the baseband shape is not flat. A global fringe fitting was applied to the data at this stage. Global fringe fitting is a generalization of the phase self-calibration technique, in which the difference between model phases and measured phases are minimized by solving for the antenna-based instrumental phase, its time slope (the fringe rate), and its frequency slope (the delay) for each antenna. In the middle panel, the spectrum after calibration of residual phase delays, the slope of phase across the bandpass has been removed, but the bandpass filter shape is still visible. In the bottom panel, the spectrum is shown after applying the bandpass correction. The last few channels, which are still corrupted, are later removed during the spectral analysis. The  $y$ -axis is the uncalibrated flux density.

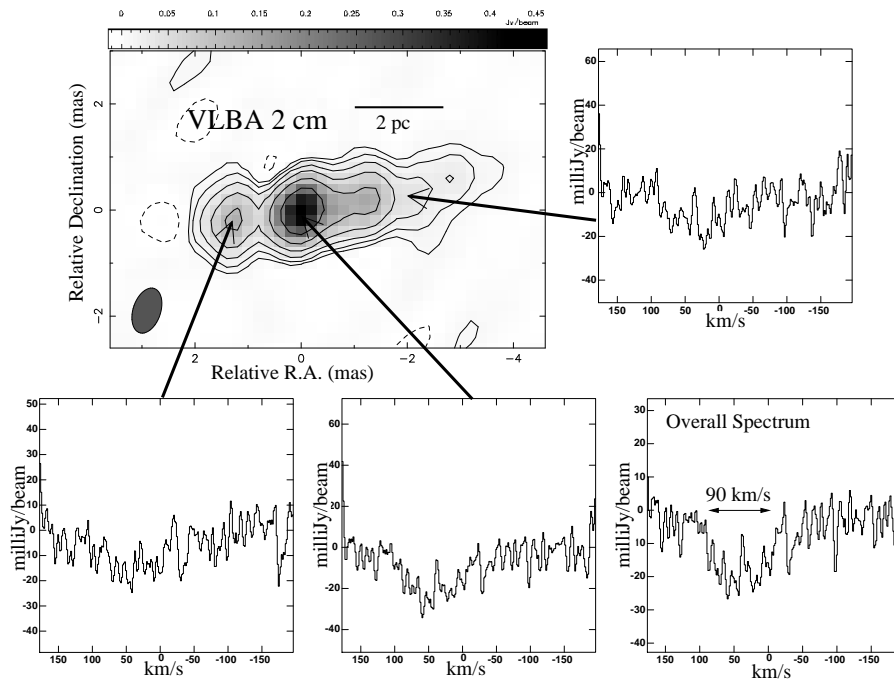
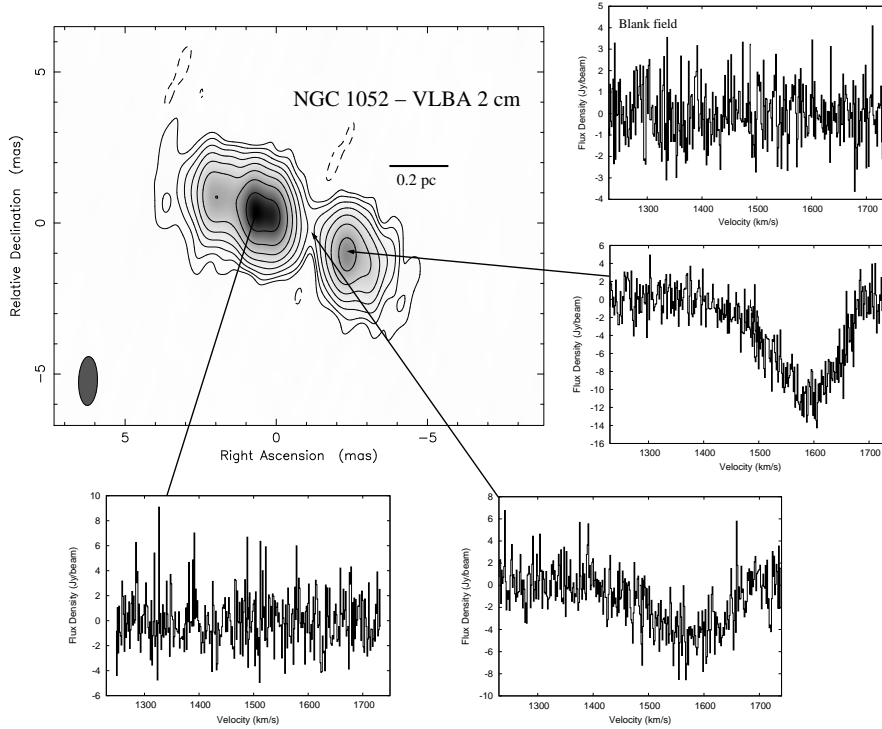


Figure 3.5: VLBA image of Cygnus A at 13.4 GHz. The synthesized beam is  $(0.879 \times 0.52) \text{ mas}^2$ . The image is contoured at -1.5, 1.5, 3, 6, 12, 24, 48, 96 percent of the map peak at  $0.453 \text{ Jy beam}^{-1}$ . The panels show a montage with selected OH absorption spectra. The bottom right panel shows the absorption spectrum integrated over the whole source. The  $x$ -axis is the velocity (in  $\text{km s}^{-1}$ ) with respect to the systemic velocity of  $16810 \text{ km s}^{-1}$ , the  $y$ -axis is the flux density (in  $\text{mJy beam}^{-1}$ ).

of  $13.434 \text{ GHz}$  was seen towards the centre of Cygnus A, at a velocity of  $+50 \text{ km s}^{-1}$  with respect to systemic. The apparent optical depth derived from the ratios of intensities of peak absorption and adjacent continuum is  $\tau = 0.125$  with a line FWHM corresponding to  $\sim 90 \text{ km s}^{-1}$ . The absorption profile towards the lobes is suggestive that part of the gas is diffuse and surrounds the inner jets, whereas a deeper and broader absorption profile is seen towards the core. The profile is strongest when integrated over the entire area containing the continuum emission, and again seems to indicate that the gas is spread over the whole source, with prevalence towards the central region. Further tests are needed to confirm this result and to rule out a spurious feature due to low-level instrumental effects only detectable after long integration times.

The tentative OH absorption line shown in Fig. 3.5 is relatively broad, which also suggests that the absorption occurs near the nucleus, and is comparable to the  $\text{CO}^+$  absorption line detected by Fuente et al. (2000) (Fig. 3.1, top panel) towards the nucleus of Cygnus A. The width of the  $\text{CO}^+$  absorption is  $\Delta V \approx 170 \text{ km s}^{-1}$ , peaking at the systemic velocity. Also at the systemic velocity, H I absorption shows a broad profile, shown in Figure 3.1 (bottom panel), though the H I spectrum is composed of two velocity widths of  $\sim 150 \text{ km s}^{-1}$ , while the  $\text{CO}^+$  appears as a single feature. The  $13.4 \text{ GHz}$  OH line, though slightly off systemic (it is blue-shifted by  $\sim 50 \text{ km s}^{-1}$ ) is however coincident with the H I absorption peak, and agrees overall with the H I and the  $\text{CO}^+$  absorption features. The H I was interpreted as part of a circumnuclear torus rotating around a radio jet oriented close to the plane of the sky (Conway & Blanco 1995). The two velocity components would then arise in the edge-brightened outer jet, sampling material redshifted and blueshifted with



*Figure 3.6:* VLBA image of NGC 1052 at 13.4 GHz. The synthesized beam is  $(1.62 \times 0.62) \text{ mas}^2$ . The image is contoured at -3, 3, 6, 12, 24, 48, 96 times the map noise of  $0.7 \text{ mJy beam}^{-1}$ . The maximum in the map is  $0.436 \text{ Jy beam}^{-1}$ . The panels show a montage with selected OH absorption spectra. The noise in the map is  $0.7 \text{ mJy beam}^{-1}$ . The top right panel shows the absorption spectrum integrated over a blank field off the source.

respect to the nucleus. The OH absorption is bound to sample a region which is closer to the centre of the source, where only one velocity component is expected, and the width of the line would reflect the velocity dispersion of the clouds within the torus. However, in the 13.4 GHz OH spectrum presented here (overall spectrum), two velocity components seem to be present. If these are confirmed, they could mimic the HI gas and thus trace redshifted and blueshifted velocity components with respect to the nucleus, supporting the view of a more spread distribution of the OH. Alternatively, the apparently double component could be due to maser emission superposed on the absorption. The continuum map of Cygnus A, shown in Fig. 3.5 traces a region of  $\sim 4 \text{ pc}$  in extent, therefore we are looking into a region that is compatible with the expected torus size (of a few parsecs; Krolik & Begelman 1988). The OH absorption seen at this frequency could be part of the putative torus sought for in Cygnus A.

### 3.4.2 NGC 1052

The continuum image of NGC 1052 from the VLBA observations is shown in Fig. 3.6. At 13.4 GHz the source structure is extended, with jets extending east–west up to  $\sim 1 \text{ pc}$  from the core, although some low-level emission was seen further out extending up to  $\sim 2 \text{ pc}$  from the core. The maximum peak flux density of the source is  $436 \text{ mJy beam}^{-1}$ , the noise in the map is  $0.7 \text{ mJy beam}^{-1}$ . Absorption of the rotationally excited OH transition at 13.434 GHz was clearly detected towards the centre of NGC 1052. Absorption was detected

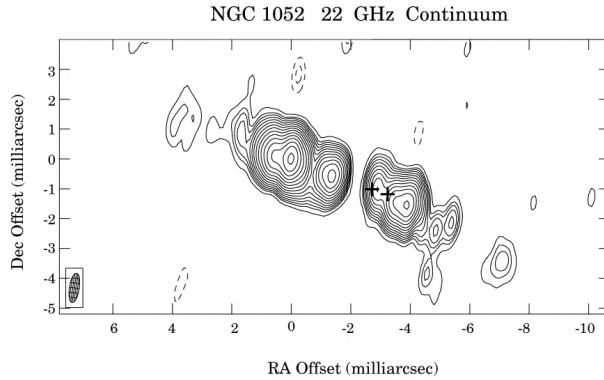


Figure 3.7: The 22 GHz continuum image of NGC 1052 (Claussen et al. 1998). The two crosses mark the positions of the two groups of water masers.

predominantly towards the western jet (the counter-jet), whereas none was found towards the eastern jet. The apparent optical depth of the spectrum taken towards the counter-jet derived from the ratios of intensities of peak absorption and adjacent continuum is  $\tau = 0.264$  with a line FWHM corresponding to  $\sim 200 \text{ km s}^{-1}$ . Towards the “gap” between the jet and the counter-jet, the apparent optical depth of the line was  $\tau = 0.230$ . Although the absorption line has a line flux density of  $-4.8 \text{ mJy}$  at the gap which is less than the line flux density at the counter jet,  $-11.2 \text{ mJy}$ , the optical depths are comparable in the two regions, due to weaker continuum in the gap.

The absorption profile observed with the VLBA suggests an obscuration of the inner jet region in an extremely compact region confined within a distance  $< 0.3 \text{ pc}$  from the core. The proximity to the core is further supported by the large line width. The line is relatively broad compared to the OH absorption spectrum associated with the nuclear region observed at  $1.67 \text{ GHz}$  (Omar et al. 2002; Vermeulen et al. 2003). Also, H I absorption, with different velocity components (a high velocity system and sharper features at low velocity), has been associated with the central few pc region. The  $1.67 \text{ GHz}$  OH and H I gas are thought to be co-located due to the similarity of their absorption profiles (see Figure 3.8). CO, HCN, and  $\text{HCO}^+$  have been detected in absorption in this source (Liszt & Lucas 2003), with line profiles that are broader than the H I and  $1.67 \text{ GHz}$  OH profiles, and are more similar to the  $13.4 \text{ GHz}$  spectrum. The broader widths of these lines are due to lower free-free opacity at mm-wavelengths which exposes higher-velocity material nearer the nucleus. The different velocity peaks at the different transitions trace slightly different components of the nuclear region. However, these agree overall in the velocity spanned. NGC 1052 is also an  $\text{H}_2\text{O}$  megamaser galaxy. The maser originating at  $0.1 \text{ pc}$  to  $0.2 \text{ pc}$  to the west of the core in the counterjet is thought to be excited by an interaction of the jet with the surrounding medium (Claussen et al. 1998). The positions of the  $\text{H}_2\text{O}$  masers are coincident with the position at which the OH absorption presented here is observed (see Fig 3.7), and it seems likely that these molecules, and the gas observed at mm-wavelength, would coexist at the same location.

Free-free absorption in NGC 1052 leads to an asymmetric central gap that opens up towards lower frequencies. The western jet is receding, and at least in the first  $1 \text{ pc}$  is partially obscured by free-free absorption. The free-free absorption towards the western jet and the gap between eastern and the western jet have been explained with the presence

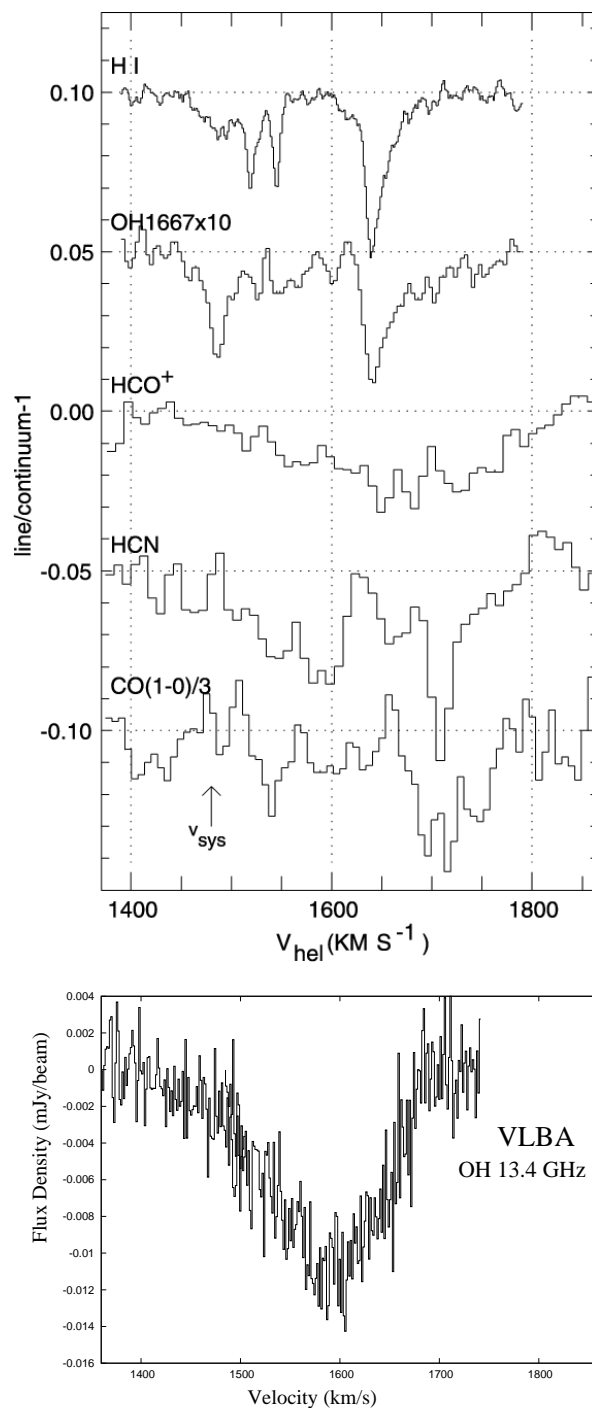


Figure 3.8: Plot showing absorption profiles of NGC 1052. Top panel shows data from the literature scaled, offset, as line/continuum ratios (from Liszt & Lucas 2004). At the top are the VLBA HI and OH profiles (Vermeulen et al. 2003), the spectra were averaged over a region corresponding to 15 mas to 20 mas (1.5 pc to 2.0 pc). Below are the HCN, HCO<sup>+</sup> and CO (J=1-0 transitions; Liszt & Lucas 2004) from the Plateau de Bure at different epochs against an unresolved mm-wave continuum. The mm-spatial distribution is compact and presumably similar to that at lower frequencies, but with a larger contribution from regions at smaller radii. The bottom panel shows my VLBA spectrum showing OH absorption at 13.4 GHz taken against the counter-jet of NGC 1052 (<1 pc).

of a geometrically thick plasma torus and a geometry of the jet-torus system in which 0.1 pc of the eastern jet and 0.7 pc of the western jet are obscured (Kameno et al. 2001). The OH absorption observed here confirms this expectation and seems to be associated with the inferred torus in this source. The H I atomic gas absorption, on the other hand, is distributed in front of the approaching, as well as the receding, jet and has sub-pc scale structure. While the OH gas at 1.67 GHz and the H I gas are likely to be co-located, they do not seem to coincide with the H<sub>2</sub>O masers, even though these are at the same velocity. Although the apparent optical depth of the 1.67 GHz line was measured to be  $\tau = 0.25$ , and is comparable to the optical depth of the 13.4 GHz line, these OH lines probably arise in different regions, that is, we are here tracing gas which is more compact and closer to the central region. It is remarkable how in the inner parsec around the AGN it appears possible for some molecular and atomic clouds to preserve a relatively quiescent existence.

### 3.5 Conclusions

I report here the results of a search for excited OH at 13.4 GHz towards the powerful and nearby galaxies Cygnus A and NGC 1052. A tentative OH detection was made towards Cygnus A and a firm detection was made towards NGC 1052. In Cygnus A, the compactness of the radio source at this frequency indicates that the absorbing material lies within 4 pc of the central engine. This is consistent with most recent results based on high-resolution IR observations of NGC 1068, which show a torus size that is no more than a few parsecs (e.g. Jaffe et al. 2004; Poncelet et al. 2006). The OH line is relatively broad and is comparable to the CO<sup>+</sup> and H I absorption lines, which have been interpreted as part of a circumnuclear torus rotating around a radio jet. The OH absorption at 13.4 GHz is bound to sample a region which is closer to the centre of the source, than the 1.67 GHz absorption, where only one velocity component is expected, and the width of the line would reflect the velocity dispersion of the clouds within the torus. However, the two absorption components present in the 13.4 GHz spectrum are similar to the H I profile previously observed, suggesting rotation of gas around the core.

A (second) definite detection of excited OH at 13.4 GHz was made towards the core of NGC 1052. Absorption was detected towards the western jet, whereas none was found towards the eastern jet. The optical depth of the absorption line was  $\tau = 0.264$  with a line FWHM of  $\sim 200 \text{ km s}^{-1}$ . The absorption profile suggests obscuration of the inner jet in a compact region confined within  $< 0.3 \text{ pc}$  from the core. The vicinity to the core is further supported by the large width of the line. The gas is likely to be associated with a geometrically thick plasma torus, which has been inferred from free-free absorption and is located 0.1 pc from the eastern jet and 0.7 pc from the western jet. Also, OH seems to be co-located with the H<sub>2</sub>O gas and perhaps with the more compact clouds of CO, HCN, and HCO<sup>+</sup>, but not with the H I and OH gas observed at 1.67 GHz, which are more evenly distributed around the nuclear region.

These observations confirm that radiative excitation effects can have an high impact and should be taken into account when studying the molecular properties in the innermost regions of AGN. In the case of Cygnus A, this result confirms that non-detections obtained for OH at 1.67 GHz and CO can be explained in terms radiative excitation effects playing an important role. These detections of excited OH at 13.4 GHz also provide independent evidence for a molecular torus at the centre of Cygnus A and NGC 1052 on parsec scale.



## Chapter 4

# A survey for extragalactic methanol

As a follow-up to the Effelsberg hydroxyl survey, I searched for the 6.7 GHz transition of methanol in a sub-sample of the Seyfert 2 galaxies that had been selected for OH observations (see Chapter 2). In the Galaxy, sites of OH masers are often coincident with sites of CH<sub>3</sub>OH masers. However, extragalactic methanol surveys at 6.7 GHz have so far yielded only non-detections. An introduction is presented in Sections 4.1 and 4.2. The sample selection, observation methods, and data reduction techniques are presented in Sections 4.3 and 4.4. In Section 4.5, the results are shown, including a discussion of the first ever detection of extragalactic methanol.

### 4.1 Introduction

The  $5_1 \rightarrow 6_0 A^+$  transition of methanol (CH<sub>3</sub>OH) at 6.7 GHz is mostly seen in emission and is one of the most prominent Galactic maser lines. This strong maser line is observed exclusively in star forming regions associated with compact H II and OH masing regions, with the CH<sub>3</sub>OH and OH masers being coincident on subarcsecond scales, suggesting that OH and CH<sub>3</sub>OH molecules cohabit (Menten et al. 1992). The masers are also commonly associated with regions containing H<sub>2</sub>O masers (Norris et al. 1993; Menten et al. 1993). With line flux densities reaching up to several thousand Jy, which is not quite as strong as the brightest 22 GHz H<sub>2</sub>O masers (e.g., Matveyenko et al. 2003) but exceeds the peak flux densities of any known OH maser. If the Galactic relationship between OH and CH<sub>3</sub>OH emission in compact H II regions scales to megamaser luminosities, then one would expect the 6.7 GHz line to be easily detectable at cosmological distances. Hundreds of Galactic 6.7 GHz methanol masers have been discovered since the early nineties (Pestalozzi et al. 2005). The large number of strong Galactic masers and the existence of superluminous H<sub>2</sub>O and OH “megamasers” provided a strong motivation to search for 6.7 GHz emission toward extragalactic targets.

Extragalactic searches for methanol have therefore mainly targeted known OH megamaser galaxies and galaxies with high infrared fluxes. Extragalactic methanol was detected as early as two decades ago in the much weaker millimetre wavelength transition in the nearby starburst galaxies M82 and NGC 253 (Henkel et al. 1987b). However, although  $\sim 400$

Galactic methanol masers are now known in the 6.7 GHz transition (e.g. Ellingsen et al. 1996), only three have been detected outside the Galaxy, all of which are in the Large Magellanic Cloud (Sinclair et al. 1992; Ellingsen et al. 1994a; Beasley et al. 1996). These are unremarkable since their isotropic integrated line luminosities are similar to Galactic methanol masers (roughly  $10^{-5} L_{\odot}$  to  $10^{-6} L_{\odot}$ ).

Surveys searching for extragalactic methanol at 6.7 GHz, targeting known OH megamaser galaxies and objects with high infrared fluxes, surprisingly turned out to be unsuccessful. Ellingsen et al. (1994b) conducted an extensive search for methanol emission towards 10 galaxies in which OH and H<sub>2</sub>O megamasers existed. Following this, Phillips et al. (1998) carried out a comprehensive search for extragalactic methanol masers towards 87 galaxies covering a variety of different types of galaxies using the Australia Telescope Compact Array (ATCA). They targeted their observations using several criteria, including FIR luminosities and the presence of OH megamasers. Another sensitive survey for 6.7 GHz methanol masers was carried out by Darling et al. (2003). They observed 25 OH megamaser galaxies with the Green Bank Telescope (GBT) achieving an rms noise levels of roughly 0.6 mJy in 150 kHz channels. All these surveys yielded non-detections. In particular, these surveys have shown that there is no analogue to OH megamasers at 6.7 GHz (Ellingsen et al. 1994b; Phillips et al. 1998; Darling et al. 2003). Even though these studies were searching for methanol emission at 6.7 GHz, they failed to detect either emission or absorption in any of the sources.

As a conclusion to these surveys it has been suggested that in extragalactic sources the physical conditions required to produce CH<sub>3</sub>OH megamasers do not exist, i.e. that the pumping is insufficient to invert the methanol transition in question above the limits for detection (Phillips et al. 1998). Alternatively, it has been suggested that the non-detections may be the result of low methanol abundances in large molecular clouds within starburst galaxies; either no methanol is formed or methanol is destroyed in harsher conditions. For example, a reduced abundance of oxygen will likely reduce both the abundance of methanol (CH<sub>3</sub>OH) and of dust, which is required to convert the short wavelength radiation from massive young stars to the infrared wavelengths required for maser pumping. Henkel et al. 1987, have detected thermal methanol emission from two galaxies, IC 342 and NGC 253, finding that the fractional abundance of methanol relative to hydrogen is  $\simeq 10^{-7.5}$ . This is similar to that found in giant molecular clouds (GMC) in the Milky Way, but is a factor of at least 100 lower than that required for the high methanol maser luminosity as discussed by Sobolev et al. (1997). However, such abundance differences are also found in hot cores in the Milky Way (high abundance), known to be the sites of methanol masers, compared with more extended molecular cloud regions (low abundance). The methanol abundance may be greatly increased in regions near hot stars by thermal evaporation of molecules frozen onto grain surfaces.

## 4.2 Enhanced absorption in the 6.7 GHz methanol line

Methanol masers form two distinct families. Whilst Class I masers are often separated from the main source of excitation, Class II masers, characterized by 12.2 GHz and stronger 6.7 GHz emission, directly trace sites of high mass star formation. The 6.7 GHz line is

the classical Class II maser, requiring warm dust (150 K) and relatively cool gas (Cragg et al. 2005). However, in regions characterized by Class I excitation, the transition is seen in absorption (Menten 1991). The inversion of Class I transitions necessarily follows from basic properties of the methanol molecule, i.e., the interplay of transition probabilities and collisional excitation rates for certain ranges of densities and temperatures in the absence of strong far-infrared fields. Hence, instead of searching for maser emission, an alternative approach involves absorption line studies against a strong background continuum, tracing lines-of-sight toward active galactic nuclei (AGN).

Molecular absorption is a useful, sensitive probe for exploring the cores of molecular clouds (Peng & Whiteoak 1992). Already in the early observations, significant CH<sub>3</sub>OH absorption was detected towards dense molecular clouds overlaying H II regions and towards dark clouds within our Galaxy. Several observations (Batra et al. 1987; Walmsley et al. 1988; Whiteoak & Peng 1989) revealed that the  $2_0 \rightarrow 3_1$  - E transition at 12.18 GHz and the  $5_1 \rightarrow 6_0$ - A<sup>+</sup> transition at 6.7 GHz, both of which can produce strong Class II masers, can be anti-inverted. Absorption in this line can not only take place in sources with significant continuum, but also against the microwave background.

The situation is dramatically different for sources in the vicinity of an intense FIR field resulting from warm  $\sim 100$  K dust heated by an embedded high-mass protostellar object surrounded by cooler gas (Sobolev et al. 2005). Here, Walmsley et al. (1988) suggested that high kinetic temperatures and a strong infrared radiation field are fundamental for maser inversion in Class II masers. Intense pumping (predominantly) to the first torsionally excited state via radiation around  $30 \mu\text{m}$  and subsequent decay determines the level populations and leads, amongst other things, to the strong maser emission in the 6.7 GHz and 12 GHz lines and weaker masers in a series of other lines (Cragg et al. 2005, Müller et al. 2004).

Figure 4.1 shows the line temperature as a function of H<sub>2</sub> density for different methanol column densities, at 10 K and 50 K, for the 6.7 GHz transition. The anti-inversion of the 12.18 GHz line happens at low densities; the anti-inversion of the 6.7 GHz line requires higher densities ( $n(\text{H}_2) > 10^4 \text{ cm}^{-3}$ ). Thermalization of the 6.7 GHz line starts around  $10^7 \text{ cm}^{-3}$ . Therefore, as already noted by Walmsley et al. (1988), at least the 12.18 GHz line can be used as a tracer of cold dust.

All this suggests that methanol absorption might be widespread, and can indeed provide a useful means of investigating the physical conditions in molecular clouds. CH<sub>3</sub>OH absorption observed towards Galactic H II regions arises mainly in clouds near the H II emission, implying that radiative excitation may also contribute to the production of the CH<sub>3</sub>OH transitions.

### 4.3 The sample

The sample of sources selected for observations of the 6.7 GHz methanol transition consists of ten Seyfert 2 or LINER galaxies. The sample is a sub-sample of the sources selected for OH observation, which were selected for having a high X-ray absorbing column density

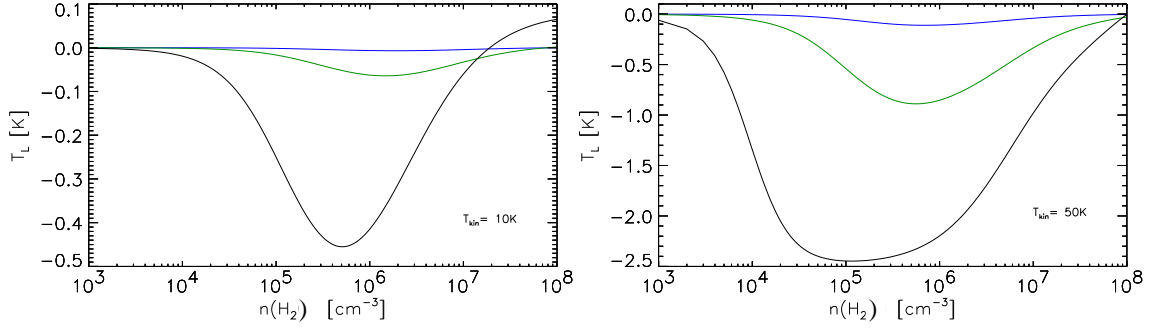


Figure 4.1: The brightness distribution of the  $5_1 \rightarrow 6_0 - A^+$  transition of methanol as a function of  $H_2$  density at 10 K (left panel) and 50 K (right panel). The blue line shows the results for calculations for a column density of  $N(\text{CH}_3\text{OH})/\Delta v = 2 \times 10^{13} \text{ cm}^{-2}/(\text{km s}^{-1})$ , the green line is for  $N(\text{CH}_3\text{OH})/\Delta v = 2 \times 10^{14} \text{ cm}^{-2}/(\text{km s}^{-1})$ , the black line is for  $N(\text{CH}_3\text{OH})/\Delta v = 2 \times 10^{15} \text{ cm}^{-2}/(\text{km s}^{-1})$  (Leurini 2004). Absorption is shown against the microwave background at a temperature of 2.7 K.

( $N_{\text{H}} > 10^{23} \text{ cm}^{-2}$ ) and a radio continuum flux density  $S_{6 \text{ cm}} > 50 \text{ mJy}$ , against which to detect absorption (see Chapter 2). The sources and the observing dates are listed in Table 4.1. In particular, those sources with a previous detection of another molecular absorption line were selected for observations of methanol. For example,  $\text{HCO}^+$ ,  $\text{HCN}$  and  $\text{CO}$  in NGC 1052 (Liszt & Lucas 2004) or a previous  $\text{OH}$  detection at 6 GHz in NGC 4261, NGC 3079, Mrk 231 and NGC 6240 (see Chapter 2). Four of the sources in the sample (Cygnus A, Mrk 3, Mrk 231 and Mrk 348) have been classified as Compton thick, i.e. they show X-ray absorbing columns  $N_{\text{H}} > 1.5 \times 10^{24} \text{ cm}^{-2}$ . All the above criteria select galaxies that show indications for the presence of absorbing material towards the central nucleus of these AGN.

#### 4.4 Observations and data reduction

The first spectroscopic observations for this project searching for the methanol line at a rest frequency of 6668.519 MHz were carried out with the 100 m telescope of the MPIfR in Effelsberg during February 2006 to June 2006. Follow-up observations for those sources with tentative detections were made between March 2007 and November 2007. During each observing run, spectroscopic observations were interspersed by continuum measurements. The front-end was the dual polarization 5 cm HEMT receiver at the primary focus. System temperatures were typically 30 K to 35 K in the zenith, corresponding to a system equivalent flux density of about 22 Jy. The full width to half power beam size was 120 arcseconds. The observations were all carried out with the same setup in a position-switching mode, integrating three minutes off-source and three minutes on-source, while defocusing by  $\lambda/8$  to reduce the standing wave ripple. The source signal was determined by subtracting the on-source and off-source scans. This method is particularly good for removing the effects of interference. The backend was the AK90 autocorrelator<sup>1</sup> with a total of eight bands, each consisting of 512 channels centred on the redshifted frequency of the line at 6668.5 MHz and covering 40 MHz. Spectra were formed of both polarizations and were averaged. The channel spacing was 78 kHz, corresponding to  $\sim 3.5 \text{ km s}^{-1}$

<sup>1</sup>At the time of writing this thesis, the AK90 spectrometer malfunctioned beyond repair.

Table 4.1: Observing parameters.

Source	Observing Date	redshift	$t_{\text{int}}$ (min)	$S_{\text{c}}^{\dagger}$ (mJy)	rms $^{\ddagger}$ (mJy)
Cygnus A	25 May 06	0.0560	14	130000	2.7
Mrk 3	25 May 06, 11 Jun 06, 14 Jul 07, 14 Sept 07	0.0135	885	352	1.2*
Mrk 231	12 Nov 07	0.0421	265	355	1.3
Mrk 348	14 Jul 07	0.0150	288	510	2.2
NGC 1052	16 Mar 06	0.0050	62	1985	3.2
NGC 2110	16 Mar 06	0.0077	11	130	8.4**
NGC 3079	21 Feb 06, 19 Mar 07, 14 Jul 07, 6 Nov 07	0.0037	840	318	0.6
NGC 4261	21 Feb 06, 11 Jun 06, 12 Nov 07	0.0074	248	1270	1.9
NGC 5135	16 Mar 06	0.0137	3	107	11.6
NGC 6240	25 May 06	0.0244	57	183	2.3

$\dagger$  6.7 GHz continuum flux density.

$\ddagger$  Noise level for channel spacings of  $3.5 \text{ km s}^{-1}$ .

\* Channel spacing is  $8.7 \text{ km s}^{-1}$ .

\*\* Channel spacing is  $1.8 \text{ km s}^{-1}$ .

per spectral channel. The pointing was accurate to about 10 arcseconds to 15 arcseconds, estimated from cross scans toward the continuum sources. Finally, amplitude calibration was based on measurements of the 6.668 GHz continuum flux of 3C 48, assuming a flux density of 2.5 Jy (Ott et al. 1994) at the observing frequency.

During and after the observations the spectra of the individual scans were inspected and edited individually, and then summed. The residual spectral baseline curvature after position switching and integrating was removed using a third-order polynomial fit to the spectra. In the case of NGC 1052 and NGC 4261, a higher order polynomial was used to (partially) remove the spectral baseline ripples across the band that were caused by the strong continuum emission from these sources setting up a standing wave due to multiple reflections between the primary and secondary foci. For Cygnus A, due to its bright lobes, the ripples were so severe that the source was observed for only 14 minutes (see Figure 4.2).

The resulting rms noise in the combined spectra (Table 4.1) is within 10% of the theoretical noise, given a channel bandwidth of 78 kHz, and system equivalent flux density of 22 Jy, and dual polarization. A collection of the resulting spectra are shown in Figure 4.3. The spectra shown were observed on the dates given in Table 4.1. A few of the sources were observed more than once. All sources, and their spectra, will be discussed in more detail in the next section.

## 4.5 Results and individual sources: The detections

The resulting spectra searching for methanol at 6.7 GHz are displayed in Figure 4.3. Seven of the observed sources do not reveal any spectral feature around the systemic velocity, these are described in the next section. Extragalactic methanol was detected for the first time towards NGC 3079 at the systemic velocity of the galaxy during the February 2006

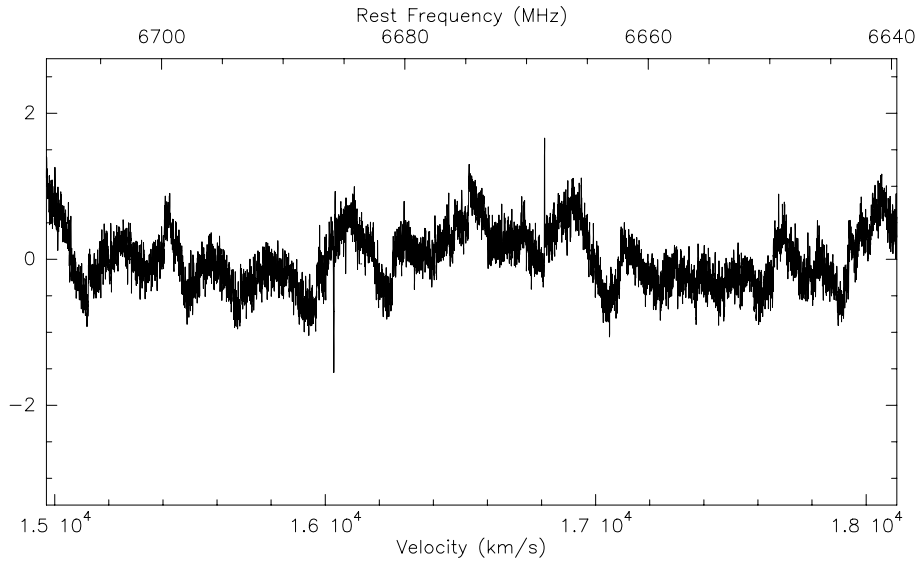


Figure 4.2: Cygnus A continuum-subtracted spectrum at 6.7 GHz taken with Effelsberg using position switching and  $\lambda/8$  defocussing showing the effects of a strong continuum on the bandpass shape. A defining characteristic of the powerful source are high surface brightness radio hot spots located at the source extremities. The flux density of the overall source including the bright lobes, as seen by Effelsberg, at 4.85 GHz is 213 Jy (Becker et al. 1991). The amplitude of the ripples caused by Cygnus A in the plot is 1 Jy, so the standing waves have an amplitude of 0.5% of the total source flux density.

observing session and was reproducible in the March 2007 observing session. However, a second spectral feature was detected at  $-109 \text{ km s}^{-1}$  from systemic main feature (see Fig. 4.4) in the March 2007 observation, therefore the source was reobserved in July 2007 and November 2007, and the authenticity of this feature could be confirmed. Tentative detections were further made in July 2007 towards two more sources, Mrk 348 and Mrk 3. In Mrk 348 a broad ( $670 \text{ km s}^{-1}$ ) absorption line was visible, and in Mrk 3 and NGC 6240 possible emission lines were detected. These sources are described here.

#### 4.5.1 NGC 3079

##### NGC 3079: General properties

NGC 3079 is an edge-on dusty spiral with a high degree of nuclear activity. Located at a distance of 15 Mpc (de Vaucouleurs et al. 1991), NGC 3079 hosts a nuclear starburst ( $L_{\text{FIR}} \sim 3 \times 10^{10} L_{\odot}$ ; Henkel et al. 1986b) and a heavily reddened active galactic nucleus of Seyfert 2 type (Ford et al. 1986; Sosa-Brito et al. 2001). Observations with the Hubble Space Telescope (HST) show narrow ionized filaments that rise from the nuclear region above the plane of the galaxy to envelop a 1.3 kpc-sized superbubble, presumably produced by a combination of stellar winds and supernova explosions at a site of massive star formation (Cecil et al. 2001). Parts of this superwind-blown structure are also traced by soft X-rays (Cecil et al. 2002). A strong 6.4 keV Fe  $K\alpha$  line further supports the presence of an AGN (Iyamoto et al. 2001; Cecil et al. 2002) with a clear correspondence between the X-rays and  $H\alpha$ -line filaments at a projected distance of 65 pc from the nucleus (Cecil, Bland-Hawthorn et al. 2002).

The source harbours a large variety and quantity of molecules, which support the idea

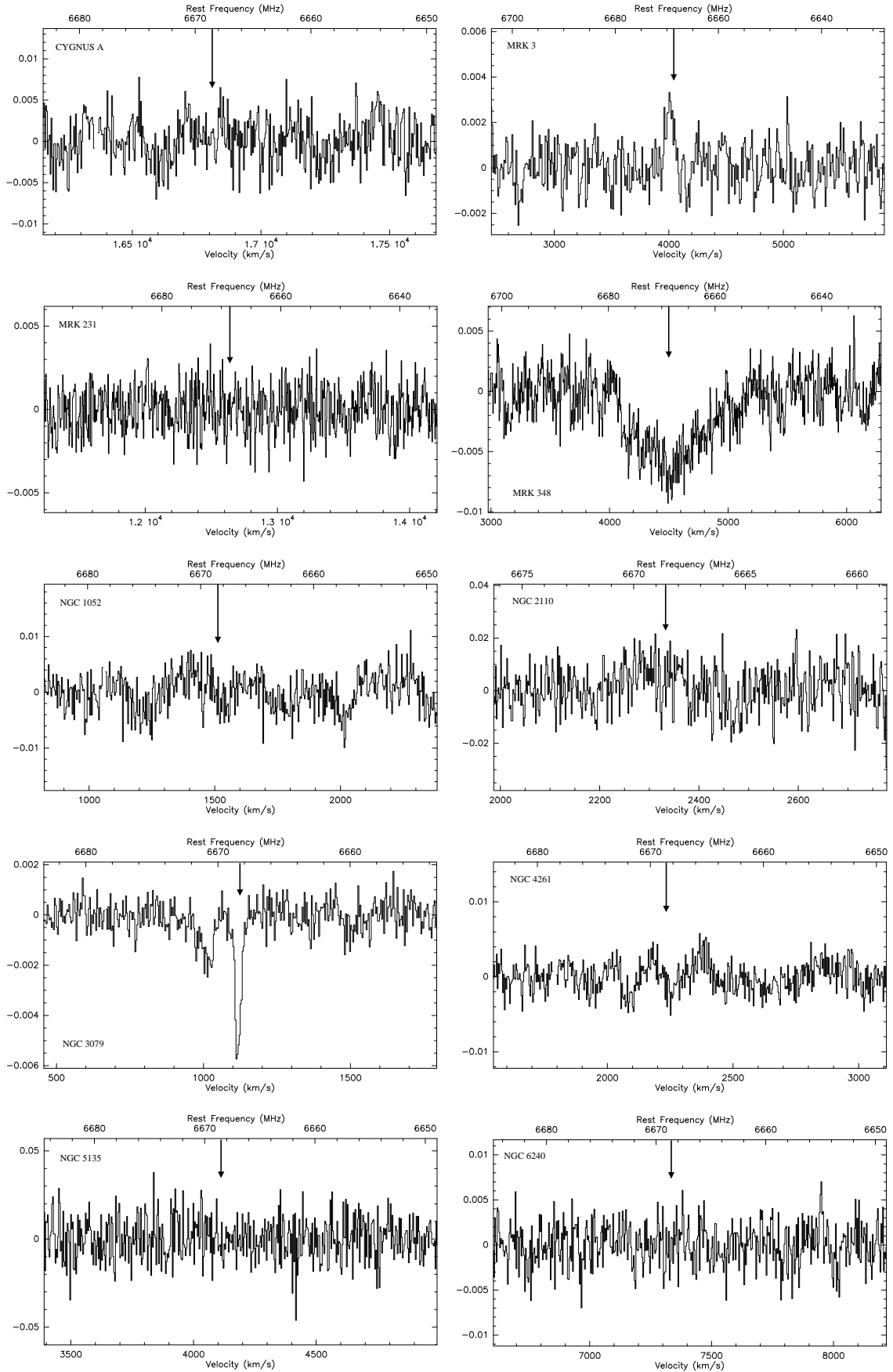


Figure 4.3: Effelsberg spectra of the ten sources observed for methanol at 6.7 GHz. The channel spacing is  $\sim 3.5 \text{ km s}^{-1}$  for all sources. The vertical axes are flux densities in Jy. The systemic velocity of each galaxy is marked by the vertical arrow.

of an edge-on torus obscuring the nucleus. NGC 3079 hosts a prominent H<sub>2</sub>O megamaser that was for a long time the most luminous known (Henkel et al. 1984; Baan & Haschick 1985). The maser indicates the presence of a nuclear disk of diameter  $\sim 2$  pc, with the plane of the disk oriented along the same north-south axis as the large-scale galactic and the kpc-sized molecular disk seen in CO. Broad ( $200 \text{ km s}^{-1}$  to  $400 \text{ km s}^{-1}$ ) and deep ( $\tau = 0.5$ ) neutral hydrogen absorption and equally broad OH absorption were found towards the compact radio nucleus of NGC 3079 (Baan & Irwin 1995). The OH absorbing gas has been interpreted to be part of the circumnuclear gas traced by CO(1-0) emission, whereas H<sub>2</sub>O maser components are distributed in an elongated disk-like structure within a few parsecs of the nucleus and are not associated with any of the jet components (Trotter et al. 1998; Kondratko et al. 2005). The blue-shifted components have been associated with molecular outflows and the nuclear superbubble and also with starburst activity (Irwin & Sofue 1992). From the rotation curve of the masers, the enclosed mass is  $\sim 2 \times 10^6 M_{\odot}$  (Trotter et al. 1998; Kondratko et al. 2005). NGC 3079 shows not only nuclear radio continuum sources (see Middelberg et al. 2007) but also prominent jet-like protrusions originating from the nuclear region (Duric & Seaquist 1988; Baan & Irwin 1995). These are associated with the superwind and also extend toward the obscured back side of the galaxy, which is not visible at optical wavelengths.

### The radio continuum

For the first data set taken on February 21, 2006 the amplitude calibration gave a flux density of  $S_c = (275 \pm 41)$  mJy for NGC 3079, which is consistent with the 260 mJy obtained by extrapolating the 5 GHz flux density of Gregory et al. (1991) using a spectral index of  $\alpha_{1.4}^5 = -0.7$  ( $S \propto \nu^{\alpha}$ ).

No suitable flux density calibrator was observed in March 19, 2007, therefore these data were calibrated by bootstrapping the flux density calibration of NGC 3079 from February 21, 2006 to the data taken on March 21, 2007 assuming that the continuum flux density of NGC 3079 remained constant between February 21, 2006 and March 19, 2007. A flux density of  $S_c = (318 \pm 47)$  mJy was obtained in the following November 2007 observations. The absolute flux density calibration is estimated to be accurate to within  $\pm 15\%$ .

### The spectra

The resulting spectra of NGC 3079 are shown in Figure 4.4. The 6.7 GHz methanol absorption line is clearly visible in all of the spectra. The systemic optical velocity of the galaxy is  $V_{\text{LSR}} = 1116 \text{ km s}^{-1}$  (Irwin & Seaquist 1991) and is labelled by the arrow. The line is relatively narrow, extending over  $\sim 25 \text{ km s}^{-1}$ , with a fitted peak flux density of 4.9 mJy. The rms noise is 0.9 mJy in the combined spectrum. The line consists of eight channels yielding a  $10 \sigma$  detection in the combined spectrum. The spectral channel containing the peak of the methanol line lies within  $2 \text{ km s}^{-1}$  of the systemic velocity of NGC 3079, defined by the HI disk emission (Irwin & Seaquist 1991), and is deeper than the fitted value (4.9 mJy). This suggests that most of the gas is contained in a compact, non-turbulent cloud with a low relative velocity to the systemic velocity of the galaxy. Therefore, the gas can be neither inflowing nor outflowing with respect to the radio core.

A second distinct absorption feature ( $2.5 \sigma$ ) which is blue-shifted with respect to the systemic velocity by  $109 \text{ km s}^{-1}$  was also visible in the March 2007 spectrum (Figure 4.4

second panel from top). The line peak is 2.3 mJy and the width is  $57 \text{ km s}^{-1}$ , which is both broader and fainter than the component at the systemic velocity. Since it was a prominent feature, it was not removed using a higher degree polynomial to the baseline fit. However, this feature was not detected in the previous observation (February 2006) and could have been the result of baseline ripples across the band, which were more severe in the March 2007 observing session due to poorer weather conditions.

However, the absorption line was later confirmed in the July 2007 and November 2007 observations (see the spectrum in Fig. 4.3, which includes all observations of NGC 3079). This blue-shifted feature could trace methanol in a cloud at a different velocity from systemic, for example infalling gas. It is notable that in this source two distinct absorption components have also been observed in both the 1667 MHz and 1665 MHz OH transitions, with one component at systemic and a second blue-shifted component at a velocity of  $-101.6 \text{ km s}^{-1}$  relative to the systemic velocity,  $V_{\text{LSR}}$  (Baan & Irwin 1995; Hagiwara et al. 2004) and in the 6 GHz OH transitions (this work, Chapter 2). A similar velocity separation is also seen in  $\text{H}_2\text{O}$  maser emission (Hagiwara et al. 2002), where components are found at the systemic velocity and blue-shifted to  $\sim 100 \text{ km s}^{-1}$  relative to systemic and velocities between  $-160 \text{ km s}^{-1}$  and  $74 \text{ km s}^{-1}$  relative to systemic. HI absorption shows one absorption trough blueshifted to  $1004 \text{ km s}^{-1}$  (and coincident with the detection presented here), one near systemic velocity at  $1130 \text{ km s}^{-1}$  and one redshifted by a similar amount to  $1250 \text{ km s}^{-1}$ . However, the main  $\text{H}_2\text{O}$  maser components are seen at  $\sim 960 \text{ km s}^{-1}$  and the redshifted maser components at  $1125 \text{ km s}^{-1}$  are very weak. A Gaussian line profile was fitted to the 6.7 GHz line and the parameters of the fit are shown in Table 4.2.

### Line apparent optical depths

Observations of emission and absorption lines are complementary. Emission commonly traces extended regions that show an excitation that is significantly above the temperature of the background source, typically the cosmic microwave background. To achieve this degree of excitation through collisions requires that the density surpasses the critical density of the line. Absorption lines have the advantage that extremely tenuous gas, below the critical density, can also be studied, that the effective beam size is confined to the sometimes extremely compact background continuum source(s), that the sensitivity depends on the background continuum source strength, which can be chosen during sample selection to be large, and that optical depths can be obtained directly by a comparison of line and continuum flux densities.

For the line profile shown in Fig. 4.3, I calculated the optical depth,  $\tau$ , using

$$\tau = -\ln \frac{-S_1}{f_c \times S_c}.$$

where  $S_1$  is the line flux density,  $S_c$  is the continuum flux density and  $f_c$  is the source covering factor. For the continuum background in NGC 3079, the continuum flux density measured in November 2007 of  $S_c = (300 \pm 45) \text{ mJy}$  was adopted, as most of the spectral data were obtained in November 2007. For the source covering factor,  $f_c = 1$  was taken, assuming that the absorber obscures uniformly all of the detected radio continuum. Whilst a uniform coverage, i.e. the absence of small-scale clumping, is highly unlikely,

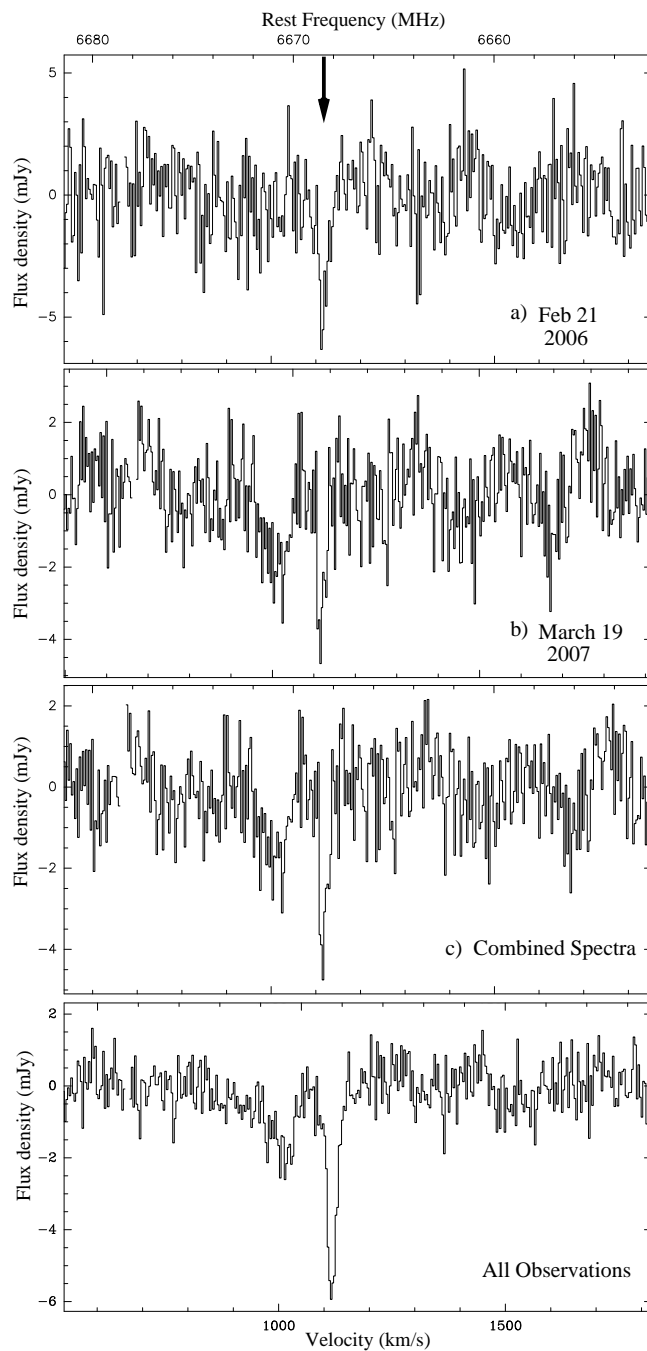


Figure 4.4: Continuum-subtracted  $5_1 \rightarrow 6_0 A^+$  methanol ( $\text{CH}_3\text{OH}$ ) absorption profiles toward NGC 3079 ( $\alpha_{J2000} = 10^{\text{h}} 01^{\text{m}} 57.8^{\text{s}}$ ,  $\delta_{J2000} = +55^\circ 40' 47''$ ) measured with Effelsberg. The channel spacing is  $3.5 \text{ km s}^{-1}$ . The systemic velocity (Irwin & Seaquist 1991) is marked by the vertical arrow in the upper panel. The baselines were removed from the spectra using a third-order polynomial in all cases. The top panel shows the spectrum of NGC 3079 taken in February 2006, the middle panel shows the spectrum taken in March 2007 and the panel below shows the two spectra combined. The bottom panel shows the spectrum all observations combined, from February 2006 to November 2007, also shown in Fig. 4.3. The fitted parameters of the above spectra are given in Table 4.2.

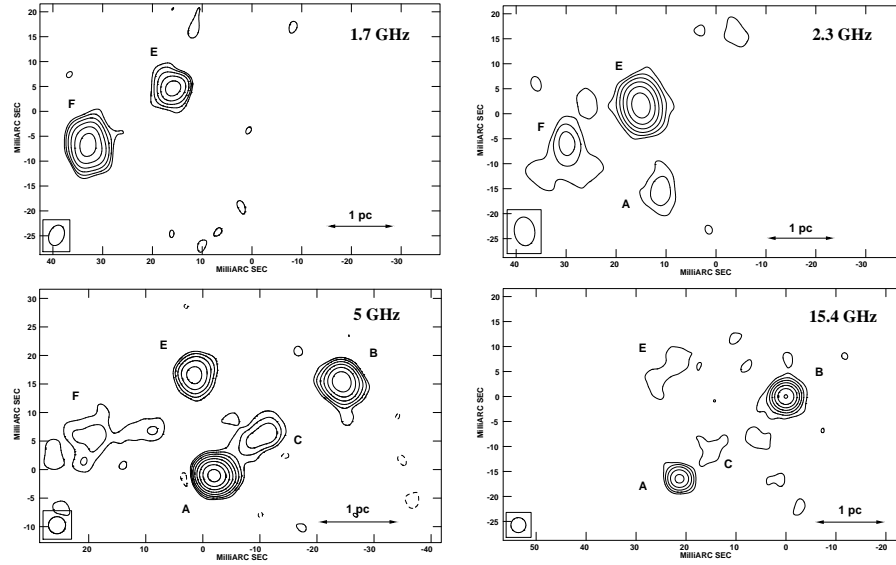


Figure 4.5: VLBI images of NGC 3079 at 1.67 GHz (top left), 2.3 GHz (top right), 5 GHz (bottom left) and 15.4 GHz (bottom right) from Middelberg et al. (2007). Components E and F are detected at 1.67 GHz to 5 GHz, whereas components A, B and C become more visible at the higher frequencies. At 5 GHz all components are visible, including the jet-like feature C, and component F is weakly detected. At 15 GHz only components A and B are detected. The flux density of components A, B, and E at 5 GHz was measured to be 43 mJy, 15 mJy and 6 mJy, respectively (Middelberg et al. 2007). The continuum components visible at 1.6 GHz are weakly detected at 5 GHz due to their steep synchrotron spectra and those visible at 5 GHz (A and B) are not detected at 1.6 GHz due to free-free absorption.

this nevertheless provides a firm lower limit to the true optical depth of the bulk of the obscuring region. The resulting optical depths are given in Table 4.2.

### Lines of sight toward NGC 3079

Against which parts of NGC 3079 do the methanol absorption features shown in Fig. 4.4 arise? Are they against the compact continuum emitted from the nuclear region, against the jet-like protrusions, or against the large-scale disk? The line parameters of the main spectral feature, i.e. narrow absorption near the systemic velocity, suggest that quiescent gas is traced along the line-of-sight toward the nuclear region, where the line-of-sight component of rotational velocity gradients of an edge-on galaxy should be minimal and hence where gas should be found near the systemic velocity. The small linewidth ( $\sim 24 \text{ km s}^{-1}$ ; Table 4.2) also indicates that the gas is likely not part of the nuclear region itself. The large linewidth of the blue-shifted component is consistent with two interpretations. It may either be caused by a high degree of turbulence near the nuclear region or by differential rotation further out. The approaching, blue-shifted sides of the nuclear molecular disk as well as the kpc-sized molecular disk are located north of the dynamical centre, and so one might find this absorption component is located at one of those locations.

To further constrain lines-of-sight, we should note that 6.7 GHz methanol is not the first radio line observed in absorption toward NGC 3079. At lower frequencies, 1.4 GHz HI and 1.67 GHz OH have already been reported (Haschick & Baan 1985; Baan & Irwin 1995, Hagiwara et al. 2004), while 4.8 GHz H<sub>2</sub>CO absorption was not seen (Mangum et al. 2008). The HI and OH lines show the same two main components that are also

observed in the 6.7 GHz CH<sub>3</sub>OH line, again with the systemic feature being stronger than the blue-shifted feature. HI reveals a third redshifted component at  $\sim 1250 \text{ km s}^{-1}$ . The 22 GHz H<sub>2</sub>O maser emission is quite different (see Hagiwara et al. 2002). Over the velocity range of  $890 \text{ km s}^{-1}$  to  $1350 \text{ km s}^{-1}$ , there is no strong emission at the systemic or blue-shifted velocities at which CH<sub>3</sub>OH and OH absorption is present. Instead, the main H<sub>2</sub>O component is seen at  $\sim 960 \text{ km s}^{-1}$ . The H<sub>2</sub>O 22 GHz maser line requires higher densities and kinetic temperatures than the other transitions and apparently traces a different gas component.

Baan & Irwin (1995) obtained interferometric HI and OH absorption maps with  $1''$  to  $2''$  resolution, and concluded that the lines originate from the central  $< 2''$  of the galaxy. Hagiwara et al. (2004) observed OH with subarcsecond resolution and suggest a nuclear outflow as the origin for the blue-shifted component. In our Galaxy, 6.7 GHz methanol is not as widespread as 1.4 GHz HI and 1.67 GHz OH. Therefore, methanol absorption in NGC 3079 is most likely also restricted to the lines-of-sight toward the nuclear region.

Line shapes of the lower frequency HI and OH and the higher frequency CH<sub>3</sub>OH lines are similar but not identical, the HI and OH, lines being broader ( $\sim 100 \text{ km s}^{-1}$ ). This may be caused in part by the more widespread spatial distributions of HI and OH already mentioned, but the radio continuum morphology must also play a role. At 1.4 GHz, 1.67 GHz and 6.7 GHz, different continuum components dominate. This is nicely illustrated by Middelberg et al. (2007) (see Fig. 4.5) who presented a collection of high resolution radio continuum maps between 1.67 GHz and 22 GHz made using VLBI. Sources E and F dominate at low frequencies, while sources A and B, located about 20 mas towards the west, dominate at high frequencies. This implies that the HI and OH trace lines of sight that are different from those traced by CH<sub>3</sub>OH; HI and OH absorb against sources E and F and methanol absorption should mainly arise toward sources A, B, and E. The similarity of the spectral line shapes requires the presence of extended molecular complexes that are at least as extended as the distance between sources B and F,  $\sim 50 \text{ mas}$  or  $4 \text{ pc}$ .

The optical depths observed here (Table 4.2) are lower limits. It is important to note that, at 5 GHz continuum sources A, B, C, D, and E contribute only 75 mJy to 80 mJy or 25% to 30% of the total flux density. If all of the methanol absorption is against component A, then the line optical depth, using the continuum flux density from Middelberg et al. (2007) of 43 mJy at 5 GHz for component A is 0.09. If the absorption is against B ( $S_{5 \text{ GHz}}=15 \text{ mJy}$ ), then the line optical depth is 0.27. The line opacities in Table 4.2 might therefore be a factor of three to four larger.

### Enhanced absorption in the 6.7 GHz methanol line

Having observed the  $J_k = 5_1 \rightarrow 6_0 \text{ A}^+$  transition of A-type methanol and having estimated line parameters and optical depths, I now discuss the physical and chemical implications. The lowest levels of the  $k = 0$  ladder of A-type methanol have lower energies than those in the neighbouring  $k$ -ladders that are connected by allowed radiative transitions. As a consequence, the energy levels of the  $k = 0$  ladder tend to be overpopulated and one expects, in the absence of a strong radiation field, enhanced absorption (also called “overcooling” or “anti-inversion”) in the  $J_k = 5_1 \rightarrow 6_0 \text{ A}^+$  transition. This is verified by the statistical equilibrium calculations of Walmsley et al. (1988) and Leurini et al. (2004) and describes a Class I methanol environment.

The situation is dramatically different for sources in the vicinity of an intense FIR

Table 4.2: Properties of Gaussian fits to the methanol absorption line and the resulting column densities calculated for  $43\text{ K}/T_{\text{ex}}$ .

Date	$V_{\text{abs}}^1$ ( $\text{km s}^{-1}$ )	$\Delta V_{1/2}^2$ ( $\text{km s}^{-1}$ )	Line peak (mJy)	$\int S dv$ (mJy $\text{km s}^{-1}$ )	$\tau(\text{CH}_3\text{OH})^3$	$N_{\text{CH}_3\text{OH}}$ ( $\text{cm}^{-2}$ )
<b>NGC 3079</b>						
21 Feb, 2006	$1116.5 \pm 2.2$	$24.6 \pm 6.2$	$-4.9 \pm 0.8$	$128 \pm 38$	0.018	$2.0 \times 10^{15}$
19 March, 2007	$1118.0 \pm 1.6$	$20.2 \pm 3.6$	$-3.9 \pm 0.5$	$79 \pm 18$	0.014	$1.2 \times 10^{15}$
Combined spectra <sup>1</sup>	$1117.6 \pm 1.4$	$19.9 \pm 3.2$	$-4.0 \pm 0.6$	$84 \pm 19$	0.015	$1.4 \times 10^{15}$
	$1009.3 \pm 4.8$	$57.1 \pm 9.1$	$-2.3 \pm 0.3$	$139 \pm 22$	0.008	$1.6 \times 10^{15}$
All observations <sup>2</sup>	$1117.9 \pm 0.6$	$24.2 \pm 1.6$	$-5.8 \pm 0.7$	$145 \pm 8$	0.020	$1.7 \times 10^{15}$
	$1009.9 \pm 3.0$	$57.4 \pm 7.4$	$-1.7 \pm 0.2$	$115 \pm 12$	0.007	$1.3 \times 10^{15}$

<sup>1</sup> Values relative to the February 21, 2006 and March 19, 2007 combined spectra

<sup>2</sup> Includes all observations in Table 4.1 and refers to the plot in Fig. 4.3.

1) Local standard of rest (LSR) velocities following the optical definition.

2) Full width to half power (FWHP) linewidth.

3) The peak optical depths are based on the observed total 6.7 GHz continuum flux of  $(275 \pm 41)$  mJy and a uniform source coverage (see Sect. 4.5.1).

The errors include uncertainties in line and continuum flux densities and are  $1\sigma$

field resulting from warm dust ( $T_d > 100$  K) heated by an embedded high-mass protostellar object surrounded by cooler gas. Here, intense pumping, predominantly to the first torsionally excited state via radiation around  $30 \mu\text{m}$ , and subsequent decay determines the level populations and leads to strong 6.7 GHz maser emission (e.g., Cragg et al. 2005).

The mere fact that we observed absorption and not emission already tells us which is the dominant excitation mechanism for methanol toward the central region of NGC 3079, namely that there is no strong FIR pumping. Whilst this does not exclude the presence of 6.7 GHz masers (a single maser that is 1000 Jy at a distance of 5 kpc would show a flux density of only 0.1 mJy at the distance of NGC 3079), absorption dominates presumably because the conditions leading to absorption are more widespread than conditions leading to emission. This is remarkable because the nuclear region of NGC 3079 appears to be more active and hence has a much more intense infrared radiation field than that of our own Galactic centre region, where absorption is also observed (Menten 1991).

### Column densities

If local thermodynamic equilibrium (LTE), characterized by a kinetic temperature,  $T_{\text{kin}}$ , is a good assumption, the optical depths listed in Table 4.2 can be used to derive the column density of methanol in the  $5_1 \rightarrow 6_0$  transitions. Following Houghton & Whiteoak (1995), one must assume some excitation temperature,  $T_{\text{ex}}$ , and then total methanol column density can be calculated assuming a rotation temperature,  $T_{\text{rot}}$ , which in LTE is equal to  $T_{\text{ex}}$  and  $T_{\text{kin}}$  ( $T_{\text{rot}} = T_{\text{ex}} = T_{\text{kin}}$ ).

For the column density calculation, it is important to note that the background continuum at 5 GHz contributed by sources A, B, C, D, and E is only 75 mJy to 80 mJy which is only  $\sim 25\%$  to  $30\%$  of the total flux density obtained in Sect. 4.5.1, and perhaps even less because the frequency of the methanol line is a little higher than 5 GHz.

The line opacities listed in Table 4.2 can be used to derive approximate values of the  $\text{CH}_3\text{OH}$  column density. For the  $5_1 \rightarrow 6_0$   $A^{+1}$  transition of  $\text{CH}_3\text{OH}$ , the Einstein coefficient,  $A$ , is  $0.1532 \times 10^{-8} \text{ s}^{-1}$ . If we assume LTE and that the absorption line shape is Gaussian with full width at half intensity of  $\delta v$  in  $\text{km s}^{-1}$ , the column density,  $N_{6,0}$ , in  $\text{cm}^{-2}$ , of the lower energy level can be calculated from

$$N_{6,0} = 1.73 \times 10^{14} \text{ cm}^{-2} (\text{km s}^{-1})^{-1} [1 - \exp(-h\nu/kT_{\text{ex}})]^{-1} \int \tau \delta v \quad (4.1)$$

where  $T_{\text{ex}}$  is the excitation temperature associated with the transition. This excitation temperature is uncertain, and a value of 43 K has been adopted on a single blackbody fit to the far-infrared (FIR) flux densities at  $12 \mu\text{m}$  to  $100 \mu\text{m}$  (Hagiwara et al. 2004). The resulting column density is given in Table 4.2. Were a value of 20 K adopted for the excitation temperature, the column densities would double. Due to the compactness of the methanol clouds and the low covering factor across the continuum source, the column densities derived for the transition represent a lower limit. These results are, however, consistent with methanol abundances found towards the Galactic centre associated with Sgr B2 with velocities near  $65 \text{ km s}^{-1}$  and  $80 \text{ km s}^{-1}$  and column densities as high as  $7.5 \times 10^{18} \text{ cm}^{-2}$  at 6.7 GHz, and  $4.2 \text{ km s}^{-1}$  and a column density of  $3.0 \times 10^{15} \text{ cm}^{-2}$  (Houghton & Whiteoak 1995; Peng & Whiteoak 1992).

It is, however, debatable whether LTE conditions are a good approximation in the case of methanol absorption at 6.7 GHz. According to the calculations of Leurini (2004),

the 6.7 GHz and 12 GHz transitions are over-cooled over a very wide range of physical conditions that includes all plausible ranges for the ISM in NGC 3079 that are absorbed by the methanol line (see Fig. 4.1).

### 4.5.2 Mrk 3

Mrk 3, an early-type (elliptical) galaxy at a distance of 57 Mpc, is one of the few Seyfert 2 galaxies that show broad emission lines in polarized light, suggesting the presence of a hidden Seyfert 1 nucleus (e.g., Miller & Goodrich 1990; Tran 1995). GINGA data have shown that the X-ray spectrum of Mrk 3 is heavily absorbed with a corresponding HI column density of  $N_{\text{HI}} = 3 \times 10^{23} \text{ cm}^{-2}$  and a strong and broad Fe K $\alpha$  line (Iwasawa et al. 1994). Further analysis of its X-ray spectrum revealed the presence of an absorber of  $1.1 \times 10^{24} \text{ cm}^{-2}$ , which makes the source a ‘Compton-thick’ candidate (Matt et al. 2000). Mrk 3 is considered a border-line object, where the torus opacity is high but not high enough to totally hide the nucleus. In the radio, MERLIN observations at 5 GHz revealed a highly collimated S-shaped radio structure with a bright radio hot spot at its western end (Kukula et al. 1993). This S-shaped distribution of the radio emission has been attributed to either a change in the ejection axis of the jets with time or to the interaction of the jets with a rotating interstellar medium.

A water maser of  $11 L_{\odot}$  has been detected in this source at a velocity of  $(4009 \pm 6) \text{ km s}^{-1}$  (Braatz et al. 2004). However, despite the evidence from X-ray data for large obscuration in front of the nucleus, very little is known of the molecular content in this galaxy. CO ( $J = 1 - 2$ ) was not detected (Vila-Vilaró et al. 1998) and even more surprisingly no 21 cm absorption was detected toward the central radio sources (Gallimore et al. 1999). Noordermeer et al. (2005) carried out an HI survey with Westerbork and pointed out that the gas distribution in Mrk 3 is irregular and seems to be connected to the gas disk of UGC 3422,  $\approx 100$  kpc to the north-west. The authors find a low projected surface density of the gas, with a maximum of only about  $0.3 M_{\odot} \text{ pc}^2$ . It appears as if the gas in Mrk 3 has been tidally drawn out of the gas disk of UGC 3422.

These results are quite surprising since the high column density found towards the source nuclear region and the relatively high source flux density in the radio regime ( $S_{5 \text{ GHz}} = 0.352 \text{ Jy} \pm 0.004 \text{ Jy}$ ; A. Roy, priv. comm.) make it a very good candidate for absorption experiments. In the search for methanol absorption, Mrk 3 was originally observed with the Effelsberg at 6.7 GHz on May 25, 2006 for 232 minutes and on June 11, 2006 for 57 minutes. The measured flux density of the source was of  $387 \text{ mJy} \pm 57 \text{ mJy}$  at the observing frequency, which is consistent with previous measurements. The resulting spectra showed a weak emission feature at the systemic velocity of the galaxy. Though weak, this feature was observed in both observing sessions, so the source was re-observed on July 14, 2007 for 408 minutes and on September 14, 2007 for 188 minutes. The July 2007 spectrum is shown in Fig. 4.3, where the arrow denotes the optical systemic velocity of Mrk 3. The resulting rms in the spectrum of Fig. 4.3 is  $1.2 \text{ mJy/channel}$  (for a channel spacing of  $4.4 \text{ km s}^{-1}$ ). The tentative line has a fitted peak of  $2.7 \text{ mJy}$ , a width of  $(45 \pm 15) \text{ km s}^{-1}$  and a velocity of  $(4012 \pm 12) \text{ km s}^{-1}$ . For comparison, the optical systemic velocity,  $V_{\text{sys}}$ , is  $4050 \text{ km s}^{-1}$  (Falco et al. 1999a). The line from the July 2007 observations might be slightly offset from the fitted position of the line from the May 2006 observations at  $(4039 \pm 14) \text{ km s}^{-1}$ , however these values are formally consistent within the errors.

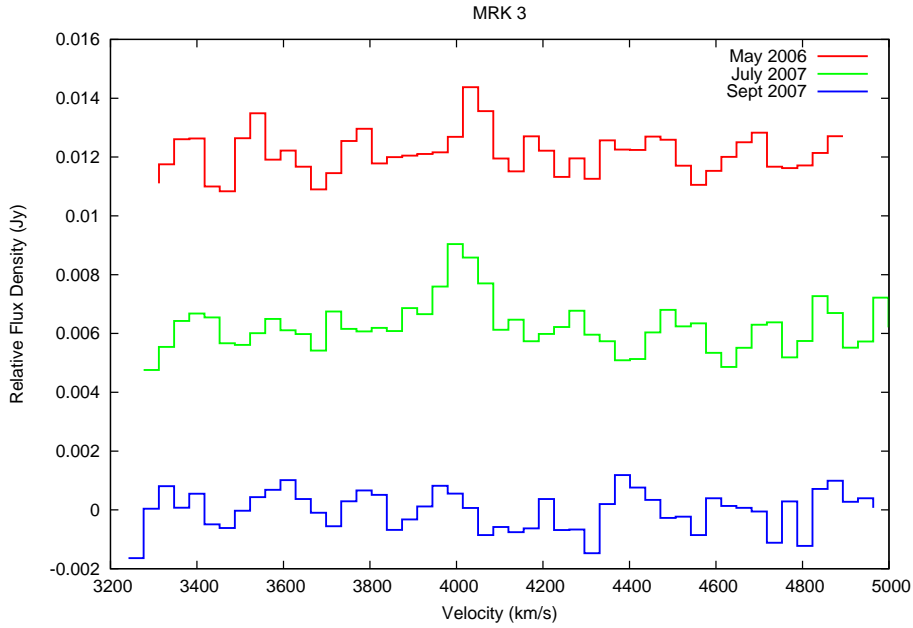


Figure 4.6: 6.7 GHz continuum-subtracted Effelsberg spectra of Mrk 3 at three epochs with a vertical offset added for clarity of presentation. The spectra have been smoothed to the same resolution of  $\sim 35 \text{ km s}^{-1}/\text{channel}$ . The top spectrum shows the July 2007 data, with an rms of 0.7 mJy, the middle spectrum shows the May 2006 data, with an rms of 0.8 mJy, and the bottom spectrum shows the September 2007 data with an rms of 1.7 mJy. The line is visible in the top two spectra with a fitted peak flux density of 2.5 mJy (May 2006) and 3 mJy (July 2007). A slight shift in the velocity of the line between those epochs is within the uncertainties. No line was seen in the September 2007 observations.

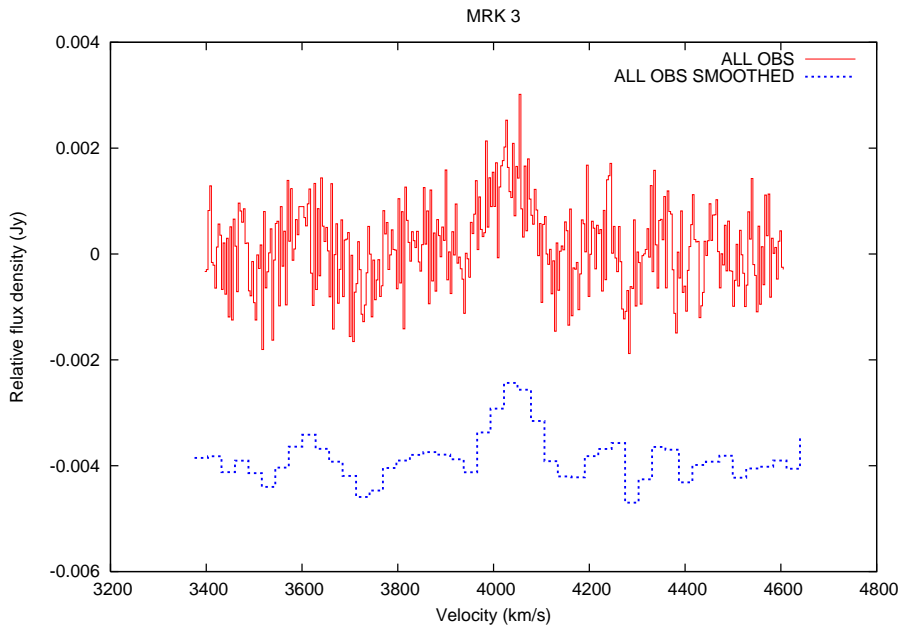


Figure 4.7: 6.7 GHz spectrum of Mrk 3 showing the spectrum resulting from the sum of all the observing epochs. The top spectrum has a resolution of  $\sim 3.5 \text{ km s}^{-1}/\text{channel}$ , with an rms of 1.6 mJy (the spectrum has a higher rms due to a noisier spectrum in June 2006 and September 2007). The fitted peak flux density in the top spectrum is 3.6 mJy. The bottom spectrum corresponds to the spectrum above, smoothed to a resolution of  $35 \text{ km s}^{-1}$ . The rms in the bottom spectrum is 0.6 mJy, the peak flux density is of 3.4 mJy.

Fig. 4.6 shows the spectra from different epochs at a resolution of  $35 \text{ km s}^{-1}/\text{channel}$ . The June 2006 observations are not shown due to the low data quality and higher rms (2 mJy) compared with the other epochs. A weak emission component is seen in the July 2007 and May 2006 observations. The fitted line parameters are consistent with each other, with a fitted line peak of 3 mJy in July 2007 and 2.6 mJy in May 2006, agreeing within the uncertainties. No emission feature is seen in the September 2007 observations above a  $3\sigma$  limit at 2.1 mJy (Fig.4.6, bottom spectrum). This could indicate variability in the line emission. Fig. 4.7 shows the sum of all the four observing epochs together. The top panel shows the result of the sum at a resolution of  $3.5 \text{ km s}^{-1}$ . The line is clearly visible at the expected velocity with a fitted peak of 3.5 mJy (rms 1.6 mJy). The width of the line is slightly larger ( $85 \text{ km s}^{-1} \pm 13 \text{ km s}^{-1}$ ) than in the epochs separately before averaging. This is probably due to the small but insignificant velocity differences in the different epochs. The bottom panel shows the spectrum smoothed to a spectral resolution of  $35 \text{ km s}^{-1}$ , reaching an rms of 0.6 mJy and a fitted line peak of 3.4 mJy.

Although the line has a formal significance of  $5.5\sigma$  in the final spectrum, the emission is intrinsically weak in all of the observing epochs, and a clear emission component is not always seen and so some caution is still warranted. If real, this would be the first detection of a type II methanol maser in an extragalactic source. The velocity of the line, close to the systemic velocity of the galaxy, indeed shows that it is coincident with the stellar systemic velocity of the galaxy, similar to the 6.7 GHz methanol masers observed in the Galaxy, which are typically associated with regions of star formation (see Sect. 4.1).

The corresponding line luminosity, assuming isotropic emission, is given by

$$L = 4\pi D_L^2 \int S d\nu, \quad (4.2)$$

where  $D_L$  is the distance to the galaxy ( $D_L = 57.4 \text{ Mpc}$  for  $H_0 = 71 \text{ km/s/Mpc}$ ,  $\Omega_\Lambda = 0.270$ , and  $\Omega_L = 0.73$ ),  $S$  is the observed peak flux density over a frequency range,  $d\nu$ , given by the width of the line. In the optical velocity definition,

$$\frac{\Delta\nu}{\nu_{\text{obs}}} = \frac{\Delta v}{c} \quad (4.3)$$

and the observing frequency is related to the rest frequency by,

$$\nu_{\text{obs}} = \frac{\nu_{\text{rest}}}{1+z} \quad (4.4)$$

so we have that the luminosity is,

$$L = \frac{4\pi\nu_{\text{rest}}}{c} \frac{D_L^2}{1+z} \int S dv. \quad (4.5)$$

Using the result for the line observed in July 2007, the peak flux density is 2.7 mJy and the fitted width is  $45 \text{ km s}^{-1}$ , yields a luminosity of  $2.7 L_\odot$ .

Detections of extragalactic methanol masers are limited to the Large Magellanic Cloud

(Sinclair et al. 1992; Ellingsen et al. 1994a; Beasley et al. 1996), which have isotropic integrated line luminosities similar to those observed for Galactic methanol masers, namely  $10^{-5} L_{\odot}$  to  $10^{-6} L_{\odot}$ , and so the emission component in Mrk 3 is much more luminous than any known masers at this frequency.

### 4.5.3 Mrk 348

Mrk 348 is a face-on spiral galaxy at a distance of 63 Mpc (de Vaucouleurs et al. 1991). It is classified as a Seyfert 2 (Koski 1978), with broad emission lines in (reflected) polarized light, showing the presence of a hidden Seyfert 1 nucleus (Miller & Goodrich 1990). Additional evidence for the presence of a dusty torus has been offered by Simpson et al. (1996), who used ground-based observations of optical emission-line and near-infrared continuum images and find a dust lane crossing the nucleus and an ionization cone. An elongated, red feature aligned perpendicular to this axis appears to be dominated by thermal emission from hot dust (1750 K) which seems to be related to the torus approximately edge-on which obscures the nucleus from direct view. The estimated X-ray column density is  $\sim 10^{23} \text{ cm}^{-2}$  (Mulchaey et al. 1992).

Mrk 348 has a relatively strong and variable radio flux density (Neff & de Bruyn 1983). VLBA images (Ulvestad et al. 1999) revealed a small-scale double continuum source, the axis of which is aligned with the optical emission (Capetti et al. 1996). Also, H I observations at 21 cm (Neff & de Bruyn 1983) revealed a bright subarcsecond triple structure with a total linear extent of 180 pc and it is not clear which one is the core. Unger et al. (1984) suggested that components 1 and 3 might constitute ejected material from the core which is expanding into the ambient gas. Lower resolution images show a faint halo extending out to 17 kpc which contributes only a few percent of the total radio flux (Baum et al. 1993). On the other hand, an enormous envelope of H I gas (175 kpc) surrounds Mrk 348 (Heckman et al. 1982). The origin of this material is unclear, it may be the result of a tidal debris from an encounter with its close neighbour NGC 266 (Heckman et al. 1982; Simkin et al. 1987; Simpson et al. 1996).

Attempts to detect the expected obscuring torus at radio wavelengths in H I (Gallimore et al. 1999) CO (Taniguchi et al. 1990) and free-free absorption (Barvainis & Lonsdale 1998) have not been successful. However, Halkides, Ulvestad, & Roy (1997) report evidence for free-free absorption below 5 GHz, but it is unclear which components of the radio triple might be absorbed. The lack of H I absorption from the medium obscuring the BLR might also be ascribed to free-free suppression of the nuclear radio continuum source at 21 cm wavelength.

Finally, a water maser has been detected towards the nuclear region of Mrk 348. The H<sub>2</sub>O line is redshifted by  $\sim 130 \text{ km s}^{-1}$  with respect to the systemic velocity, and it is extremely broad, with a FWHM of  $130 \text{ km s}^{-1}$ , with no detectable high-velocity components within  $1500 \text{ km s}^{-1}$  on either side of the line (Peck et al. 2001). VLBA observations have shown that the maser is located toward the base of the radio jet, emanating from a region  $>0.25 \text{ pc}$  in extent.

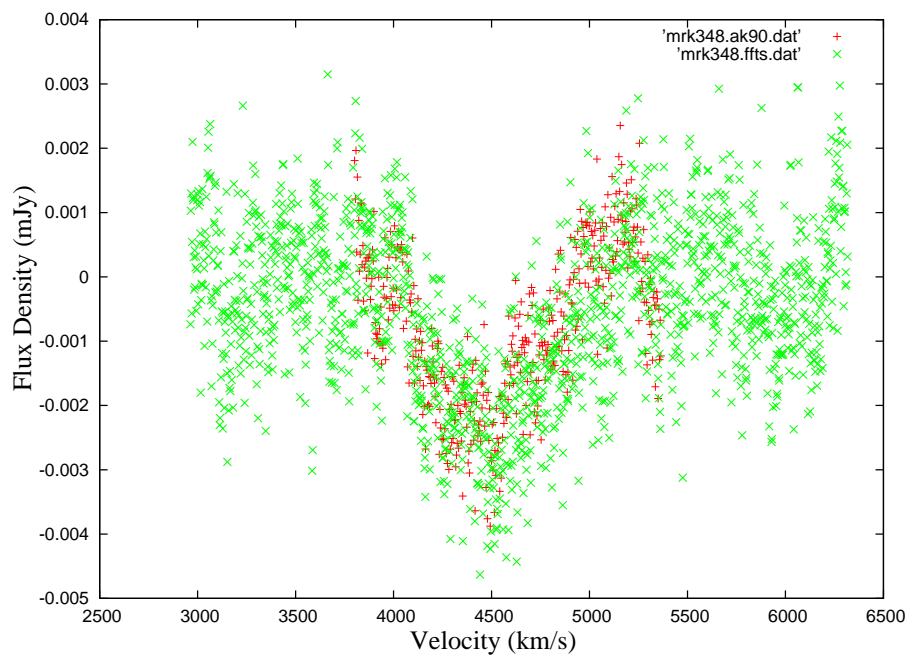


Figure 4.8: 6.7 GHz Effelsberg spectra of Mrk 348 observed on the July 14, 2007. The plot shows a comparison between the spectrum obtained with the AK90 autocorrelator (red points) and the Fast Fourier Transform digital Spectrometer (FFTS; green points). The FFTS yields a higher spectral resolution and bandwidth compared to the AK90. The FFTS shows that the spectrum remains flat beyond the edges of the AK90 band. Third-order polynomials were fitted and subtracted from both of the spectra plotted above.

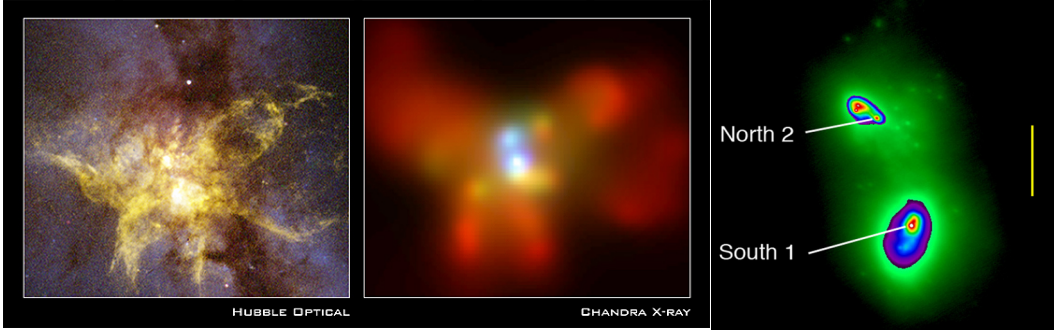


Figure 4.9: *Left:* Hubble optical image of NGC 6240 showing distorted tidal tails of stars, gas, and dust are visible from the image (credit: R.P. van der Marel & J.Gerssen (STScI)). *Middle:* Chandra image of the central region of NGC 6240 shows the butterfly-shaped galaxy as a product of the collision of two smaller galaxies, containing two active black holes, shown in the image in false-colour (shaded blue) (credit: NASA/CXC/MPE/S. Komossa & G. Hasinger (MPE)). *Right:* adaptive optics image taken in infrared light with the Keck II telescope showing the double nucleus of NGC 6240. “North 2” labels the the position of the northern supermassive black hole within the north nucleus. The southern supermassive black hole is located in the south nucleus and labelled by “South 1”. The yellow vertical line represents 1 arcsecond, or 490 parsecs (credit: C. Max, G. Canalizo, and W. de Vries).

The source was observed with Effelsberg at 6.7 GHz with the AK90 spectrometer on the July 14, 2007 for 288 minutes. The sub-spectra were averaged and a second-order polynomial was fitted to the baseline and subtracted. The resulting spectrum is shown in Fig. 4.3, with a spectral resolution of  $4.4 \text{ km s}^{-1}$  and an rms of  $1.7 \text{ mJy}$ . A broad absorption line is visible in the spectrum at the systemic velocity,  $V_{\text{systemic}}$ , of the galaxy ( $4505 \text{ km s}^{-1}$ ) marked by the arrow. This broad line has a fitted peak velocity of  $(4498 \pm 12) \text{ km s}^{-1}$  and a FWHM of  $(555 \pm 26) \text{ km s}^{-1}$ . The fitted peak flux density is  $-4.8 \text{ mJy}$ . In Fig. 4.8, the spectrum produced with the digital Fourier-transform spectrometer (FFTS, green points) is shown for comparison with the spectrum simultaneously produced by the AK90 spectrometer (red points). The two spectra are comparable and show the same width. The FFTS can process larger bandwidths than the AK90 and shows the baseline on either side of this feature being flat. Though this feature is formally significant when the spectrum is smoothed, it is extremely broad and could conceivably be caused by residual ripples across the baseline. The measured flux density of Mrk 348 is  $475 \text{ mJy}$  and the spectral dynamic range of Effelsberg with the 5 cm receiver is 0.5 % (see for an example Fig.4.2), so one expects standing wave ripple of  $\sim 2.5 \text{ mJy}$  peak-to-peak. It is also worth noticing that broad lines have been observed in this source in other molecules, in particular the  $\text{H}_2\text{O}$  spectral emission feature seen towards the jet foot-point is  $130 \text{ km s}^{-1}$  wide (Peck et al. 2001), which is significantly larger than typical water masers of a few  $\text{km s}^{-1}$  (Lo 2005). Future interferometric observations, where instabilities in the baseline are less severe, are necessary to confirm if the line is real and to match it spatially with the source.

#### 4.5.4 NGC 6240

NGC 6240 is a nearby (97 Mpc; Vaucouleurs et al. 1991) ultra-luminous infrared galaxy (ULIRG). Early  $\text{H}\alpha$  studies revealed extended emission with two independent and almost perpendicular disk systems (Bland-Hawthorn et al. 1991). In fact, the galaxy is the result of a merging pair of smaller galaxies (Fosbury & Wall 1979; Fried & Schulz 1983) which resulted in a single larger galaxy with two distinct nuclei and a perturbed structure

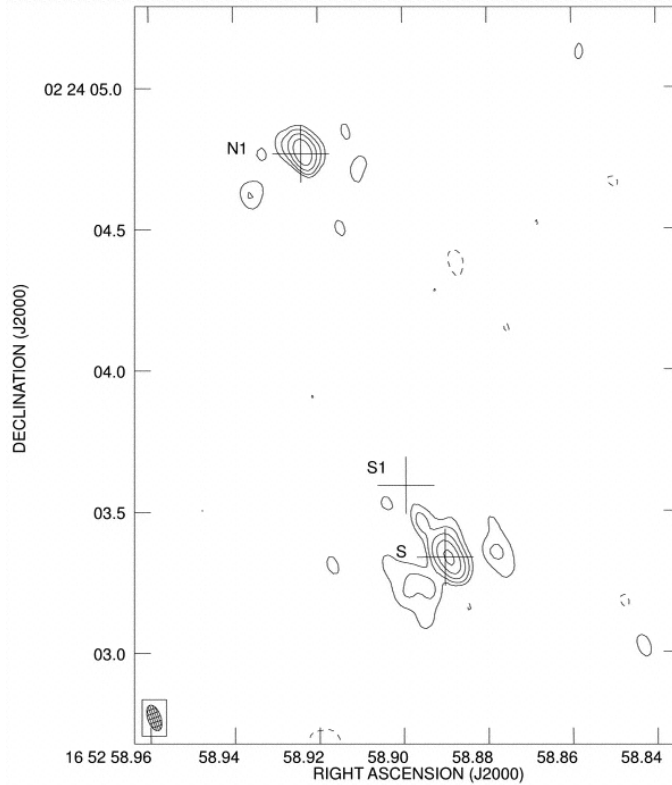


Figure 4.10: Radio continuum map of NGC 6240 at 5 GHz (MERLIN; Gallimore & Beswick 2004). The image shows the two distinct radio nuclei (S and N) in the source.

(see Fig. 4.9) and it is unclear where the dynamical centre lies. Large velocity widths have been reported in this source resulting from the rotation in each of the galaxies, the orbital velocity component of the two galaxies, and the inflow and outflow due to the interaction. The radial velocity difference between the nuclei is  $150 \text{ km s}^{-1}$  in  $\text{H}_2$  and  $100 \text{ km s}^{-1}$  in  $\text{CO} (J = 2 - 1)$  (Tecza et al. 2000). Due to the violent merger, NGC 6240 has a large infrared luminosity,  $L_{\text{FIR}} \sim 10^{11} L_{\odot}$  (Wright, Joseph, & Meikle 1984; Sanders et al. 2003). The merger stage is still ongoing (e.g. Tacconi et al. 1999) and evidence for nuclear activity in both of the parent nuclei comes from the X-ray (Komossa et al. 2003) and radio (Beswick et al. 2001) observations. A 6.4 keV Fe  $K\alpha$  emission line in the galaxy has been detected, showing the presence of an AGN though its position is uncertain (Iwasawa & Comastri 1998; Ikebe et al. 2000) and the X-ray spectrum shows absorption by an equivalent hydrogen column density of  $2 \times 10^{24} \text{ cm}^{-2}$ . High-resolution MERLIN maps at 5 GHz showed two compact radio sources (double nuclei) in the nuclear region separated by  $1.5''$  (Beswick et al. 2001, Fig. 4.10). The radio spectral properties of the two radio nuclei (N and S) are not significantly different from each other (Colbert et al. 1994), suggesting that both nuclei could house an AGN. The radio continuum flux in the galaxy is dominated by a starburst component, and only a small portion arises from the low-luminosity AGN.

The large width of the H I absorption line across the central part of the source confirms the violent dynamics of the system. Beswick et al. (2001) found H I absorption components towards both nuclei, towards the south component blueshifted by  $\sim 50 \text{ km s}^{-1}$  relative

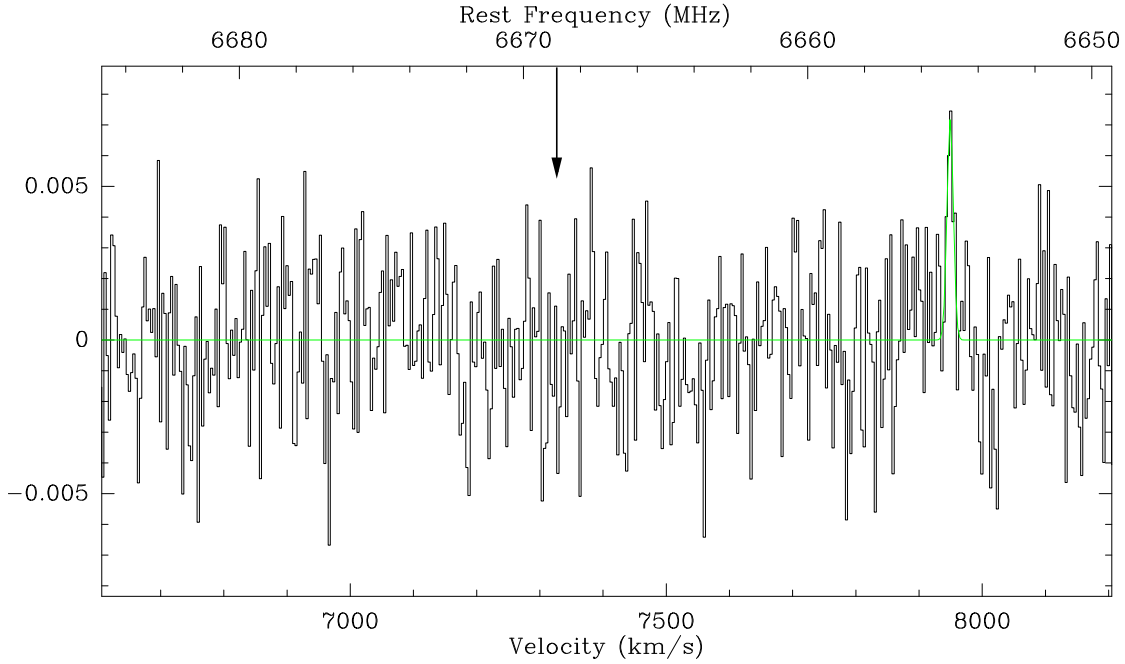


Figure 4.11: Effelsberg spectrum of NGC 6240 at 6.7 GHz, repeated from Fig. 6.3.

to the systemic velocity, and redshifted by about  $130 \text{ km s}^{-1}$  to the systemic velocity towards the north component. These correspond to  $7258 \text{ km s}^{-1}$  and  $7440 \text{ km s}^{-1}$  in the optical heliocentric definition, and can be adopted as a more accurate approximation of the systemic velocities of the two nuclei. A significant amount of CO molecular gas has been found between the IR/radio double nuclei (Tacconi et al. 1999; Bryant et al. 1999), showing that the gas has not yet settled into a central thin disk. The velocities of CO emission ( $J = 1-0, 2-1$ ) span a velocity width of  $\pm 500 \text{ km s}^{-1}$  centered on the systemic velocity. The HI and OH velocity gradients for the central region are much smaller than that of the CO(2-1), which may suggest that the different observations detect distinctly different scale sizes within these structures. Also, VLA observations revealed HI and 1.67 GHz OH absorption, which agree with those of  $\text{H}_2$ , CO, and  $\text{H}\alpha$  (Baan et al. 2007). Water masers have also been detected towards the source (Hagiwara et al. 2002) with apparent maser luminosity of about  $40 L_{\odot}$ , well above that of the typical starforming masers and so is likely to arise from the AGN activity. It is, however, not clear if the AGN is responsible for the large infrared luminosity, as the location of the predicted active nucleus in the double nuclei system is still uncertain.

The richness in molecular species known in this source, including the presence of OH at both 1.67 GHz (Baan et al. 2007) and 6 GHz (this work, see Chapter 2) provide the motivation to search for methanol. Effelsberg observations at 6.7 GHz were carried out on of May 25, 2006 for a total of 57 minutes, reaching an rms of 2.3 mJy for a channel spacing of  $3.5 \text{ km s}^{-1}$ . The total flux density of the source was measured to be 183 mJy. The resulting spectral baseline was flat, and the run was easy to calibrate. The resulting spectrum, shown in Fig. 4.3 (bottom right) shows no prominent features near the expected velocity of the line ( $7340 \text{ km s}^{-1}$ ), above a  $3\sigma$  limit of 7 mJy assuming a line width equal to the channel width of  $3.5 \text{ km s}^{-1}$ , however a weak emission feature can be seen at the redshifted velocity

of  $(7949 \pm 1.4) \text{ km s}^{-1}$ . The spectrum is shown again enlarged in Fig. 4.11 for clarity. The candidate line is redshifted from the systemic velocity of NGC 6240 by  $610 \text{ km s}^{-1}$ . The fitted peak of the feature is  $7.2 \text{ mJy}$  with a FWHM of  $(12 \pm 3) \text{ km s}^{-1}$ , yielding a  $5.8\sigma$  detection, and thus is formally significant. The redshift is large, but Hagiwara et al. (2003) report two water masers towards the southern component redshifted by  $\sim 500 \text{ km s}^{-1}$  relative to the systemic velocity and, thus, such greatly redshifted molecular gas is already known to be present in this system. In addition, absorption is seen over a velocity range of more than  $500 \text{ km s}^{-1}$ , and so the high-velocity methanol component might be real and might be tracing an infalling component towards a perturbed nucleus. Future observations in this source should be carried out to confirm this tentative detection.

## 4.6 Results and individual sources: The non-detections

### 4.6.1 Cygnus A (3C 405)

Cygnus A, at a distance of  $224 \text{ Mpc}$  (Owen et al. 1997) is a prototypical FR II radio galaxy. Hosted by an elliptical galaxy with complex optical structure, radio observations of the source show prominent and finely-structured jets ranging from kpc to sub-parsec scales. Despite its large distance from us, it is still by far the closest powerful radio galaxy and one of the brightest radio sources in the sky. Cygnus A has famous double radio lobes fed by elongated radio jets of energetic particles beamed from the compact radio core between them. The giant lobes are formed when these jets are slowed down by the tenuous gas in the intergalactic medium, forming high surface brightness hotspots at the extremities of the radio source. The region in between the radio hotspots is filled with extended, low surface brightness, often filamentary emission, known as radio lobes.

As described in Chapter 3, Cygnus A is an excellent candidate for studying the composition of the putative torus around the nucleus, and, in particular, for searches for molecular species. However, the strength of its radio lobes makes it very hard to carry out single-dish spectroscopic studies in this source since one needs exceptionally high spectral dynamic range (300000:1) to detect weak lines in the presence of such strong continuum. The beam of the Effelsberg telescope at  $6.7 \text{ GHz}$  is  $134''$  which is similar to the angular extent of Cygnus A. Therefore, the contribution of the radio lobes dominates that of the nucleus when measured with Effelsberg. Nevertheless, Cygnus A was observed briefly with the Effelsberg telescope at  $6.7 \text{ GHz}$  with the AK90 spectrometer on May 25, 2006 for 14 minutes. The continuum results in standing waves seen in Figure 4.2 that limit the spectral dynamic range to 200:1. A high-order polynomial was fitted and subtracted from this spectrum to see if any prominent features were visible at the expected line frequency. The resulting spectrum is shown in Fig. 4.3. No methanol emission or absorption was detected above a  $3\sigma$  upper limit of  $8 \text{ mJy}$ , assuming a line width equal to a channel width of  $3.5 \text{ km s}^{-1}$ . To observe the core of this source one needs high resolution interferometric observations to resolve out the lobe emission, leaving only the core emission (see Chapter 3).

### 4.6.2 Mrk 231

Mrk 231, at a distance of 172 Mpc (de Vaucouleurs et al. 1991), is the most luminous infrared galaxy in the local Universe (Sanders et al. 2003). The nuclear source shows a Seyfert 1 type spectrum (Baan et al. 1998), even though the nucleus is heavily obscured. The galaxy is undergoing a merger as indicated by the large CO concentration in the central few kpc (Scoville et al. 1989) and tidal tails observed in the optical (e.g. Canalizo & Stockton 2000 and references therein). The unification scheme would suggest that the observer has a direct, unobscured view into the broad-line emission region at parsecs scale. However, Ulvestad et al. (1999) find an average ionized gas density of  $n_e > 10^5 \text{ cm}^{-3}$  at 0.5 pc from the nucleus estimated by assuming that the jet/counterjet ratio is intrinsically unity and that the observed jet/counterjet brightness asymmetry due to free-free absorption in front of the counterjet. The column density necessary to produce the absorption is about  $10^{23} \text{ cm}^{-2}$ , which is consistent with that measured from X-ray absorption.

The radio structure of Mrk 231 is quite complex on a variety of scales. It consists of both a compact, high surface-brightness feature and regions of more diffuse emission extending to 2.4 kpc to the south (Hutchings & Neff 1987; Carilli et al. 1998). VLBA observations have resolved the source into a core-lobe structure (Ulvestad et al. 1999; Carilli et al. 1998) with a bright central component and southern lobe separated by 30 mas (20 pc), and a weaker lobe 20 mas (14 pc) to the north. At higher frequencies, the core region has been resolved into a 2 mas (1.5 pc) triple source that is misaligned with the the extended emission (Ulvestad et al. 1998) and with a self-absorbed central component. Also, both the northern lobe and the southern component are free-free absorbed at the lowest frequencies. A kiloparsec-scale CO(1-0) structure (Bryant & Scoville 1996; Downes & Solomon 1998) and a more compact CO(2-1) distribution (Downes & Solomon 1998) extending up to 850 pc have been detected in the Mrk 231. The diffuse radio structure has been interpreted as synchrotron emission from the inner part of the molecular gas disk detected in CO. HI absorption has been observed with the VLA against a central radio halo or disk of continuum emission 440 mas (350 pc) across (Dickey 1982), which is similar to the CO emission. Also, OH megamaser emission at 1.67 GHz (Klöckner et al. 2003) has been detected towards the nuclear region, with velocity fields that are in agreement with those of HI absorption (Carilli et al. 1998). The integrated HI velocity dispersion ( $193 \text{ km s}^{-1} \pm 25 \text{ km s}^{-1}$ ) has been found to agree with the velocity dispersion of the OH lines, leading to the conclusion that the OH emission also originates in the central regions of a circumnuclear rotating disk or torus, where the outer structure is traced by the CO emission (Klöckner et al. 2003). No H<sub>2</sub>O megamaser emission has been detected (Braatz et al. 1996).

Mrk 231 has a variety of molecules towards the core region, including OH absorption in the excited state at 6 GHz (see Chapter 2). It was therefore included for follow-up observations at 6.7 GHz. The source was observed with Effelsberg using the AK90 spectrometer on the of July 14, 2007 for 113 minutes and was re-observed on November 12, 2007 for 152 minutes. The final spectrum, after a second-order baseline was subtracted and the amplitude scale was calibrated, is shown in Figure 4.3. The rms was 1.3 mJy and the channel spacing  $4.4 \text{ km s}^{-1}$ . The final spectrum shows no emission or absorption features of methanol down to a  $3\sigma$  limit of 3.9 mJy, assuming a line width equal to the

channel width of  $4 \text{ km s}^{-1}$ .

### 4.6.3 NGC 1052

NGC 1052 is a nearby elliptical galaxy (19.4 Mpc; Tonry et al. 2001), with two-sided radio jets and a heavily obscured core region. Evidence for obscuration in this source has been described in some detail in Chapter 2. Here, I report on the search for methanol towards the core of NGC 1052.

The source was observed with Effelsberg on March 16, 2006, for 62 minutes. The final spectrum is shown in Figure 4.3. The measured flux density was 1.9 Jy, which was high enough to excite a noticeable standing-wave ripple in the baseline, which could not easily be removed using a low-order polynomial. Since the ripples are still clearly visible in the final spectrum, no prominent emission or absorption can be seen at the expected velocity of the line, down to a  $3\sigma$  upper limit of 10 mJy assuming a line width equivalent to a channel width of  $3.5 \text{ km s}^{-1}$ . As in the case of Cygnus A, to search for absorption in the cores of these sources with greater sensitivity requires interferometric observations at higher resolution (like that done for OH absorption; see Chapter 3).

### 4.6.4 NGC 2110

NGC 2110, an elliptical galaxy at a distance of 33 Mpc, is classified as a type 2 Seyfert galaxy based on its nuclear optical spectrum, which is dominated by narrow emission lines (McClintock et al. 1979). Optically, NGC 2110 is classified as a S0 galaxy, although broad-band *HST* observations have shown the presence of spiral-like dust lanes with a distribution consistent with a single-armed spiral. The presence of a hidden type 1 nucleus is implied by X-ray observations, which indicate heavy absorption of the soft X-ray spectrum and a derived H I column density of  $2.8 \times 10^{22} \text{ cm}^{-2}$  (Turner et al. 1997). Despite a number of searches for broad emission lines in both the optical (Shuder 1980; Veilleux 1991) and near-infrared (Veilleux et al. 1997; Storchi-Bergmann et al. 1999; Knop et al. 2001; Lutz et al. 2002), there has been no conclusive evidence that NGC 2110 harbours a hidden broad-line region. Only recently, Moran et al. (2008) have reported the discovery of a broad, double-peaked H $\alpha$  emission line in the polarized flux spectrum of this object, concluding that NGC 2110 contains a disk-like hidden BLR.

The VLA radio continuum maps show a symmetrical jet-counterjet radio emission that extends  $\sim 4''$  ( $\sim 600 \text{ pc}$ ) along the north-south direction (Ulvestad & Wilson 1983; Nagar et al. 1999). VLBA observations at 8.4 GHz also show a compact ( $\ll 1 \text{ pc}$ ) radio core aligned with the 400 pc scale radio jet (Mundell et al. 2000). H I spectral-line mapping (Gallimore et al. 1999) indicates the presence of a small-scale disk that may partially obscure the southern radio jet. This absorption is redshifted by about  $290 \text{ km s}^{-1}$  with respect to the systemic velocity,  $2335 \text{ km s}^{-1}$ , calculated by Strauss et al. (1992) using the nuclear optical emission lines.

Spectral observations of NGC 2110 at 6.7 GHz were carried out with Effelsberg on March 16, 2006 for 11 minutes. The resulting spectrum is shown in Fig. 4.3. No line detection was made in this source, with a  $3\sigma$  upper limit of 25 mJy for a line width equal to the channel

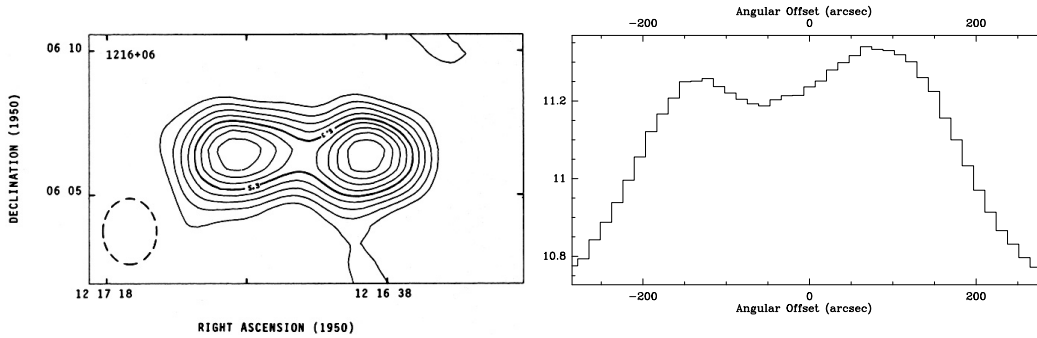


Figure 4.12: Azimuthal pointing with the Effelsberg telescope on NGC 4261 reveals a two peaks  $\sim 250$  arcseconds apart resolved by the  $120''$  beam of Effelsberg (see right panel). This double-peaked structure is seen also in the continuum image of the source at 160 MHz in a  $114''$  beam (left panel; Slee 1977). This feature is due to the bright lobes in the source.

width of  $1.8 \text{ km s}^{-1}$  (rms is  $8.4 \text{ mJy}$  with channel width  $1.8 \text{ km s}^{-1}$ ). The continuum flux density of NGC 2110 at this frequency was measured to be  $75 \text{ mJy}$ .

#### 4.6.5 NGC 4261 (3C 270)

NGC 4261 is a nearby (35.8 Mpc; Nolthenius 1993) elliptical galaxy associated with a low-luminosity FR I radio source. The nucleus of NGC 4261 is known for the impressive images of a 300 pc-scale nuclear disk of gas and dust taken with the Hubble Space Telescope (HST) around the central supermassive black-hole (Jaffe et al. 1996). Ferrarese et al. (2006) report that the disk is offset with respect to the nucleus by  $(4 \pm 2) \text{ pc}$ , interpreted as a consequence of a past merging event where the equilibrium position has not yet been reached.

In the radio band the source exhibits a compact core and nearly-symmetric kpc-scale jets extending east-west, oriented at  $63^\circ$  with respect to the line of sight (Piner, Jones, & Wehrle 2001). VLBI images of this galaxy at 1.6 GHz and 8 GHz (Jones & Wehrle 1997) detected a parsec-scale jet and counterjet aligned with the kiloparsec-scale jets with a gap in emission in the radio counterjet, at a projected distance of 0.1 pc, which is interpreted as absorption by a small dense inner accretion disk. Subsequent high-resolution VLBI imaging confirmed free-free absorption of the radio emission by a geometrically thin parsec-scale disk of ionized gas and allowed estimates to be made of the electron density and magnetic field of the accretion disk on subparsec scales (Jones et al. 2001). VLBI observations also revealed neutral hydrogen absorption towards the counter-jet at a projected distance of 2.5 pc from the core with an HI column density of  $2.5 \times 10^{21} \text{ cm}^{-2}$  (van Langevelde et al. 2000). Consistent with the expected torus invoked by unified models, CO(2-1) absorption has also been observed in this source (Jaffe & McNamara 1994).

In the hard-X-rays band, a point source is detected at the position of the radio core in a Chandra image; its continuum is described by thermal emission plus a hard power law plus moderate absorption by an equivalent hydrogen column density of  $6 \times 10^{22} \text{ cm}^{-2}$  (Chiaberge et al. 2003). Interestingly, an unresolved narrow (1 keV) Fe  $K\alpha$  line was marginally detected at 6.7 keV with ASCA (Terashima et al. 2002; Sambruna et al. 1999).

Amongst all the objects observed, NGC 4261 is unique in showing optical dust, HI and CO absorption and VLBI-scale free-free absorption. NGC 4261 is also a copious source of radio continuum emission, providing a unique opportunity to detect gas in absorption as well as in emission. For these reasons, the source was selected for observations at 6.7 GHz with Effelsberg on three observing sessions. It was observed on the 21<sup>st</sup> of February, 2006 for 60 minutes, on June 11, 2006 for 75 minutes, and on the November 12, 2007 for 113 minutes. The final spectrum of the source is shown in Figure 4.3, showing the June 2006 and the November 2007 observations combined. Adding the February 2006 data did not significantly improve the quality of the spectrum. Unfortunately, the flux density of NGC 4261, measured to be 1.35 Jy at 6.7 GHz, was high enough to produce significant ripples across the band. After removing a 5<sup>th</sup> order polynomial from the spectrum, residual ripples were still evident. The resulting rms noise was 1.9 mJy with a channel width of 3.5 km s<sup>-1</sup>. No significant features were seen above a 3  $\sigma$  limit of 5.7 mJy, assuming a line width equal to the channel width of 3.5 km s<sup>-1</sup>. The bright lobes caused standing wave ripples, which can be seen in the pointing scans taken during the observations and shown in Figure 4.12. On the right hand side is the azimuthal pointing scan showing a double structure, with peaks 250'' apart. Each peak corresponds to one of the bright radio lobes in the source, shown in the continuum map on the left hand side.

#### 4.6.6 NGC 5135

NGC 5135 is relatively nearby, at a distance of 59 Mpc, and is a barred spiral galaxy, optically classified as a Seyfert 2 on the basis of high-excitation lines with line ratios typical of a Seyfert 2 nucleus (Phillips et al. 1983). It contains a powerful starburst within 200 pc of the nucleus evident at ultraviolet energies (González-Delgado et al. 1998). In X-rays, characteristic unresolved non-thermal continuum emission powered by accretion onto the central black hole is seen (Turner et al. 1997), and also a dominant X-ray signature of a starburst is distinguished (Dahlem et al. 1998). Recently, Levenson et al. (2004) observed NGC 5135 with Chandra, finding absorption by an equivalent hydrogen column density of  $N_{\text{H}} > 10^{24}$  cm<sup>-2</sup>, giving indications that the source is obscured by Compton-thick material.

Radio continuum maps at arcsec resolution with the A and B arrays of the VLA at 4.9 GHz and 1.4 GHz show an asymmetric structure with faint emission extended to the northeast of the bright core source (Ulvestad & Wilson 1989). The overall linear extent is about 9'' (3.6 kpc). Radio images at 2.3 GHz also show considerable extended structure (Bransford et al. 1997). Despite the large radio flux density of the nucleus at lower resolutions (Ulvestad & Wilson 1989), no radio emission is observed at the nucleus at 8.4 GHz in the VLA A-configuration observations (Thean et al. 2000). Wynn-Williams & Becklin (1993) suggested that most of the radio emission emanates from structures on either side of the nucleus rather than from the nucleus itself.

NGC 5135 was observed with Effelsberg on March 16, 2006 for a total of 3 minutes. The short integration time was due to the source having a low declination (-29°). The spectrum is shown in Fig. 4.3. No spectral line was seen above a 3  $\sigma$  limit of 35 mJy assuming a line width equal to the channel width of 3.5 km s<sup>-1</sup>.

## 4.7 Conclusions

It was shown here that the 6.7 GHz methanol transition is detectable in an AGN, indicating significant methanol abundance. Ten type 2 AGN were observed at 6.7 GHz in the search for methanol absorption. Of the ten sources, six show non-detections. In one case, NGC 3079, there was a firm detection, and in three further cases (Mrk 3, Mrk 348 and NGC 6240) tentative detections were made.

The 6.7 GHz transition of methanol is one of the most common Galactic maser lines, and it was for the first time detected here in a source located well beyond the Magellanic Clouds. NGC 3079 has the appropriate excitation conditions to produce the 6.7 GHz transition in absorption. The spectrum shows two absorption components with opacities of 0.02 and 0.0067. This is the signature of a Class I environment, where the absence of a strong infrared radiation field inhibits the inversion of the level populations. Instead, the line is characterized by “anti-inversion” or “over-cooling”.

Most of the absorption, however, likely occurs toward the nuclear continuum sources A, B, and E. With no information on the density and kinetic temperature of the gas, the A-methanol column density is poorly constrained and may be  $\sim 1.4 \times 10^{15} \text{ cm}^{-2}$  assuming an excitation temperature,  $T_{\text{ex}}$ , of 43 K. This is comparable to column densities found towards the Galactic Centre associated with Sgr B2 of  $3.0 \times 10^{15} \text{ cm}^{-2}$  to  $7.5 \times 10^{18} \text{ cm}^{-2}$  (Houghton & Whiteoak 1995, Peng & Whiteoak 1992).

The detection of the  $5_1 \rightarrow 6_0 \text{ A}^+$  line of  $\text{CH}_3\text{OH}$  towards the nucleus of NGC 3079 fits into a scenario of molecular abundance around the nuclear region. It is, however, unclear if the methanol is associated with the active nucleus or the starburst around the source and possibly connected to the superbubble. The blue-shifted feature in the spectrum also indicates that methanol is present in the large-scale molecular outflows.

Tentative detections of methanol absorption were made towards three further sources. In Mrk 3 an emission line was observed near the systemic velocity of the galaxy. The line has a fitted peak flux density of 2.7 mJy ( $6\sigma$ ) and a FWHM  $45 \text{ km s}^{-1}$ . Although suggestive, the emission is intrinsically weak, and in one of the three epochs a clear emission component was not seen. If real, this would be the first detection of a type II methanol maser in an extragalactic source. Galactic 6.7 GHz methanol masers are typically associated with regions of star formation. At the distance of Mrk 3, the line would correspond to an isotropic luminosity of  $2.7 L_{\odot}$ . This is higher than typical methanol masers found in the Galaxy, with isotropic line luminosities of the order of  $10^{-6} L_{\odot}$  to  $10^{-5} L_{\odot}$  (Sinclair et al. 1992; Ellingsen et al. 1994b; Beasley et al. 1996).

In Mrk 348 a broad absorption feature was observed at the systemic velocity of the galaxy, with a fitted peak of  $-4.8 \text{ mJy}$  and a FWHM of  $\sim 550 \text{ km s}^{-1}$ . The profile is very broad and could be caused by standing waves across the band. However, broad lines have been observed in this source in other molecular species, such as  $\text{H}_2\text{O}$  with a width of  $130 \text{ km s}^{-1}$  seen towards the jet foot-point (Peck et al. 2001). Future interferometric observations with VLBI are necessary to confirm the methanol detection.

In NGC 6240, a tentative emission line was observed with a fitted peak of  $7.2 \text{ mJy}$  ( $3\sigma$ ), a FWHM of  $\sim 12 \text{ km s}^{-1}$ , and a velocity offset from systemic of  $610 \text{ km s}^{-1}$ , which is quite high. However, other large-scale high-velocity components with velocity ranges of more than  $900 \text{ km s}^{-1}$  have been seen already in this interacting galaxy. Future single-dish

observations should be carried out to confirm this tentative detection.

It was reconfirmed that single-dish spectral line work on strong continuum sources like Cygnus A and NGC 1052 are very difficult due to standing waves. For these strong sources interferometric observations would likely yield better results. Also, interferometric measurements will be needed to reliably convert “apparent” into “true” optical depths in those objects where methanol was detected. The presence of 6.7 GHz CH<sub>3</sub>OH absorption in NGC 3079 and Mrk 348 and in emission in Mrk 3 and NGC 6240, suggests that such gas can be found in other extragalactic sources. To reveal the physical parameters of the interstellar medium traced by the 6.7 GHz line, the detection of additional methanol lines would be desirable. Suitable candidates are the  $2_0 - 3_{-1}$  E (12.2 GHz),  $4_{-1} - 3_0$  E (36.2 GHz), and  $7_0 - 6_1$  A<sup>+</sup> (44.1 GHz) transitions.



## Chapter 5

# First detection of water vapour in the early Universe

### 5.1 Introduction

The presence of dense molecular clouds around the powerful central engines of active galaxies can result in extremely luminous shock-excited line emission, the most spectacular of which is seen in the  $6_{16}-5_{23}$  water vapour transition at 22.23508 GHz.

The origin of such emission differs from the widespread molecular emission commonly found in AGN in which the background radiation is highly amplified in the surrounding interstellar medium creating spectacular and extremely luminous maser lines due to maser action. Extragalactic masers are found in high-density molecular gas and can reach luminosities of up to  $\sim (10^2 \text{ to } 10^4) L_{\odot}$  (for a review see Lo 2005 and references therein). Such water “megamasers” or “gigamasers” are rare compared to molecular emission but when observed at large distances hold the promise to reveal the physical properties of galactic cores at early stages of evolution billions of years ago, to provide direct geometrical distances constraining cosmological models and to prove the existence of water in the early Universe (Greenhill et al. 2004; Morganti et al. 2004).

Luminous extragalactic water masers, with isotropic luminosities of  $L(\text{H}_2\text{O}) \gg 10 L_{\odot}$ , are known to be associated with the nuclear activity of their host galaxies. So far, VLBI studies have been carried out for  $\sim 10$  extragalactic water masers and all indicate that the maser emission originates from within a few parsecs of the central engine, being associated with i) nuclear accretion disks (e.g. Greenhill et al. 1995; Miyoshi et al. 1995; Ishihara et al. 2001), ii) interactions between the jet(s) emerging from the nucleus and ambient molecular clouds (e.g. Claussen et al. 1998; Peck et al. 2003), and iii) nuclear outflows (Greenhill et al. 2003). For example, Fig. 5.1 shows the different characteristic spectral signatures for a nearly edge-on disk and for a jet maser. Detailed studies of disk masers can trace the geometry of accretion disks, yield estimates of the enclosed masses, determine accurate distances to the parent galaxies with an entirely geometrical method (Herrnstein et al. 1999), and have the potential to constrain the equation of state of dark energy through an accurate measurement of the Hubble constant. Jet-masers can provide information on the evolution of jets and their hot-spots. Furthermore, simultaneous mea-

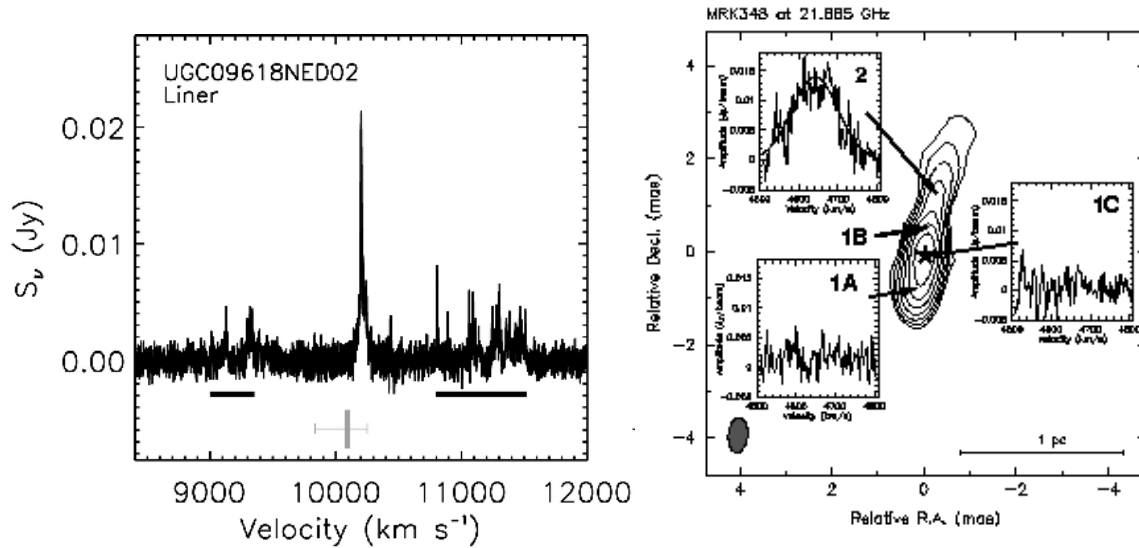


Figure 5.1: Examples from the literature of the characteristics of extragalactic water masers. **Left:** Spectrum of UGC 096 observed with the Green Bank Telescope (GBT; Konratko et al. 2006) showing the characteristic spectral line profile of a water maser seen from an edge-on disk. It displays a spectral complex in the vicinity of the systemic velocity of the galaxy (marked by the line at the bottom) and two spectral complexes approximately symmetric around the systemic velocity. These masers tend to be highly variable over time-scales of weeks to months (Lo 2005). **Right:** Spectrum of Mrk 348 observed with the VLBA showing the position of the water maser superposed on the continuum emission map in the northern jet at 21.885 GHz (Peck et al. 2003). The characteristic spectral line profile of the jet maser is a broad linewidth ( $\sim 130 \text{ km s}^{-1}$ ) and it is redshifted from the systemic velocity of the galaxy. The maser of Mrk 348 lies on the radio jet at  $\sim 0.3 \text{ pc}$  from the nucleus. The asterisk denotes the presumed position of the galactic nucleus.

measurements of the line and continuum flux densities, through reverberation mapping, also allows the speed of the material in the jet to be determined (Peck et al. 2003). Finally, outflow-masers trace the velocity and geometry of the nuclear wind.

Until recently, the most redshifted water maser known was detected towards the FR II radio galaxy 3C 403 ( $z = 0.06$ ; Tarchi et al. 2003). However, the discovery of an H<sub>2</sub>O maser with an apparent isotropic luminosity of  $23\,000 L_\odot$  in the type 2 quasar SDSS J0804+3607 at  $z = 0.66$  (Barvainis & Antonucci 2005) demonstrates that water masers can be detected at higher redshifts (Fig. 5.2). The discovery of water masers at cosmological distances ( $z > 0.3$ ) allows us to study the parsec-scale environment around powerful radio sources at earlier evolutionary stages, investigate the physical conditions of the molecular gas in the inner parsecs of quasars, measure black-hole masses at earlier epochs, and potentially constrain cosmological parameters.

In this chapter, I describe observations of the gravitationally lensed quasar MG J0414+0534 made with the 100 m Effelsberg radio telescope and the Extended Very Large Array (EVLA) to find a water maser at an even higher redshift. Observing a gravitational lens system i) targeted a luminous radio source already known to be at a cosmological distance

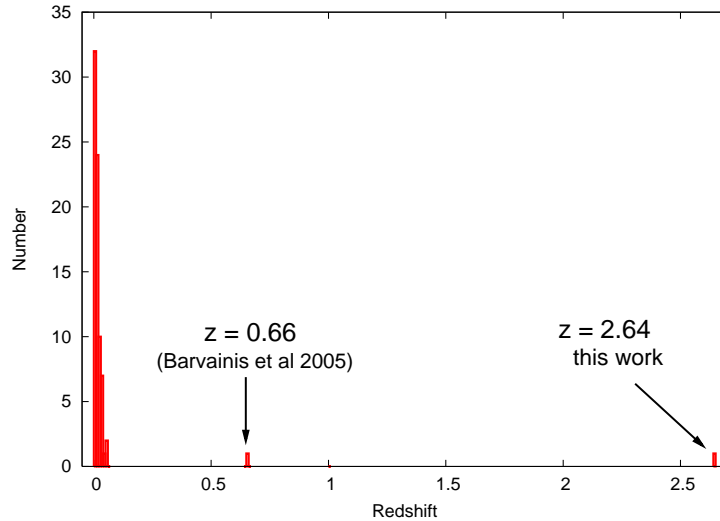


Figure 5.2: Redshift distribution of known H<sub>2</sub>O masers. Most masers are at a redshift  $\ll 0.06$ , Barvainis & Antonucci (2005) showed that masers can be detected at higher redshift.

( $z > 1.5$ ) and ii) used the lens as a “cosmic telescope” to probe a luminosity regime not easily reachable with current instrument sensitivities. Lens magnifications can increase the flux-density by 10 to 60 times the intrinsic source flux density.

In Section 5.2, the lens system MG J0414+0534 is introduced and a review of the previous observations is given. The Effelsberg discovery observations of a water maser in this system are described in Section 5.3. In Section 5.4 the EVLA confirmation observations are described. Finally, in Section 5.6 and Section 5.7 the discussion and the conclusions are presented.

## 5.2 MG J0414+0534

MG J0414+0534 consists of a background quasar at a redshift of 2.639 (Hewitt et al. 1992; Lawrence et al. 1995a) and a massive elliptical foreground galaxy at a redshift of 0.958, which acts as a gravitational lens (Tonry & Kochanek 1999). It is composed of four gravitationally lensed images of the highly reddened radio-loud quasar (Fig. 5.3). The foreground elliptical galaxy provides a total source magnification of  $\sim 34$  (Trotter et al. 2000; Ros et al. 2000). High resolution imaging with VLBI has shown the four lensed images to have a rich core-jet structure (Fig 5.4; Trotter et al. 2000; Ros et al. 2000). The red nature of the lensed quasar is thought not to be due to dust in the lensing galaxy because the level of dust extinction required ( $A_V \sim 5$  mag) is much too large for a typical early-type galaxy (Lawrence et al. 1995b; Falco et al. 1999b; Eliasdottir et al. 2006). Furthermore, radio spectroscopy failed to detect OH absorption in the spectrum of the lensing galaxy, which led Curran et al. (2007) to conclude that most of the reddening is occurring from within the host galaxy of the lensed quasar. There are known to be several Fe II absorption systems at the same redshift as the background quasar, which were detected in the optical spectrum (Lawrence et al. 1995b). Also, CO (3-2) emission

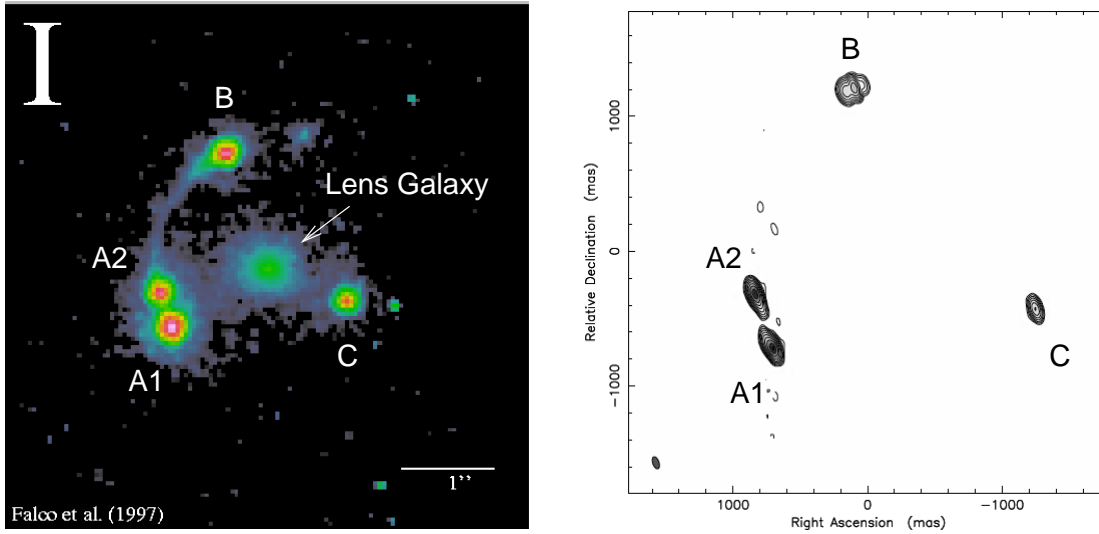


Figure 5.3: The MG J0414+0534 gravitational lens system is composed of four radio-loud lensed images (A1, A2, B and C) and a massive elliptical lensing galaxy. Left: The I-band (8140-Å) image taken with the Hubble Space Telescope (Falco et al. 1997). Right: The 5 GHz MERLIN radio map. The contours are  $(-0.25, 0.25, 0.5, 1, 2, 4, \dots) \times 2.6 \text{ mJy beam}^{-1}$  (King et al. 1999.)

associated with the lensed quasar has been detected and extends  $\pm 300 \text{ km s}^{-1}$  around the systemic velocity (Fig 5.5; Barvainis et al. 1998). Finally, H I absorption was found at  $-301 \text{ km s}^{-1}$  and  $-113 \text{ km s}^{-1}$  from the systemic velocity of the lensed quasar (Fig. 5.6; Moore et al. 1999). The detection of CO emission, H I absorption, and the reddened colour of the lensed quasar are signatures of a dense interstellar medium and provided the selection criteria for a search for water. MG J0414+0534 had been previously observed for water maser emission by Wilner et al. (1999) using the ATCA (Australia Telescope Compact Array). However, those observations failed to detect any water vapour from MG J0414+0534 down to a channel rms of  $3.3 \text{ mJy beam}^{-1}$ .

### 5.3 Single dish 100 m Effelsberg radio telescope observation

Observations of the  $\text{H}_2\text{O } 6_{16} - 5_{23}$  (rest-frame frequency 22.235 GHz) transition were made with the 100 m Effelsberg radio telescope at the redshifted frequency of 6.1 GHz on July 16 and 17, 2007. Further follow-up observations were conducted on September 13 and 14, 2007, to confirm the detection of a water maser in MG J0414+0534.

#### 5.3.1 Observations

The 6 GHz receiver, tuned to a centre frequency of 6112.2 MHz with 40 MHz bandwidth, was used throughout. At this frequency, the primary beam of the Effelsberg radio telescope is  $\sim 130$  arcsec, which is easily large enough to encompass all four of the lensed images; the maximum image separation being 2 arcsec. The data were processed through the AK90 spectrometer, giving a spectral resolution of  $78.125 \text{ kHz channel}^{-1}$ , or  $3.832 \text{ km s}^{-1} \text{ channel}^{-1}$  in velocity space. The data from both epochs were taken in the

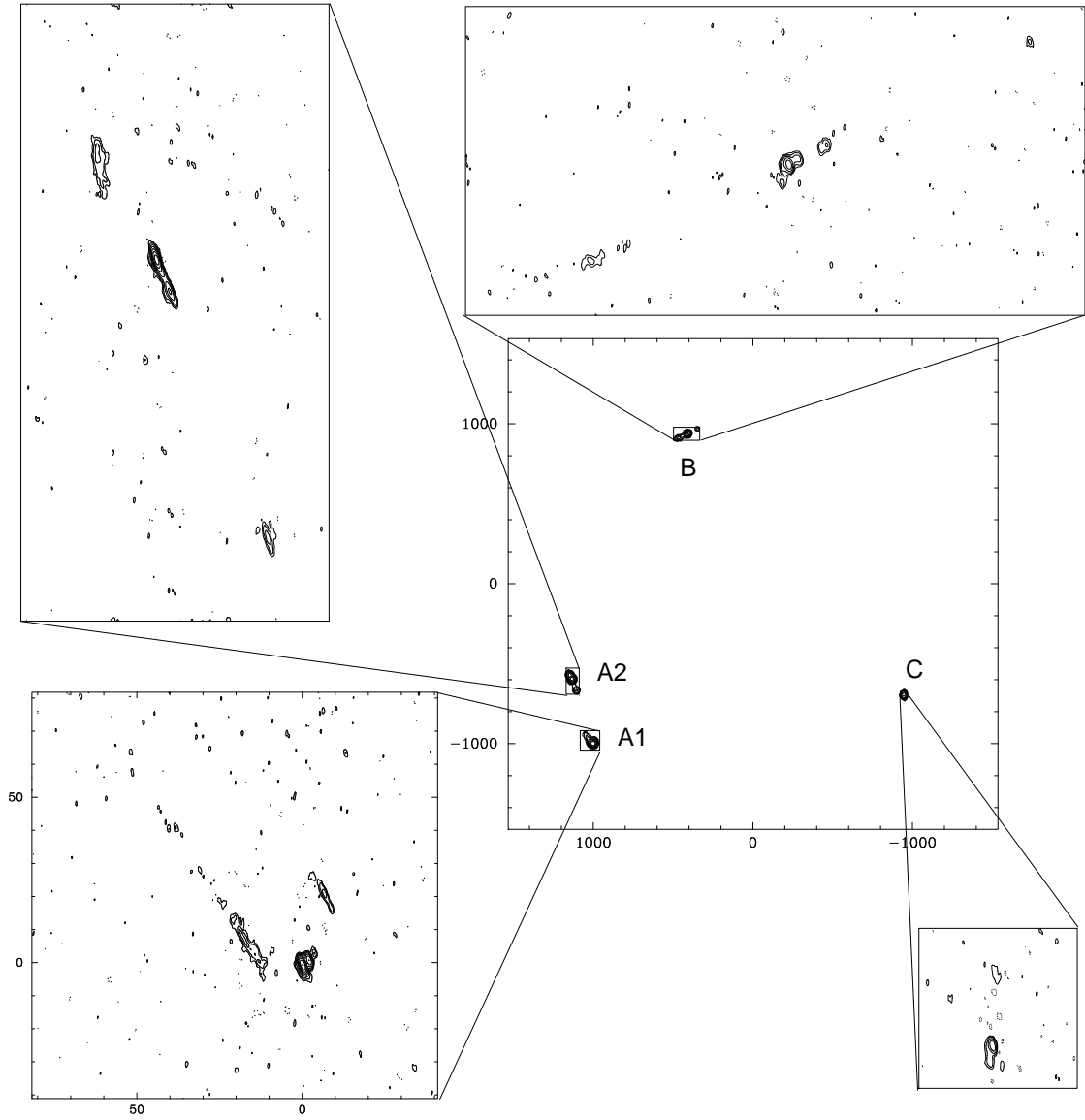


Figure 5.4: Image of MG J0414+0534 at 8.4 GHz with global VLBI (Ros et al. 2000). All of the lensed images show extended structure consistent with a core-jet radio source. The beam size of the sub-panels is  $2.6 \text{ mas} \times 1.1 \text{ mas}$  and the contours are  $(-1, 1, 2, \dots) \times 0.5 \text{ mJy beam}^{-1}$ . Axis units are milliarcseconds.

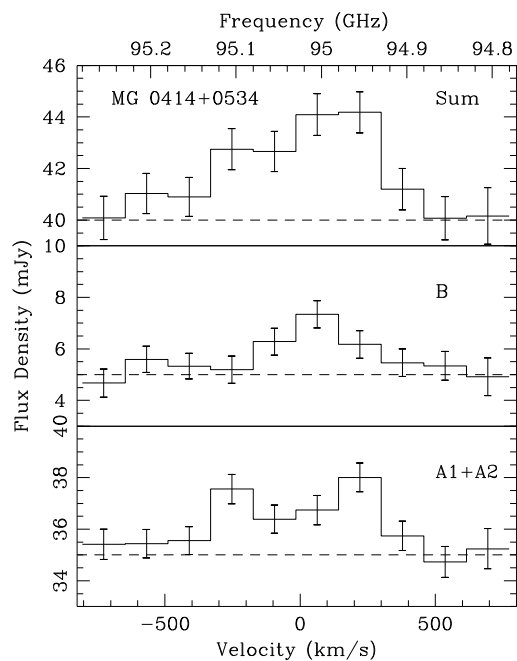


Figure 5.5: CO (3–2) emission from MG J0414+0534 measured with the IRAM Plateau de Bure Interferometer (Barvainis et al. 1998). The two strongest lensed images (A1 and A2) show the strongest CO emission.

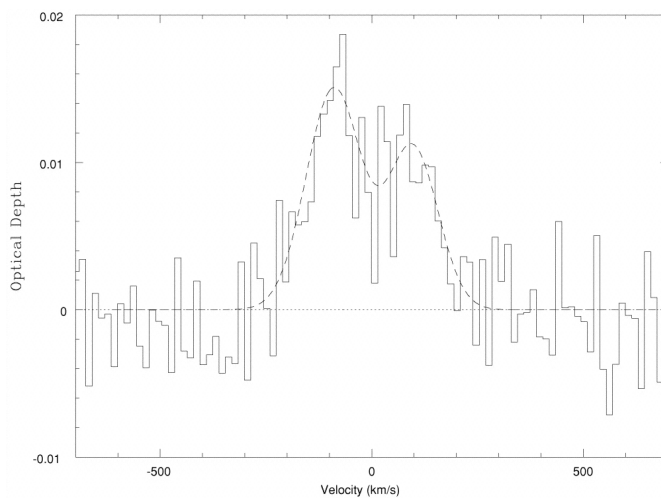


Figure 5.6: H I absorption measured from MG J0414+0534 with the Westerbork Synthesis Radio Telescope (Moore et al. 1999). Note that the peak in the H I absorption is  $-301 \text{ km s}^{-1}$  from the systemic velocity of the lensed quasar, the zero point of the velocity scale in this plot corresponds to  $-197 \text{ km s}^{-1}$  from systemic. The absorption spectrum is displayed in optical depth.

“on-off” mode to remove the sky signal from the spectrum. During each run,  $\sim 7$  h was spent observing MG J0414+0534, giving a total integration time of  $\sim 14$  h, of which half was spent on source and half off source. The resulting rms noise for both observations was 1.0 mJy, for the combined dataset the rms was 0.6 mJy (see Fig. 5.7). The source 3C 161 was observed for  $\sim 1$  h during each run to calibrate the flux-density scale and determine the shape of the bandpass.

### 5.3.2 Data reduction

For both observing runs on MG J0414+0534, the spectrum from each scan was analyzed individually. Scans were removed from the dataset when there was evidence of interference (e.g. a sharp spike) or a particularly bad bandpass shape (the effect is time-variable). This time consuming detailed inspection can reduce the effective observing time significantly but can greatly improve the quality of the data when observing weak signals. After initial editing, the data from each individual AK channel (8 spectra) were averaged and a low-order polynomial was fitted and removed from the resulting spectra, which were then averaged to produce a final spectrum.

The spectra were flux density calibrated by comparing with the primary flux-density calibrators 3C 161 and 3C 286, which were observed regularly throughout. At the observing frequency of 6.112 GHz, the flux density of 3C 161 was assumed to be 5.30 Jy and that of 3C 286 was assumed to be 4.05 Jy (Ott et al. 1994). The source 3C 161 was also observed in spectral line mode for 70 minutes with the same setup as MG J0414+0534 for a more accurate calibration of the bandpass.

### 5.3.3 Results

The 6.1 GHz Effelsberg radio spectra of MG J0414+0534 are presented in Fig. 5.7. The spectrum from July 2007 shows a clear 3.5 mJy peak at  $-294 \text{ km s}^{-1}$  relative to the systemic velocity, which was identified as a water maser, detected at  $3.5 \sigma$ . The emission line has a fitted Gaussian peak flux density of 2.8 mJy and a full width at half-maximum (FWHM) of  $45 \text{ km s}^{-1}$ . The spectrum of MG J0414+0534 that was taken during the September 2007 observations shows a less prominent emission line, possibly showing evidence for variability of the water maser emission. After combining the datasets from the two observations to maximize the signal-to-noise ratio there is a clear 2.9 mJy peak ( $4.8 \sigma$ ) at  $-299 \text{ km s}^{-1}$  relative to the systemic velocity. The emission line has a fitted Gaussian peak flux density of 2.2 mJy and a full width at half-maximum (FWHM) of  $40 \text{ km s}^{-1}$ . The properties of the fitted line are given in Table 4.1.

As a confirmation that the emission line was real and not caused by ripples across the baseline, the spectrum of the calibrator 3C 161 was used for bandpass calibration. A raw spectrum of the calibrator 3C 161 was formed by on-source, off-source differencing in the same manner that the raw spectrum of the target source was formed. A high-order polynomial was fitted to the spectrum and normalized to unity average amplitude. The normalized polynomial was divided into the raw target spectrum to remove the baseline ripple that was common to both spectra. The polynomial was normalized before dividing so as not to change the flux density calibration of the target spectra. I chose to divide

by the normalized polynomial rather than by the raw calibrator spectrum so as not to introduce the thermal noise from the calibrator spectrum into the bandpass-calibrated target spectrum. In the resulting spectrum, the line was clearly visible and the baseline ripples were removed (Fig. 5.8). The radio continuum measured from MG J0414+0534 at 6.1 GHz was  $0.55 \text{ Jy} \pm 0.06 \text{ Jy}$  in July 2007 and  $0.57 \text{ Jy} \pm 0.06 \text{ Jy}$  in September 2007, which are both consistent with previous measurements (e.g. Wilner et al. 1999).

## 5.4 The Expanded Very Large Array

The Very Large Array (VLA) is part of the National Radio Astronomy Observatory (NRAO) and it consists of 27 independent radio antennas located west of Socorro, New Mexico, USA. Each dish has a diameter of 25 m. The antennas are positioned along three arms of the Y-shaped array, each of which has a maximum length of 21 km, allowing aperture synthesis interferometry with a maximum baseline of 36 km. The highest angular resolution that can be reached is about 0.05 arcseconds at a wavelength of 7 mm.

The array has four main configurations which change every four months: A configuration (the largest) down to D configuration (the smallest, in which all dishes are within 600 m). Moves between configurations are done in two stages, first shortening the east and west arms and later shortening the north arm. This is referred to as a hybrid configuration. During observations the data from the antennas are correlated in real time, avoiding the need for raw data storage, allowing fast access to the correlated data.

The VLA was built in the late seventies and became functional in 1980. With a view to upgrading the venerable 1970s technology with which the VLA was built, recent funding has been allocated for the conversion of the VLA into the Expanded Very Large Array (EVLA). The upgrade will enhance the instrument's sensitivity, frequency range, and spectral capability. Significant for this project was that the upgrade adds a capability to observe in the 6 GHz band, which was lacking in the VLA and enabled a timely confirmation of the Effelsberg discovery. A second phase of this upgrade to add up to eight additional dishes in other parts of the state of New Mexico, up to 300 km away, is currently unfunded. The EVLA upgrade is currently underway. The antennas were initially upgraded at a rate of one every month, which will later change to one antenna every two months (see the EVLA upgrade timeline in Fig 4.9). After the EVLA antennas are retrofitted they are returned to the operational VLA. However, these antennas are operated in a transition mode and they are to date still less reliable than unmodified VLA antennas. The full EVLA with all 27 upgraded antennas is expected to be completed by 2013.

### 5.4.1 Observations

To independently verify the detection of water emission and to confirm that the maser was coincident with the lensed images of MG J0414+0534, interferometric observations with the EVLA were carried out. Interferometric observations were also preferable over further single-dish observations in order to obtain an independent confirmation of the line using the greatest possible difference in techniques.

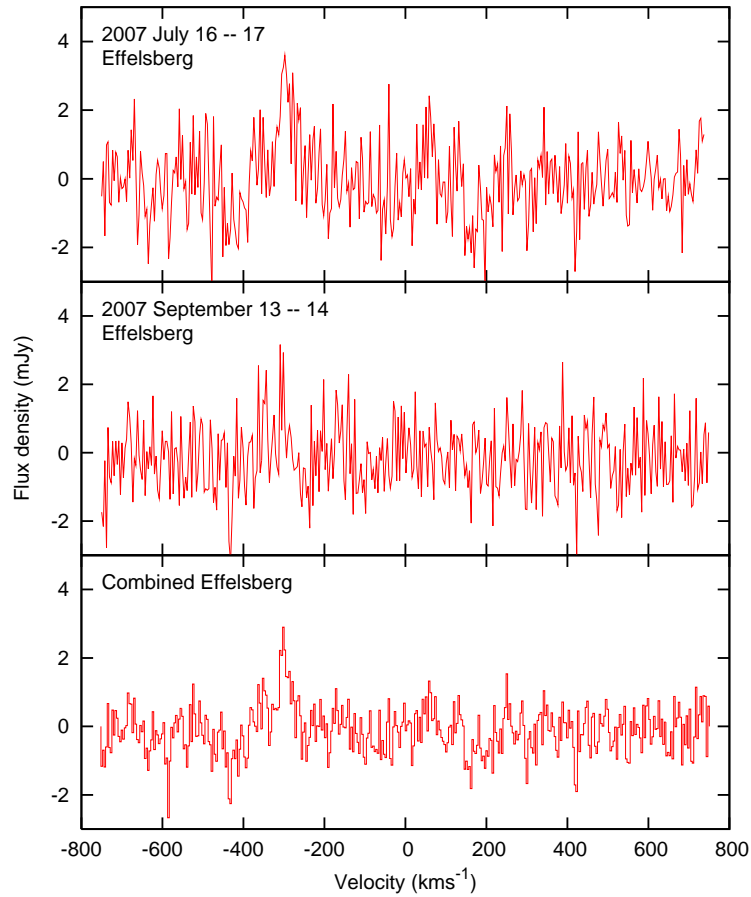


Figure 5.7: Effelsberg spectra of MG J0414+0534. In the velocity scale, zero corresponds to the systemic velocity of the galaxy. The spectral resolution of the spectra is of  $3.8 \text{ km s}^{-1} \text{ channel}^{-1}$ . Top panel: Spectrum taken in July 2007. The fitted velocity of emission is  $-294 \text{ km s}^{-1}$  from the systemic velocity. The width of the emission is  $45 \text{ km s}^{-1}$  and the peak flux density is  $2.9 \text{ mJy}$ . The rms in the spectrum is  $1.0 \text{ mJy}$ . Middle panel: Spectrum taken in September 2007. The fitted velocity is  $-303 \text{ km s}^{-1}$  from systemic, the width of the emission is  $22 \text{ km s}^{-1}$  and the peak flux density is  $1.3 \text{ mJy}$ . The rms in the spectrum is  $0.97 \text{ mJy}$ . Bottom Panel: Combined Effelsberg spectra. The fitted velocity is  $-299 \text{ km s}^{-1}$  from systemic, the width is  $40 \text{ km s}^{-1}$  and the fitted peak flux density is  $2.2 \text{ mJy}$ . The rms is  $0.6 \text{ mJy}$ .

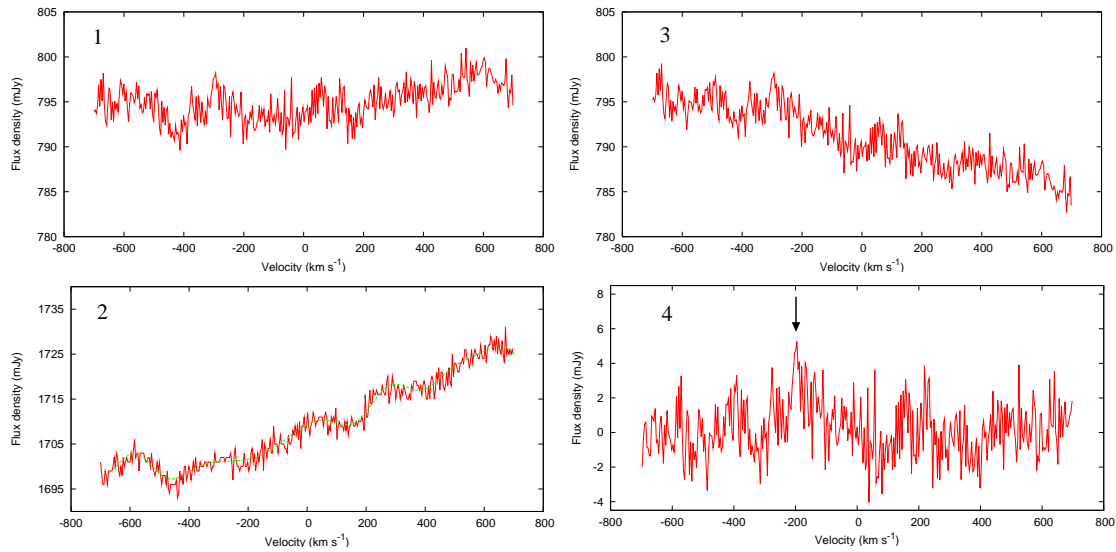


Figure 5.8: Bandpass shape correction of MG J0414+0534 using the calibrator 3C 161. The first panel shows the raw spectrum of MG J0414+0534 taken with Effelsberg, where ripples across the band are clearly visible. The second panel shows the raw spectrum of the calibrator 3C 161, the shape of the band is very similar to the one above. A high order polynomial resulting from a fit to the spectrum was normalized to unity. The spectrum of MG J0414+0534 was then divided by this polynomial function. The result is shown in the third panel. A straight line was then fitted to the final spectrum after division. The result is shown in the fourth panel. The line is clearly visible, its position marked by the arrow. The velocity scale shows zero at the systemic velocity of the quasar.

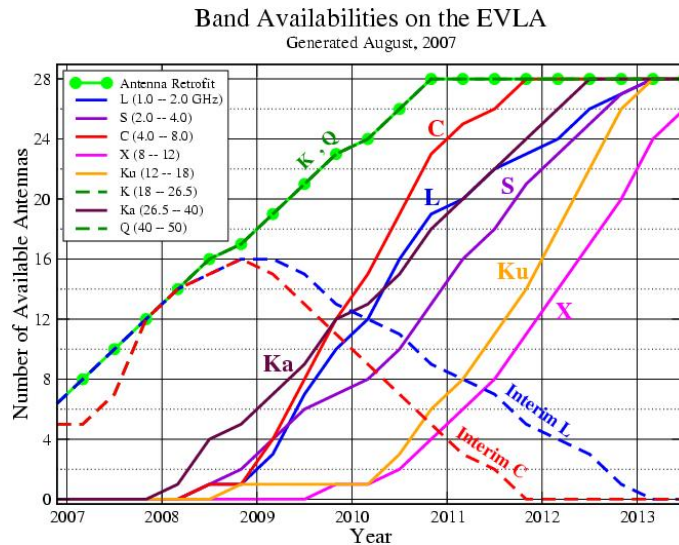


Figure 5.9: The planned availability of the various bands of the EVLA. The full upgrade is planned for 2013. From <http://www.vla.nrao.edu/astro/guides/evlareturn/receivers.shtml>.

The aim of these observations was to detect the water maser emission from the two strongest lensed images (A1 and A2; Fig. 5.4) which are separated by 0.4 arcsec in the north-south direction. For this purpose it was necessary to carry out observations in A- or BnA-configuration to achieve the required resolution on the sky in this direction. The status of the EVLA in October 2007 was nominally eleven antennas upgraded with the new C-band receiver, i.e. less than half the VLA antennas. The EVLA antennas were spaced out across the array to provide close to the standard resolution during the transition stages.

For an estimated line peak of  $\sim 1.4$  mJy channel $^{-1}$  (at A1 and A2), assuming a system temperature of 25 K for the EVLA antennas and an aperture efficiency of 25 % at 6.1 GHz (Rick Perley, priv. comm.), 20 h on-source were estimated to obtain a  $5\sigma$  detection (rms 0.28 mJy channel $^{-1}$ ) of the line from images A1 and A2. The data were taken during five observing runs on September 24, 18 and 30, 2007, and on October 1 and 7, 2007. On each run, MG J0414+0534 was observed for 3.5 h. The calibrator J0414–013 was observed every 26.5 min for phase and bandpass calibration. The final array consisted of 11 upgraded EVLA antennas in the hybrid BnA configuration. The observations were carried out using dual polarization and a 25 MHz bandwidth to ensure sufficient line-free baseline, centred on the line frequency (6.116 GHz). The band was divided into 32 spectral channels each 781.25 kHz wide. This corresponds to a velocity resolution of 38.3 km s $^{-1}$  channel $^{-1}$ .

#### 5.4.2 EVLA Data Reduction

In this Section, I describe the calibration steps used in the reduction of the EVLA dataset, with some details on the calibration philosophy and the tasks used.

**Loading the data** The task FILLM loads the data from a VLA observation creating two files: a large file containing the line data only and a smaller file containing the “channel-0 data”. The channel-0 data contains the continuum data computed from the line data by vector averaging 3/4 of the observing band. Note that all of the calibration and editing steps, except bandpass calibration and continuum subtraction, are performed on the channel-0 dataset and the solutions are later applied to the line dataset. The task FILLM also allows one to concatenate datasets from different observing dates into one file.

**Data inspection and editing** At each stage of the data calibration it is important to get an impression of the data quality and to edit any data that are corrupted. A general initial method of inspecting the data is to check the start and stop times and the number of visibilities delivered per scan for consistency to see whether the EVLA antennas all contributed to the visibilities and whether the VLA antennas were correctly omitted from the correlation (such scan listing can be generated with LISTR in AIPS). I inspected the visibilities by plotting or printing the visibility amplitude or phase against  $uv$ -distance or time (task UVPLT and PRTUV). From this analysis it became clear that i) the VLA antennas delivered visibilities with low amplitudes (visible as noise or non-zero amplitude on the  $uv$ -plot) and ii) two of the EVLA antennas (11 and 13) failed to observe and they delivered zero amplitudes on all baselines. These antennas were flagged (edited) as bad and not to be used in the later calibration and imaging (task UVFLG). Further data editing was done on the channel-0 data by displaying amplitude vs time for all baselines

and all times (for one IF and one spectral channel at a time; task TVFLG) or on the spectral-line data to remove data corrupted by RFI (task SPFLG). These editing tasks create an output in the flag table (FG) which is copied to the line file. After editing the EVLA data, nine EVLA antenna provided useful data and the total usable time on-source was 12.2 h.

**Flux-density calibration** The main steps of the flux-density calibration are using the known flux density of the primary flux density calibrator and the ratio of the measured visibility amplitudes on the primary and secondary calibrators to estimate the flux density of the secondary calibrator (termed flux-density bootstrapping), and then using periodic measurements of the visibility amplitude on the secondary calibrator to monitor the system gain factor needed for converting fringe visibilities into calibrated flux density. First, I calculated the flux density of the primary flux density calibrator 3C 48 (4.3 Jy at 6.1 GHz based on Baars et al. 1977) (and entered this in the source (SU) table using the task SETJY). The ratio of the visibility amplitudes for the primary and secondary calibrators was measured by performing amplitude self-calibration (task CALIB) on the primary and secondary calibrators, creating antenna-based gain estimates needed to convert the fringe visibility amplitude to the flux density adopted for the source in the self-calibration model (stored in an SN table). The total flux adopted for the model for the primary calibrator was that calculated above, and for the secondary calibrator was 1.0 Jy. Then, the flux density of each secondary flux-density calibrator was determined by using the rate of the gain estimates for the primary and secondary calibrators and thus using the flux density of the primary calibrator (this procedure is implemented in the task GETJY). The calibration solutions were checked at all stages by plotting the gain and phase solutions for each antenna as a function of time (task SNPLT). After measuring the flux densities of the secondary calibrators, I determined the instrumental gains on the calibrator sources using amplitude self-calibration with the correct flux densities in the model (task CALIB), and those gain solutions were linearly interpolated in time to the target source (task CLCAL).

Note that the amplitude calibration used here is different from the calibration method used with VLBI, which makes use of the system temperatures (TY) of the antennas to derive the gains. This difference is due to the fact that calibrators are mostly resolved by VLBI or are variable and would therefore not be reliable flux-density calibrators.

**Phase calibration** After the flux-density scale was set, the phase time series were inspected (task UVPLT), then further runs of self-calibration were made, this time on the secondary calibrators to calibrate the instrumental and atmospheric phases, which were changing on time-scales of the order of a minute, as estimated from inspecting the phase time series and to correct residual amplitude calibration errors. This improved the dynamic range of the images. At this stage, CALIB compares the input  $uv$ -dataset with the predicted visibilities that would correspond with a source model (a point source or the best set of CLEAN components) and the differences are decomposed into a set of antenna-based amplitude and phase corrections as a function of time that bring the data into better agreement with the model. This was done by carrying out self-calibration on the calibrators and interpolating the solutions to the target source. After this, many cycles of phase self-calibration were run on the target source, with a final cycle of self-calibration with a long solution interval (one day). The last set of calibration coefficients (contained in the CL table) was copied to the line dataset (task TACOP).

**Bandpass calibration** This is the most crucial step in spectral-line data analysis and is performed after amplitude and phase calibration has been applied to the data. The procedure is to take the visibility data from specified calibrators (here 3C 48 and J0423-013) to determine the antenna-based complex bandpass functions. The data are divided by a (frequency independent) source model, or channel-0, which should leave the data with unit amplitude and zero phase (as if it were an observation of a 1 Jy point source), except that instrumental amplitude variation across the passband is still present. The antenna gains are determined as a function of frequency using amplitude self calibration on each spectral channel, adopting a 1 Jy point source as the model for self calibration. The antenna based gain solutions then contain the bandpass shapes, factorized from the baseline-based bandpasses, and are written into a bandpass (BP) table which is applied to calibrate the visibility amplitudes during imaging. Bandpass determination is implemented in the task BPASS.

**Making an image and producing a spectrum** After the visibility data have been calibrated it was possible to produce an image and to look at the first spectrum. To form an image one must weight the visibility measurements according to ones goals (e.g. unity weights for maximum sensitivity in a uniform array, or down weight according to the local density of visibility measurements in the  $uv$ -plane for a good beam shape), one must grid the irregularly placed  $uv$ -plane visibility measurements onto a regular  $uv$  plane grid, to enable use of the fast Fourier. One Fourier transforms the visibility data making a dirty image from the visibility measurements and a dirty beam from the  $uv$  plane sampling, which determines how a point source will be spread in the image plane by the diffraction pattern of the synthesized aperture. One can then deconvolve the point-spread function from the dirty image using, for example a Högbom CLEAN as modified by Clark (1980) with subtraction of the model from the visibilities. These algorithms are implemented in the task IMAGR, which was used to make the continuum image and the spectral line data cube. In the case of the continuum image, all frequency channels were averaged together before imaging and deconvolving. However, for spectral line data, each frequency of the data cube was imaged separately and no deconvolution was applied. In both cases, the gain and phase solutions (CL table), the bandpass correction (BP table) as well as the data flags (FG table) were applied to the data.

**Continuum subtraction** For a weak emission or absorption line it is advisable to subtract the continuum emission from the line data before making the data cube. This is done since CLEAN is a non-linear algorithm where minor fluctuations (e.g. different noise in different channels) may converge to different solutions; the task itself may increase the noise in the signal. If the continuum is removed from the line data, no CLEANing is required and this potential increase of the noise is avoided. I tested the continuum removal in the  $uv$  domain and in the image domain; using the tasks UVLSF and IMLIN, the latter of which gave better results. In the  $uv$  domain one fits a linear spectral baseline to the real and imaginary parts of each visibility spectrum, choosing the line-free channels, and the linear fit is subtracted from the data (UVLIN). In the image domain, a similar linear fit to the spectrum is performed, but at each pixel of the image cube. The resulting fits are subtracted from each spectrum (task IMLIN). After two separate runs of IMAGR, the continuum image and data cube were created and it was finally possible to look at the

Parameter	Effelsberg	EVLA <sup>†</sup>	Units
Velocity	$-299 \pm 3$	$-296 \pm 9$	$\text{km s}^{-1}$
Line width	$40 \pm 12$	$70 \pm 27$	$\text{km s}^{-1}$
Line peak	$2.2 \pm 0.2$	$1.4 \pm 0.1$	mJy
Integrated profile	$97 \pm 14$	$121 \pm 20$	mJy $\text{km s}^{-1}$
Luminosity <sup>††</sup>	300 000	370 000	$L_{\odot}$
Unlensed Luminosity <sup>††</sup>	9 000	13 000	$L_{\odot}$

Table 5.1: The properties of Gaussian profiles fitted to the water maser line from the Effelsberg and EVLA datasets. <sup>†</sup> The EVLA data are for images A1 and A2 only. <sup>††</sup> Assumes  $H_0 = 71 \text{ km s}^{-1} \text{ Mpc}^{-1}$ ,  $\Omega_m = 0.27$  and  $\Omega_{\Lambda} = 0.73$ .

Image	$\Delta\alpha$ (mas)	$\Delta\delta$ (mas)	Flux density (mJy)
A1	$0 \pm 1$	$0 \pm 1$	$241 \pm 12$
A2	$+131 \pm 1$	$+394 \pm 1$	$205 \pm 10$
B	$-595 \pm 3$	$+1907 \pm 3$	$89 \pm 4$
C	$-1951 \pm 20$	$-287 \pm 20$	$34 \pm 2$

Table 5.2: The flux densities and positions of the lensed images at 6.1 GHz measured with the EVLA.

spectra interactively from different positions on the image (task ISPEC). The resulting spectra had an rms noise of  $0.3 \text{ mJy beam}^{-1}$  when integrated over one beam area.

### 5.4.3 Results

The uniformly weighted 6.1 GHz radio image of MG J0414+0534 together with the spectra measured from the lensed images are shown in Fig. 5.10. All four of the lensed images have been detected at 6.1 GHz with the EVLA. Their positions and flux-ratios (see Table 5.4.3) are consistent with previous observations at cm-wavelengths (Katz et al. 1997). The total flux density from the lens system is  $0.57 \text{ Jy} \pm 0.03 \text{ Jy}$ , which is in excellent agreement with the Effelsberg single-dish measurement. A clear emission line is detected with a peak of  $1.5 \text{ mJy}$  ( $5.1 \sigma$ ) at  $-296 \text{ km s}^{-1}$ , when integrating from the emission over the position of the two strongest lensed images A1 and A2. The peak of a Gaussian fitted to the spectral line is  $1.4 \text{ mJy}$  and the FWHM is  $70 \text{ km s}^{-1}$ . These EVLA data have confirmed that the  $\text{H}_2\text{O}$  emission is coincident with the strongest continuum images of the lensed quasar. Note that the signal-to-noise ratio of the data was not good enough to detect the water maser line from the weaker lensed images B and C (see Fig. 5.10). The non-detection of the line in those images was expected and it was an excellent confirmation of the authenticity of the detection.

## 5.5 Results from combined datasets

After smoothing the Effelsberg spectrum to the resolution of the EVLA data, the EVLA and Effelsberg spectra were combined to produce the highest signal-to-noise ratio spectrum

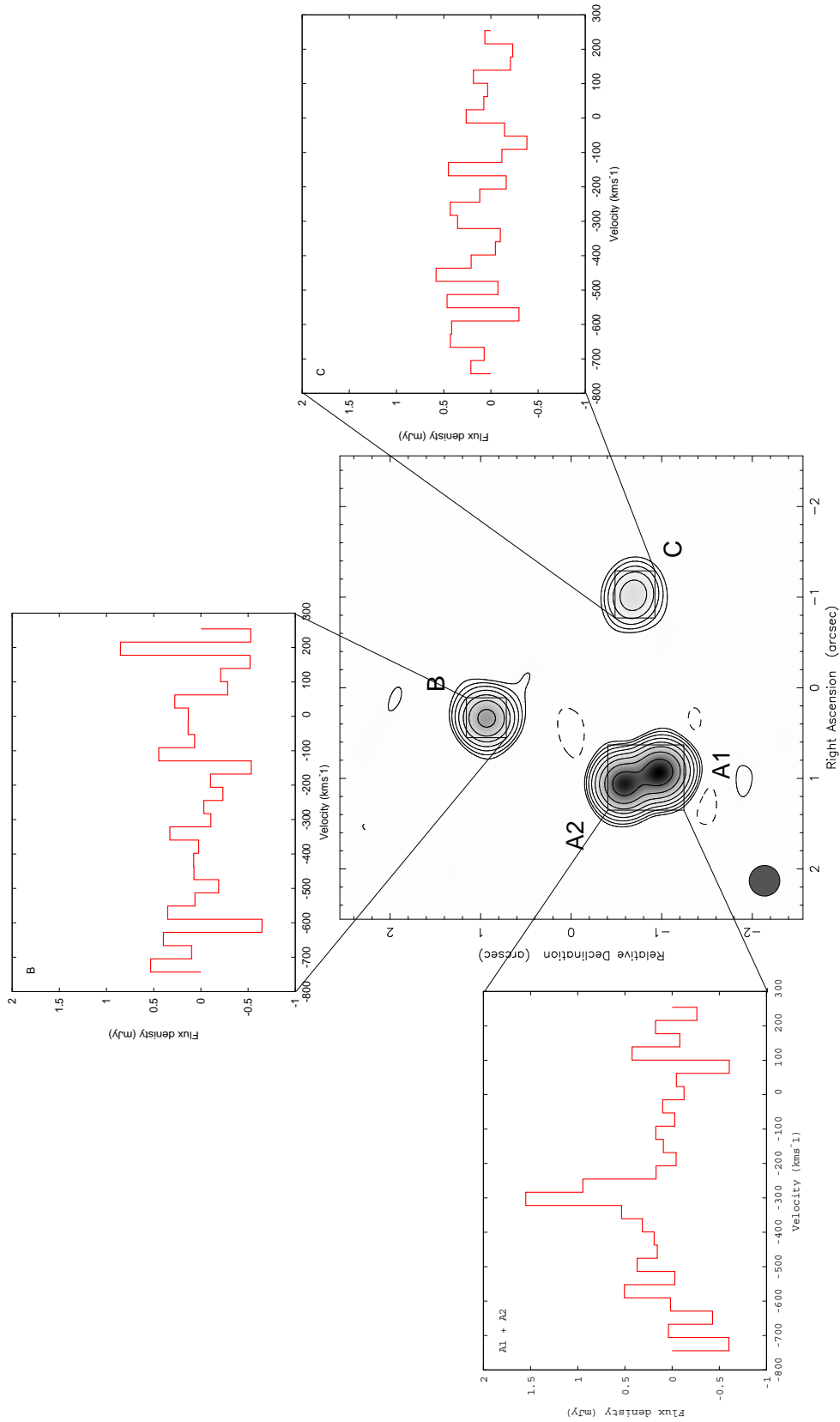


Figure 5.10: The 6.1 GHz EVLA radio image of MG J0414+0534 taken during the period between September 24, 2007 to October 7, 2007. The image has been restored using a circular beam with a FWHM size of 0.34 arcsec. The rms map noise is 0.37 mJy beam<sup>-1</sup>. The total radio continuum flux density is  $(0.57 \pm 0.03)$  Jy. The image contours are (-3, 3, 6, 12, 24, 48, 96, 192, and 384)  $\times$  0.37 mJy beam<sup>-1</sup>. The panels show the spectra taken at the positions indicated in the figure, corresponding to components A1+A2, B and C.

of the MG J0414+0534 water maser (see Fig. 5.11). The resulting spectrum has an rms noise of  $0.16 \text{ mJy channel}^{-1}$ . The water maser emission in the combined spectrum has a fitted peak flux-density of  $1.4 \text{ mJy}$  ( $9 \sigma$ ) at  $-299 \text{ km s}^{-1}$  and has a FWHM of  $52 \text{ km s}^{-1}$ .

## 5.6 Discussion

### 5.6.1 The highest redshift water maser

The first question to be addressed is whether the line is a genuine detection of a high redshift water maser. The radio spectra of MG J0414+0534 taken with the Effelsberg radio telescope and the EVLA detect an emission line to the  $4.8 \sigma$  and  $5.1 \sigma$  level, respectively. In the combined dataset the line is detected at  $9 \sigma$  and so has a confidence level of  $> 99.99 \%$  (see Table 5.4.3). The detection is consistent with a previously reported non-detection that did not reach sufficient sensitivity (Wilner et al. 1999). The radial velocities measured with Effelsberg and the EVLA ( $-299 \pm 3 \text{ km s}^{-1}$  and  $-296 \pm 8 \text{ km s}^{-1}$ ) agree within the uncertainties. Also, the EVLA data showed that the  $\text{H}_2\text{O}$  emission is coincident with the strongest continuum component (A1+A2) from the lensed quasar (Fig. 5.10). The feature cannot be associated with the lensing galaxy at redshift 0.958 or a nearby ‘‘local’’ object because there are no known strong maser lines at the corresponding rest frequencies ( $11.975 \text{ GHz}$  and  $6.116 \text{ GHz}$ , respectively). The case for the feature being a genuine emission line is further strengthened by the fact that the radio spectra from each dataset were taken independently over different time periods (months) and with different observing systems. Further evidence for the line being a water maser from MG J0414+0534 is that it is coincident in velocity with the CO emission and the HI absorption already reported from the lensed quasar (Fig. 5.5). In Fig. 5.11 the positions of the peaks in the CO emission from the two strongest lensed images are marked (note that the uncertainty in this velocity is  $\pm 79 \text{ km s}^{-1}$ ). Also shown are the two peaks in the HI absorption, which have  $(10 \text{ to } 13) \text{ km s}^{-1}$  uncertainty. It is clear that the emission line is coincident with the HI absorption at  $-301 \text{ km s}^{-1}$  and the CO emission at  $-248 \text{ km s}^{-1}$  (Barvainis et al. 1998; Moore et al. 1999). There is no evidence of water maser emission at the velocities of the other peaks in the CO emission spectrum ( $+226 \text{ km s}^{-1}$ ) or HI absorption spectrum ( $-113 \text{ km s}^{-1}$ ). The redshift of the water emission line is  $z = 2.6354 \pm 0.0001$ , which differs from the systemic redshift of  $z = 2.639 \pm 0.002$  that was measured from broad  $\text{H}\alpha$  emission in the infrared spectrum of MG J0414+0534 (Lawrence et al. 1995a). However, such differences between (optical/infrared based) systemic and water maser redshifts have been found before in other objects (e.g. Barvainis & Antonucci 2005). It is not clear whether in such cases the water maser lies at the true systemic velocity of the quasar, or if it is due to a satellite water vapour cloud of the active nucleus.

The transition observed requires gas temperatures in excess of  $300 \text{ K}$  and particle densities  $n(\text{H}_2) \geq 10^7 \text{ cm}^{-3}$ . It is the first time that such a dense interstellar gas component has been observed in the early Universe.

### 5.6.2 An extremely luminous water maser

The isotropic luminosity of the water maser can be calculated using:

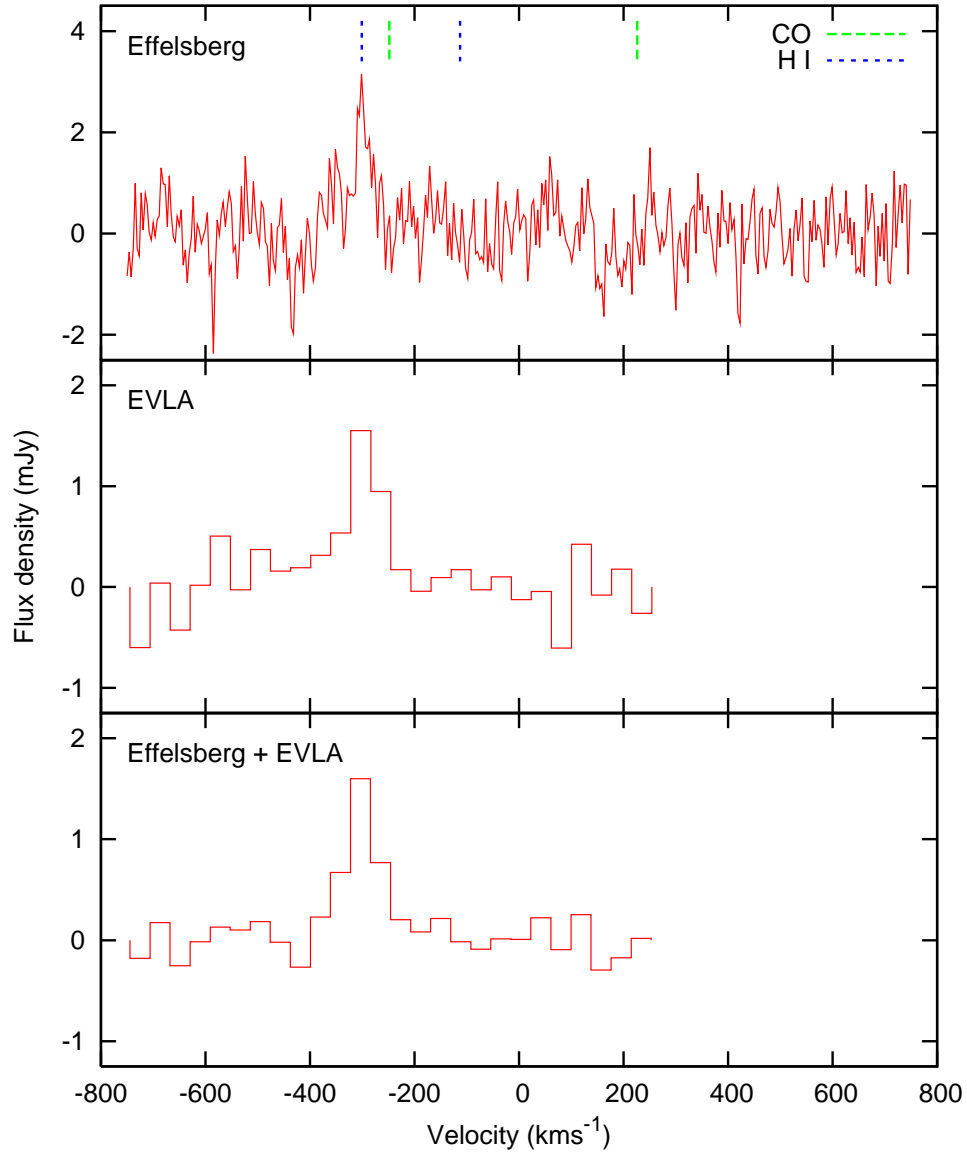


*Figure 5.11:* 6.1 GHz spectra of the lensed quasar MG J0414+0534 plotted vs velocity for the 22.235 GHz water line. Top panel: Effelsberg spectrum taken between July and September 2007 (on-source integration time 14 hours, channel spacing  $3.83 \text{ km s}^{-1}$ ,  $1\sigma$  noise level 0.6 mJy). Middle panel: EVLA spectrum taken between September and October 2007 (on-source integration 12 hours, channel spacing  $38.4 \text{ km s}^{-1}$ ,  $1\sigma$  noise level 0.3 mJy). Lower panel: combined Effelsberg and EVLA spectrum (channel spacing  $38.4 \text{ km s}^{-1}$ ,  $1\sigma$  noise level 0.16 mJy). The velocity scale is relative to the optical  $\text{H}\alpha$  systemic velocity of the lensed quasar ( $z = 2.639$ ; Lawrence et al. 1995). The blue lines correspond to the peaks in the  $\text{H I}$  absorption from the system (accuracy  $\pm 13 \text{ km s}^{-1}$ ). The green lines are the peaks in the CO emission from the lensed images A1 and A2 (accuracy  $\pm 70 \text{ km s}^{-1}$ ).

$$\frac{L_{\text{H}_2\text{O}}}{L_{\odot}} = \frac{1}{m} \frac{0.023}{1+z} \times \frac{\int S dv}{[\text{Jy km s}^{-1}]} \times \frac{D_{\text{L}}^2}{[\text{Mpc}^2]} \quad (5.1)$$

where  $\int S dv$  is the integrated line profile,  $D_{\text{L}}$  is the luminosity distance,  $z$  is the redshift, and  $m$  is the lensing magnification. For galaxy-scale lens systems, an isothermal mass distribution is often a remarkably good approximation for the form of the lensing potential, from which the image magnifications can be established (e.g. Koopmans et al. 2006). The case of MG J0414+0534 is made slightly more complicated by the presence of a dwarf galaxy which is believed to be a satellite of the main lensing galaxy (Schechter & Moore 1993). Dwarf galaxies can cause local perturbations to the global mass model which in turn can change the predicted magnification of one or more of the lensed images (e.g. Chen et al. 2007; McKean et al. 2007). An analysis of the lensing mass distribution of MG J0414+0534, which included the dwarf galaxy, gave a total source magnification of  $\sim 34$  (Trotter et al. 2000; Ros et al. 2000).

Using this value for the source magnification and a luminosity distance of  $D_{\text{L}} = 22.1$  Gpc, results in an apparent isotropic luminosity of  $9\,000 L_{\odot}$  for the water maser associated with MG J0414+0534. This luminosity is derived using the Effelsberg spectrum. Not only is the MG J0414+0534 water maser the most distant known, it is also the second most luminous. The most luminous water maser is from SDSS J0804+3607 at  $z = 0.660$ , with an isotropic luminosity of  $23\,000 L_{\odot}$  (Barvainis & Antonucci 2005), and the third is TXS 2226–184 at  $z = 0.025$  (Koekemoer et al. 1995) with  $6\,800 L_{\odot}$ . The apparent gravitationally lensed isotropic luminosity of the maser is  $L_{\text{H}_2\text{O}} \sim 300\,000 L_{\odot}$ , which is 15 times more luminous than any other maser reported to date (Barvainis & Antonucci 2005).

These apparent lensed and unlensed luminosities have been calculated based on the standard assumption of isotropic emission of radiation, for comparisons with the luminosity estimates of other masers. However, masers are likely to emit anisotropically (Neufeld et al. 1994). Beaming is expected since differences in the gain path due to irregularities in the cloud shape and velocity coherence cause exponential changes in maser output brightness. Beaming may also occur in some cases due to the alignment of masing clouds occurring only in restricted directions or due to competitive pumping in saturated masers, in which the stimulated emission in one direction mode dominates over other directional modes. The resulting beamwidths are uncertain, but arguments have been made for values from 7 degrees (Miyoshi et al. 1995) down to as low as milliarcseconds (Tarchi et al. 2002). This expectation is testable for the first time using the gravitationally lensed water maser since the light seen through each of the lensed images was emitted in slightly different directions from the background quasar. The angle subtended between image regions A1 and A2, as seen from the quasar, is 0.5 arcseconds, and between images A1 and B is 2.3 arcseconds. The maser line is seen in the spectra of both lensed images A1 and A2 from the EVLA observations and so the maser beaming angle is greater than 0.5 arcseconds, ruling out milli-arcsecond beaming angles for this system. Furthermore, from a beaming angle  $> 0.5$  arcseconds, the intrinsic luminosity of the water maser must be greater than  $5 \times 10^{-9} L_{\odot}$ .

### 5.6.3 Where does the maser originate?

Of the  $\sim 100$  galaxies known to host 22.2 GHz water masers (Braatz et al. 2008), most are in type 2 Seyfert or LINER galaxies at redshifts  $< 0.06$ . The notable exception is a type 2 quasar at redshift 0.66 (Barvainis & Antonucci 2005). This is consistent with unification models (Antonucci 1993) in which the type 2 optical spectrum is due to an edge-on orientation of the circumnuclear disk, causing the active nucleus to be hidden behind a large column of dust and gas. This geometry provides a long maser gain path-length for amplification and so the prevalence of masers in type 2 active galactic nuclei fits naturally with unification models. MG J0414+0534 is an intriguing object as it is one of the few type 1 active galactic nuclei and the only known type 1 quasar to show water maser activity.

At low redshifts, at least one third of known water masers are associated with the orbiting molecular clouds of circumnuclear accretion disks (Braatz et al. 2008). These water masers are typically found within 0.1 parsec to 1.0 parsec of the supermassive black hole and tend to have multiple blue-shifted, red-shifted, and systemic velocity components, where individual components have narrow line widths of  $< 5 \text{ km s}^{-1}$  (Herrnstein et al. 1999; Myoshi et al. 1995; Kondratko et al. 2008). In three cases, luminous water masers have also been found in the inner parsec of relativistic jets that are ejected from some central engines (Claussen et al. 1998; Peck et al. 2003; Gallimore et al. 1996). These masers have relatively broad line widths, up to  $100 \text{ km s}^{-1}$ , and have velocities that tend to be offset from the systemic velocity of the host galaxy. Whether the water maser in MG J0414+0534 is associated with the circumnuclear accretion disk or is induced by a relativistic jet interacting with a gas cloud is not conclusive from the data presented here alone. However, given that only a single emission line has been detected, and that it is broad and offset from the systemic velocity by  $-300 \text{ km s}^{-1}$ , the jet-maser scenario seems most likely. The type 1 optical spectrum and beamed radio continuum emission of the quasar provide further support, since unification models of type 1 objects have the nucleus being viewed from above the plane of the disk. Masers originating from the circumnuclear accretion disk, however, are preferentially beamed in the plane of the disk. Therefore, disk masers are unlikely to be seen in active galactic nuclei of type 1, while masers associated with nuclear jets may well be detectable.

Future high-resolution imaging of the water maser line with VLBI will provide the exact location of the emission relative to the core-jet radio structure already observed in MG J0414+0534 (Ros et al. 2000; Trotter et al. 2000). Resolving such maser component distributions with VLBI would usually be challenging at cosmological redshifts since the angular resolution of global VLBI arrays operating at 6.1 GHz is  $\sim 2$  milliarcseconds, which corresponds to a spatial resolution of  $\sim 15$  parsec at redshift 2.639. However, for MG J0414+0534, the apparent angular extent of the radio structure is increased due to the foreground gravitational lens by a factor of  $\sim 15$  for the two strongest lensed images, A1 and A2 (Trotter et al. 2000). Hence, the spatial resolution of a VLBI image will be  $\sim 1$  parsec. Furthermore, it will be possible to distinguish water masers separated by  $\sim 0.5$  parsec in the background source if each masing component is detected with a signal-to-noise ratio of at least ten, thus matching or even resolving the  $> 0.5$  parsec outer diameter of known maser disks in the Circinus galaxy and NGC 1068 (Gallimore et al. 1996; Greenhill et al. 2003). Thus, VLBI imaging of gravitationally magnified water masers has the

powerful potential to trace the sub-parsec scale structure surrounding accretion disks at cosmological distances.

## 5.7 Conclusions

In summary, the discovery of the most distant water maser known was presented here, in the gravitationally lensed quasar MG J0414+0534 at  $z = 2.64$ . With a gravitationally magnified isotropic luminosity of  $300\,000 L_{\odot}$ , it is by far the most luminous maser known and the first to show significant gravitational amplification.

This result demonstrates that it is possible to detect water vapour out to cosmological distances with current instrument sensitivities. Although the intrinsic power of the maser ( $9000 L_{\odot}$ ) is at the upper end of those observed so far, this discovery has been possible only due to the magnification provided by the foreground galaxy; it acts as a cosmic telescope reducing the integration time required for a detection by a factor of  $\sim 1000$ . Light was emitted from the quasar at a time when the volume density of radio-loud quasars was highest (Dunlop & Peacock 1990). Therefore more such masers may be detectable at this redshift. However, systematic searches will require a significant improvement in instrument sensitivity.

The advent of new high-sensitivity facilities with wide spectral bands, such as the EVLA and the Square Kilometer Array, will allow water masers from a lower luminosity regime to be routinely investigated at even higher source redshifts. The detection of water at a look-back time of 11 Gyr demonstrates that maser observations of highly redshifted sources are possible, opening up a huge parameter space for research related to AGN and cosmology in the early Universe.

## Chapter 6

# Summary and Outlook

One of the main aims of this thesis was to provide direct evidence for the presence of a molecular torus at the centre of active galaxies. The torus is a key component of unified models for AGN since it provides the obscuration required to hide the missing broad line region of type 2 AGN. The distribution of the absorbing material also plays a fundamental role in feeding the central engine and affects the degree of shielding of the strong continuum from various viewing angles. The accreting gas later emits intense radiation from the radio to X-ray bands, which further affects the structure and energetics of the parent galaxy.

Indeed, small-scale ( $< 1$  pc), clumpy tori have been detected through interferometric infrared studies of the hot dust emission in the cores of AGN (Jaffe et al. 2004, Tristram et al. 2007), and water-vapour masers could map the central few parsecs of an active nucleus (Herrnstein et al. 1999), tracing the rotation of nuclear accretion disks. However, the small thickness of these disks cannot account for the frequently observed spatial obscuration and little evidence has emerged for the larger-scale ( $> 1$  pc) molecular components invoked in torus models.

### 6.1 A search for radiatively excited OH

Radio observations present a great means to investigate the inner region of an AGN, since, provided that the background source has a reasonably strong continuum flux density, it is much easier to detect molecular absorption and it is not distance limited. The high sensitivity of molecular absorption line observations means that molecular species much rarer than CO can be observed. Extragalactic hydroxyl (OH) is the second most common molecular absorption line seen in galaxies after CO, and has been shown to display the characteristics of the circumnuclear environment of active galaxies, tracing the low density component of the molecular environment. However, despite many efforts to directly detect the expected molecular absorption of the ground-state transition at 1.67 GHz in a number of previous surveys, the detection rates have been very low ( $\sim 4\%$ ; Baan et al. 1992). Does the torus really exist? Or are molecules destroyed in the harsh environment? These are two fundamental questions addressed by this thesis.

Assuming that the torus is molecular, the non-detections can be explained by taking radiative excitation effects into account, which enforce a high excitation temperature and suppress the opacity in the lowest transitions (Maloney, Begelman & Rees 1994). Following these arguments, in this work we changed the observing strategy for detecting OH in the

tori of AGN by looking for the higher excited states of OH at 4.7 GHz, 6.0 GHz and 13.4 GHz. A sample of 31 Seyfert 2 galaxies was selected for having polarized broad line emission, high absorption in soft X-ray indicating a large foreground gas column, and a 6 cm flux density  $>50$  mJy. Sources in which the ground state 1.67 GHz transition had been searched for and not detected or that previously showed the presence of other molecules, like CO, were also included in the sample.

### 6.1.1 Effelsberg observations

A sample of 31 sources was observed with the Effelsberg 100 m telescope at 4.7 GHz and 6.0 GHz. Of these, three sources, NGC 1068, Cygnus A and NGC 1052, were too strong for sensitive study with single dish observations, as their high flux density caused significant standing-wave ripple across the band. Of the remaining 28 sources, rotationally-excited, broad OH lines were detected in absorption towards five sources, yielding a detection rate of 19%, which is higher than the detection rates from previous surveys. The results obtained here confirm for the first time that radiative excitation effects play a role when searching for molecular absorption. However, the detections in this survey cannot support the hypothesis of radiative excitation models alone to explain the previous lack of molecular detections, since almost all the sources that have been detected at 6.0 GHz have also been detected at 1.67 GHz either in absorption or emission. Moreover, all of the sources with known non-detections at 1.67 GHz also yielded non-detections at 6.0 GHz. However, the observed line widths ranged from a few  $100 \text{ km s}^{-1}$  to  $2000 \text{ km s}^{-1}$ , with narrow absorption features at the systemic line frequency. The broad component suggests that the gas in all sources is indeed close to the central region, either rotating around the central engine, infalling or outflowing.

A further interesting result of this survey is that high absorbing column densities did not guarantee a detection of OH absorption. Given the high X-ray absorbing columns in these systems, the non-detections still need to be explained. Since the nature of the X-ray and optically absorbing material is not clear, one possibility is that it may be non-molecular in most galaxies. Finally, the search for 4.7 GHz absorption turned up only non-detections, showing for those galaxies that the excitation in the OH clouds by the non-thermal radiation is not large enough to populate the higher 4.7 GHz energy levels.

The overall picture that emerged from this work was of a bimodal distribution of molecular abundances, where some sources seem to be devoid of OH, whereas those detected at 6 GHz show a large variety of molecular species. This bimodal distribution of absorption could be explained by invoking the presence of compact clouds that cross the line of sight in a few sources, producing absorption. The covering factor of such clouds, inferred from the detection rate, would need to be  $\sim 20\%$ .

### 6.1.2 VLBA observations

Two of the strong sources from the Effelsberg sample that were affected by standing-wave ripple, Cygnus A and NGC 1052, were chosen for high resolution VLBA observations of OH at 13.4 GHz. The resulting detections provide independent evidence for a parsec-scale torus in the cores of those two systems.

A tentative OH detection was made towards Cygnus A. The compactness of the radio source at this frequency indicates that the absorbing material lies within 4 pc along the

line of sight to the central engine. This result is also consistent with the high-resolution IR observations of NGC 1068, which show a torus size that is no more than a few parsecs wide (e.g. Jaffe et al. 2004; Poncelet et al. 2006). The width of the OH line is also comparable to the CO<sup>+</sup> and H I absorption lines, which have been interpreted as part of a circumnuclear torus rotating around a radio jet. Moreover, the two absorption components present in the 13.4 GHz spectrum resemble the H I profile previously observed (Conway & Blanco 1995), suggesting rotation of gas around the core. Furthermore, a firm detection was made towards the core of NGC 1052. Absorption was detected towards the western jet, whereas none was found in the eastern jet. The absorption profile suggests an obscuration of the inner jet in a compact region confined within < 0.3 pc from the core. The proximity to the core is further supported by the large width of the line. The gas is likely to be associated with a geometrically thick plasma torus, which has been inferred from free-free absorption and is located 0.1 pc from the eastern jet and 0.7 pc from the western jet. Also, the OH seems to be co-located with the H<sub>2</sub>O gas and perhaps with the more compact clouds of CO, HCN, and HCO<sup>+</sup>, but not with the H I or the OH gas observed at 1.67 GHz, which are more evenly distributed around the nuclear region.

These observations confirm that radiative excitation effects have a large impact and should be taken into account when studying the molecular properties in the innermost regions of AGN. Especially in the case of Cygnus A, the results confirm that non-detections obtained for OH at 1.67 GHz and CO might be the result of radiative excitation effects in the core of this powerful galaxy.

### 6.1.3 Future Work

For the five new OH detections at 6.0 GHz, future interferometric studies with the EVN or the EVLA will be able to locate where the absorption takes place. This will facilitate a better estimate of the filling factors and more accurate optical depths for absorption, and thus a more confident estimate of the OH column densities. Moreover, higher-resolution studies will be able to better determine the dynamics of the gas in those systems and determine whether it is compatible with a torus-like structure. Also for this purpose and to get a more complete picture of the inner region of these systems, it will be important to compare the OH gas with other molecular or atomic gas components. Also, for the 6 GHz detections, it will be very interesting to look for the 13.4 GHz transition, which require higher excitation, to get a more complete picture of the excitation scenario in those sources. To further investigate where 6.0 GHz OH absorption takes place in Mrk 231, spectral line VLBI observation have been carried out (EVN project, EI007), analysis is in progress. In Cygnus A, a further study will be necessary to confirm this potentially exciting new result. This will require new observations of the source to a higher signal-to-noise ratio. Also for NGC 1052, the kinematics of the gas that was observed in absorption will be studied in detail, to find if the rotation or a redshifted/blueshifted component can be mapped.

As it was shown from the results on NGC 1052, high resolution observations are extremely useful when studying the inner regions of an AGN. With the advent of the EVLA and eMERLIN and increasing bandwidths, we will be able to probe further OH absorption systems to higher redshift, enabling us to study the evolution over time in these sources. While the EVLA will provide a great sensitivity, eMERLIN will provide a better resolution, which will allow detailed studies of the central few parsecs.

## 6.2 A survey for extragalactic methanol

As a follow-up to the Effelsberg hydroxyl survey, the 6.7 GHz transition of methanol was observed in a sub-sample of 10 Seyfert 2 galaxies that had been selected for OH observations. The 6.7 GHz methanol transition is mostly seen in emission and is one of the most prominent Galactic maser lines. It is usually closely associated with OH, in fact these molecules often cohabit (Menten et al. 1992). Because of this, extragalactic searches for methanol have previously mainly targeted known OH megamaser galaxies. Even though these studies were searching for methanol emission at 6.7 GHz, they failed to detect either emission or absorption in any of the surveys. It has, therefore, been suggested that in extragalactic environments either no methanol is formed or methanol is destroyed due to the harsher conditions.

In our survey, the first extragalactic 6.7 GHz methanol transition was observed beyond the Magellanic Clouds towards the nucleus of NGC 3079. Three further tentative detections were made in Mrk 348 also in absorption, and in Mrk 3 and NGC 6240 in emission. It was shown that the 6.7 GHz methanol transition is detectable in AGN, implying significant methanol abundance.

The spectrum obtained toward NGC 3079 shows two absorption components with line-to-continuum ratios of 1/50 and 1/150, respectively. This is the signature of a Class I environment, where the absence of a strong infrared radiation field inhibits the inversion of the level populations. Instead, the line is characterized by “anti-inversion” or “over-cooling”. Most of the absorption is likely to occur toward the nuclear continuum sources A, B, and E, with a column density of  $\sim 1.4 \times 10^{15} \text{ cm}^{-2}$  assuming an excitation temperature,  $T_{\text{ex}}$ , of 43 K. This is comparable to column densities found towards the Galactic centre associated with Sgr B2 of  $3.0 \times 10^{15} \text{ cm}^{-2}$  to  $7.5 \times 10^{18} \text{ cm}^{-2}$  (Houghton & Whiteoak 1995, Peng & Whiteoak 1992). It is, however, unclear if the methanol is associated with the active nucleus or the starburst around the source and possibly connected to the superbubble. The blue-shifted feature in the spectrum also indicates that methanol is present in the large-scale molecular outflows.

In Mrk 3, an emission line was observed near the systemic velocity of the galaxy. The emission seen is intrinsically weak (with a fitted peak flux density of 2.7 mJy) in two of the three observing epochs, which might be caused by variability in the line. If real, it would be the first detection of a class II methanol maser in an extragalactic source. Classical Class II masers directly trace sites of high mass star formation and require warm dust (150 K) and relatively cool gas (Cragg et al. 2005). At the distance of Mrk 3, the line would correspond to an isotropic luminosity of  $2.7 L_{\odot}$ , which is higher than typical methanol masers found in the Galaxy. In Mrk 348 a broad absorption feature was observed at the velocity of the galaxy, with a fitted peak of  $-4.8 \text{ mJy}$  and a FWHM of  $\sim 550 \text{ km s}^{-1}$ . Finally, a tentative detection was made towards the source NGC 6240. The line has a fitted peak of 7.2 mJy ( $3\sigma$ ) with a FWHM of  $\sim 12 \text{ km s}^{-1}$  and a redshift from systemic of  $610 \text{ km s}^{-1}$ , which is quite high. However, large-scale velocity components have been associated with this interacting galaxy.

### 6.2.1 Future Work

Interferometric measurements of NGC 3079 will allow to reliably convert “apparent” into “true” optical depths. To reveal the physical parameters of the interstellar medium traced

by the 6.7 GHz line, the detection of additional methanol lines would be desirable. Suitable candidates are the 12.2 GHz, 36.2 GHz, and 44.1 GHz transitions that should also be mapped, for comparison, toward the Galactic centre region. Also for Mrk 348 and Mrk 3, EVLA observations should be carried out to confirm the detections. Especially in Mrk 348, the very broad profile could be caused by standing waves across the band. Finally for NGC 6240 future single-dish observations should be carried out to confirm the tentative detection.

### 6.3 The detection of water vapour in the early Universe

Luminous extragalactic water masers are known to be associated with the nuclear activity of their host galaxies. So far, VLBI studies indicate that the maser emission originates from within a few parsecs of the central engine, being associated with nuclear accretion disks, interactions between the jet(s) emerging from the nucleus and ambient molecular clouds, and iii) nuclear outflows. Detailed studies of disk masers can trace the geometry of accretion disks, yield estimates of the enclosed masses, determine accurate distances to the parent galaxies with an entirely geometrical method (Herrnstein et al. 1999). Jet-masers can provide information on the evolution of jets and their hot-spots. Furthermore, simultaneous measurements of the line and continuum flux densities, through reverberation mapping, also allows the speed of the material in the jet to be determined (Peck et al. 2003). Finally, outflow-masers trace the velocity and geometry of the nuclear wind.

Recently, the discovery of an  $H_2O$  maser with an apparent isotropic luminosity of  $23\,000 L_\odot$  in the type 2 quasar SDSS J0804+3607 at  $z = 0.66$  (Barvainis & Antonucci 2005) demonstrated that water masers can be detected at higher redshifts. The discovery of water masers at cosmological distances ( $z > 0.3$ ) would allow us to study the parsec-scale environment around powerful radio sources at earlier evolutionary stages, investigate the physical conditions of the molecular gas in the inner parsecs of quasars, measure black-hole masses at earlier epochs, and potentially constrain cosmological parameters.

Here, the detection of the most distant water maser known was reported from the gravitationally lensed quasar MG J0414+0534 at  $z = 2.64$ . With a gravitationally magnified isotropic luminosity of  $300\,000 L_\odot$ , it is by far the most luminous maser known and the first to show significant gravitational amplification. Observations were carried out with the 100 m Effelsberg radio telescope and the Extended Very Large Array (EVLA). This result demonstrates that it is possible to detect water vapour out to cosmological distances with current instrument sensitivities. Although the intrinsic power of the maser is at the upper end of those observed so far, this discovery has been possible only due to the magnification provided by the foreground galaxy; it acts as a cosmic telescope reducing the integration time required for a detection by a factor of  $\sim 1000$ .

#### 6.3.1 Future work

Light was emitted from MG 0414+0534 at a time when the volume density of radio-loud quasars was highest (Dunlop & Peacock 1990). Therefore more such masers may be detectable at this redshift. A follow-up project to study more gravitationally lensed, high-redshift quasars has already been started with Effelsberg observations of another ten candidates. Also, a further source observed with Effelsberg, IRAS F10214+4724, was followed up with the EVLA and the data reduction will be carried out soon.

There are still a few open questions regarding the maser in MG 0414+0534 which, if answered, will lead to a more detailed understanding of the properties in this quasar. For example, is it a jet or disk maser? What is the magnification of the lens? Is the maser varying? High-resolution, global-VLBI experiments are being carried out in continuum at three different frequencies and in spectral line mode at 6 GHz. The continuum observations will help to better constrain the lens models, whereas the spectral line observations will map the location of the maser relative to the source continuum flux density. Lens magnifications can increase the flux density by 10 to 60 times the intrinsic source flux density, but can also increase the spatial resolution by the same factor. The global-VLBI observations will thus allow us to locate whether emission is in the jet, or if it is associated with the accretion disk in the source. The two observations combined will further lead to a more accurate estimate of its true unlensed luminosity.

Also, the maser will be monitored with the Arecibo 305 m telescope in Puerto Rico, to study its variability on short time-scales. Through simultaneous observations of the continuum flux density behaviour of the source, and assuming that the maser originates at the interface between the jet and the ambient medium, we will be able to study the evolution of the jet in the source.

Future systematic searches of high-redshift masers that are not gravitationally lensed will require a significant improvement in instrument sensitivity. The advent of new high-sensitivity facilities with wide spectral bands, such as the EVLA, eMERLIN and the Square Kilometer Array, will allow water masers from a lower luminosity regime to be routinely investigated at even higher source redshifts. The detection of water at a look-back time of 11 Gyr demonstrates that maser observations of highly redshifted sources are possible, opening opening up a huge parameter space for research related to AGN and cosmology in the early Universe.

## Appendix A

### 6016 MHz satellite lines

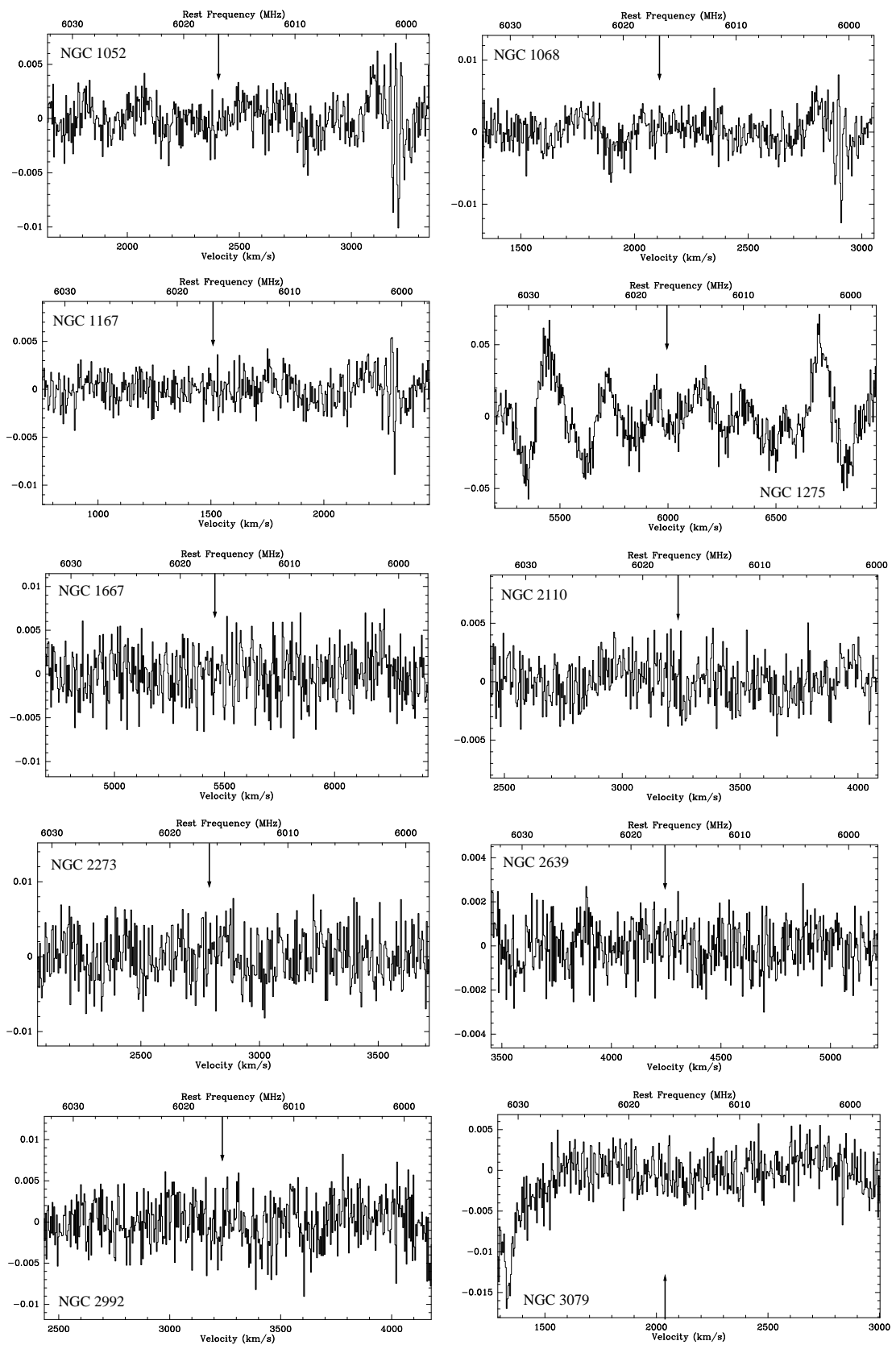


Figure A.1

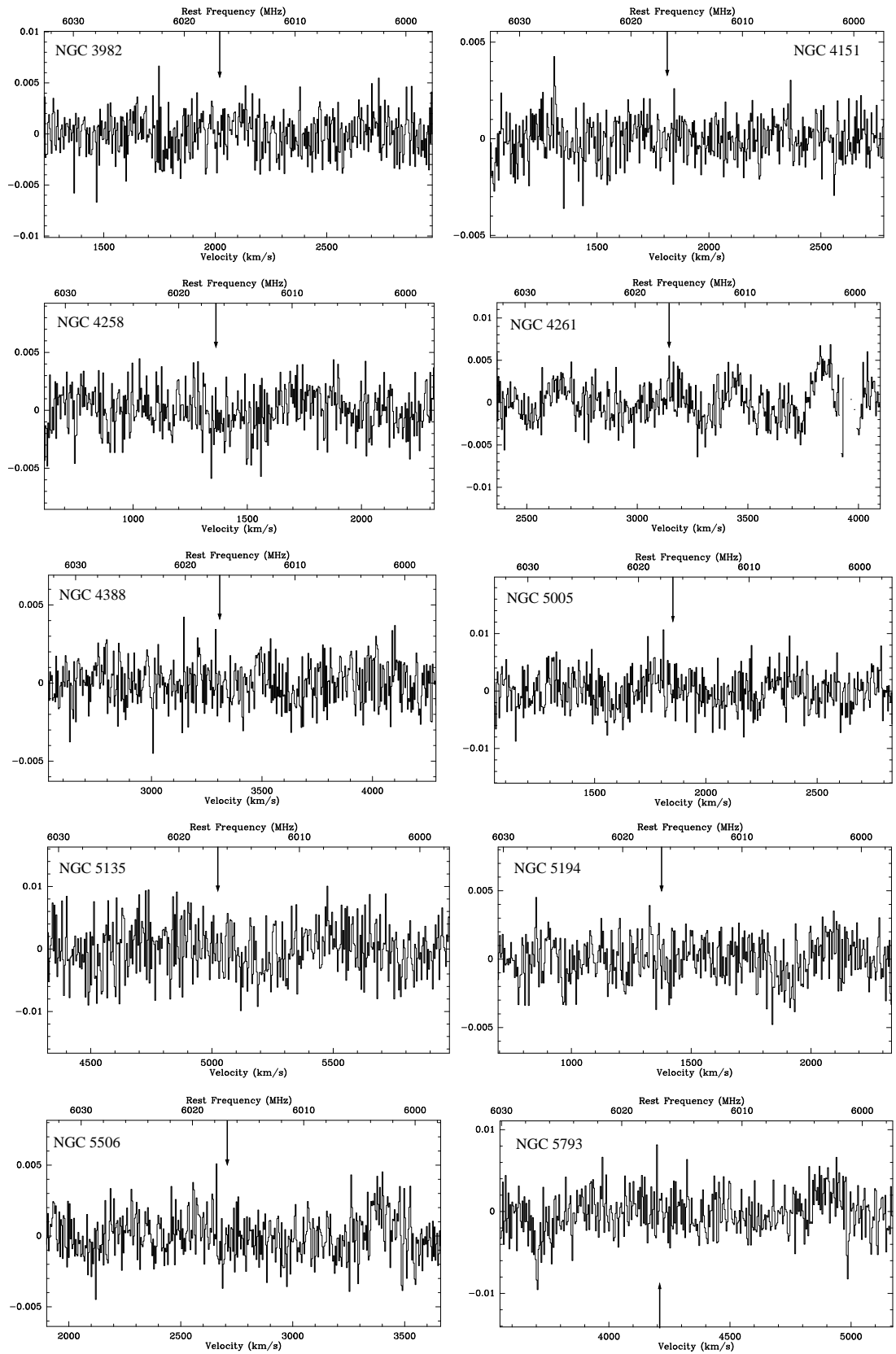


Figure A.1

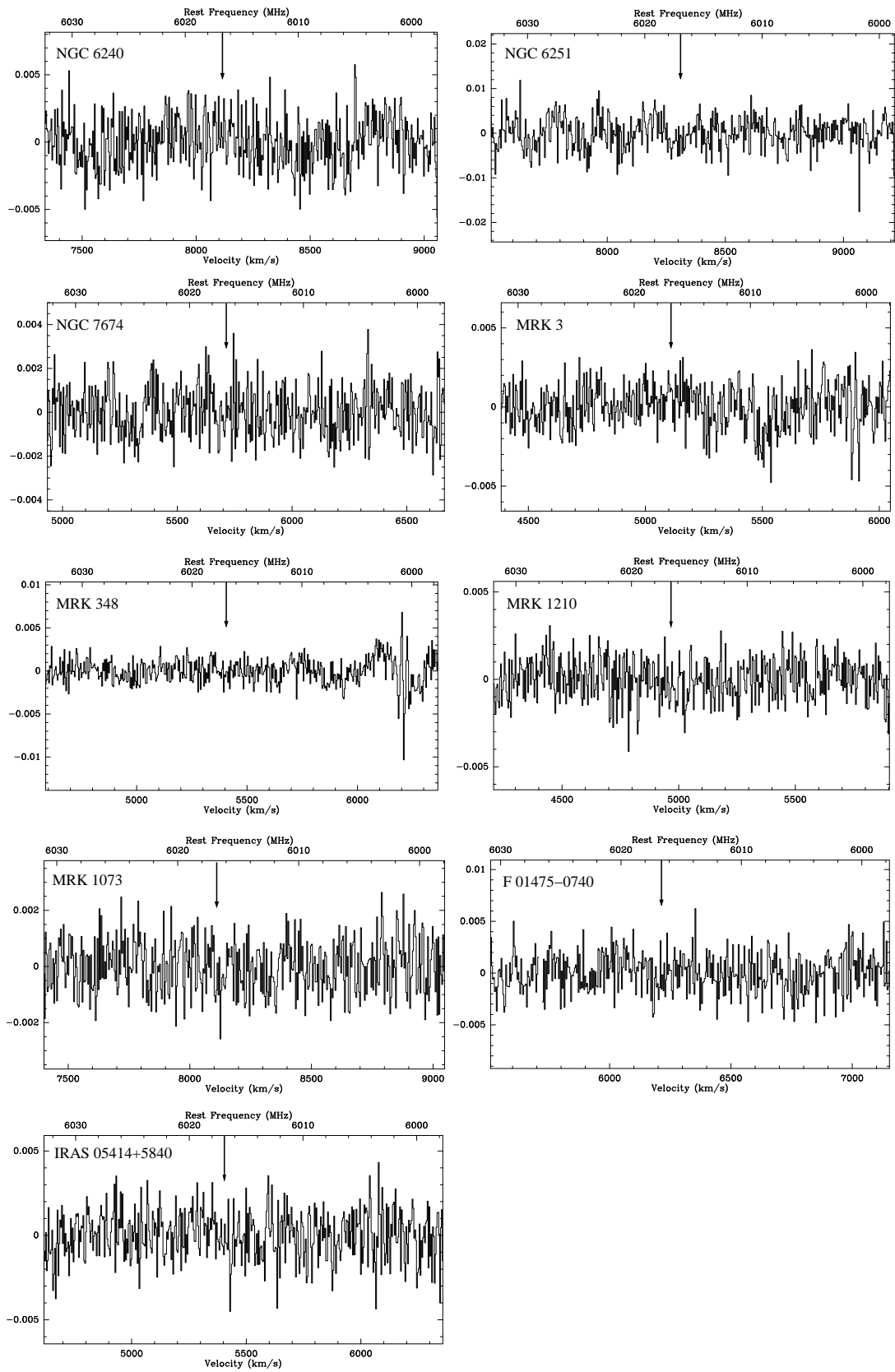


Figure A.1

## Appendix B

### 6049 MHz satellite lines

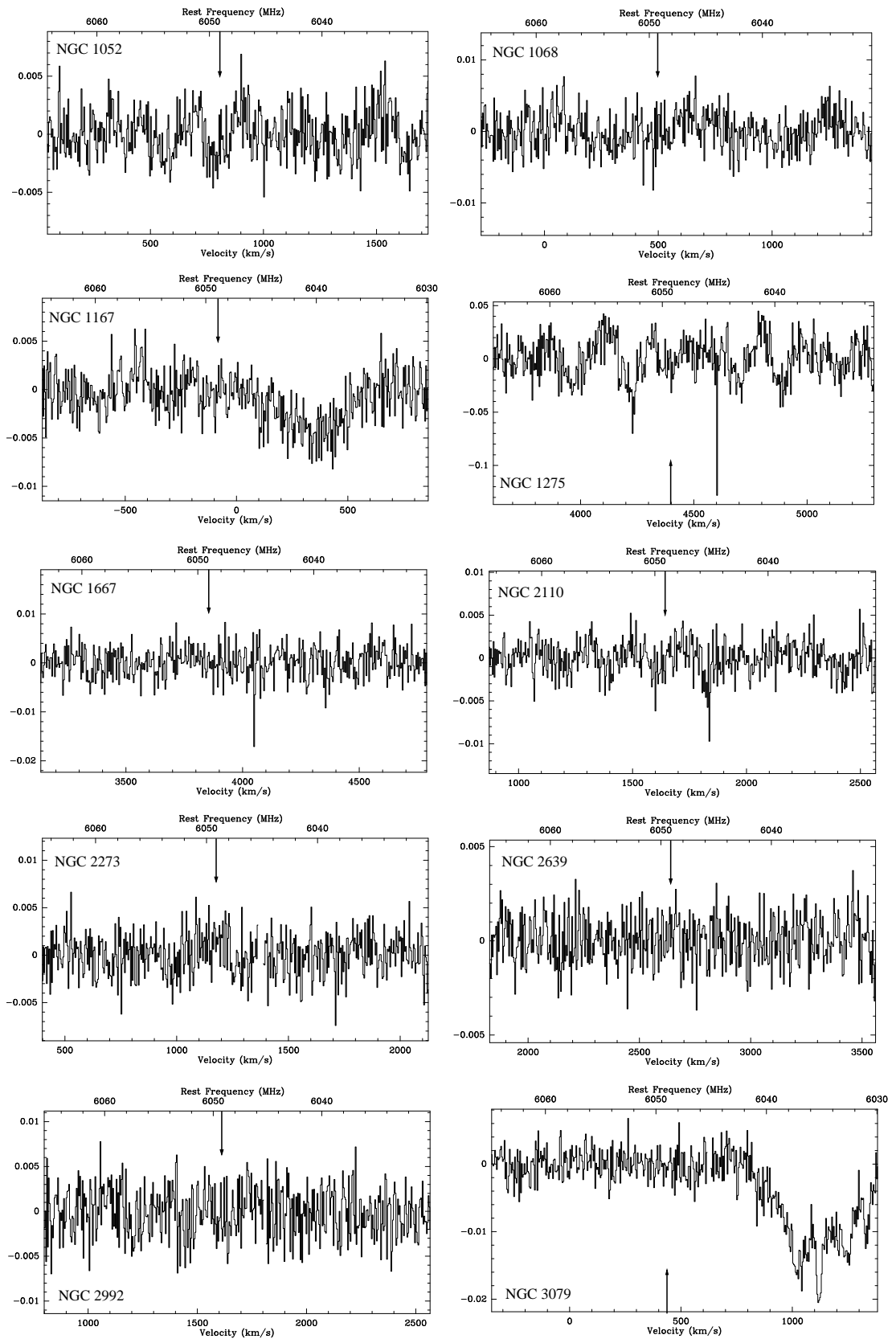


Figure B.1

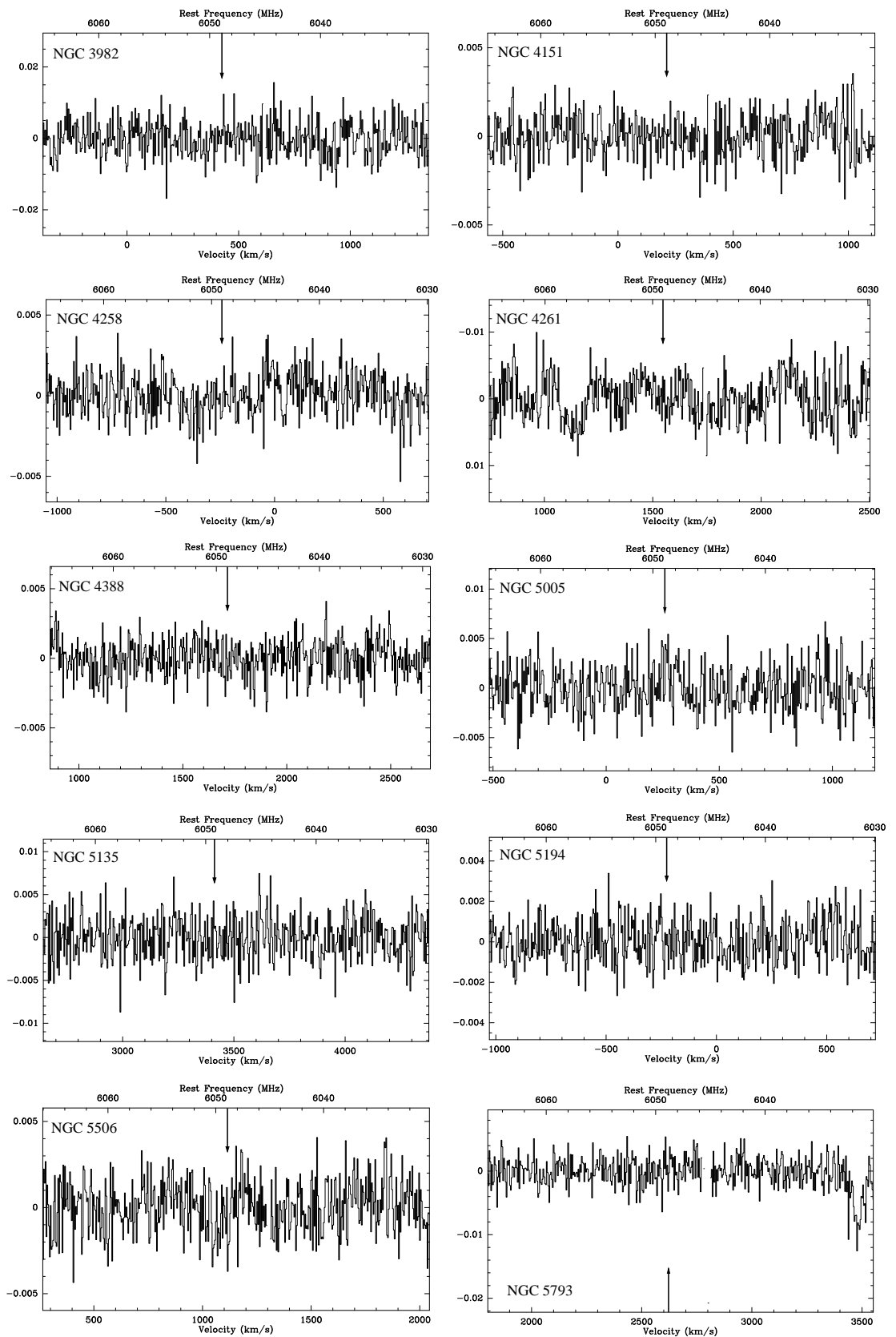


Figure B.1

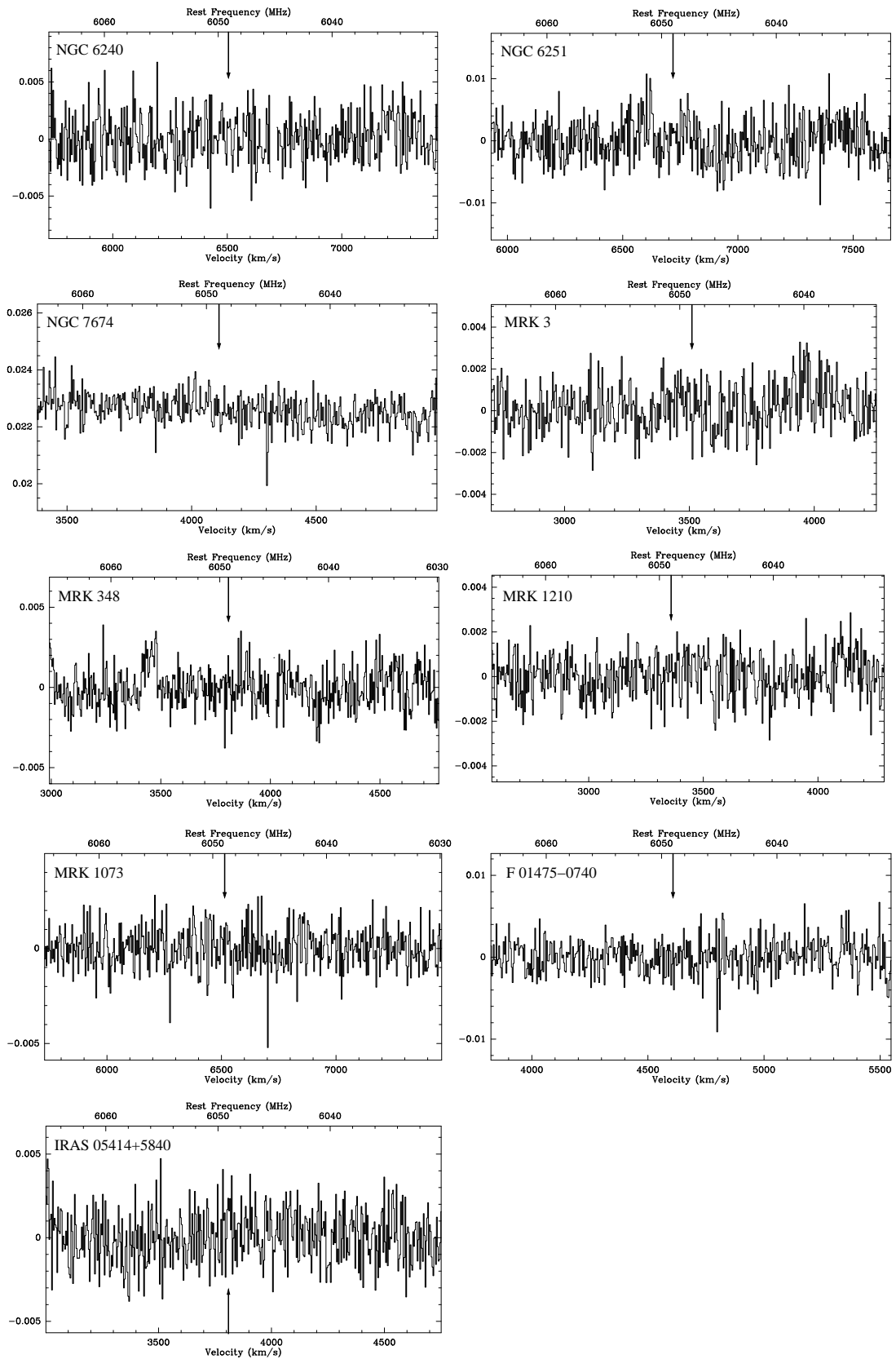


Figure B.1

## Appendix C

### 4765 MHz satellite lines

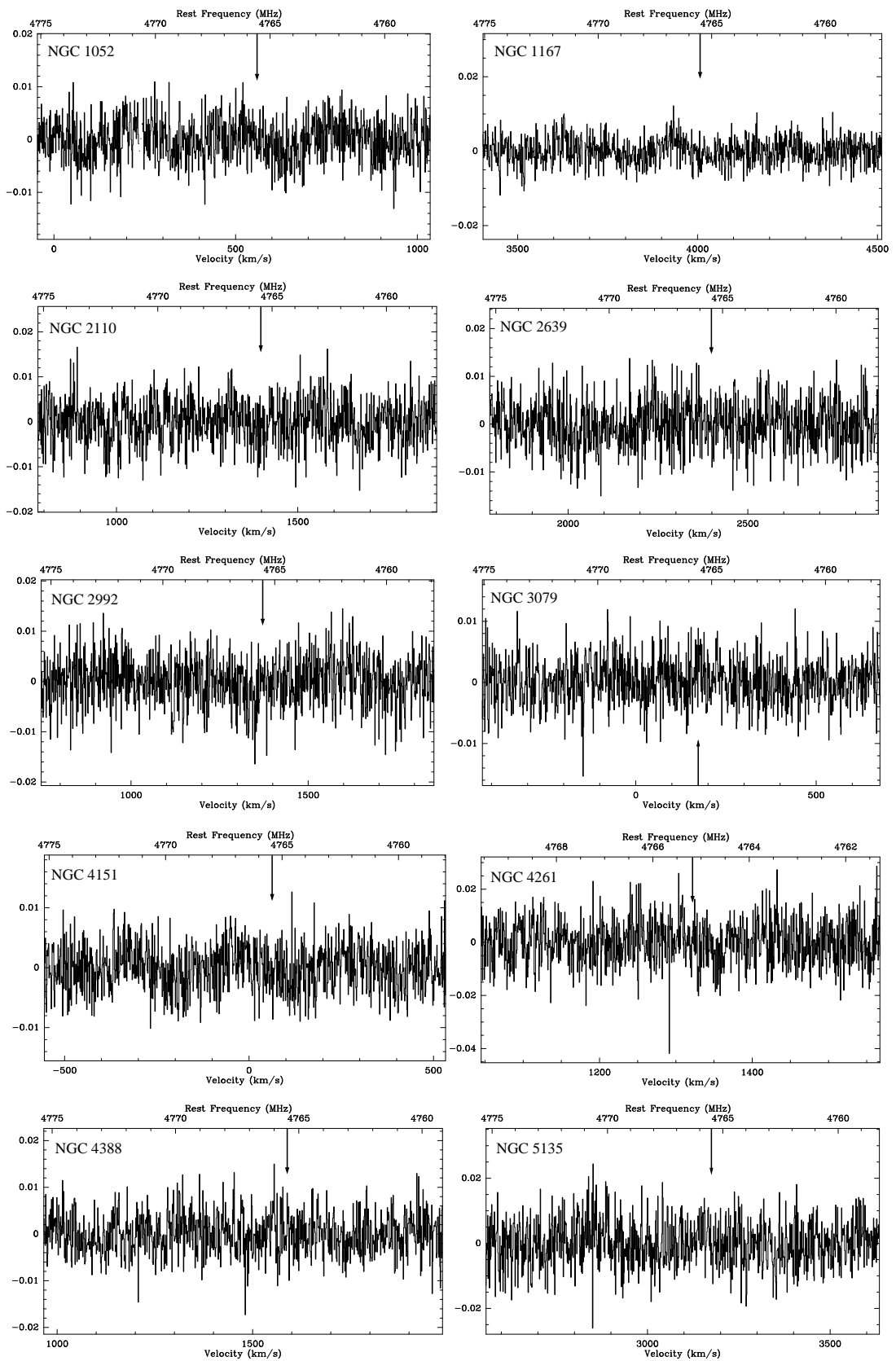


Figure C.1

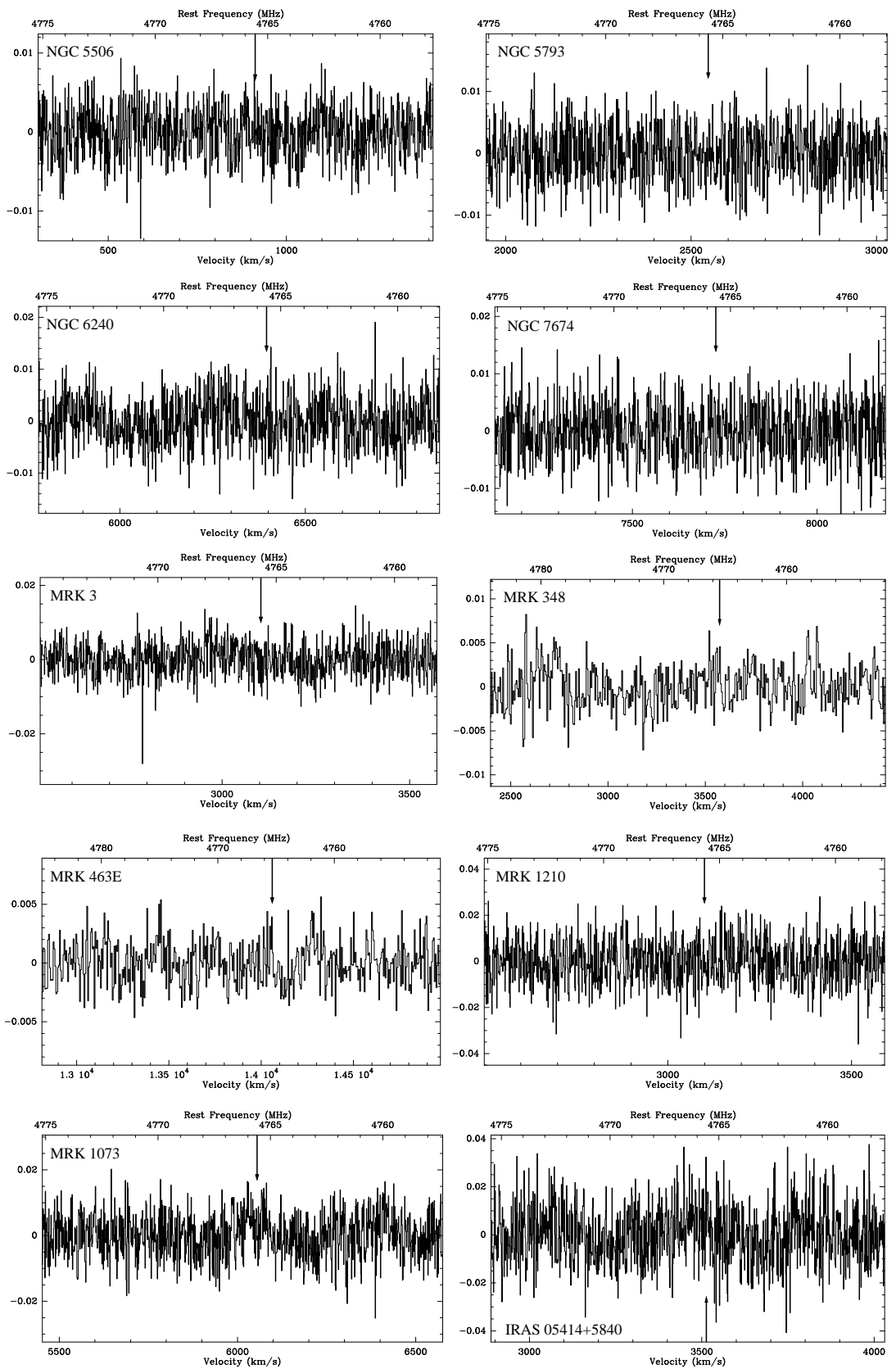


Figure C.1



## Appendix D

### 4660 MHz satellite lines

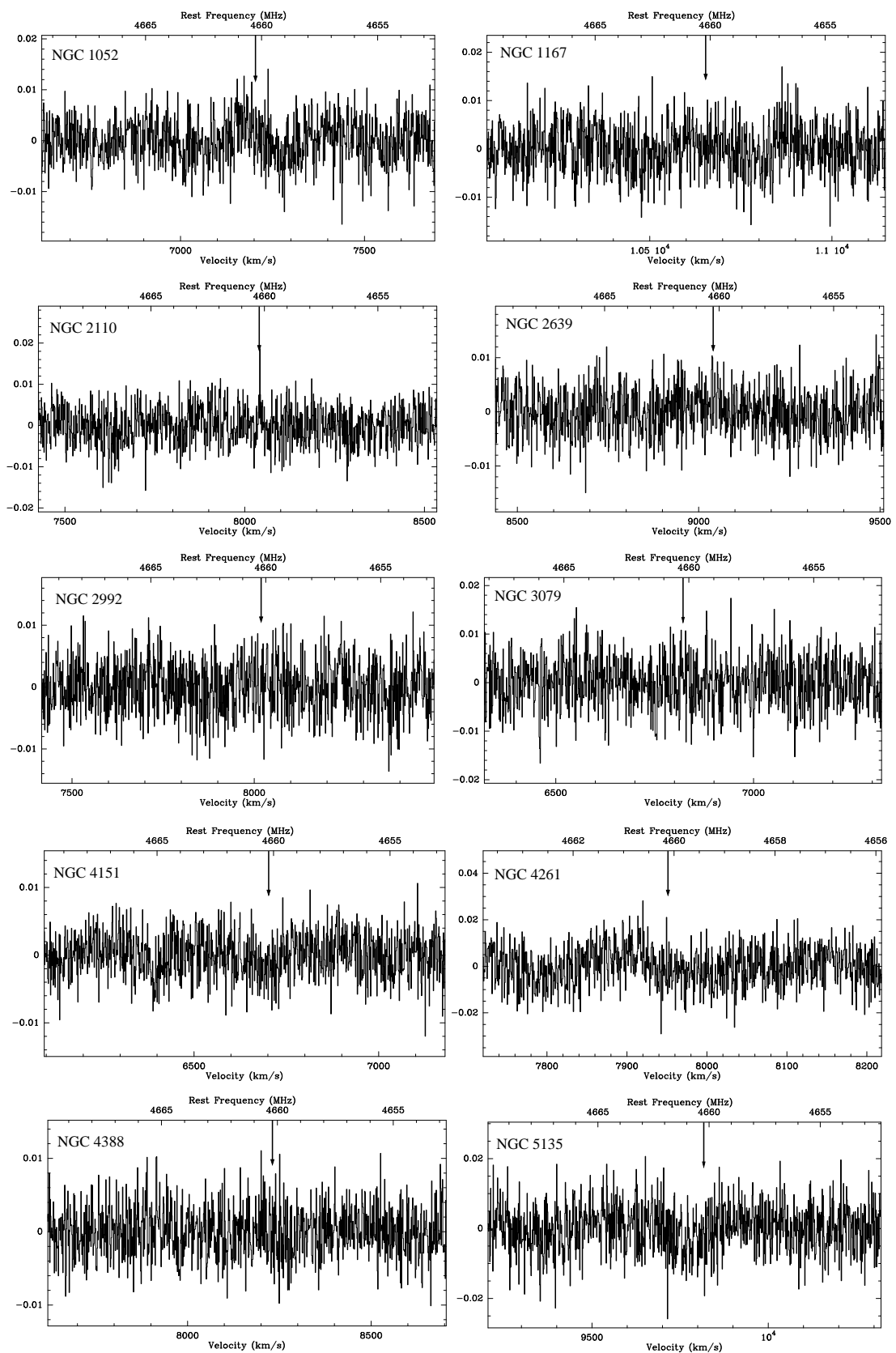


Figure D.1

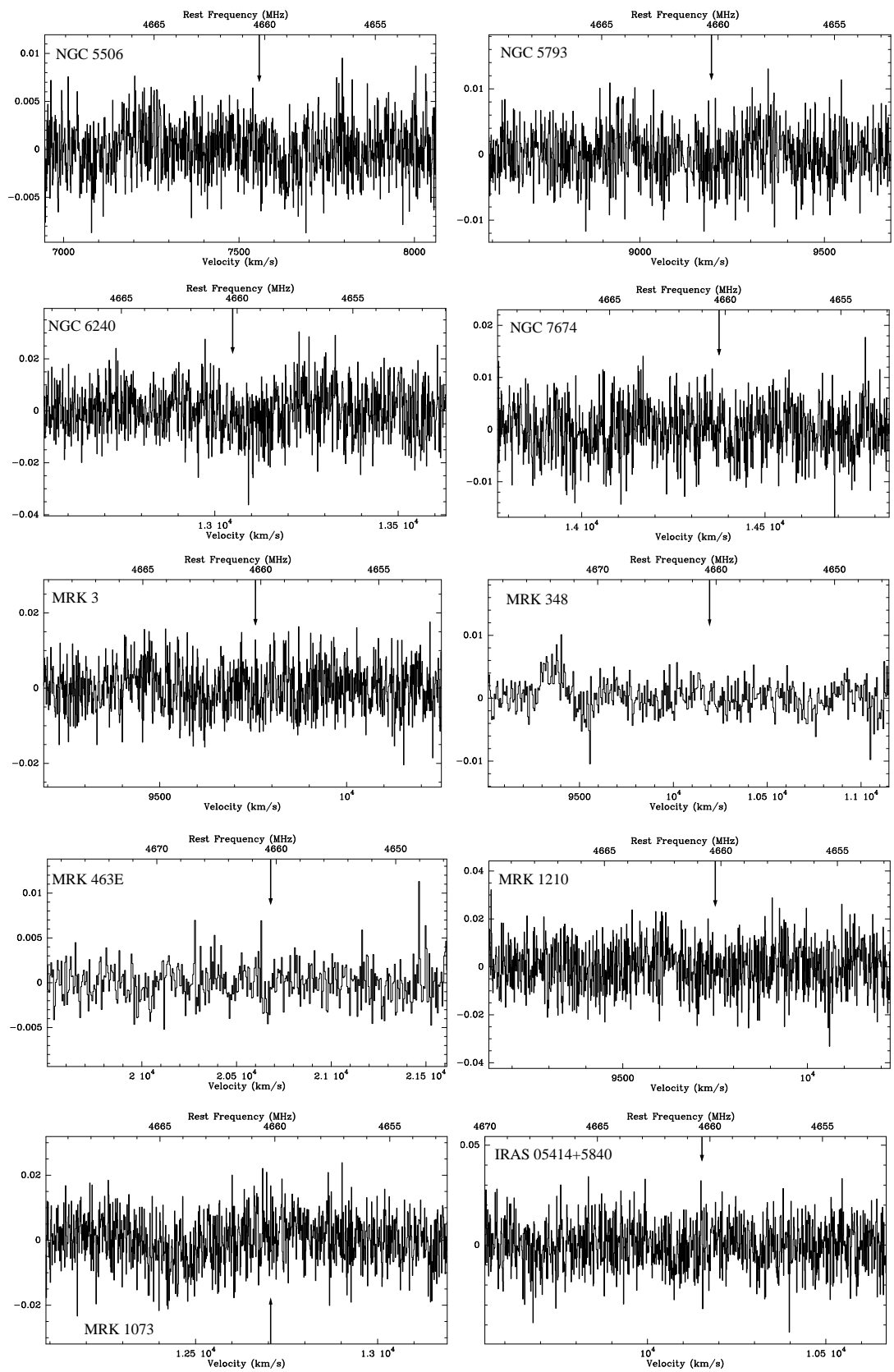


Figure D.1



# Bibliography

- Antonucci, R., & Miller, J. S. 1985, *ApJ*, 297, 621
- Antonucci, R. 1993, *ARA&A*, 31, 473
- Antonucci, R., Hurt, T., & Kinney, A. 1994, *Nature*, 371, 313
- Baade, W., & Minkowski, R. 1954, *ApJ*, 119, 215
- Baan, W. A., Wood, P. A. D., & Haschick, A. D. 1982, *ApJ*, 260, L49
- Baan, W. A. 1985, *Nature*, 315, 26
- Baan, W. A., Haschick, A. D., Buckley, D., & Schmelz, J. T. 1985, *ApJ*, 293, 394
- Baan, W. A., Haschick, A. D., & Henkel, C. 1989, *ApJ*, 346, 680
- Baan, W. A. 1991, *Atoms, Ions and Molecules: New Results in Spectral Line Astrophysics*, 16, 45
- Baan, W. A., Haschick, A., & Henkel, C. 1992, *AJ*, 103, 728
- Baan, W. A., & Irwin, J. A. 1995, *ApJ*, 446, 602
- Baan, W. A., Hagiwara, Y., & Hofner, P. 2007, *ApJ*, 661, 173
- Baars, J. W. M., Genzel, R., Pauliny-Toth, I. I. K., & Witzel, A. 1977, *A&A*, 61, 99
- Barvainis, R. 1987, *ApJ*, 320, 537
- Barvainis, R., & Antonucci, R. 1994, *AJ*, 107, 1291
- Barvainis, R., & Lonsdale, C. 1998, *AJ*, 115, 885
- Barvainis, R., Alloin, D., Guilloteau, S., & Antonucci, R. 1998, *ApJ*, 492, L13
- Barvainis, R., & Antonucci, R. 2005, *ApJ*, 628, L89
- Barth, A. J., Filippenko, A. V., & Moran, E. C. 1999, *ApJ*, 525, 673
- Bassani, L., Dadina, M., Maiolino, R., Salvati, M., Risaliti, G., della Ceca, R., Matt, G., & Zamorani, G. 1999, *ApJS*, 121, 473
- Batrla, W., Matthews, H. E., Menten, K. M., & Walmsley, C. M. 1987, *Nature*, 326, 49

- Baum, S. A., O'Dea, C. P., Dallacassa, D., de Bruyn, A. G., & Pedlar, A. 1993, *ApJ*, 419, 553
- Beasley, A. J., Ellingsen, S. P., Claussen, M. J., & Wilcots, E. 1996, *ApJ*, 459, 600
- Becker, R. H., White, R. L., & Edwards, A. L. 1991, *ApJS*, 75, 1
- Bergman, P., Aalto, S., Black, J. H., & Rydbeck, G. 1992, *A&A*, 265, 403
- Beswick, R. J., Pedlar, A., Mundell, C. G., & Gallimore, J. F. 2001, *MNRAS*, 325, 151
- Beswick, R. J., Pedlar, A., & McDonald, A. R. 2002, *MNRAS*, 335, 1091
- Bianchi, S., Guainazzi, M., Matt, G., Chiaberge, M., Iwasawa, K., Fiore, F., & Maiolino, R. 2005, *A&A*, 442, 185
- Black, J. H. 1998, *The Molecular Astrophysics of Stars and Galaxies*, 469
- Blanco, P. R., Ward, M. J., & Wright, G. S. 1990, *MNRAS*, 242, 4P
- Bland-Hawthorn, J., Wilson, A. S., & Tully, R. B. 1991, *ApJ*, 371, L19
- Boksenberg, A., Carswell, R. F., Allen, D. A., Fosbury, R. A. E., Penston, M. V., & Sargent, W. L. W. 1977, *MNRAS*, 178, 451
- Braatz, J. A., Wilson, A. S., & Henkel, C. 1994, *ApJ*, 437, L99
- Braatz, J. A., Wilson, A. S., & Henkel, C. 1996, *ApJS*, 106, 51
- Braatz, J. A., Wilson, A. S., & Henkel, C. 1997, *ApJS*, 110, 321
- Braatz, J. A., Henkel, C., Greenhill, L. J., Moran, J. M., & Wilson, A. S. 2004, *ApJ*, 617, L29
- Braatz, J. A., & Gugliucci, N. E. 2008, *ApJ*, 678, 96
- Bradt, H. V., Burke, B. F., Canizares, C. R., Greenfield, P. E., Kelley, R. L., McClintock, J. E., Koski, A. T., & van Paradijs, J. 1978, *ApJ*, 226, L111
- Braine, J., Wyrowski, F., Radford, S. J. E., Henkel, C., & Lesch, H. 1995, *A&A*, 293, 315
- Braito, V., et al. 2004, *A&A*, 420, 79
- Bransford, M. A., Appleton, P. N., Heisler, C. A., Norris, R. P., & Marston, A. P. 1998, *ApJ*, 497, 133
- Bryant, P. M., & Scoville, N. Z. 1996, *ApJ*, 457, 678
- Bryant, P. M., & Scoville, N. Z. 1999, *AJ*, 117, 2632
- Canalizo, G., & Stockton, A. 2000, *AJ*, 120, 1750
- Capetti, A., Axon, D. J., Macchetto, F., Sparks, W. B., & Boksenberg, A. 1996, *ApJ*, 469, 554

- Carilli, C. L., Wrobel, J. M., & Ulvestad, J. S. 1998, *AJ*, 115, 928
- Carilli, C. L., & Taylor, G. B. 2000, *ApJ*, 532, L95
- Cecil, G., Bland-Hawthorn, J., Veilleux, S., & Filippenko, A. V. 2001, *ApJ*, 555, 338
- Cecil, G., Bland-Hawthorn, J., & Veilleux, S. 2002, *ApJ*, 576, 745
- Chen, J., Rozo, E., Dalal, N., & Taylor, J. E. 2007, *ApJ*, 659, 52
- Chengalur, J. N., de Bruyn, A. G., & Narasimha, D. 1999, *A&A*, 343, L79
- Chiaberge, M., Gilli, R., Macchetto, F. D., Sparks, W. B., & Capetti, A. 2003, *ApJ*, 582, 645
- Clark, B. G. 1980, *A&A*, 89, 377
- Claussen, M. J., & Lo, K.-Y. 1986, *ApJ*, 308, 592
- Claussen, M. J., Diamond, P. J., Braatz, J. A., Wilson, A. S., & Henkel, C. 1998, *ApJ*, 500, L129
- Colbert, E. J. M., Wilson, A. S., & Bland-Hawthorn, J. 1994, *ApJ*, 436, 89
- Comastri, A. 2004, *Supermassive Black Holes in the Distant Universe*, 308, 245
- Combes, F. 2001, *Galaxy Disks and Disk Galaxies*, 230, 213
- Condon, J. J., Helou, G., Sanders, D. B., & Soifer, B. T. 1996, *ApJS*, 103, 81
- Conway, J. E. 1999, *New Astronomy Review*, 43, 509
- Conway, J. E., & Blanco, P. R. 1995, *ApJ*, 449, L131
- Conselice, C. J., Gallagher, J. S., III, & Wyse, R. F. G. 2001, *AJ*, 122, 2281
- Cragg, D. M., Sobolev, A. M., & Godfrey, P. D. 2005, *MNRAS*, 360, 533
- Curran, S. J., Darling, J., Bolatto, A. D., Whiting, M. T., Bignell, C., & Webb, J. K. 2007, *MNRAS*, 382, L11
- Dahlem, M., Weaver, K. A., & Heckman, T. M. 1998, *ApJS*, 118, 401
- Darling, J., & Giovanelli, R. 2002, *AJ*, 124, 100
- Darling, J., Goldsmith, P., Li, D., & Giovanelli, R. 2003, *AJ*, 125, 1177
- Davies, R. I., et al. 2006, *ApJ*, 646, 754
- de Vaucouleurs, G., de Vaucouleurs, A., Corwin, H. G., Jr., Buta, R. J., Paturel, G., & Fouque, P. 1991, *Volume 1-3, XII*, 2069 pp. 7
- Diamond, P. J., Lonsdale, C. J., Lonsdale, C. J., & Smith, H. E. 1999, *ApJ*, 511, 178
- Dickey, J. M. 1982, *ApJ*, 263, 87

- Downes, D., & Solomon, P. M. 1998, *ApJ*, 507, 615
- Drinkwater, M. J., et al. 1997, *MNRAS*, 284, 85
- Dunlop, J. S., & Peacock, J. A. 1990, *MNRAS*, 247, 19
- Duric, N., & Seaquist, E. R. 1988, *ApJ*, 326, 574
- Eddington, A. S. 1925, *MNRAS*, 85, 408
- Edelson, R. A. 1987, *ApJ*, 313, 651
- Elíasdóttir, Á., Hjorth, J., Toft, S., Burud, I., & Paraficz, D. 2006, *ApJS*, 166, 443
- Elitzur, M. 2006, *New Astronomy Review*, 50, 728
- Ellingsen, S. P., Whiteoak, J. B., Norris, R. P., Caswell, J. L., & Vaile, R. A. 1994a, *MNRAS*, 269, 1019
- Ellingsen, S. P., Norris, R. P., Whiteoak, J. B., Vaile, R. A., McCulloch, P. M., & Price, M. G. 1994b, *MNRAS*, 267, 510
- Ellingsen, S. P., von Bibra, M. L., McCulloch, P. M., Norris, R. P., Deshpande, A. A., & Phillips, C. J. 1996, *MNRAS*, 280, 378
- Elvis, M., Briel, U. G., & Henry, J. P. 1983, *ApJ*, 268, 105
- Elvis, M., Risaliti, G., Nicastro, F., Miller, J. M., Fiore, F., & Puccetti, S. 2004, *ApJ*, 615, L25
- Evans, I. N., Ford, H. C., Kinney, A. L., Antonucci, R. R. J., Armus, L., & Caganoff, S. 1991, *ApJ*, 369, L27
- Evans, D. A., Worrall, D. M., Hardcastle, M. J., Kraft, R. P., & Birkinshaw, M. 2006, *ApJ*, 642, 96
- Fabian, A. C., & Rees, M. J. 1995, *MNRAS*, 277, L55
- Falco, E. E., et al. 1999a, *PASP*, 111, 438
- Falco, E. E., et al. 1999b, *ApJ*, 523, 617
- Fanaroff, B. L., & Riley, J. M. 1974, *MNRAS*, 167, 31P
- Fath, E. A. 1908, *Lick Observatory Bulletin*, 5, 71
- Ferrarese, L., Ford, H. C., & Jaffe, W. 1996, *ApJ*, 470, 444
- Ferrarese, L., & Ford, H. C. 1999, *ApJ*, 515, 583
- Filippenko, A. V., & Sargent, W. L. W. 1985, *ApJS*, 57, 503
- Filippenko, A. V., & Sargent, W. L. W. 1992, *AJ*, 103, 28
- Ford, H. C., Dahari, O., Jacoby, G. H., Crane, P. C., & Ciardullo, R. 1986, *ApJ*, 311, L7

- Fosbury, R. A. E., & Wall, J. V. 1979, MNRAS, 189, 79
- Francis, P. J., Hewett, P. C., Foltz, C. B., Chaffee, F. H., Weymann, R. J., & Morris, S. L. 1991, ApJ, 373, 465
- Fried, J. W., & Schulz, H. 1983, A&A, 118, 166
- Fuente, A., Black, J. H., Martín-Pintado, J., Rodríguez-Franco, A., García-Burillo, S., Planesas, P., & Lindholm, J. 2000, ApJ, 545, L113
- Gallimore, J. F., Baum, S. A., O’Dea, C. P., Brinks, E., & Pedlar, A. 1996, ApJ, 462, 740
- Gallimore, J. F., Baum, S. A., O’Dea, C. P., Pedlar, A., & Brinks, E. 1999, ApJ, 524, 684
- Gallimore, J. F., & Beswick, R. 2004, AJ, 127, 239
- Gardner, F. F., & Whiteoak, J. B. 1986, MNRAS, 221, 537
- Gardner, F. F., Whiteoak, J. B., Norris, R. P., & Diamond, P. J. 1992, MNRAS, 258, 296
- Garwood, R. W., Dickey, J. M., & Helou, G. 1987, ApJ, 322, 88
- Ghisellini, G., Haardt, F., & Matt, G. 1994, MNRAS, 267, 743
- Ghosh, H., Pogge, R. W., Mathur, S., Martini, P., & Shields, J. C. 2007, ApJ, 656, 105
- Gilli, R., Maiolino, R., Marconi, A., Risaliti, G., Dadina, M., Weaver, K. A., & Colbert, E. J. M. 2000, A&A, 355, 485
- Gillmon, K., Sanders, J. S., & Fabian, A. C. 2004, MNRAS, 348, 159
- Giovannini, G., Cotton, W. D., Feretti, L., Lara, L., & Venturi, T. 2001, ApJ, 552, 508
- Goodrich, R. W., Veilleux, S., & Hill, G. J. 1994, ApJ, 422, 521
- González Delgado, R. M., Heckman, T., & Leitherer, C. 2001, ApJ, 546, 845
- Granato, G. L., & Danese, L. 1994, MNRAS, 268, 235
- Greenhill, L. J., Jiang, D. R., Moran, J. M., Reid, M. J., Lo, K. Y., & Claussen, M. J. 1995, ApJ, 440, 619
- Greenhill, L. J., & Gwinn, C. R. 1997, Astrophysics and Space Science, 248, 261
- Greenhill, L. J., et al. 2003, ApJ, 590, 162
- Greenhill, L. J. 2004, New Astronomy Review, 48, 1079
- Gregory, P. C., & Condon, J. J. 1991, ApJS, 75, 1011
- Griffiths, R. E., Schwartz, D. A., Schwarz, J., Doxsey, R. E., Johnston, M. D., & Blades, J. C. 1979, ApJ, 230, L21
- Griffith, M. R., Wright, A. E., Burke, B. F., & Ekers, R. D. 1994, ApJS, 90, 179
- Gu, Q., Maiolino, R., & Dultzin-Hacyan, D. 2001, A&A, 366, 765

- Guainazzi, M., & Antonelli, L. A. 1999, MNRAS, 304, L15
- Guainazzi, M., Oosterbroek, T., Antonelli, L. A., & Matt, G. 2000, A&A, 364, L80
- Guainazzi, M., Matt, G., Fiore, F., & Perola, G. C. 2002, A&A, 388, 787
- Guainazzi, M., Grandi, P., Comastri, A., & Matt, G. 2003, A&A, 410, 131
- Gupta, N., Salter, C. J., Saikia, D. J., Ghosh, T., & Jeyakumar, S. 2006, MNRAS, 373, 972
- Halkides, D., Ulvestad, J., & Roy, A. 1997, Bulletin of the American Astronomical Society, 29, 1375
- Hagiwara, Y., Kohno, K., Kawabe, R., & Nakai, N. 1997, PASJ, 49, 171
- Hagiwara, Y., Diamond, P. J., Nakai, N., & Kawabe, R. 2000, A&A, 360, 49
- Hagiwara, Y., Henkel, C., Sherwood, W. A., & Baan, W. A. 2002, A&A, 387, L29
- Hagiwara, Y., Diamond, P. J., Miyoshi, M., Rovilos, E., & Baan, W. 2003, MNRAS, 344, L53
- Hagiwara, Y., Klöckner, H.-R., & Baan, W. 2004, MNRAS, 353, 1055
- Haschick, A. D., & Baan, W. A. 1985, Nature, 314, 144
- Haschick, A. D., Baan, W. A., Schneps, M. H., Reid, M. J., Moran, J. M., & Guesten, R. 1990, ApJ, 356, 149
- Heckman, T. M., Sancisi, R., Balick, B., & Sullivan, W. T., III 1982, MNRAS, 199, 425
- Henkel, C., Guesten, R., Downes, D., Thum, C., Wilson, T. L., & Biermann, P. 1984, A&A, 141, L1
- Henkel, C., Guesten, R., & Batrla, W. 1986a, A&A, 168, L13
- Henkel, C., Wouterloot, J. G. A., & Bally, J. 1986b, A&A, 155, 193
- Henkel, C., Guesten, R., & Baan, W. A. 1987a, A&A, 185, 14
- Henkel, C., Jacq, T., Mauersberger, R., Menten, K. M., & Steppe, H. 1987b, A&A, 188, L1
- Herrnstein, J. R., Moran, J. M., Greenhill, L. J., Diamond, P. J., Miyoshi, M., Nakai, N., & Inoue, M. 1997, ApJ, 475, L17
- Herrnstein, J. R., Greenhill, L. J., Moran, J. M., Diamond, P. J., Inoue, M., Nakai, N., & Miyoshi, M. 1998, ApJ, 497, L69
- Herrnstein, J. R., et al. 1999, Nature, 400, 539
- Hewitt, J. N., Turner, E. L., Lawrence, C. R., Schneider, D. P., & Brody, J. P. 1992, AJ, 104, 968

- Ho, L. C., Filippenko, A. V., & Sargent, W. L. W. 1993, *ApJ*, 417, 63
- Hogbom, J. A. 1984, *Indirect Imaging. Measurement and Processing for Indirect Imaging*, 247
- Houghton, S., & Whiteoak, J. B. 1995, *MNRAS*, 273, 1033
- Hubble, E., & Humason, M. L. 1931, *ApJ*, 74, 43
- Humason, M. L. 1932, *PASP*, 44, 267
- Ho, L. C., Filippenko, A. V., Sargent, W. L. W., & Peng, C. Y. 1997, *ApJS*, 112, 391
- Hopkins, A. M., & Beacom, J. F. 2006, *ApJ*, 651, 142
- Hopkins, P. F., Bundy, K., Hernquist, L., & Ellis, R. S. 2007, *ApJ*, 659, 976
- Humphreys, E. M. L., Argon, A. L., Greenhill, L. J., Reid, M. J., & Moran, J. M. 2005, *Astrophysics and Space Science*, 295, 285
- Hutchings, J. B., & Neff, S. G. 1987, *Observational Evidence of Activity in Galaxies*, 121, 399
- Ikebe, Y., Leighly, K., Tanaka, Y., Nakagawa, T., Terashima, Y., & Komossa, S. 2000, *MNRAS*, 316, 433
- Inoue, M. Y., Kamenno, S., Kawabe, R., Inoue, M., Hasegawa, T., & Tanaka, M. 1996, *AJ*, 111, 1852
- Irwin, J. A., & Seaquist, E. R. 1988, *ApJ*, 335, 658
- Irwin, J. A., & Seaquist, E. R. 1991, *ApJ*, 371, 111
- Irwin, J. A., & Sofue, Y. 1992, *ApJ*, 396, L75
- Ishihara, Y., Nakai, N., Iyomoto, N., Makishima, K., Diamond, P., & Hall, P. 2001, *PASJ*, 53, 215
- Iwasawa, K., Yaqoob, T., Awaki, H., & Ogasaka, Y. 1994, *PASJ*, 46, L167
- Iwasawa, K., Fabian, A. C., & Matt, G. 1997, *MNRAS*, 289, 443
- Iwasawa, K., & Comastri, A. 1998, *MNRAS*, 297, 1219
- Iyomoto, N., Fukazawa, Y., Nakai, N., & Ishihara, Y. 2001, *ApJ*, 561, L69
- Jaffe, W., & McNamara, B. R. 1994, *ApJ*, 434, 110
- Jaffe, W., et al. 2004, *Nature*, 429, 47
- Jaffe, W., Ford, H., Ferrarese, L., van den Bosch, F., & O'Connell, R. W. 1996, *ApJ*, 460, 214
- Jenkins, C. R. 1983, *MNRAS*, 205, 1321

- Jones, D. L., et al. 1986, *ApJ*, 305, 684
- Jones, D. L., & Wehrle, A. E. 1997, *ApJ*, 484, 186
- Jones, D. L., Wehrle, A. E., Piner, B. G., & Meier, D. L. 2001, *ApJ*, 553, 968
- Kadler, M., Ros, E., Kerp, J., Falcke, H., Zensus, J. A., Pogge, R. W., & Bicknell, G. V. 2003, *New Astronomy Review*, 47, 569
- Kadler, M., Kerp, J., Ros, E., Falcke, H., Pogge, R. W., & Zensus, J. A. 2004, *A&A*, 420, 467
- Kameno, S., Sawada-Satoh, S., Inoue, M., Shen, Z.-Q., & Wajima, K. 2001, *PASJ*, 53, 169
- Kartje, J. F., Königl, A., & Elitzur, M. 1999, *ApJ*, 513, 180
- Katz, C. A., Moore, C. B., & Hewitt, J. N. 1997, *ApJ*, 475, 512
- Keel, W. C. 1983, *ApJS*, 52, 229
- Keel, W. C. 1984, *ApJ*, 282, 75
- Kennicutt, R. C., Jr. 1992, *ApJS*, 79, 255
- Kinney, A. L., Bohlin, R. C., Calzetti, D., Panagia, N., & Wyse, R. F. G. 1993, *ApJS*, 86, 5
- Klöckner, H.-R., Baan, W. A., & Garrett, M. A. 2003, *Nature*, 421, 821
- Klöckner, H.-R., & Baan, W. A. 2004, *A&A*, 419, 887
- Klöckner 2004, Ph.D Thesis
- Knop, R. A., Armus, L., Matthews, K., Murphy, T. W., & Soifer, B. T. 2001, *AJ*, 122, 764
- Koda, J., Sofue, Y., Kohno, K., Nakanishi, H., Onodera, S., Okumura, S. K., & Irwin, J. A. 2002, *ApJ*, 573, 105
- Koekemoer, A. M., Henkel, C., Greenhill, L. J., Dey, A., van Breugel, W., Codella, C., & Antonucci, R. 1995, *Nature*, 378, 697
- Kollatschny, W., & Fricke, K. J. 1989, *A&A*, 219, 34
- Komossa, S., Burwitz, V., Hasinger, G., Predehl, P., Kaastra, J. S., & Ikebe, Y. 2003, *ApJ*, 582, L15
- Kondratko, P. T., Greenhill, L. J., & Moran, J. M. 2005, *ApJ*, 618, 618
- Kondratko, P. T., Greenhill, L. J., & Moran, J. M. 2008, *ApJ*, 678, 87
- Koopmans, L. V. E., Treu, T., Bolton, A. S., Burles, S., & Moustakas, L. A. 2006, *ApJ*, 649, 599
- Koski, A. T. 1978, *ApJ*, 223, 56

- Krolik, J. H., & Begelman, M. C. 1986, *ApJ*, 308, L55
- Krolik, J. H., & Begelman, M. C. 1988, *ApJ*, 329, 702
- Krolik, J. H., & Lepp, S. 1989, *ApJ*, 347, 179
- Krolik, J. H. 1999, *ApJ*, 515, L73
- Krolik, J. H. 2007, *ApJ*, 661, 52
- Kukula, M. J., Ghosh, T., Pedlar, A., Schilizzi, R. T., Miley, G. K., de Bruyn, A. G., & Saikia, D. J. 1993, *MNRAS*, 264, 893
- Lawrence, A., Ward, M., Elvis, M., Fabbiano, G., Willner, S. P., Carleton, N. P., & Longmore, A. 1985, *ApJ*, 291, 117
- Lawrence, C. R., Cohen, J. G., & Oke, J. B. 1995a, *AJ*, 110, 2583
- Lawrence, C. R., Elston, R., Januzzi, B. T., & Turner, E. L. 1995b, *AJ*, 110, 2570
- Lawrence, C. R., Zucker, J. R., Readhead, A. C. S., Unwin, S. C., Pearson, T. J., & Xu, W. 1996, *ApJS*, 107, 541
- Laurini 2004, Ph.D Thesis
- Laurini, S., Schilke, P., Menten, K. M., Flower, D. R., Pottage, J. T., & Xu, L.-H. 2004, *A&A*, 422, 573
- Levenson, N. A., Weaver, K. A., & Heckman, T. M. 2001, *ApJ*, 550, 230
- Levenson, N. A., Weaver, K. A., Heckman, T. M., Awaki, H., & Terashima, Y. 2004, *ApJ*, 602, 135
- Liszt, H., & Lucas, R. 2004, *A&A*, 428, 445
- Lo, K. Y. 2005, *ARA&A*, 43, 625
- Lonsdale, C. J., Lonsdale, C. J., Diamond, P. J., & Smith, H. E. 1998, *ApJ*, 493, L13
- Lonsdale, C. J., Lonsdale, C. J., Smith, H. E., & Diamond, P. J. 2003, *ApJ*, 592, 804
- Lumsden, S. L., Alexander, D. M., & Hough, J. H. 2004, *MNRAS*, 348, 1451
- Lutz, D., Maiolino, R., Moorwood, A. F. M., Netzer, H., Wagner, S. J., Sturm, E., & Genzel, R. 2002, *A&A*, 396, 439
- Lynden-Bell, D. 1969, *Nature*, 223, 690
- Maccacaro, T., Perola, G. C., & Elvis, M. 1982, *ApJ*, 257, 47
- Maia, M. A. G., Machado, R. S., & Willmer, C. N. A. 2003, *AJ*, 126, 1750
- Maiolino, R., & Rieke, G. H. 1995, *ApJ*, 454, 95
- Maiolino, R., Salvati, M., Bassani, L., Dadina, M., della Ceca, R., Matt, G., Risaliti, G., & Zamorani, G. 1998, *A&A*, 338, 781

- Makishima, K., et al. 1994, PASJ, 46, L77
- Malaguti, G., et al. 1998, A&A, 331, 519
- Malaguti, G., et al. 1999, A&A, 342, L41
- Maloney, P. R., Begelman, M. C., & Rees, M. J. 1994, ApJ, 432, 606
- Maloney, P. R. 2002, Publications of the Astronomical Society of Australia, 19, 401
- Mangum, J. G., Darling, J., Menten, K. M., & Henkel, C. 2008, ApJ, 673, 832
- Matt, G. 1997, Memorie della Societa Astronomica Italiana, 68, 127
- Matt, G., et al. 1997, A&A, 325, L13
- Matt, G., Fabian, A. C., Guainazzi, M., Iwasawa, K., Bassani, L., & Malaguti, G. 2000, MNRAS, 318, 173
- Matveyenko, L. I., Zakharin, K., Diamond, P. J., & Graham, D. A. 2003, Ap&SS, 287, 187
- McClintock, J. E., Remillard, R. A., Canizares, C. R., Veron, P., & van Paradijs, J. 1979, ApJ, 233, 809
- McKean, J. P., et al. 2007, MNRAS, 378, 109
- Meier, D. L. 2002, New Astronomy Review, 46, 247
- Menten, K. M. 1991, ApJ, 380, L75
- Menten, K. M., Reid, M. J., Pratap, P., Moran, J. M., & Wilson, T. L. 1992, ApJ, 401, L39
- Menten, K. M., Reid, M. J., Pratap, P., Moran, J. M., & Wilson, T. L. 1993, Sub-arcsecond Radio Astronomy, 78
- Middelberg, E., Agudo, I., Roy, A. L., & Krichbaum, T. P. 2007, MNRAS, 377, 731
- Miller, J. S., & Goodrich, R. W. 1990, ApJ, 355, 456
- Minezaki, T., Yoshii, Y., Kobayashi, Y., Enya, K., Suganuma, M., Tomita, H., Aoki, T., & Peterson, B. A. 2004, ApJ, 600, L35
- Mirabel, I. F. 1982, ApJ, 260, 75
- Miyoshi, M., Moran, J., Herrnstein, J., Greenhill, L., Nakai, N., Diamond, P., & Inoue, M. 1995, Nature, 373, 127
- Moore, C. B., Carilli, C. L., & Menten, K. M. 1999, ApJ, 510, L87
- Moran, J. M., Greenhill, L. J., & Herrnstein, J. R. 1999, Journal of Astrophysics and Astronomy, 20, 165

- Moran, E. C., Kay, L. E., Davis, M., Filippenko, A. V., & Barth, A. J. 2001, *ApJ*, 556, L75
- Morganti, R., Greenhill, L. J., Peck, A. B., Jones, D. L., & Henkel, C. 2004, *New Astronomy Review*, 48, 1195
- Müller, H. S. P., Menten, K. M., Mäder, H. 2004, *A&A*, 428, 1019
- Mulchaey, J. S., Myshotzky, R. F., & Weaver, K. A. 1992, *ApJ*, 390, L69
- Mulchaey, J. S., Wilson, A. S., Bower, G. A., Heckman, T. M., Krolik, J. H., & Miley, G. K. 1994, *ApJ*, 433, 625
- Mulchaey, J. S., Wilson, A. S., & Tsvetanov, Z. 1996, *ApJS*, 102, 309
- Mundell, C. G., Pedlar, A., Baum, S. A., O’Dea, C. P., Gallimore, J. F., & Brinks, E. 1995, *MNRAS*, 272, 355
- Mundell, C. G., Wilson, A. S., Ulvestad, J. S., & Roy, A. L. 2000, *ApJ*, 529, 816
- Nagar, N. M., Wilson, A. S., Mulchaey, J. S., & Gallimore, J. F. 1999, *ApJS*, 120, 209
- Neff, S. G., & de Bruyn, A. G. 1983, *A&A*, 128, 318
- Nenkova, M., Ivezić, Ž., & Elitzur, M. 2002, *ApJ*, 570, L9
- Neufeld, D. A., Maloney, P. R., & Conger, S. 1994, *ApJ*, 436, L127
- Neufeld, D. A., & Maloney, P. R. 1995, *ApJ*, 447, L17
- Nguyen, Q.-R., Jackson, J. M., Henkel, C., Truong, B., & Mauersberger, R. 1992, *ApJ*, 399, 521
- Nieto, J.-L., Coupinot, G., Lelievre, G., & Madsen, C. 1983, *MNRAS*, 203, 39P
- Nolthenius, R. 1993, *ApJS*, 85, 1
- Noordermeer, E., van der Hulst, J. M., Sancisi, R., Swaters, R. A., & van Albada, T. S. 2005, *A&A*, 442, 137
- Norris, R. P., Gardner, F. F., Whiteoak, J. B., Allen, D. A., & Roche, P. F. 1989, *MNRAS*, 237, 673
- Norris, R. P., Whiteoak, J. B., Caswell, J. L., Wieringa, M. H., & Gough, R. G. 1993, *ApJ*, 412, 222
- O’Dea, C. P., & Baum, S. A. 1987, *AJ*, 94, 1476
- Omar, A., Anantharamaiah, K. R., Rupen, M., & Rigby, J. 2002, *A&A*, 381, L29
- Osterbrock, D. E., & Koski, A. T. 1976, *MNRAS*, 176, 61P
- Osterbrock, D. E., Shaw, R. A., & Veilleux, S. 1990, *ApJ*, 352, 561

- Ott, M., Witzel, A., Quirrenbach, A., Krichbaum, T. P., Standke, K. J., Schalinski, C. J., & Hummel, C. A. 1994, *A&A*, 284, 331
- Owen, F. N., O'Dea, C. P., & Keel, W. C. 1990, *ApJ*, 352, 44
- Owen, F. N., Ledlow, M. J., Morrison, G. E., & Hill, J. M. 1997, *ApJ*, 488, L15
- Pappa, A., Georgantopoulos, I., Stewart, G. C., & Zezas, A. L. 2001, *MNRAS*, 326, 995
- Pavlakis, K. G., & Kylafis, N. D. 2000, *ApJ*, 534, 770
- Peck, A. B., Taylor, G. B., & Conway, J. E. 1999, *ApJ*, 521, 103
- Peck, A. B., & Taylor, G. B. 2001, *ApJ*, 554, L147
- Peck, A. B., Henkel, C., Ulvestad, J. S., Brunthaler, A., Falcke, H., Elitzur, M., Menten, K. M., & Gallimore, J. F. 2003, *ApJ*, 590, 149
- Pedlar, A., Mundell, C. G., Gallimore, J. F., Baum, S. A., & O'Dea, C. P. 1996, *Vistas in Astronomy*, 40, 91
- Peng, R. S., & Whiteoak, J. B. 1992, *MNRAS*, 254, 301
- Pestalozzi, M. R., Minier, V., & Booth, R. S. 2005, *A&A*, 432, 737
- Phillips, M. M., Charles, P. A., & Baldwin, J. A. 1983, *ApJ*, 266, 485
- Phillips, C. J., Ellingsen, S. P., Rayner, D. P., & Norris, R. P. 1998, *MNRAS*, 294, 265
- Phinney, E. S. 1989, *Nature*, 340, 595
- Pier, E. A., & Krolik, J. H. 1992, *ApJ*, 401, 99
- Pier, E. A., & Krolik, J. H. 1993, *ApJ*, 418, 673
- Pihlström, Y. M., Conway, J. E., Booth, R. S., Diamond, P. J., & Polatidis, A. G. 2001, *A&A*, 377, 413
- Pihlström, Y. M., Fish, V. L., Sjouwerman, L. O., Zschaechner, L. K., Lockett, P. B., & Elitzur, M. 2008, *ApJ*, 676, 371
- Piner, B. G., Jones, D. L., & Wehrle, A. E. 2001, *AJ*, 122, 2954
- Planesas, P., Scoville, N., & Myers, S. T. 1991, *ApJ*, 369, 364
- Pogge, R. W. 1989, *ApJ*, 345, 730
- Poncelet, A., Perrin, G., & Sol, H. 2006, *A&A*, 450, 483
- Pringle, J. E. 1996, *MNRAS*, 281, 357
- Radovich, M., & Rafanelli, P. 1996, *A&A*, 306, 97
- Raluy, F., Planesas, P., & Colina, L. 1998, *A&A*, 335, 113
- Richards, G. T., et al. 2006, *AJ*, 131, 2766

- Rinn, A. S., Sambruna, R. M., & Gliozzi, M. 2005, *ApJ*, 621, 167
- Risaliti, G., Maiolino, R., & Salvati, M. 1999, *ApJ*, 522, 157
- Risaliti, G., Elvis, M., & Nicastro, F. 2002, *ApJ*, 571, 234
- Rodríguez-Ardila, A., Pastoriza, M. G., Viegas, S., Sigut, T. A. A., & Pradhan, A. K. 2004, *A&A*, 425, 457
- Ros, E., Guirado, J. C., Marcaide, J. M., Pérez-Torres, M. A., Falco, E. E., Muñoz, J. A., Alberdi, A., & Lara, L. 2000, *A&A*, 362, 845
- Rush, B., Malkan, M. A., & Edelson, R. A. 1996, *ApJ*, 473, 130
- Salpeter, E. E. 1964, *ApJ*, 140, 796
- Salvati, M., & Maiolino, R. 2000, Large Scale Structure in the X-ray Universe, Proceedings of the 20-22 September 1999 Workshop, Santorini, Greece, eds. Plionis, M. & Georgantopoulos, I., Atlantisciences, Paris, France, p.277, 277
- Sambruna, R. M., Eracleous, M., & Mushotzky, R. F. 1999, *ApJ*, 526, 60
- Sambruna, R. M., Gliozzi, M., Eracleous, M., Brandt, W. N., & Mushotzky, R. 2003, *ApJ*, 586, L37
- Sanders, D. B., & Mirabel, I. F. 1985, *ApJ*, 298, L31
- Sanders, D. B., & Mirabel, I. F. 1996, *ARA&A*, 34, 749
- Sanders, D. B., Mazzarella, J. M., Kim, D.-C., Surace, J. A., & Soifer, B. T. 2003, *AJ*, 126, 1607
- Sawada-Satoh, S., Inoue, M., Shibata, K. M., Kamenno, S., Migenes, V., Nakai, N., & Diamond, P. J. 2000, *PASJ*, 52, 421
- Schartmann, M., Meisenheimer, K., Camenzind, M., Wolf, S., & Henning, T. 2005, *A&A*, 437, 861
- Schechter, P. L., & Moore, C. B. 1993, *AJ*, 105, 1
- Schinnerer, E., Eckart, A., Tacconi, L. J., Genzel, R., & Downes, D. 2000, *ApJ*, 533, 850
- Schmelz, J. T., Baan, W. A., Haschick, A. D., & Eder, J. 1986, *AJ*, 92, 1291
- Schmelz, J. T., & Baan, W. A. 1988, *AJ*, 95, 672
- Schmidt, G. D., & Miller, J. S. 1985, *ApJ*, 290, 517
- Sergeev, V. I., Pronik, S. G., & Sergeeva, E. A. 2001, *ApJ*, 554, 245
- Seyfert, C. K. 1943, *ApJ*, 97, 28
- Shakura, N. I., & Syunyaev, R. A. 1973, *A&A*, 24, 337

- Shankar, F., Salucci, P., Granato, G. L., De Zotti, G., & Danese, L. 2004, MNRAS, 354, 1020
- Shostak, G. S., Sanders, R. H., Goss, W. M., van Gorkom, J. H., Ekers, R. D., & Cornwell, T. J. 1983, A&A, 119, L3
- Simkin, S. M., Su, H.-J., van Gorkom, J., & Hibbard, J. 1987, Science, 235, 1367
- Simpson, C., Mulchaey, J. S., Wilson, A. S., Ward, M. J., & Alonso-Herrero, A. 1996, ApJ, 457, L19
- Sinclair, M. W., Carrad, G. J., Caswell, J. L., Norris, R. P., & Whiteoak, J. B. 1992, MNRAS, 256, 33P
- Sobolev, A. M., Cragg, D. M., & Godfrey, P. D. 1997, A&A, 324, 211
- Sobolev, A. M., Sutton, E. C., Cragg, D. M., & Godfrey, P. D. 2005, Ap&SS, 295, 189
- Soifer, B. T., et al. 2000, AJ, 119, 509
- Sosa-Brito, R. M., Tacconi-Garman, L. E., Lehnert, M. D., & Gallimore, J. F. 2001, ApJS, 136, 61
- Scoville, N. Z., Sanders, D. B., Sargent, A. I., Soifer, B. T., & Tinney, C. G. 1989, ApJ, 345, L25
- Shuder, J. M. 1980, ApJ, 240, 32
- Slee, O. B. 1977, Australian Journal of Physics Astrophysical Supplement, 43, 1
- Staveley-Smith, L., Cohen, R. J., Chapman, J. M., Pointon, L., & Unger, S. W. 1987, MNRAS, 226, 689
- Staveley-Smith, L., Norris, R. P., Chapman, J. M., Allen, D. A., Whiteoak, J. B., & Roy, A. L. 1992, MNRAS, 258, 725
- Storchi-Bergmann, T., Wilson, A. S., & Baldwin, J. A. 1992, ApJ, 396, 45
- Storchi-Bergmann, T., Winge, C., Ward, M. J., & Wilson, A. S. 1999, MNRAS, 304, 35
- Strauss, M. A., Huchra, J. P., Davis, M., Yahil, A., Fisher, K. B., & Tonry, J. 1992, ApJS, 83, 29
- Swain, M., et al. 2003, ApJ, 596, L163
- Tacconi, L. J., Genzel, R., Tecza, M., Gallimore, J. F., Downes, D., & Scoville, N. Z. 1999, ApJ, 524, 732
- Tacconi, L. J., Genzel, R., Lutz, D., Rigopoulou, D., Baker, A. J., Iserlohe, C., & Tecza, M. 2002, ApJ, 580, 73
- Tananbaum, H., Gursky, H., Kellogg, E. M., Levinson, R., Schreier, E., & Giacconi, R. 1972, ApJ, 174, L143

- Taniguchi, Y., Kameya, O., Nakai, N., & Kawara, K. 1990, *ApJ*, 358, 132
- Tarchi, A., Henkel, C., Peck, A. B., & Menten, K. M. 2002, *A&A*, 385, 1049
- Tarchi, A., Henkel, C., Chiaberge, M., & Menten, K. M. 2003, *A&A*, 407, L33
- Taylor, G. B. 1996, *ApJ*, 470, 394
- Terashima, Y., Iyomoto, N., Ho, L. C., & Ptak, A. F. 2002, *ApJS*, 139, 1
- Thean, A., Pedlar, A., Kukula, M. J., Baum, S. A., & O'Dea, C. P. 2000, *MNRAS*, 314, 573
- Thompson, R. I. 1995, *ApJ*, 445, 700
- Thorne, K. S., & Price, R. H. 1975, *ApJ*, 195, L101
- Thornton, R. J., Jr., Stockton, A., & Ridgway, S. E. 1999, *AJ*, 118, 1461
- Tonry, J. L., & Kochanek, C. S. 1999, *AJ*, 117, 2034
- Tonry, J. L., Dressler, A., Blakeslee, J. P., Ajhar, E. A., Fletcher, A. B., Luppino, G. A., Metzger, M. R., & Moore, C. B. 2001, *ApJ*, 546, 681
- Tran, H. D., Miller, J. S., & Kay, L. E. 1992, *ApJ*, 397, 452
- Tran, H. D. 1995, *ApJ*, 440, 565
- Tran, H. D. 2001, *ApJ*, 554, L19
- Tristram, K. R. W., et al. 2007, *A&A*, 474, 837
- Trotter, A. S., Greenhill, L. J., Moran, J. M., Reid, M. J., Irwin, J. A., & Lo, K.-Y. 1998, *ApJ*, 495, 740
- Trotter, C. S., Winn, J. N., & Hewitt, J. N. 2000, *ApJ*, 535, 671
- Turner, T. J., & Pounds, K. A. 1989, *MNRAS*, 240, 833
- Turner, T. J., George, I. M., Nandra, K., & Mushotzky, R. F. 1997, *ApJS*, 113, 23
- Ueno, S., Koyama, K., Nishida, M., Yamauchi, S., & Ward, M. J. 1994, *ApJ*, 431, L1
- Ulrich, M.-H. 2000, *A&AR*, 10, 135
- Ulvestad, J. S., & Wilson, A. S. 1983, *ApJ*, 264, L7
- Ulvestad, J. S., & Wilson, A. S. 1984, *ApJ*, 285, 439
- Ulvestad, J. S., & Wilson, A. S. 1989, *ApJ*, 343, 659
- Ulvestad, J. S., Wrobel, J. M., & Carilli, C. L. 1999, *ApJ*, 516, 127
- Unger, S. W., Pedlar, A., Neff, S. G., & de Bruyn, A. G. 1984, *MNRAS*, 209, 15P
- Urry, C. M., & Padovani, P. 1995, *PASP*, 107, 803

- van Driel, W., & Buta, R. J. 1991, *A&A*, 245, 7
- van Gorkom, J. H., & Ekers, R. D. 1983, *ApJ*, 267, 528
- van Gorkom, J. H., et al. 2003, *Ap&SS*, 285, 219
- van Langevelde, H. J., Pihlström, Y. M., Conway, J. E., Jaffe, W., & Schilizzi, R. T. 2000, *A&A*, 354, L45
- Veilleux, S. 1991, *ApJS*, 75, 383
- Veilleux, S., Cecil, G., Bland-Hawthorn, J., Tully, R. B., Filippenko, A. V., & Sargent, W. L. W. 1994, *ApJ*, 433, 48
- Veilleux, S., Goodrich, R. W., & Hill, G. J. 1997, *ApJ*, 477, 631
- Vermeulen, R. C., Ros, E., Kellermann, K. I., Cohen, M. H., Zensus, J. A., & van Langevelde, H. J. 2003, *A&A*, 401, 113
- Vignati, P., et al. 1999, *A&A*, 349, L57
- Vila-Vilaró, B., Taniguchi, Y., & Nakai, N. 1998, *AJ*, 116, 1553
- Walmsley, C. M., Menten, K. M., Batrla, W., & Matthews, H. E. 1988, *A&A*, 197, 271
- Ward, M. J., Wilson, A. S., Penston, M. V., Elvis, M., Maccacaro, T., & Tritton, K. P. 1978, *ApJ*, 223, 788
- Ward, M. J., Blanco, P. R., Wilson, A. S., & Nishida, M. 1991, *ApJ*, 382, 115
- Wardle, M. 2007, *Ap&SS*, 311, 35
- Warwick, R. S., Koyama, K., Inoue, H., Takano, S., Awaki, H., & Hoshi, R. 1989, *PASJ*, 41, 739
- Weaver, K. A., et al. 1994, *ApJ*, 423, 621
- Weaver, K. A., Nousek, J., Yaqoob, T., Mushotzky, R. F., Makino, F., & Otani, C. 1996, *ApJ*, 458, 160
- Weaver, K. A., Wilson, A. S., Henkel, C., & Braatz, J. A. 1999, *ApJ*, 520, 130
- Webster, B. L., & Murdin, P. 1972, *Nature*, 235, 37
- Weigelt, G., Wittkowski, M., Balega, Y. Y., Beckert, T., Duschl, W. J., Hofmann, K.-H., Men'shchikov, A. B., & Schertl, D. 2004, *A&A*, 425, 77
- Werner, P. N., Worrall, D. M., & Birkinshaw, M. 2000, *MNRAS*, 317, 105
- Whiteoak, J. B., & Gardner, F. F. 1987, *Proceedings of the Astronomical Society of Australia*, 7, 88
- Whiteoak, J. B., & Peng, R.-S. 1989, *MNRAS*, 239, 677

- Wilner, D. J., Bourke, T. L., Ho, P. T. P., Killeen, N. E. B., & Calabretta, M. 1999, *AJ*, 117, 1139
- Wilson, A. S., Braatz, J. A., & Henkel, C. 1995, *ApJ*, 455, L127
- Wilkes, B. J., Schmidt, G. D., Smith, P. S., Mathur, S., & McLeod, K. K. 1995, *ApJ*, 455, L13
- Wilson, A. S., & Baldwin, J. A. 1985, *ApJ*, 289, 124
- Wright, G. S., Joseph, R. D., & Meikle, W. P. S. 1984, *Nature*, 309, 430
- Wynn-Williams, C. G., & Becklin, E. E. 1993, *ApJ*, 412, 535
- Xia, X. Y., Xue, S. J., Mao, S., Boller, T., Deng, Z. G., & Wu, H. 2002, *ApJ*, 564, 196
- Yang, Y., Wilson, A. S., & Ferruit, P. 2001, *ApJ*, 563, 124
- Yankulova, I. M. 1999, *A&A*, 344, 36
- Yates, J. A., Richards, A. M. S., Wright, M. M., Collett, J. L., Gray, M. D., Field, D., & Cohen, R. J. 2000, *MNRAS*, 317, 28
- Young, J. S., & Devereux, N. A. 1991, *ApJ*, 373, 414
- Zakamska, N. L., et al. 2005, *AJ*, 129, 1212
- Zel'Dovich, Y. B. 1964, *Soviet Physics Doklady*, 9, 195

Acknowledgments

# Acknowledgments

I could say that it has taken me longest to write the acknowledgments, being the last part of my thesis. But figuratively this statement should be true, since a big part of this work has been supported, in so many ways, by many people - and it should take the longest to write. I am very grateful to all of them.

I would like to thank first of all my *Referenten* Prof. Ulrich Klein and Priv. Doz. Dr. Walter Huchtmeier for being part of my thesis committee and the many constructive suggestions to improve this work at various stages. I would also like to thank Prof. Karl Maier and Prof. Stephen Miller for agreeing to be in my examination board.

Also, my gratitude goes to Dr. Arno Witzel for encouraging me to start my PhD here at the institute and for letting me know he believes in me throughout the years. I am thankful to him for his trust and his enthusiasm towards my work. I thank Prof. A. Zensus for taking me on in his group and for the financial support over the years. I also particularly thank Richard Porcas, for the many discussions about physics, the 'daily quizzes' on the blackboard, and for his support and advice in all areas of my work - and of course for helping find the appropriate arrangement of the desks, we can fit four people now!

I especially thank my supervisor Alan Roy, for the great help and presence at any time and all stages of this thesis, through detailed data reduction - trying to understand a funny 'step' in the spectrum or learning Parseltongue - to the the fascination for physics, even in its every-day manifestations, he has passed on to me. Alan has been a backbone to this work.

I would like to thank all the people I have worked with in the last few years. The 'troop' members Christian Henkel, his passion for 'science' is contagious and Paola Castangia, it has been great working with her, and always ready to help even during my moaning periods. I thank Alex Kraus, who has been a friend and a real support in all ways during my time in Bonn and in Effelsberg - thank you also for trusting me to use the telescope alone right for the start ('now fire'). I would like to thank the other 'troop members' Andreas Brunthaler and Olaf Wucknitz, our amazing project would not be quite the same without them. I thank Thomas Krichbraum and Prof. Karl Menten for their great contributions in different projects.

I owe my gratitude to all colleagues, office mates and friends in the institute, who have helped me and encouraged me in many ways, from existential problems to nagging AIPS ones, and for making me laugh from time to time. For this I thank Simone Bernhart, Silvia Leurini, Konrad Tristram (who has just brought a croissant, danke!), Manolis Angelakis, Sang-Sung Lee, Marios Karouzos, Anupreeta More and Elena Cenacchi.

My biggest thank you, though he probably doesn't know it, goes to John McKean, for his support, and infinite patience. Without him, I would have probably finished much,

much sooner, but would not be where I am now. Finally, behind me all these years have been my parents, to them I dedicate this work, they helped me get out of bad times and were always joying with me when good times would come. Grazie.

Ich versichere, daß ich die vorliegende Arbeit selbständig verfaßt und keine anderen als die angegebenen Quellen und Hilfsmittel benutzt sowie die Zitate kenntlich gemacht habe.

Referent: Prof. Dr. U. Klein  
Koreferent: Priv.-Doz. Dr. W. K. Huchtmeier